

Improved Predictions for Geotechnical Vibrations

Improved Predictions for Geotechnical Vibrations
2016 D. Macijauskas

D. Macijauskas



PhD-FSTC-2015-65
The Faculty of Sciences, Technology and Communication

DISSERTATION

Defence held on 11/12/2015 in Luxembourg

to obtain the degree of

DOCTEUR DE L'UNIVERSITÉ DU LUXEMBOURG EN SCIENCES DE L'INGÉNIEUR

by

Darius MACIJAUSKAS

Born on 25 January 1986 in Utena, Lithuania

IMPROVED PREDICTIONS FOR GEOTECHNICAL VIBRATIONS

Dissertation defence committee

Prof. Dr. Ir. Stefan Van Baars, dissertation supervisor
Professor, Université du Luxembourg

Prof. Dr.-Ing. Christoph Odenbreit, Chairman
Professor, Université du Luxembourg

Prof. Dr.-Ing. Andreas Zilian, Vice Chairman
Professor, Université du Luxembourg

Prof. Dr. Ir. Alain Holeymans
Professor, Université catholique de Louvain

Dr. Ir. Paul Hölscher
Postdoctoral Researcher, Delft University of Technology
Senior Expert, Deltares

ABSTRACT

In urban areas where the infrastructure is dense and construction of new structures is near existing and sensitive buildings, frequently vibrations, caused by human activities, occur. Generated waves in the soil may adversely affect surrounding buildings. These vibrations have to be predicted a priori by using currently available knowledge of the soil dynamics. Current research, conducted by Deltares research institute, showed that the reliability of methods for prediction of man-made vibrations is disappointingly low. Therefore the models for vibrations in the soil should be improved in order to get more accurate predictions.

The main aim of this thesis is to increase the knowledge on dynamic soil behaviour with respect to the fundamental geotechnical aspects of the soil, like non-viscous damping, inhomogeneity, anisotropy, variable degree of saturation, etc. and to give an improved prediction method.

The scientific investigations of this thesis started with the following setup: an oscillating plate on an elastic, homogeneous and isotropic half-space, where the plate oscillates harmonically in vertical direction and the soil is unsaturated. In this way, the geotechnical aspects have been left aside in order to check first whether it is possible to predict the vibration amplitudes of the oscillating plate and of the soil surface, without additional complexities.

This setting allowed to compare the present analytical methods with the results, obtained from the finite element method (FEM) calculations, and showed that the analytical methods have their limitations. Therefore the wave-field near an oscillating plate had to be investigated more carefully. Unfortunately the state of the art in soil dynamics is such that only the particle vibration velocities are measured without knowing which part of the velocities/vibrations belongs to which type of basic wave (compressional, shear or Rayleigh wave). Therefore first of all, a technique to decompose the measured signal into its basic waves was developed. This new technique showed remarkably that all three basic waves have phase shifts and these phase shifts are all different from each other. The decomposition technique is an important tool for researching soil dynamics. Also a qualitative evaluation of the energy transmission between the basic waves near the vibration source was given, which showed that the R-wave energy starts at zero just at the source and grows in the near-field zone due to an energy transmission (body waves are transferring energy to the R-wave). This means that even without uncertainties in the soil body, there is a lack of understanding of the behaviour of the different waves.

A real field test is performed with a shaker on a soft peaty site in the Netherlands, as an attempt to replicate the FE model experiments. It showed the limitations of the analytical methods and highlighted the indispensability of the FEM. Still, for engineering purposes, an improved analytical method is suggested, which is able to predict the geotechnical vibrations with good accuracy. Herein, one of the fundamental aspects, the material damping, was used and a hypothesis was made, that with a more correct physical model of the soil material damping, the vibration predictions with FEM can be improved.

The 1D frictional damping model, first suggested by Van Baars (2011), was extended for the 3D and incorporated into the FEM software Plaxis as a User Defined Soil Material model. The results are very interesting scientifically, but do not give much better results as the already existing Rayleigh damping model.

ACKNOWLEDGEMENTS

I would like to express my greatest gratitude to my supervisor Professor Stefan Van Baars. I thank him for giving me an opportunity to make this dissertation in the University of Luxembourg. I am also very grateful for his support, encouragement and guidance throughout the development of this thesis. I thank my dissertation committee members' Professor Andreas Zilian and Professor Christoph Odenbreit for their valuable comments and advices. I am thankful to Robert Pytlik for his help with on-site experiments. Likewise I would like to thank all the members of the Research Unit in Engineering Science for being supportive, friendly and for the pleasant years in the University of Luxembourg.

CONTENT

ABSTRACT	III
ACKNOWLEDGEMENTS	IV
LIST OF SYMBOLS.....	VII
1 INTRODUCTION.....	11
1.1 BACKGROUND OF THE PROBLEM	11
1.2 GOALS OF THIS WORK.....	12
1.3 OUTLINE OF THE THESIS	12
2 INTRODUCTION INTO SOIL DYNAMICS.....	13
2.1 INTRODUCTION.....	13
2.2 WAVES IN A SOIL BODY	13
2.3 DAMPING.....	14
2.4 ATTENUATION.....	19
2.5 HETEROGENEITY	24
2.6 ANISOTROPY	25
2.7 DEGREE OF SATURATION.....	26
2.8 AIR CONTENT	27
2.9 LAYERING	27
2.10 AMPLITUDE OF A HARMONICALLY OSCILLATING PLATE	28
2.11 SURFACE VIBRATIONS NEAR A HARMONICALLY OSCILLATING PLATE.....	33
2.12 WAVES FIELD UNDER A HARMONICALLY OSCILLATING PLATE	35
2.13 CONCLUSIONS	36
3 HARMONICALLY OSCILLATING PLATE	37
3.1 INTRODUCTION.....	37
3.2 THEORY VERSUS FEM.....	37
3.3 CONCLUSIONS	42
4 DECOMPOSITION OF WAVES.....	45
4.1 INTRODUCTION.....	45
4.2 DECOMPOSITION TECHNIQUE	45
4.3 NUMERICAL SIMULATION	47
4.4 SIMULATION RESULTS	48
4.5 ENERGY BALANCE.....	51
4.6 NEAR-FIELD PROBLEM.....	56
4.7 CONCLUSIONS	59
5 SHAKER TEST.....	61
5.1 INTRODUCTION.....	61
5.2 SHAKER DESIGN	61
5.3 INFORMATION ABOUT THE SITE	64
5.4 VIBRATION MEASUREMENTS	67
5.5 MEASUREMENTS VS. ANALYTICAL AND FEM CALCULATIONS	70
5.6 CONCLUSIONS	73
6 DEVELOPED VIBRATION PREDICTION METHOD	75
6.1 INTRODUCTION.....	75
6.2 DERIVATION OF THE METHOD.....	75
6.3 POST-DICTION OF THE SHAKER TEST VIBRATIONS.....	77
6.4 COMPARISON WITH FEM CALCULATIONS	77
6.5 CONCLUSIONS	80

7	FRICTIONAL DAMPING MODEL.....	81
7.1	INTRODUCTION.....	81
7.2	1D STATE	81
7.3	3D STATE	83
7.4	DAMPED ENERGY IN A 3D STATE.....	85
7.5	USER DEFINED SOIL MATERIAL MODEL.....	86
7.6	VERIFICATION TESTS	90
7.7	VALIDATION TESTS	94
7.8	PULSE LOAD – RAYLEIGH DAMPING VERSUS FRICTIONAL DAMPING	99
7.9	CONCLUSIONS	101
8	CONCLUSIONS AND RECOMMENDATIONS	103
8.1	CONCLUSIONS	103
8.2	RECOMMENDATIONS	105
BIBLIOGRAPHY.....		107
APPENDIX A. MATLAB CODE FOR DECOMPOSITION OF WAVES		113
APPENDIX B. TECHNICAL DATA OF VIBRATORS AND GEOPHONES		119
APPENDIX C. VIBRATION MEASUREMENTS ON PEAT SITE.....		123
APPENDIX D. DEVELOPED VIBRATION PREDICTION METHOD COMPARISON WITH FEM RESULTS		127
APPENDIX E. PASCAL CODE FOR UDSM OF FRICTIONAL DAMPING MODEL.....		141
CURRICULUM VITAE		152

LIST OF SYMBOLS

Latin

a	Acceleration
a_0	Dimensionless frequency
b	Dimensionless mass ratio
c	Viscosity
e_{ii}	Normal deviatoric strains ($i = x, y$ or z)
e_{ij}	Tangential deviatoric strains ($ij = x, y$, or z , but $i \neq j$)
\hat{e}_{ii}	Normal deviatoric strain amplitude ($i = x, y$ or z) in $\tau' - e'$ coordinates
\hat{e}_{ij}	Tangential deviatoric strain amplitude ($i = x, y$ or z) in $\tau' - e'$ coordinates
f_1, f_2	Displacement (compliance) functions
f_{1s}, f_{2s}	Displacement (compliance) functions for the surface vibration
i	Angle of incidence
k	Spring stiffness (or the coefficient analogues to the spring stiffness)
k_m	Empirical absorption coefficient
k_s	S-wave number
k_{sct}	Empirical scattering coefficient
k_p	P-wave number
k_r	R-wave number
m	Attenuation rate
m_c	Material constant
m_{vib}	Mass of a vibrating object
r	Radius (distance) from the source to the point of interest
r_{ff}	Start of the far-field
r_0	Radius (distance) from the source to the point where the amplitude is known
r_{pl}	Radius of a plate
t	Time
u	Displacement
$u_{j,i}(r, t)$	displacement of the j -wave in time and space (i indicates the direction)
u_h	Horizontal displacement
u_v	Vertical displacement
$\hat{u}_{v,nf}$	Vertical soil displacement amplitude in the near-field
$\hat{u}_{v,ff}$	Vertical soil displacement amplitude in the far-field
$u_{v,plate}$	Vertical displacement of a plate
u_k	Measured displacements
u_k'	Back-calculated displacements
\hat{u}	Displacement amplitude

\hat{u}_0	Displacement at known distance r_0
\hat{u}_b	Displacement amplitude of a body wave
\hat{u}_B	Displacement amplitude from Barkan's solution
$\hat{u}_{p,i}$	P-wave displacement amplitude (i indicates the direction)
$\hat{u}_{r,i}$	R-wave displacement amplitude (i indicates the direction)
$\hat{u}_{s,i}$	S-wave displacement amplitude (i indicates the direction)
\hat{u}_{stat}	Static displacement
\bar{u}_k	Average of the measured displacements
v	Velocity
v_p	P-wave velocity
v_r	R-wave velocity
v_s	S-wave velocity
\vec{v}_i	Velocity vector in i (x, y, z) direction.
$\{u\}$	Displacements' vector
$\{\dot{u}\}$	Velocities' vector
$\{\ddot{u}\}$	Accelerations' vector
$\{x\}$	Vector of unknowns (amplitudes)
$\{x'\}$	The least squares solution
B	Modified dimensionless mass ratio
D_p	Diameter of a pile
E	Elastic (Young's) modulus
E'	Energy per unit area
E_{kin}^*	Kinetic energy per volume
E_p	Peak potential energy during a single cycle
E_{pv}	Potential strain energy which changed the volume (related to K)
E_{ps}	Potential strain energy which changed the shape (related to G)
ΔE	Dissipated energy per cycle
E_{tot}	Total energy per cycle
E_{tot}^*	Total energy per volume
$E_{tot,p}$	Total energy in the P-wave per cycle
$E_{tot,r}$	Total energy in the R-wave per cycle
$E_{tot,s}$	Total energy in the S-wave per cycle
F_0	Amplitude of a vertically exciting force
G	Shear modulus
G_0	Small strain shear modulus (or maximum shear modulus)
G_{mod}	Modified shear modulus
G_{sec}	Secant shear modulus
J_0	Bessel function of the first kind, zero order
J_1	Bessel function of the first kind, first order
K	Bulk modulus

M_e	Eccentric moment
P_0	Amplitude of a soil reaction force
R^2	Correlation factor
X	Dimensionless damping parameter
$[A]$	Coefficient matrix
$[B]$	Strain interpolation matrix
$[C]$	Damping matrix
$[D]$	Elasticity matrix
$[D_G]$	Elasticity matrix of the shape change
$[D_K]$	Elasticity matrix of the volume change
$[K]$	Stiffness matrix
$[M]$	Mass matrix
$\{F\}$	Force vector

Greek

α	Influence coefficient of mass in the system's damping,
β	Influence coefficient of stiffness in the system's damping,
γ	Shear strain
γ_{ij}	Shear strain ($ij = x, y, \text{ or } z$, but $i \neq j$)
γ_{max}	Stored maximum shear strain
γ_{min}	Stored minimum shear strain,
$\hat{\gamma}$	Shear strain amplitude
$\hat{\gamma}'$	Shear strain amplitude in a modified coordinates system
ε_{ii}	Normal strain ($i = x, y, \text{ or } z$)
ε_{ij}	Shear strain ($ij = x, y, \text{ or } z$, but $i \neq j$)
ε_{vol}	Volumetric strain
ζ	The ratio of the dissipated energy to the peak energy
λ	Wave length
λ_p	P-wave length
λ_r	R-wave length
λ_s	S-wave length
$\bar{\lambda}$	Lamé's first parameter
ν	Poisson's ratio
ξ	Damping ratio
ρ	Density
ς	Empirical coefficient
σ_0	Isotropic stress
σ_{ii}	Normal stress ($i = x, y, \text{ or } z$)
σ_{ij}	Shear stress ($ij = x, y, \text{ or } z$, but $i \neq j$)
τ	Shear stress

τ_{ii}	Normal deviatoric stress ($i = x, y, \text{ or } z$)
τ_{ij}	Tangential deviatoric stress ($ij = x, y, \text{ or } z, \text{ but } i \neq j$)
τ_{min}	Stored minimum shear stress
$\tau_{out,down}$	Shear stresses of the descending outer line
$\tau_{out,up}$	Shear stresses of the rising outer line
τ_{vir}	Virgin shear stress of the soil
τ'	Shear stress in a modified coordinates system
$\hat{\tau}'$	Shear stress amplitude in a modified coordinates system
$\hat{\tau}'_{ii}$	Normal deviatoric stress amplitude ($i = x, y \text{ or } z$) in $\tau' - e'$ coordinates
$\hat{\tau}'_{ij}$	Tangential deviatoric stress amplitude ($i = x, y \text{ or } z$) in $\tau' - e'$ coordinates
$\Delta\phi$	Phase shift
ω	Angular frequency
ω_c	Characteristic angular frequency
θ	Angular coordinate (often called the polar angle)
$\{\varepsilon\}$	Strain vector
$\{\sigma\}$	Stress vector

ABBREVIATIONS

FE	Finite element
FEM	Finite element method
FFT	Fast Fourier Transform
P-wave	Pressure wave
R-wave	Rayleigh wave
S-wave	Shear wave
SH-wave	Shear horizontal wave
SV-wave	Shear vertical wave
UDSM	User Defined Soil Model
L-wave	Love wave
PPV	Peak particle velocity

1 INTRODUCTION

1.1 Background of the problem

In urban areas where the infrastructure is dense and construction of new structures is near existing ones, frequently vibrations, caused by human activities, occur. Generated waves in the soil may adversely affect surrounding buildings. The most known sources of man-made vibrations are traffic (trains, buses, lorries) and civil construction activities (installation of piles or sheet piles, tunnelling, demolishing structures, etc.).

Because of environmental requirements, the level of the vibrations should not exceed certain threshold values which are recommended (or prescribed depending on country regulations) in order to protect people from discomfort, existing structures from damage or technological processes (where vibration sensitive instruments are used) from disturbance. This means that the level of vibration must be predicted before the start of activities which cause vibrations.

The prediction of vibrations is a complex task. The total vibrations system consists of three main components: source-soil, soil-soil and soil-structure. The vibration level is usually measured in the structure. These three main parts are presented in Figure 1-1.

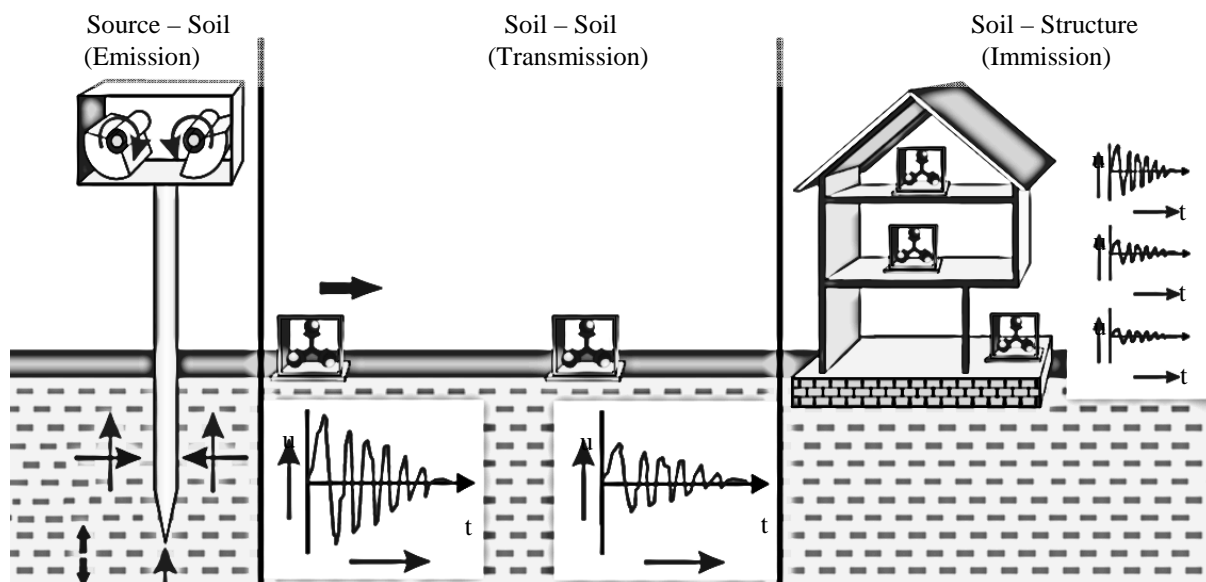


Figure 1-1. Complexity of the vibrations predictions (ThyssenKrupp brochure).

According to research in Deltares (Hölscher & Waarts, 2003), the reliability of methods for prediction of environmental vibrations is disappointingly low and the uncertainty in the soil-soil (transmission) part is larger than in the soil-structure system. In fact neither the soil models nor soil-structure models are accurate enough. Therefore the models for vibrations in the soil should be improved in order to get more accurate predictions.

Generally four methods to predict the vibrations can be found in literature: expert judgment, analytical, ray trace and numerical methods (Van Baars, 2009). The latter method is the most accurate. Nevertheless according to the hypothesis (Van Baars & Hölscher, 2010), the current method of dynamic modelling neglects several fundamental geotechnical aspects such as

non-viscous damping, inhomogeneity, anisotropy, variable degree of saturation and others. Or maybe something else is fundamentally wrong or missing. In order to confirm or reject this hypothesis fundamental research in the field of soil dynamics should be done. All known aspects which can be a cause of low prediction reliability, are filled in the table below.

Table 1-1. List of aspects causing problems in dynamic modelling.

Aspect	Discussed by
Inhomogeneity	Bodare, (1998), Andersen (2006), Jones and Hunt (2012a), (2012b)
Anisotropy	Helbig (1993), Andersen (2006)
Degree of saturation	Biot (1941), (1955), (1956a), (1956b), Hölscher (1995), Nakagawa and Soga (1995), Carcione et al. (2004)
Damping	Masoumi et al. (2008) (2008b), Van Baars (2011)
Air Content	Smeulders (1992)
Layering	Auersch (1995), Kramer (1996), Baidya (2000), Andersen (2006)
Non-Viscous damping	Bolton & Wilson (1990), Van Baars (2011)

1.2 Goals of this work

The goal of this study is to make an improved method, which should be able to predict the vibrations of the soil more accurately.

The first step to achieve the goal is to collect the knowledge on soil behaviour during dynamic loading with respect to fundamental soil mechanical aspects, and to find the main causes of the inaccuracy of the predictions, which might be related to the:

- inhomogeneity,
- anisotropy,
- variable degree of saturation,
- non-viscous damping,
- and layering

of the soil. These main causes could be tested systematically by modelling and testing.

1.3 Outline of the thesis

The thesis consists of eight chapters. In the first chapter, called Introduction, the problem statement is made, goals are formed and this outline of the thesis is given. In the second chapter (Introduction into soil dynamics) a summary from the large field of soil dynamics is presented, with a focus on man-made geotechnical vibrations. The investigation of man-made geotechnical vibrations for probably the simplest case to start with, a harmonically vertically oscillating plate, is started in the 3rd chapter. In the 4th chapter, called Decomposition of waves, the problem is split into three different, smaller problems, by decomposing the superposed wave on the soil surface into different soil waves. In the 5th chapter real field tests of a shaker on the ground surface of real soil have been performed. The test results are discussed, by comparing them with the results obtained by analytical and numerical methods. In the 6th chapter an improved prediction method is developed. The 7th chapter deals with a frictional damping model, which was first suggested by Van Baars (2011) in one dimensional form. This model was extended for three dimensions and incorporated into finite element method (FEM) software calculation scheme. In the last, 8th chapter, the findings of the work are summarised, and conclusions are given.

2 INTRODUCTION INTO SOIL DYNAMICS

2.1 Introduction

There are many books where the fundamentals of the soil dynamics are described by Kramer (1996), Verruijt (2006), Van Baars (2009), Das & Ramana (2011). Unfortunately some of them focus more on applications to earthquake engineering or machine foundations and do not handle a lot, or at all, about man-made geotechnical vibrations. In this chapter a summary from the large field of soil dynamics is presented, with a focus on man-made geotechnical vibrations.

2.2 Waves in a soil body

Energy in the soil travels in a form of waves. The waves move the soil and we notice these as vibrations. There are different kinds of waves: body and surface waves. Analysing the simplest case, an elastic homogeneous isotropic half-space, there are three basic waves – the Compressional (P-wave), Shear (S-waves) and Rayleigh wave (Rayleigh, 1885) (R-wave) (Figure 1-1).

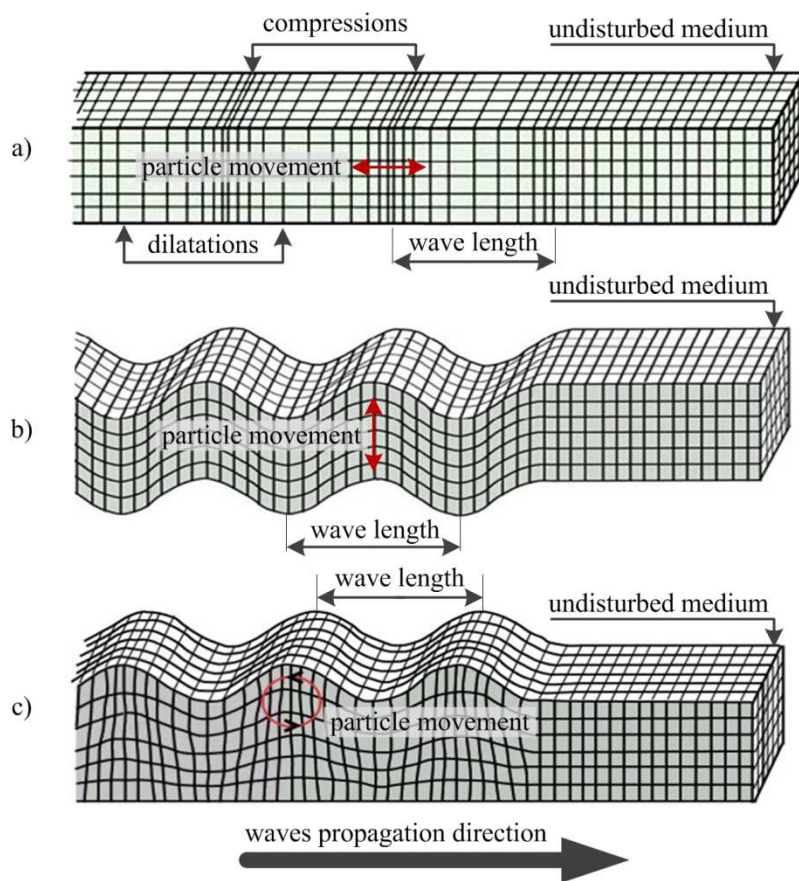


Figure 2-1. Basic waves in a soil body a) Compressional wave b) Shear wave c) Rayleigh wave (Kramer, 1996).

The first two are body waves, the last is a surface wave. Although for a homogeneous case these three basic waves are non-dispersive (wave velocity does not depend on a vibration frequency), these waves still have different attenuations, different propagation laws (wave

velocity) and different damping laws. Vibration caused by basic waves is a superposition of the individual behaviour of these basic waves.

If an elastic half-space is not homogeneous (i.e. the soil is layered), then the R-wave becomes a dispersive wave (wave velocity depends on a vibration frequency). Also, if an upper layer of a half-space has a lower body wave velocity than the rest of the half-space below it, the Love wave (Love, 1927) can appear. L-waves are always dispersive. Moreover, layering causes reflection and refraction of waves (both phenomena are briefly introduced in the following subchapters). So, the total picture of waves in a layered soil, in terms of energy transformation between waves, is very complex.

2.3 Damping

The energy travels in a form of waves and in a real medium the total amount of energy is always damped. Material damping is a loss of vibration energy, because part of the energy of the travelling waves in a material is converted into heat. The heat is produced due to friction between soil particles or between soil particles and pore water. This energy loss per volume can also be seen as an absorption damping.

A simple way to illustrate material damping mathematically is to use the Kelvin-Voigt model (Figure 2-2). The Kelvin–Voigt model, also called the Voigt model, can be represented by a purely viscous damper and purely elastic spring connected in parallel (Wikipedia).

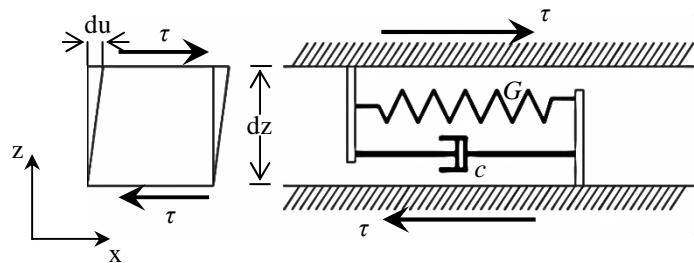


Figure 2-2. Kelvin-Voigt model.

Total shear resistance is the sum of an elastic component (a spring) and a viscous component (a dashpot).

$$\tau = G\gamma + c \frac{\partial \gamma}{\partial t}, \quad (2-1)$$

in which:

τ	=	shear stress,	$[\text{N}/\text{m}^2]$
G	=	shear modulus,	$[\text{N}/\text{m}^2]$
γ	=	shear strain,	$[-]$
c	=	viscosity,	$[\text{Ns}/\text{m}^2]$
t	=	time.	$[\text{s}]$

For the harmonic shear strain of the form:

$$\gamma = \hat{\gamma} \sin(\omega t), \quad (2-2)$$

$$\frac{\partial \gamma}{\partial t} = \hat{\gamma} \omega \cos(\omega t), \quad (2-3)$$

where:

$$\begin{aligned} \hat{\gamma} &= \text{shear strain amplitude,} & [-] \\ \omega &= \text{angular frequency.} & [\text{rad/s}] \end{aligned}$$

The shear stress will be:

$$\tau = G \hat{\gamma} \sin(\omega t) + c \hat{\gamma} \omega \cos(\omega t). \quad (2-4)$$

The dissipated energy ΔE with an elliptical stress-strain loop in a single cycle:

$$\Delta E = \int_{t_0}^{t_0 + 2\pi/\omega} \tau \frac{\partial \gamma}{\partial t} dt = \pi c \omega \hat{\gamma}^2. \quad (2-5)$$

The equation above indicates that the dissipated energy is proportional to the frequency of loading ω .

The peak energy E_p during a single cycle is calculated as follows:

$$E_p = \frac{1}{2} G \hat{\gamma}^2. \quad (2-6)$$

And the damping ratio ξ will be:

$$\xi = \frac{1}{4\pi} \frac{\Delta E}{E_p} = \frac{c \omega}{2G}. \quad (2-7)$$

There are other parameters to describe energy dissipation, like the quality factor, loss factor or the specific damping capacity. All these parameters are functions of the dissipated energy and the peak energy per cycle.

Although viscous damping is rather simple to implement into constitutive soil material models, it is frequency depended. This is not the case for the physics of soils. Some researchers try to eliminate frequency dependence by using an equivalent viscosity. The problem is illustrated by considering a superposition of waves with multiple frequencies, for which there can be no equivalent viscosity for all waves at the same time (Van Baars, 2011). From cyclic tests on sand, it was concluded, that the stress-strain behaviour of the soil is hysteretic and its corresponding damping parameters are strain dependent, though they are independent of the frequency up to 100 Hz (Bolton & Wilson, 1990).

Soil damping dependence from the cyclic shear strain amplitude is a known phenomenon. The bigger the shear strain amplitude, the bigger the amount of energy which is transformed into heat through friction (Figure 2-3).

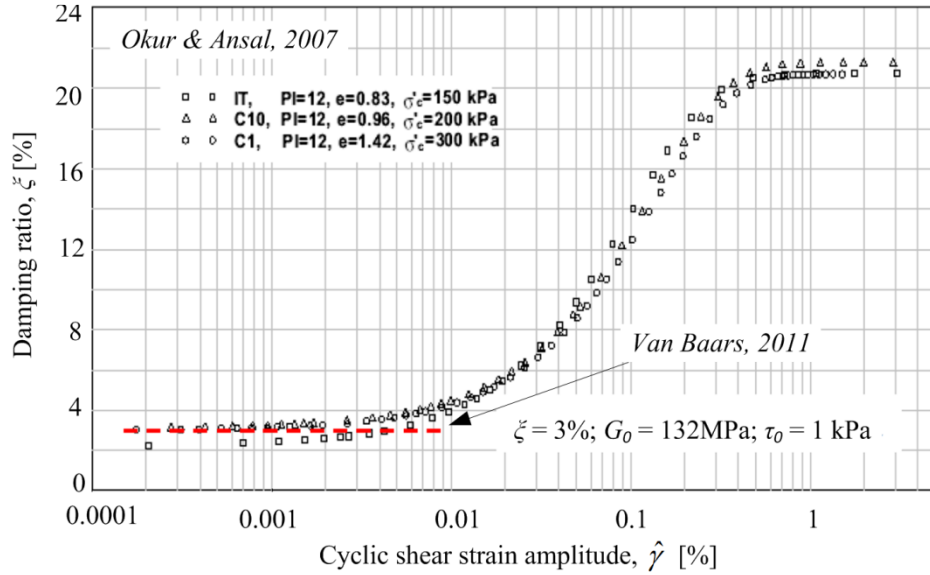


Figure 2-3. Damping ratio dependence on cyclic shear strain amplitude of natural fine grained soils (Okur & Ansal, 2007).

Therefore, for man-made geotechnical vibrations problems (where frequencies are usually rather low and shear amplitudes are small), the damping should be independent from frequency and shear strain amplitudes.

One model was suggested by Van Baars – Frictional soil damping (Van Baars, 2011). The suggested damping model is based on a force-displacement curve that has an exponential form. The model is derived in a modified coordinates system $\tau' - \gamma'$. The modified coordinates depend on the shear strain and shear stress amplitudes. The relationship can be defined as follows:

$$\gamma' = \gamma + \hat{\gamma}, \quad (2-8)$$

$$\tau' = \tau + \hat{\tau}, \quad (2-9)$$

where:

$$\begin{aligned} \hat{\gamma} &= \text{shear strain amplitude,} & [-] \\ \hat{\tau} &= \text{shear stress amplitude.} & [\text{N/m}^2] \end{aligned}$$

If the initial shear stress and shear strain in the $\tau' - \gamma'$ system of coordinates are zero, then the shear stress for loading, in a modified system of coordinates, is written in the form:

$$\tau' = G_{mod}(\gamma')^X, \quad (2-10)$$

where:

$$\begin{aligned} G_{mod} &= \text{modified shear modulus of soil,} & [\text{N/m}^2] \\ X &= \text{dimensionless damping parameter} (\leq 1). & [-] \end{aligned}$$

The shear stress for unloading depends on the peak point, where the shear stress amplitude $\hat{\tau}'$ and the shear strain amplitude $\hat{\gamma}'$ are reached, and is defined according to the following equation:

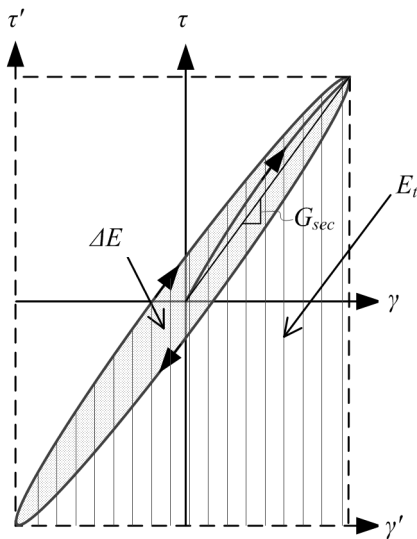
$$\tau' = \hat{\tau}' - G_{mod}(\hat{\gamma}' - \gamma')^X. \quad (2-11)$$

The modified shear modulus for this exponential damping model can be found when it is compared with the secant shear modulus G_{sec} . The secant shear modulus G_{sec} is a secant shear modulus during the full cycle (see Figure 2-4). Then the following equality is valid:

$$\hat{\tau}' = G_{sec} \hat{\gamma}' \quad (2-12)$$

At the same peak also the equity $\hat{\tau}' = G_{mod}(\hat{\gamma}')^X$ is valid. Equating the latter two and having Equation (2-8) in mind, the relationship between G_{mod} and G_{sec} can be written as follows:

$$\frac{G_{mod}}{G_{sec}} = \frac{2\hat{\gamma}'}{(2\hat{\gamma}')^X}. \quad (2-13)$$



The area hatched with vertical lines (including the ellipse) is expressed as:

$$E_t = \int_{\gamma'} \tau' d\gamma' = \frac{1}{X+1} G_{mod} (\hat{\gamma}')^{(X+1)}. \quad (2-14)$$

The area of the ellipse, which represents the dissipated energy per cycle, is defined as:

$$\Delta E = 2E_t - \hat{\tau}' \hat{\gamma}' = \frac{1-X}{1+X} G_{mod} (\hat{\gamma}')^{(X+1)}. \quad (2-15)$$

The peak energy per cycle is:

$$E_p = \frac{1}{2} \hat{\tau}' \hat{\gamma}' = \frac{1}{8} \hat{\tau}' \hat{\gamma}' = \frac{1}{8} G_{mod} (\hat{\gamma}')^{(X+1)}. \quad (2-16)$$

The ratio of the dissipated energy versus the peak energy ζ shows the energy loss per cycle:

$$\zeta = \frac{\Delta E}{E_p} = 8 \frac{1-X}{1+X}. \quad (2-17)$$

This energy loss per cycle ratio ζ is related to the damping ratio ξ as follows: $\zeta = 4\pi\xi$. With these parameters, the dimensionless damping parameter X can be defined:

$$X = \frac{8 - \zeta}{8 + \zeta}, \text{ or equally } X = \frac{2 - \pi\zeta}{2 + \pi\zeta}. \quad (2-18)$$

Hysteretic damping is in fact a damping resulting from frictional shear deformation. Isotropic compression causes probably little or no damping.

In P-waves there is a deformation due to mostly isotropic compression but also some shear deformation, in S-waves there is only pure shear deformation and in R-waves there is a combination of mostly shear deformation but also deformation due to isotropic compression. Therefore the energy will damp differently for each basic wave. This is still a subject of study.

Because it is not clear yet how different the material damping is for the individual basic waves, in current vibration problems a combined empirical absorption coefficient k_m is used to represent the material damping of the soil. Usually the exponential decay attenuation law suggested by Bornitz (1931) is used:

$$\hat{u} \propto e^{-k_m(r-r_0)}, \quad (2-19)$$

in which:

\hat{u}	=	displacement amplitude,	[m]
k_m	=	empirical absorption coefficient,	[1/m]
r	=	radius (distance) from the source to the point of interest,	[m]
r_0	=	radius (distance) from the source to the point where the displacement amplitude is known.	[m]

Other sources of amplitude attenuation will be discussed in the following subchapter.

Table 2-1. Summary of empirical absorption coefficients k_m (Amick & Gendreau, 2000).

Researcher	Soil type	k_m [m ⁻¹]
Frossblad in 1965	Silty gravelly sand	0.13
Richart	4-6 in concrete slab over compact granular fill	0.02
Woods in 1967	Silty fine sand	0.26
	Saturated fine grain sand	0.1
	Saturated fine grain sand in frozen state	0.06
	Saturated sand with laminae of peat and organic silt	0.04
Barkan in 1962	Clayey sand, clay with some sand, and silt above water level	0.04
	Marly chalk	0.1
	Loess and loessial soil	0.1
	Saturated clay with sand and silt	0 - 0.12
Dalmatov et al. in 1968	Sand and silts	0.026 - 0.36
Clough and Chameau	Sand fill over Bay Mud	0.05 - 0.2
	Dune sand	0.026 - 0.065
Peng in 1972	Soft Bangkok clay	0.026 - 0.44

In Table 2-1 the summary of the empirical absorption coefficients proposed by different authors, depending on the soil type, is presented. The summary was published by Amick & Gendreau (2000).

Auersch & Said (2010) noticed that it is not clear whether other attenuation laws, like geometrical attenuation, scattering and dispersion are included or excluded in this table.

2.4 Attenuation

In vibration problems, it is important to know the attenuation laws for the displacement, velocity or acceleration amplitudes. A theoretical and experimental study was performed by Auersch & Said (2010) in order to get a better insight in these attenuation laws. The authors concluded that the attenuation of vibration amplitudes is generally caused by: material damping, geometrical attenuation, scattering and dispersion.

Geometrical attenuation (radiation)

When waves are traveling in multiple directions, the total energy will be spread. Even when the elastic energy is conserved (no conversion to other forms of energy takes place), vibration amplitudes will decrease due to spreading of the total energy over a greater material volume. This principle is known as radiation damping, geometric damping or attenuation.

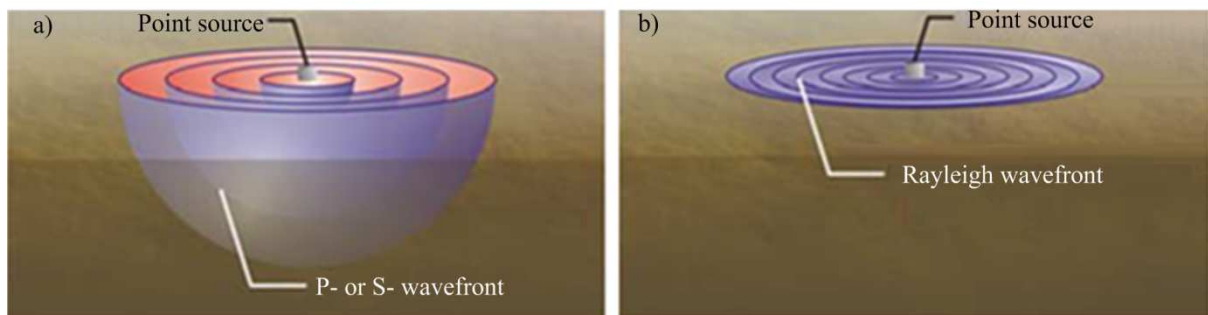


Figure 2-5. Geometrical attenuation of different waves a) Body waves b) Surface waves (Andersen, 2006).

The energy of body waves (see a) in Figure 2-5) is distributed over an area that increases with the square of the radius:

$$E' \propto \frac{1}{r^2}, \quad (2-20)$$

in which:

$$E' \quad = \quad \text{energy per unit area.} \quad [\text{N/m}^2]$$

Knowing that the displacement amplitude is proportional to the square root of the energy per unit area, the amplitude will be inversely proportional to the radius:

$$\hat{u} \propto \frac{1}{r}. \quad (2-21)$$

The energy of surface waves (see b) in Figure 2-5) is distributed over an area that increases linearly with the radius:

$$E' \propto \frac{1}{r}. \quad (2-22)$$

Knowing that the displacement amplitude is proportional to the square root of the energy per unit area, the amplitude will be inversely proportional to the square root of the radius:

$$\hat{u} \propto \frac{1}{r^{0.5}}. \quad (2-23)$$

Scattering in a heterogeneous medium

Scattering is a general physical process where some forms of radiation, such as light, sound, or moving particles, are forced to deviate from a straight trajectory by one or more paths due to localized non-uniformities in the medium through which they pass (Wikipedia). Soil waves are scattered at random heterogeneities of the soil and a part of the wave energy disappears in the depth of the half-space. Scattering effect can be expressed in similar exponential amplitude – distance relationship as the material damping:

$$\hat{u} \propto e^{-k_{sct}(r-r_0)}, \quad (2-24)$$

where:

$$k_{sct} \quad = \quad \text{empirical scattering coefficient.} \quad [1/\text{m}]$$

The attenuation must be a function of the ratio between the scattering dimension and the wave length. It can be proportional to the diameter, the cross section or the volume (Auersch & Said, 2010).

$$k_{sct} \propto 1/\lambda \dots 1/\lambda^3, \quad (2-25)$$

where:

$$\lambda \quad = \quad \text{wave length.} \quad [\text{m}]$$

This means, that scattering attenuation may depend either linearly, or even very strongly on the frequency. However, by measuring only vibrations on the soil surface it is hardly possible to distinguish damping from scattering without any additional information. Van Wijk and Levshin (2004) investigated the influence of vertical scatterers to the dispersion of surface waves. They concluded that a combination of isolated scatterers and layering in the sub-surface creates dispersion of surface waves.

Dispersion

As mentioned before, if an elastic half-space is not homogeneous, then R-waves become dispersive waves (wave velocity depends on a vibration frequency).

Therefore, a short pulse travelling from a source point will not arrive as a short pulse at an observation point far away. Instead the pulse will be spread over distance since the waves with different frequencies travel with different speeds. Taking the conservation of energy into account, the vibration amplitudes attenuate due to this energy spreading. This is illustrated in Figure 2-6. In this case the total energy is conserved over space and time. However, an additional attenuation due to the dispersive nature of an inhomogeneous soil occurs.

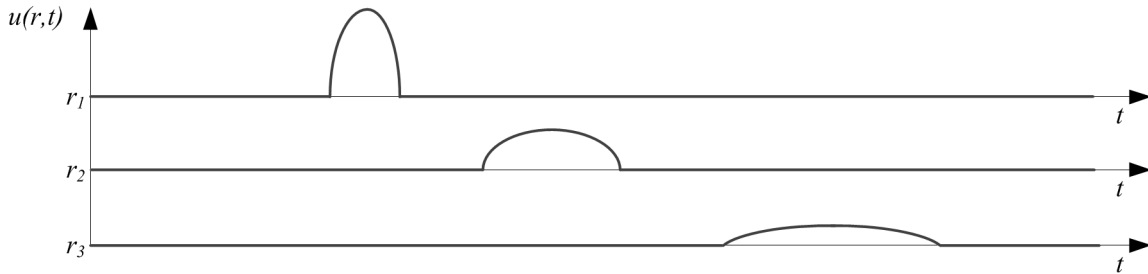


Figure 2-6. Dispersion of an impulse excitation.

It was measured from impulsive excitations by Auersch and Said (2010) that there is an additional dispersion attenuation factor $\hat{u} \propto r^{-0.5}$ due to the dispersive nature of an inhomogeneous soil. The authors state, that this statement holds for the maximum of the time records (maximum vibration component of 3 directions). For their root mean square vibration values (the square root of the sum of the squares of maximum values of the three vibration components in x , y and z directions), which means the additional dispersion attenuation was weaker, than the latter.

Overall attenuation

Taking all the mentioned attenuation factors into account (material damping, radiation, scattering, and dispersion) the overall attenuation for surface waves, according to Auersch and Said (2010), can be calculated as follows:

$$\hat{u}_r(r) = \hat{u}_0 \sqrt{\frac{1}{r}} e^{-k_m(r-r_0)} e^{-k_{scr}(r-r_0)}, \quad (2-26)$$

in which:

$$\begin{aligned} \hat{u}_r &= \text{displacement amplitude of a Rayleigh wave,} & [\text{m}] \\ \hat{u}_0 &= \text{displacement amplitude at known distance } r_0. & [\text{m}] \end{aligned}$$

For the body waves only the radiation law would be different:

$$\hat{u}_b(r) = \hat{u}_0 \frac{1}{r} e^{-k_m(r-r_0)} e^{-k_{scr}(r-r_0)}, \quad (2-27)$$

in which:

$$\hat{u}_b = \text{displacement amplitude of a body wave.} \quad [\text{m}]$$

The dispersion relation in Equation (2-26) and Equation (2-27) could be introduced by multiplying to by factor of $r^{-0.5}$. However, this attenuation law holds only for the maximum of the time records in three directions.

The attenuation of vibrations is frequently described by a linear log-log relationship where all the discussed effects are lumped.

$$PPV = \zeta \cdot r^{-m}, \quad (2-28)$$

where:

PPV	$=$	peak particle velocity, [m/s]
ζ	$=$	empirical coefficient, [s ⁻¹]
m	$=$	attenuation rate (also the slope in a log-log curve). [-]

Equation (2-28) can be written in the following logarithmic form:

$$\log(PPV) = \log(\zeta) - m \log(r). \quad (2-29)$$

Particle velocities are usually measured in three different directions. Therefore a peak particle velocity (PPV) can be defined in different ways. There are at least three different methods to define the PPV from the measurements data:

1. Peak component – the maximum of the vertical, transversal and radial components:

$$PPV = \max(\max(\vec{v}_x), \max(\vec{v}_y), \max(\vec{v}_z));$$

2. True vector sum (TVS) – the maximum of the vector sum:

$$PPV = \max(\vec{v}), \text{ where } \vec{v} = (\vec{v}_x + \vec{v}_y + \vec{v}_z);$$

3. Root mean square method (RMS):

$$PPV = \sqrt{(\max(\vec{v}_x))^2 + (\max(\vec{v}_y))^2 + (\max(\vec{v}_z))^2},$$

where:

$$\vec{v}_i = \text{velocity vector in } i \text{ direction.} \quad [\text{m/s}]$$

The PPV defined by the peak component method may be up to 25 % lower than defined by the true vector sum method. Also the PPV defined by RMS method may exceed the true vector sum value by 50 % (Athanasopoulos & Pelekis, 2000). It is also noted that the true vector sum method can be over conservative (Ali, et al., 2003).

From experimental studies of measurements of ground vibrations at nineteen different sites and also induced by different sources (Auersch & Said, 2010), typical measured attenuation values are presented in Table 2-2.

Differences of the attenuation rate m in a source group (e.g. explosion) authors explain by different dynamite weight equivalents used for explosions, different drop masses, different

train speeds i.e., different energy from the source. Also the influence of the different soils is discussed. The measurements can be found graphically in Figure 2-7.

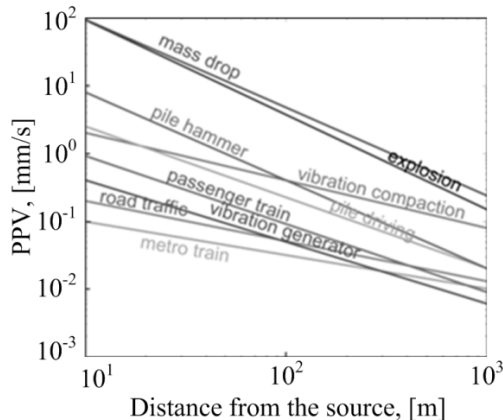


Figure 2-7. Attenuation rates from technically induced vibrations (Auersch & Said, 2010).

The reported attenuation rate m was between 0.5 and 2.0. The upper value agrees well with the measurements of Wiss (1981), where he reported the attenuation rate m to be between 1.0 and 2.0.

The dissipation rate of pile-driving vibrations was studied by Ali et al. (2003) in order to determine the influence radius around vibration sources. For this purpose Equation (2-28) was used. The sources were two types - pile driving and sheet-pile driving.

From the experimental data, it was concluded, that the attenuation rate m for that site was between 0.88 and 1.02 which is in a good agreement with Auersch and Said (2010) measurements for pile driving (Table 2-2).

Table 2-2. Attenuation rate m from experimental studies (Auersch & Said, 2010).

Source	min	Attenuation rate m		Number of sites
		average	max	
Road traffic		0.5		1
Metro train		0.5		1
Vibration compaction		0.7		1
Pile driving		1.1		1
Explosion	1.2	1.3	1.4	3
Mass drop	1	1.3	1.6	2
Passenger train	0.5	1	1.5	6
Hammer impulse	1.3	1.65	2	4

A comprehensive review of man-made ground vibrations and measurements of ground vibration caused by vibratory sheet-pile driving in recent soil deposits was made by Athanasopoulos and Pelekis (2000). The results of an attenuation rate of vibrations with distance were compared with published results by other studies and satisfactory agreement was found (Figure 2-8).

A summary table of the attenuation rates of different authors for various soil types was published by Ali, et al. (2003) (Table 2-3). Unfortunately no clear pattern can be seen. Some authors were looking into stiffness; others indicated just the name of the soil, from which an approximate size of the soil particle can be known. However the latter does not help while for only sand the attenuation rates still vary from 0.8 to 1.5.

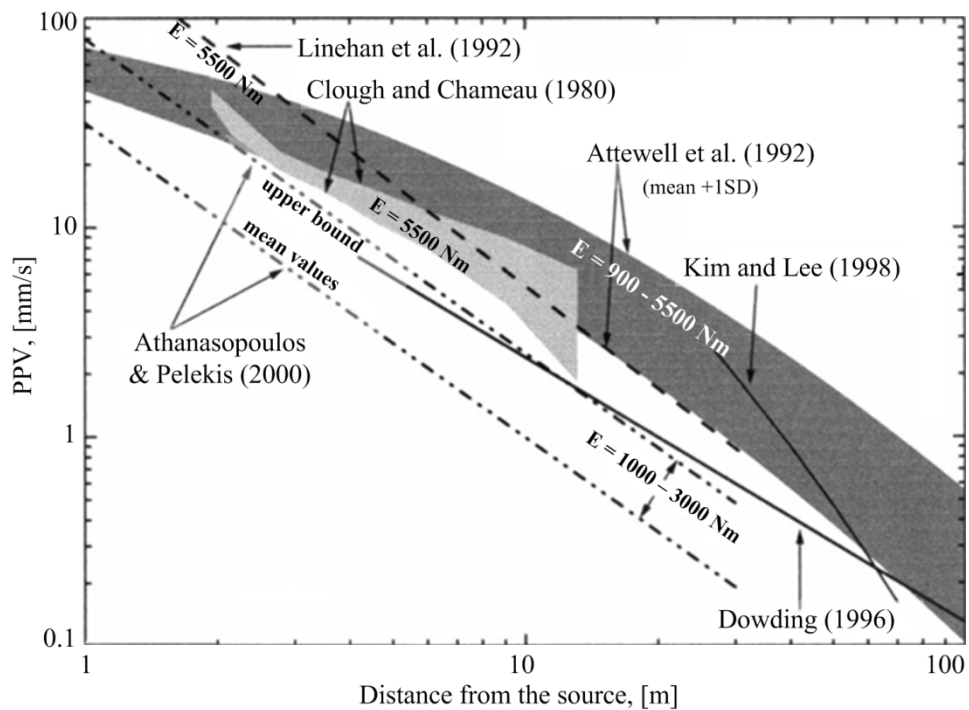


Figure 2-8. Attenuation of vibrations with distance from vibratory sheetpile driving (Athanasopoulos & Pelekis, 2000).

Table 2-3. Published attenuation rates for pile-driving in various soil types (Ali, et al., 2003).

Researcher	Soil type	m
Amich and Unger	Clay	1.5
Attewell and Farmer	Various soils, generally firm	1
Brenner and Chittikuladiok	Surface sands	1.5
	Sand fill, over soft clays	0.8 - 1.0
Martin	Clay	1.4
	Silt	0.8
Nicholls, Johnson and Duvall	Firm soils and rock	1.4 - 1.7
Wiss	Sands	1
	Clays	1.5
Woods and Jedebe	Dense compacted sands (15<N<50)	1.1
	Most sands (5<N<15)	1.5

2.5 Heterogeneity

On micro level soil is clearly a heterogeneous material composed by different particles of minerals and/or organics. The particles vary significantly in size and shape (Figure 2-9).

Similar as for inhomogeneity in the dynamics of structures, inhomogeneity in soils can be divided into local and global. Local inhomogeneity can be understood as the variation of material properties over a distance that is much smaller than the characteristic wave length (Andersen, 2006). If the wave length is many times longer than the characteristic dimension of the inhomogeneity, the material interacts as a homogeneous material to the wave. On the

contrary, if the wave length is many times smaller than the characteristic dimension of the inhomogeneity, the wave will be scattered in all directions into the material (Bodare, 1998).

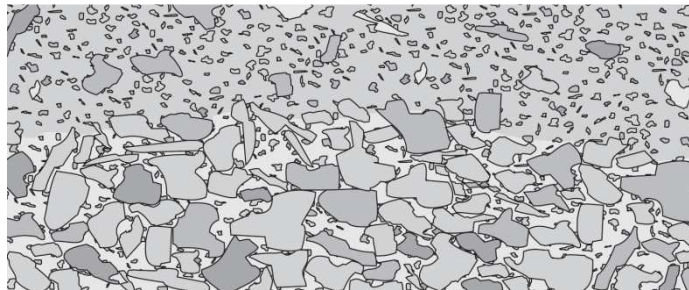


Figure 2-9. Inhomogeneous soil (Andersen, 2006).

Since the Rayleigh wave's velocity is in most soils above 100 m/s, the wave length of the man-made vibrations is in the order of meters whereas the grain size of the soil is the order of millimetres or even smaller. Therefore the local variations of the density and the strength of material are of little importance to wave propagation in soil (Andersen, 2006).

Global inhomogeneity can be understood as the variation of material properties over a distance close to or larger than the characteristic wave length. The global inhomogeneity exists in any real soil deposit because the stiffness, like the strength properties varies over depth due to a sedimentation process, a pre-stressing from overlaying soil or an over-consolidation from ice.

Models commonly assume ground to be homogeneous. Simplifying the soil as a homogeneous material adds a level of uncertainty to the predictions which is not well understood (Jones & Hunt, 2012a). The goal of Jones and Hunt work was to quantify the effect of the soil inhomogeneity on the surface vibration. They suggested that not only global, but also local soil heterogeneity can significantly affect surface velocity predictions. The effect of variability of the horizontal elastic modulus on the confidence interval appears to be negligible when modelling ground vibration from underground railways.

In practice, usually a schematisation of one or two layers overlaying a homogeneous half-space is sufficient for modelling wave propagation in soil (Andersen, 2006).

2.6 Anisotropy

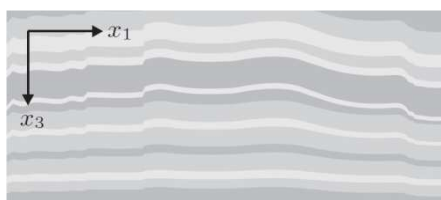


Figure 2-10. An anisotropic material (Andersen, 2006).

of an anisotropic material is found in Figure 2-10.

Anisotropy is the material's physical property dependence on the direction, as opposed to isotropy, which implies identical properties in all directions. Probably the best example of an anisotropic material in the field of civil engineering is timber, but it also applies to many kinds of rock and most sedimentary soil. Even sand shows an anisotropic behaviour, which is a result of the way in which the grains are initially deposited (Andersen, 2006). Graphical representation

It was also stated by Andersen, that the main difference in elastodynamics between isotropic and anisotropic materials is the fact that in isotropic materials, the wave speed is the same in

all directions, whereas in anisotropic materials the wave speed varies. It can influence some or even all of the wave types in a medium.

In geophysics the variation of the wave speed with direction is called seismic anisotropy and it is an indicator of long term order in a material. Even rock-forming minerals are anisotropic, including quartz and feldspar. The anisotropy of minerals can be seen in their optical properties.

Actually, a real soil medium almost always displays some degree of elastic anisotropy, therefore the wave propagation has to be assumed to be anisotropic, unless the soil stiffness has been shown to be effectively isotropic (Helbig, 1993).

2.7 Degree of saturation

In soil dynamics, the soil is usually treated as an elastic (or viscoelastic) material. This type of modelling is acceptable for dry granular materials, which may adequately be described as a single-phase system. However in saturated porous materials the pore pressure in the fluid phase interacts with the stresses of the solid phase (effective stresses). This results in a second P-wave. Dynamical behaviour of the saturated porous media theory developed by Biot (1941), (1955), (1956a), (1956b) and the latter generalised to multi-phase systems (Carcione, et al., 2004). The second P-wave in a fully saturated porous medium propagates at a speed which is much lower than the usual P- and S-wave speeds. Therefore it is often referred to as the slow P-wave (Andersen, 2006).

Paul Hölscher describes and discusses in his thesis “Dynamical response of saturated and dry soils” (Hölscher, 1995) the dynamics of porous media. The phenomena of wave-propagation and consolidation are solved by using non-linear behaviour of the soil. Analytical solutions near interfaces between solid and fluid are derived by using Fourier transformations. The author concludes that near the interface between water and soil particle, the effective stress is influenced by the second P-wave. This may lead to a decrease in the effective stress of up to 70 %. The latter effect cannot be described by a single phase approach. This means that ground vibration predictions of saturated soil, modelled by a single-phase approach, can lead to an error of up to 70 %. For shear waves only minor differences are to be expected by using a two-phase or single phase approach.

Nakagawa and Soga (1995) measured the propagation of P- and S-waves in dry and saturated sand samples. A conventional triaxial soil testing system was combined with the pulse transmission method. The velocities of the second kind P-wave were only 1/10 to 1/3 of those measured for the first kind P-waves. The measured wave velocities agreed well with the theoretical values calculated using Biot's two-phase theory.

The degree of saturation also effects pile drivability. The literature concerning this effect was overviewed by Viking (2002). Laboratory test of driving pile in a sand container, filled with non-cohesive soil, were performed and reported by Rao (1993) and Wang (1994). Two pore-water pressure transducers were placed in the test cylinder at distances $1D_p$ and $2.25D_p$ from the pile shaft, where D_p is the pile diameter. The results were compared with a finite element analysis and it was concluded that the excess pore-pressure amplitude decayed very quickly with increasing radial distance from the oscillating shaft surface. Nevertheless the mean excess pore-pressure was found to be similar at different distances from the oscillating shaft surface. According to Viking (2002), the similarity in the value of the mean pore-pressure,

regardless of the distance to the pile, could also be related to improper boundary conditions (at the tank limits), due to fact that there was no dissipation of the excess pore-pressure in relation to the distance from the driven pile. Viking concluded that the degree of saturation is one of the primary subsoil-related factors affecting vibro-driveability, but not the most important.

2.8 Air content

Smeulders (1992) did research on wave propagation in saturated and partially saturated porous media. The propagation and damping of compressional waves in a porous medium was investigated, both theoretically and experimentally, in case the pore liquid contains a small volume fraction of gas. Close to gas bubble resonant frequencies, the compressional waves are very strongly damped. Even a minor gas fraction largely influences the dynamic fluid bulk modulus and also the wave propagation phenomena in a porous medium.

2.9 Layering

In general, layering in soil dynamics can be understood as a global inhomogeneity such as discussed in Chapter 2.5. Layers are formed during geological processes or formed by man (embankments, filled soils).

When a wave meets a new layer it can reflect and/or refract. Reflection and refraction also occurs at the surface, which is in fact a layer of the soil interacting with the atmosphere, which is also an inhomogeneity.

The path with a minimum travel time of a seismic pulse in the soil is called a ray (a vector) and a surface with rays of equal travel time is called a wave front. Snell considered the change of direction of ray paths at interfaces between materials (in this case two soil layers) with different wave propagation speed. Snell showed that the angle between the ray path and the normal to the interface and velocity of the wave is constant:

$$\frac{\sin i}{v} = \text{const}, \quad (2-30)$$

where:

$$\begin{array}{llll} i & = & \text{angle of incidence,} & [\text{rad}] \\ v & = & \text{velocity.} & [\text{m/s}] \end{array}$$

This relationship holds for reflected and refracted (or transmitted when the angle of incidence is zero) waves. Different body waves, reflected and refracted at the interface of two layers, are presented graphically in Figure 2-11. In the figure P, SH and SV represents compression, horizontal shear and vertical shear waves respectively.

Since an incident P- and SV- involve a particle motion perpendicular to the plane of the interface; they will each produce both reflected and refracted P- and SV-waves. An incident SH-wave does not involve any particle motion perpendicular to the interface; consequently, only SH-waves are reflected and refracted (Kramer, 1996). Following Snell's law, the angle of incidence is equal to the angle of reflected wave. The sinus of the angle of the refracted wave is proportional to the wave velocity for both Layer 1 and Layer 2.

In geophysics, the refraction method uses a refracted wave with a critical angle of incidence to determine the layering of subsoil. The critical angle of incidence is defined as the smallest angle which produces a refracted wave that travels parallel to the interface (Kramer, 1996).

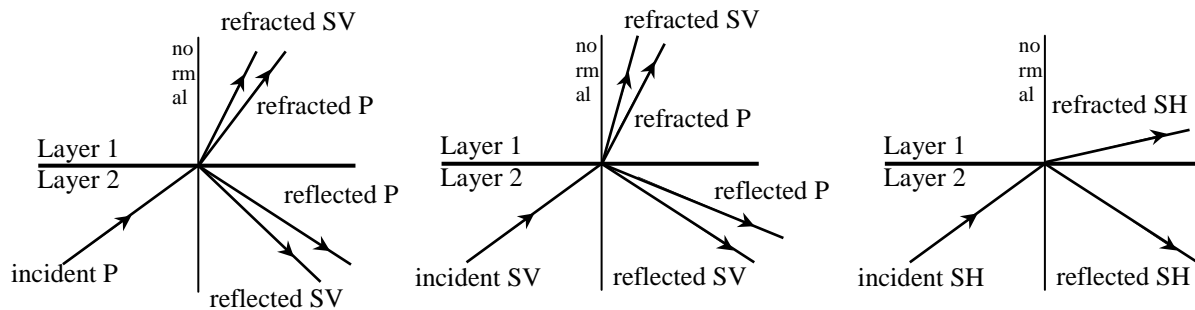


Figure 2-11. Reflection and refraction of incident body waves.

If an incident SV-wave hits the free boundary at the angle smaller than the critical, the two body waves reflect: P-wave and SV-wave (as it can be seen in the middle sketch of Figure 2-11). However, if an incident SV-wave hits the free boundary at the angle larger than the critical, only the SV-wave is reflected. The energy that for smaller angles is reflected as a P-wave is instead captured as a surface wave with exponential decay of the amplitude in the horizontal direction, as it is shown in Figure 2-12 (Andersen, 2006).

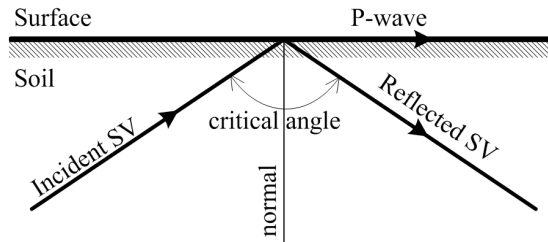


Figure 2-12. Reflected P-waves are captured at the surface.

Baidya (2000) observed that the dominant frequency, (the frequency at which an oscillating foundation-soil system is experiencing the highest displacements), of the layered soil system decreases due to presence of the soft layer at the top whereas it increases due to presence of stiff layer at the top.

2.10 Amplitude of a harmonically oscillating plate

Reissner's method

Lamb (1904) solved the response caused by a vertical or horizontal point load, suddenly applied onto the surface of an elastic half-space, in two and three dimensions. The latter is also known as the dynamic Boussinesq problem. The solution is obtained by using the complex analysis, which is a branch of mathematical analysis, where the separate real and imaginary parts of any analytic function must satisfy Laplace's equation. The equations of motion were casted into the Laplace-radial wave number domain. An inverse Laplace transform into the time domain was performed by contour integration, a method of evaluating certain integrals along paths in the complex plane. Unfortunately the final solution was an indefinite integral whereby the solution is not known and difficult to solve analytically and boundary limits are either plus or minus infinity or zero approaching the infinity (Chowdhury & Dasgupta, 2009). Therefore for practical purposes, calculation of the surface displacements from an applied force, this solution was not finished yet.

Reissner (1936) used the same Lamb's approach but assumed a uniform stress distribution (or uniformly loaded flexible circular area) instead of a point load on an elastic half-space and determined the vertical steady state response. The vertical displacements at the centre of the flexible loaded area are given by:

$$u(t) = \frac{F_0 e^{i\omega t}}{Gr_{pl}} (f_1 + i f_2), \quad (2-31)$$

where:

u	=	displacement,	[m]
F_0	=	amplitude of vertically exciting force,	[N]
r_{pl}	=	radius of a plate,	[m]
f_1, f_2	=	displacement (compliance) functions.	[-]

The displacement functions are functions of the dimensionless frequency a_0 and Poisson's ratio ν .

The dimensionless frequency a_0 is calculated as follows:

$$a_0 = \omega r_{pl} \sqrt{\frac{\rho}{G}} = \frac{\omega r_{pl}}{\nu_s}, \quad (2-32)$$

in which:

$$\rho = \text{density of the medium.} \quad [\text{kg/m}^3]$$

Reissner was able to deduce the displacement functions, which were needed to obtain data of engineering interest, for $\nu = 0$, $\nu = 0.25$ and $\nu = 0.5$. Because he left Germany and moved to USA, he was not aware that his solution did not agree with experimental data. Only a number of years later it was discovered by others that there was a sign mistake in one of the terms of his half space solution (Reissner, 1996). Hereby the corrected displacement functions are given:

$$\left. \begin{aligned} f_1 &= -0.319(1 - 0.291a_0^2 + 0.023a_0^4 + \dots) \\ f_2 &= 0.282 J_1(1.145a_0) + 0.0516a_0(1 - 0.056a_0^2 + \dots) \end{aligned} \right\} \text{for } \nu = 0 \quad (2-33)$$

$$\left. \begin{aligned} f_1 &= -0.239(1 - 0.25a_0^2 + 0.0175a_0^4 + \dots) \\ f_2 &= 0.1835 J_1(1.09a_0) + 0.048a_0(1 - 0.063a_0^2 + \dots) \end{aligned} \right\} \text{for } \nu = 0.25 \quad (2-34)$$

$$\left. \begin{aligned} f_1 &= -0.159(1 - 0.25a_0^2 + 0.0153a_0^4 + \dots) \\ f_2 &= 0.109 J_1(1.047a_0) + 0.046a_0(1 - 0.065a_0^2 + \dots) \end{aligned} \right\} \text{for } \nu = 0.5 \quad (2-35)$$

where:

$$\begin{aligned} a_0 &= \text{dimensionless frequency,} & [-] \\ J_1 &= \text{Bessel function of the first kind, first order.} & [-] \end{aligned}$$

The displacement functions graphically are represented in Figure 2-13.

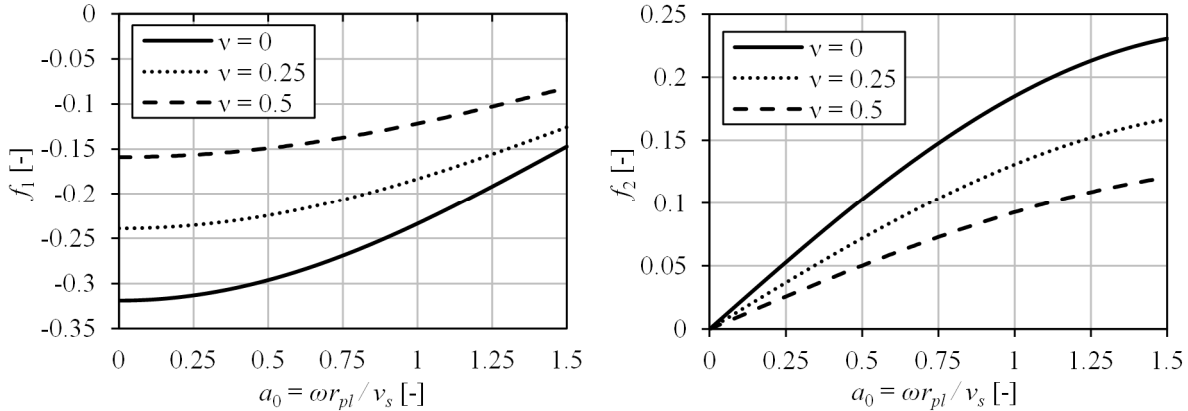


Figure 2-13. Reissner's displacement functions for a flexible circular plate.

Reissner's solution for the displacement amplitude of oscillator motion is given by:

$$\hat{u} = \frac{F_0}{Gr_{pl}} \sqrt{\frac{f_1^2 + f_2^2}{(1 + ba_0^2 f_1)^2 + (ba_0^2 f_2)^2}}, \quad (2-36)$$

where b is a dimensionless mass ratio:

$$b = \frac{m_{vib}}{\rho r_{pl}^3}, \quad (2-37)$$

in which:

$$m_{vib} = \text{mass of a vibrating object.} \quad [\text{kg}]$$

The phase shift $\Delta\phi$ between an exciting force and the soil response is given by:

$$\Delta\phi = \tan^{-1} \left(\frac{-f_2}{f_1 + ba_0^2 (f_1^2 + f_2^2)} \right). \quad (2-38)$$

Reissner's solution was derived for uniform vertical stresses (or a flexible plate). Knowing that different stiffness of a plate causes different contact vertical stresses in the soil, researches were working on derivation of corresponding displacement functions.

Lysmer's method

Reissner and Sagoci (1944) developed a method for the torsional mode of vibration of a rigid circular footing resting on the surface of an elastic half-space.

Sung (1953) and Quinlan (1953) independently solved a problem of the dynamic response of a circular footing resting on an elastic half-space for three probable contact vertical stresses: uniform, parabolic and rigid base approximation.

Arnold et al. (1955) computed the dynamic response of a rigid circular foundation on an elastic half-space not only for the vertical vibration mode but also for the rocking and sliding motion.

Bycroft (1956) noted that contact vertical stresses used by Sung (1953) and Quinlan (1953) are the equivalent dynamic stresses of their static counterparts. Beneath the rigid footing the uniform displacement distribution is not always correctly predicted because it varies with the frequency. Therefore a weighted average of the displacements beneath the footing and an average magnitude of displacement (compliance) functions f_1 and f_2 were evaluated. The solution was valid only for small frequency ratios ($\alpha_0 < 1.5$). Therefore later Bycroft (1977) extended the solution for large frequencies. Vertical, horizontal, rocking and yawing (rotation around the vertical axis) vibration modes were evaluated.

Meanwhile Hsieh (1962) attempted to modify the original solution of Reissner. The aim was to develop a mechanical analogue in a form of single-degree of freedom system. Hsieh was the first who showed that the elastic half space can be converted into a mechanical analogue of a spring and a dashpot (Chowdhury & Dasgupta, 2009).

The equation of the vertical vibration of a rigid circular footing with a mass m_{vib} resting on an elastic half-space is as follows:

$$am_{vib} + cv + ku = P_0 e^{i\omega t}, \quad (2-39)$$

in which:

a	=	acceleration of the footing,	$[\text{m/s}^2]$
v	=	velocity of the footing,	$[\text{m/s}]$
c	=	coefficient, analogues to viscous damping,	$[\text{Ns/m}]$
k	=	coefficient, analogues to spring stiffness,	$[\text{N/m}]$
P_0	=	amplitude of the soil reaction force.	$[\text{kN}]$

Hsieh (1962) calculated the coefficients for analogues spring and dashpot:

$$k = Gr_{pl} \frac{f_1}{f_1^2 + f_2^2}, \quad (2-40)$$

$$c = \frac{Gr_{pl}}{\omega} \frac{-f_2}{f_1^2 + f_2^2}. \quad (2-41)$$

The advantage of the spring – dashpot analogue, is that one can use the standard single degree of freedom system, which has classical solutions for amplitudes and displacements. The only difference is that in this case, the equivalent damping and stiffness are given by the coefficients k and c and these are frequency and Poisson's ratio dependent.

Lysmer (1965) used Reissner's solution but he also took into account the work of Hsieh, who demonstrated that an elastic half space can be converted into a mechanical analogue of a spring and dashpot, as well as the work of Bycroft, who was able to define the displacement functions for rigid circular foundation, and proposed a simplified model for a vertical motion of a rigid circular foundation. Lysmer treated stress distribution under the foundation as a function of frequency: for low frequencies the stress is similar to the stress distribution for the static case, whereas for high frequencies the stress distribution approach the solution for uniformly loaded half space. The rings method (superposition of uniformly loaded rings) was used to solve the response of different stress distributions. For that Lysmer used IBM 7090 computer. Finally he simplified the solution and developed frequency independent expressions for the coefficients k and c for a rigid plate case:

$$k = \frac{4Gr_{pl}}{1-\nu}, \quad (2-42)$$

$$c = \frac{3.4r_{pl}^2}{1-\nu} \sqrt{G\rho}. \quad (2-43)$$

Amongst different methods developed in the past for vibratory response of foundations, Lysmer's method is quite popular because of its simplicity. This methodology has been proved to be quite accurate for the analysis of a foundation in a low to medium frequency range (Baidya, 2000). Nevertheless it is worth to mention that it is an approximate method, because the damping is taken such, that it would be a best fit for a dimensionless frequency $0.3 < a_0 < 0.8$. Lysmer found that an error for small frequencies $a_0 < 0.8$ does not exceed 8 % and for larger values of a_0 and small values of B the relative error might be as great as 35 %.

Lysmer used a slightly different dimensionless mass ratio than Reissner:

$$B = \frac{1-\nu}{4} b = \frac{1-\nu}{4} \frac{m_{vib}}{\rho r_{pl}^3}. \quad (2-44)$$

The displacement amplitude according to Lysmer is calculated as follows:

$$\hat{u} = \frac{F_0 / k}{\sqrt{(1 - Ba_0^2)^2 + (0.85a_0^2)}}. \quad (2-45)$$

And the phase shift between an exciting force and the dynamic response:

$$\Delta\varphi = \tan^{-1} \left(\frac{-0.85a_0}{Ba_0^2 - 1} \right). \quad (2-46)$$

Hall (1967) followed Lysmer's success and developed equivalent static springs for both the sliding and rocking mode and a solution for coupled rocking and sliding motion.

Confined elasticity approach

Another approximate solution was suggested by Verruijt (2006). The author suggests to neglect horizontal displacements (while they are very small compared to the vertical ones)

and to use a confined elasticity. This approach was first proposed by Westergraad (1938) and generalised for elastodynamics by Barends (1980). Then the coefficients k and c for a rigid circular plate on a confined elastic half space would be:

$$k = \frac{(\bar{\lambda} + 2G)\pi r_{pl}}{m_c} \frac{\omega/\omega_c}{\tan(\omega/\omega_c)}, \quad (2-47)$$

$$c = \frac{1}{2}\pi m_c r_{pl}^2 \sqrt{\rho G}, \quad (2-48)$$

in which:

$$\begin{aligned} \bar{\lambda} &= \text{Lamé's first parameter, } \bar{\lambda} = Ev/[(1+\nu)(1-2\nu)] & [\text{N/m}^2] \\ m_c &= \text{material constant, } m_c^2 = 2(1-\nu)/(1-2\nu) & [-] \\ \omega_c &= \text{characteristic angular frequency } \omega_c^2 = 4G/(\rho r_{pl}^2). & [\text{rad/s}] \end{aligned}$$

The displacement amplitude according to the confined elasticity theory is given by:

$$\hat{u} = \left| \left(\frac{\omega}{\omega_c} \frac{\exp(i\omega/\omega_c)}{\sin(\omega/\omega_c)} - \frac{16B}{\pi m_c (1-\nu)} \left(\frac{\omega}{\omega_c} \right)^2 \right)^{-1} \right| \hat{u}_{stat}, \quad (2-49)$$

where:

$$\hat{u}_{stat} = \text{static displacement.} \quad [\text{m}]$$

The static displacement is defined as follows:

$$\hat{u}_{stat} = \frac{F_0}{\pi r_{pl}} \frac{m_c}{\bar{\lambda} + 2G}, \quad (2-50)$$

The characteristic frequency is given by:

$$\omega_c = \sqrt{\frac{4G}{r_{pl}\rho}}. \quad (2-51)$$

The phase shift between the exciting force and the dynamic response yields:

$$\Delta\phi = \frac{\omega r_{pl}}{2\nu_s} = \frac{a_0}{2}. \quad (2-52)$$

2.11 Surface vibrations near a harmonically oscillating plate

According to Barkan (1962), vertical displacements of the surface at small distances from the source of waves can be calculated by:

$$u_v = -\frac{F_0 \omega}{v_s G} \cdot \sqrt{f_{1s}^2 + f_{2s}^2} \sin(\omega t - \Delta\varphi), \quad (2-53)$$

in which:

$$\begin{aligned} v_s &= \text{shear wave velocity,} & [\text{m/s}] \\ f_{1s}, f_{2s} &= \text{displacement (compliance) functions for the surface vibration. [-]} \end{aligned}$$

The phase shift $\Delta\varphi$ between loading and displacements is calculated by:

$$\Delta\varphi = \tan^{-1} \frac{f_{1s}}{f_{2s}}. \quad (2-54)$$

The compliance functions usually are expanded into a series. These are the recommended f_{1s} and f_{2s} functions for Poisson's ratio $\nu = 0.25$ and for small values of $k_s \cdot r$:

$$\begin{aligned} f_{1s} &= -0.119 \frac{1}{k_s r} + 0.0895 k_s r - 0.0104 (k_s r)^3 + 0.000466 (k_s r)^5 \\ &\quad - 0.0000109 (k_s r)^7 + \dots, \end{aligned} \quad (2-55)$$

$$\begin{aligned} f_{2s} &= -0.0988 J_0(1.08777 k_s r) + 0.0484 - 0.00595 (k_s r)^2 + 0.000240 (k_s r)^4 \\ &\quad - 0.00000484 (k_s r)^6 + \dots, \end{aligned}$$

in which:

$$\begin{aligned} k_s &= \text{shear wave's number,} & [\text{m}^{-1}] \\ J_0 &= \text{Bessel function of the first kind, zero order.} & [-] \end{aligned}$$

Displacements of the surface at large distances from the wave source can be calculated as follows:

$$u_h = -\frac{k_r F_0}{2G} \cdot \frac{k_r \left(k_r^2 - k_s^2 - 2\sqrt{k_r^2 - k_p^2} \sqrt{k_r^2 - k_s^2} \right)}{\frac{\partial g_k}{\partial k_r}} \sqrt{\frac{2}{\pi k_r r}} \sin\left(\omega t - k_r r - \frac{\pi}{4}\right), \quad (2-56)$$

$$u_v = \frac{k_r F_0}{2G} \cdot \frac{k_s^2 \sqrt{k_r^2 - k_p^2}}{\frac{\partial g_k}{\partial k_r}} \sqrt{\frac{2}{\pi k_r r}} \cos\left(\omega t - k_r r - \frac{\pi}{4}\right). \quad (2-57)$$

in which:

$$\begin{aligned} k_p &= \text{compressional wave's number,} & [-] \\ k_r &= \text{Rayleigh wave's number.} & [-] \end{aligned}$$

The Rayleigh function g_k (which has one real positive root, which gives the ratio between v_s and v_r) is defined as follows:

$$g_k = (2k_r^2 - k_s^2)^2 - 4k_r \sqrt{k_r^2 - k_p^2} \sqrt{k_r^2 - k_s^2}. \quad (2-58)$$

Here the assumption is made, that displacements at large distances are caused only by R-waves.

Barkan suggests to distinguish two different fields, the near-field and the far-field, where vibrations follow different laws. This is remarkable, since the material is elastic and linear so, there should be no reason for a change of the wave propagation laws. Therefore this issue will be discussed and checked in Chapter 4.

For the near-field Barkan confined himself only to the investigation of the vertical components of vibration. Barkan explained that this is because of practical interest. He also solved, for the far-field the equations for both vertical and horizontal displacements, but not the horizontal component for the near-field.

2.12 Waves field under a harmonically oscillating plate

Miller and Pursey (1955) analysed the energy distribution between waves in the far-field. Because it is a far-field situation, amplitudes of the body waves are rather small on the surface, and are taken as zero.

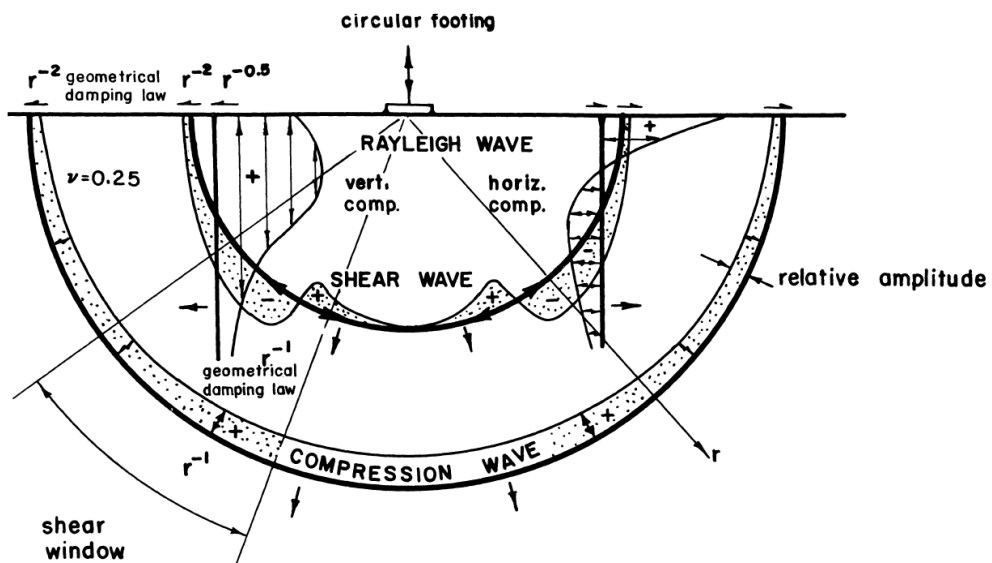


Figure 2-14. Distribution of displacement waves from a circular footing on a homogeneous, isotropic, elastic half-space (Woods, 1968).

Miller and Pursey calculated the distribution of the total energy between the P-, S- and R-waves for homogenous half-space for $\nu = 0.25$. They found a distribution of: 67.4 % of R-waves, 25.8 % of S-waves and 6.9 % of P-waves. Therefore approximately 2/3 of the input energy goes to a surface (Rayleigh) wave and 1/3 to the body waves (S- and P-wave) for this Poisson's ratio.

The variation of the displacement amplitudes of the P-, S- and R-waves was presented by Woods (1968) in a well-known figure, see Figure 2-14. The wave-fronts have spacing between them according to the velocities of the propagating waves. The shaded zones along the wave fronts of the body waves indicate the relative amplitude of particle displacement as a function of the dip angle. The Rayleigh wave's vertical and horizontal components are also shown on the leftward- and rightward-propagating parts of the wave respectively. The region in the figure of the shear-wave front in which the larger amplitudes occur is called the shear-window.

This solution was the first step to investigate separate wave types and their laws causing the superposed vibration on the surface.

In Figure 2-14 there is a mistake regarding the body waves' attenuation law on the surface: the attenuation law of body waves on the surface is shown to be r^{-2} and in the body r^{-1} . Maybe this is a misinterpretation of Lamb's finding (Auersch & Said, 2010), because as it is already mentioned in Chapter 2.4, it is r^{-1} at both surface and body.

2.13 Conclusions

Even in the simplest case, when the soil is homogeneous and isotropic and with the surface as boundary, energy will travel with at least three basic waves. The basic waves travel with different propagation, radiation and material damping laws. For man-made geotechnical vibrations (where the shear strain amplitude $\hat{\gamma}$ is smaller than 0.01 %) the material damping for each basic wave is expected to be nearly constant. Unfortunately a distribution of the individual material damping laws in these basic waves is unknown yet.

If the soil is heterogeneous, additional effects will occur, like scattering, dispersion, reflection and/or refraction. This makes the vibration predictions far more complex.

Also the existence of additional phases in the soil makes the predictions of the vibrations even more complex. For instance gas bubbles will damp vibrations considerably and pore water will create a second kind of P-wave.

Therefore it is decided to start this research on vibration prediction from the simplest case – an oscillating plate on an elastic, homogeneous and isotropic half-space, where the plate oscillates harmonically in vertical direction and the soil is unsaturated.

3 HARMONICALLY OSCILLATING PLATE

3.1 Introduction

The simplest case to start with the investigation of man-made geotechnical vibrations near the surface is a case of a plate on an elastic homogeneous, non-saturated isotropic half-space, harmonically oscillating in vertical direction. Analytical methods, which were discussed in the previous chapter will be compared to the FEM calculation results.

3.2 Theory versus FEM

In order to check the analytical solutions described in Chapter 2.10 and Chapter 2.11 the finite element method software Plaxis 2D is used.

Soil and FE model properties

The used geometry of the model can be found in Figure 3-1.

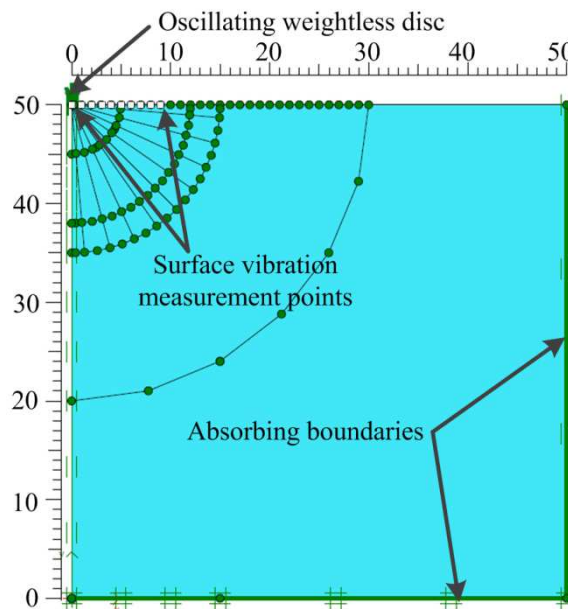


Figure 3-1. Geometry of the FE model for vibrations.

The general force-displacement is based on the following equation:

$$[M]\{\ddot{u}\} + [C]\{\dot{u}\} + [K]\{u\} = \{F\}, \quad (3-1)$$

in which:

$[M]$	=	mass matrix,	$[\text{kg}]$
$[C]$	=	damping matrix,	$[\text{N}/(\text{m}/\text{s})]$
$[K]$	=	stiffness matrix,	$[\text{N}/\text{m}]$
$\{F\}$	=	force vector,	$[\text{N}]$
$\{u\}$	=	displacements vector,	$[\text{m}]$
$\{\dot{u}\}, \{\ddot{u}\}$	=	velocities and accelerations vectors.	$[\text{m}/\text{s}], [\text{m}/\text{s}^2]$

The mesh was updated for the surface vibration calculations depending on the frequency. This was done in order to make sure that there were at least 5 elements per wave length. Also the time step was controlled in order to prevent a wave to travel more than one element per time step.

The modelled area is 50 m in both length and depth. Surface calculation points for vibration recordings were placed from radius 1 m to 20 m, at 1 m distance from each other. The soil is modelled with 15-node triangle elements (Figure 3-2).

An element with 15-nodes provides a fourth order interpolation for displacements and the numerical integration involves twelve Gauss points (stress points).

The model's elastic properties are the Young's modulus $E = 50$ MPa and the Poisson's ratio $\nu = 0.25$. Unit weight of the soil medium $\gamma = 20$ kN/m³. The weightless rigid plate has a radius $r_{pl} = 1.0$ m. The interface between the plate and the soil is modelled as rigid. The plate is loaded by a harmonical vertical stress σ_y , which has an amplitude of 10 kPa. Different loading frequencies are used.

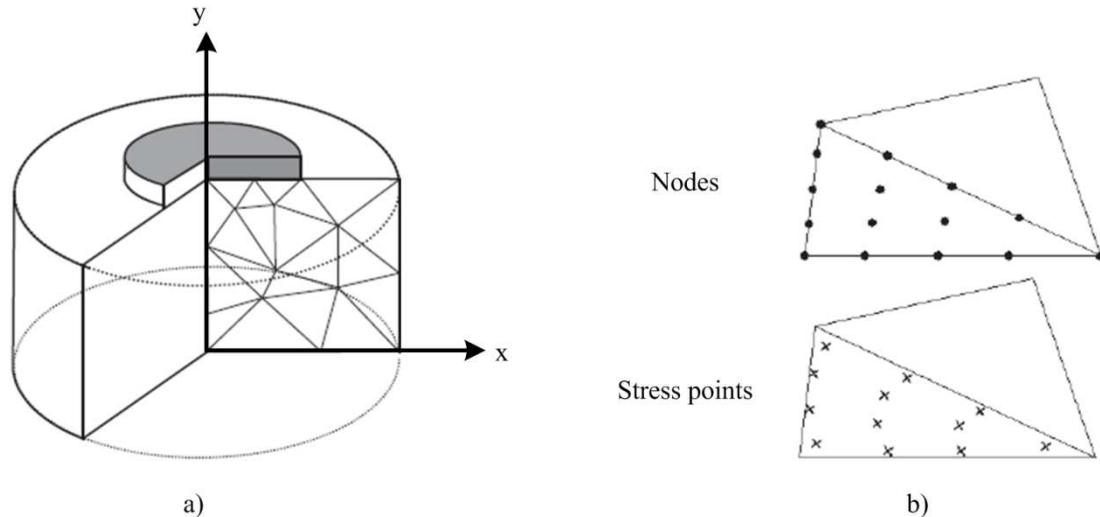


Figure 3-2. a) Axisymmetric problem b) 15-node triangular soil elements (Plaxis bv, 2015).

The damping matrix $[C]$ represents the material damping. In Plaxis 2D, Rayleigh damping is used, where $[C]$ is a function of the mass and stiffness matrices, according:

$$[C] = \alpha[M] + \beta[K], \quad (3-2)$$

where:

$$\begin{aligned} \alpha &= \text{determines the influence of mass in the system's damping, } [-] \\ \beta &= \text{determines the influence of stiffness in the system's damping. } [-] \end{aligned}$$

The coefficients α and β were kept zero in this simulation, to avoid any type of material damping.

Results: amplitude of the shaker

All analytical methods, described to evaluate the dynamic amplitude of an oscillating rigid plate, were compared with the results of Finite Element simulations performed by Plaxis 2D software.

The ratio of the dynamic displacement to the static displacement (Boussinesq solution) is used in the vertical axis, and the dimensionless frequency in the horizontal axis in Figure 3-3 a). The figure shows, that Reissner's solution with Sung's (1953) displacement functions f_1 and f_2 for a weightless rigid plate oscillating on an elastic half space with Poisson's ratio $\nu = 0.25$, as well as the Confined Elasticity approach is acceptable for very small dimensionless frequencies a_0 , but for higher frequencies rapidly becomes inaccurate. But Lysmer's solution corresponds to the FEM results very accurately.

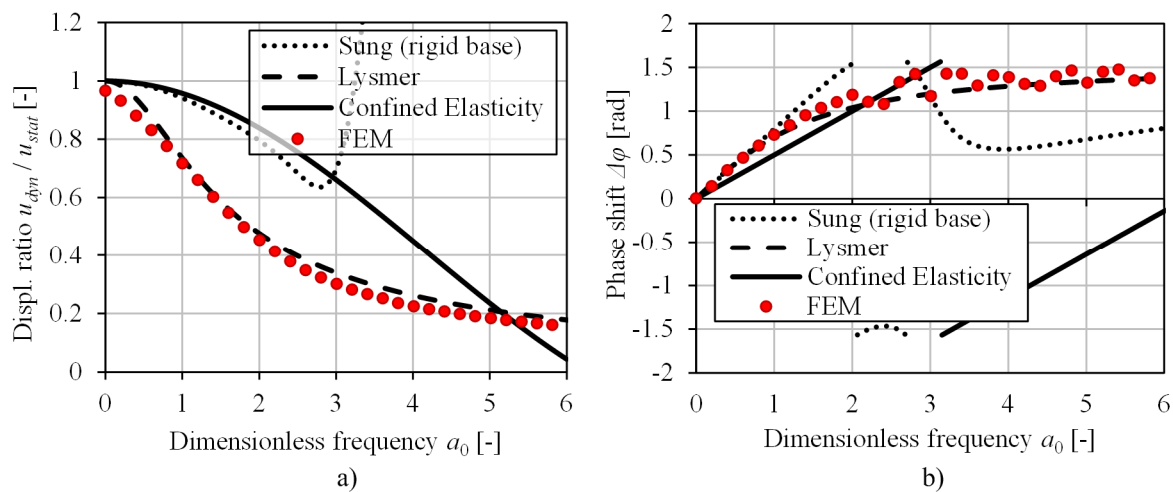


Figure 3-3. Comparison of analytical solutions to FEM: weightless rigid plate a) Relative displacement amplitudes; b) Phase shifts.

The displacement functions deduced by Sung (1953) can be calculated as follows:

$$\begin{aligned} f_1 &= -(0.1875 - 0.0703131 a_0^2 + 0.006131 a_0^4), \\ f_2 &= 0.148594 a_0 - 0.023677 a_0^3 + 0.001291 a_0^5. \end{aligned} \quad (3-3)$$

Also a comparison between the analytical and numerically obtained phase shifts has been made and showed in Figure 3-3 b). Here Lysmer's solution also shows the best match with the FEM results.

Verrijt noticed that in practice only in case of very rapid fluctuations the dimensionless frequency may be larger than one. An example of such a phenomenon is pile driving, by hammering or by high frequency vibrating (Verrijt, 2006). Therefore for an oscillating plate's problem any of the solutions can be used, nevertheless the Lysmer's solution has the lowest error over a total range of dimensionless frequencies.

The amplitudes of the rigid plate also checked for a vibrating rigid plate with mass. The calculations were performed with four different modified mass ratios $B = 0.5, 1.0, 2.0$ and 5.0 and the results can be seen in Figure 3-4.

As it can be seen from the figure below, Lysmer's approach is the most accurate, and the others two over predict the amplitudes of vibration.

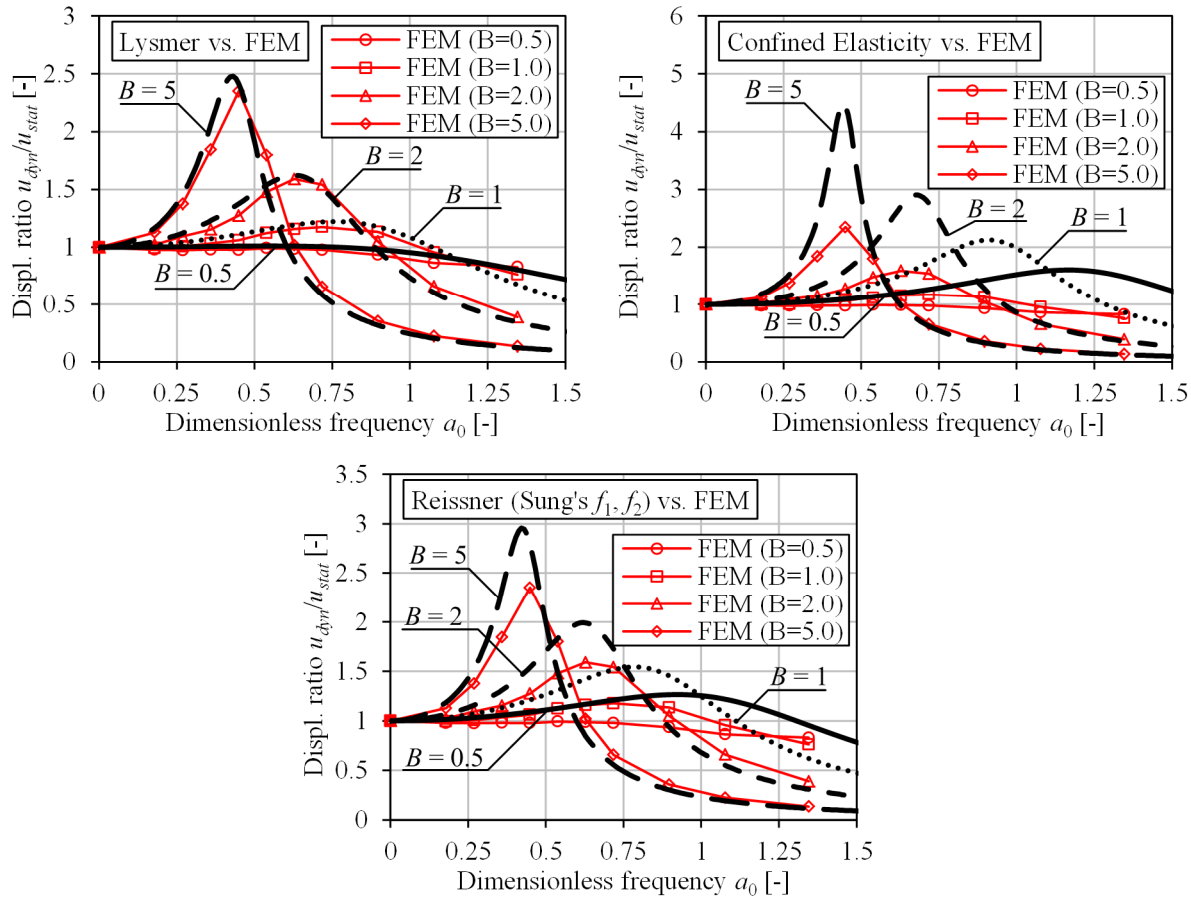


Figure 3-4. Comparison of analytical solutions to FEM: rigid plate with mass.

Results: amplitudes on the surface

Barkan's solution for the vibration amplitudes on the soil surface is also compared with the results of FE modelling. The vibration frequency was changed in order to compare different dimensionless frequencies a_0 . Figure 3-5 shows, that the vertical displacements for a weightless rigid plate in the near-field (up to 1 to 4 m, depending on a_0) can be rather well represented by the Barkan near-field equation.

Nevertheless the far-field solution for the vertical amplitudes of displacements provides comparable results only for low dimensionless frequencies (probably for $a_0 < 0.3$).

From Figure 3-6 it can be seen, that Barkan's far-field solution for horizontal displacement amplitudes is also only correct for small dimensionless frequencies ($a_0 < 0.3$). For the higher dimensionless frequencies, just like the far-field solution for the vertical amplitudes, the far-field solution for the horizontal amplitudes provides values, very different from the FEM results.

The sudden jumps of the near-field solution, when it goes to infinity, come from the fact that this solution was derived for small values of $k_s \cdot r$ only. After this jump, Barkan (1962)

suggested to use a far-field solution, in which only the R-wave is taken into account. This shows that the solution itself is not continuous.

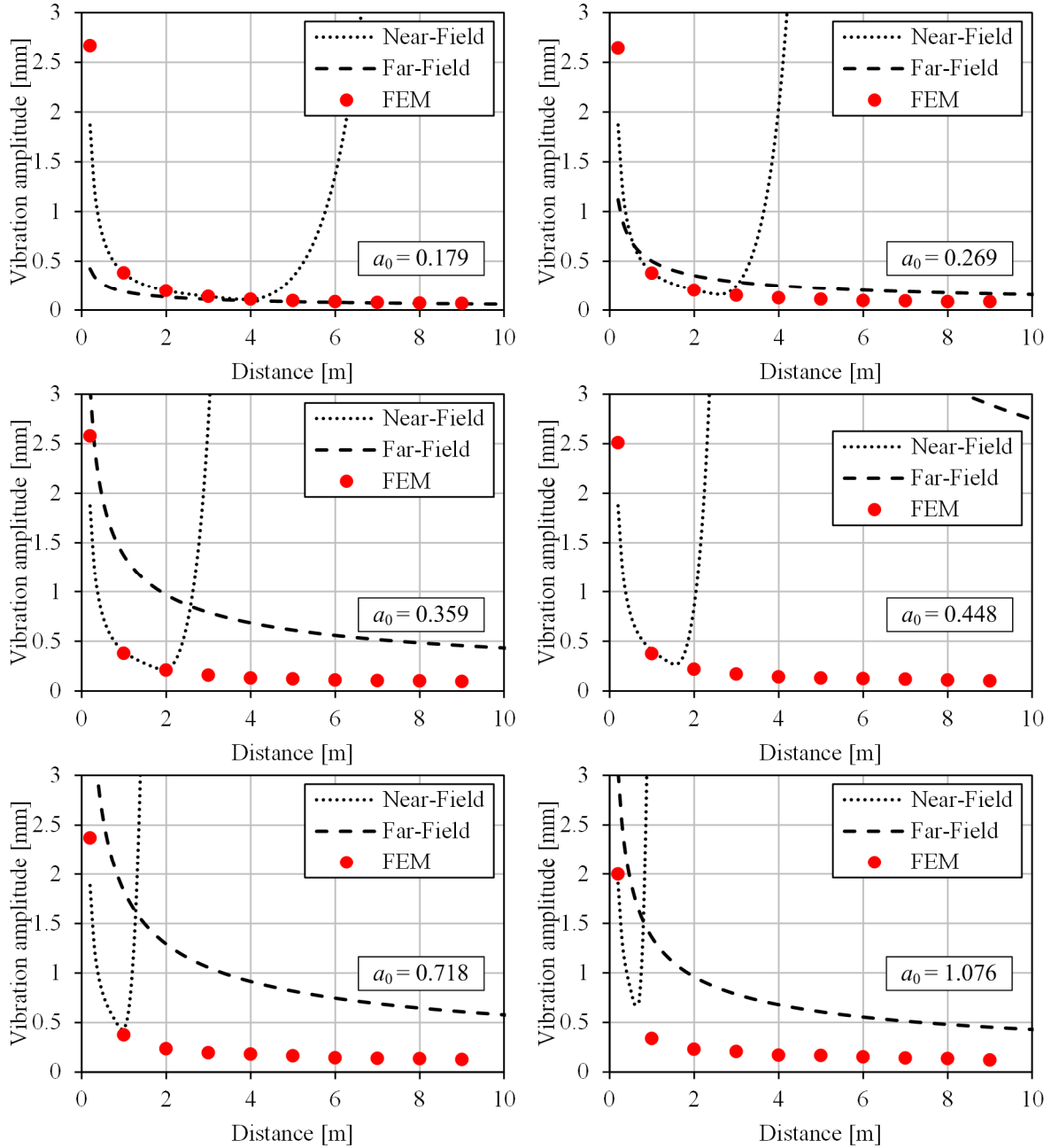


Figure 3-5. Vertical displacement amplitudes on the surface at different dimensionless frequencies a_0 .

It is worth mentioning, that the shape of the far-field solutions (both vertical and horizontal) is quite good, but the positioning of the curve is wrong. In other words, it might be possible to use the far-field solution's curve by correcting it by an additional frequency dependent variable. Frequency dependence is required, because the vertical position of the curve changes with different frequencies (as can be seen in Figure 3-5 and Figure 3-6).

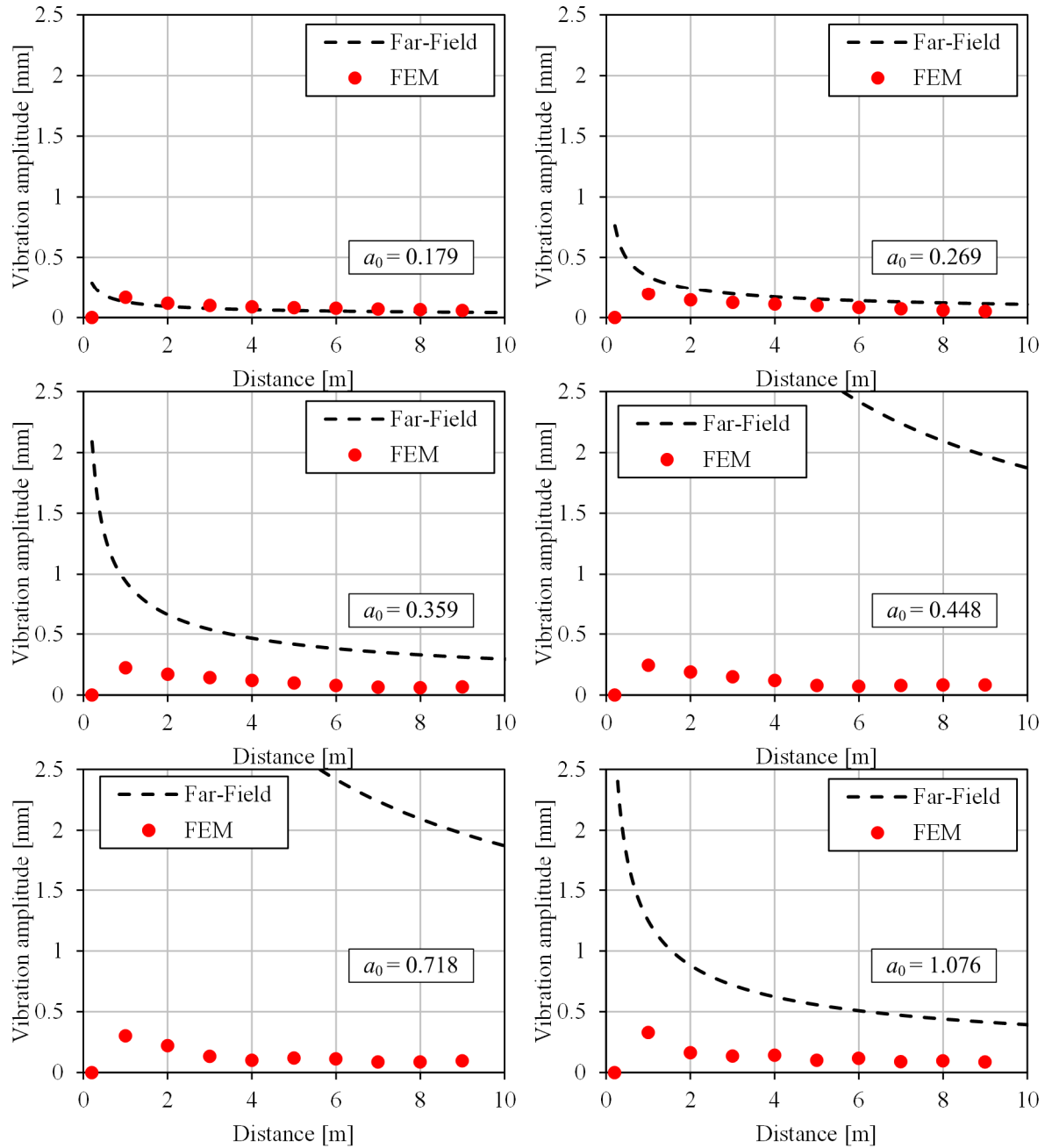


Figure 3-6. Horizontal displacement amplitudes on the surface at different dimensionless frequencies a_0 .

3.3 Conclusions

Analytical solutions, for a harmonically oscillating plate on an elastic homogeneous isotropic half-space, have been compared with the FEM calculation results. There are quite a few solutions to calculate vibration amplitudes and phase shifts of the plate itself, but there is only Barkan's method, to calculate the amplitudes and phase shifts of the surface vibration, further away from the source.

The comparison of the analytical solutions with the FEM showed that for the vertical vibration amplitude of an oscillating rigid plate, Lysmer's analytical solution demonstrates

similar results as the FEM calculations. The confined elasticity solution as well as the Reissner's solution (with Sung's displacement functions) could be used for very low dimensionless frequencies only.

The comparison of Barkan's solution, which is unfortunately for weightless plates only, and FEM showed similar results only for the near-field zone, whereas the far-field zone gave similar results for the FEM calculations only for low dimensionless frequencies ($a_0 < 0.3$).

Barkan's far-field solution still could be used if it would be modified in such a way, that it becomes a smooth continuation of the near-field solution. This could be achieved by introducing an additional frequency dependent variable.

Barkan's division of the wave field into the near- and far-field was unexpected, because the problem is linear. This, and the disagreements between some analytical solutions and FEM results, encouraged to investigate the problem of an oscillating circular rigid plate more carefully, by inspecting the wave-field itself. This is done in the following chapter.

4 DECOMPOSITION OF WAVES

4.1 Introduction

A wave on the soil surface can be seen as a superposition of several types of waves with each its own behaviour. Therefore to have a better insight into the propagation of vibrations in a soil medium, the measured signal has to be decomposed into the basic waves and analysed separately. A main problem in the field is that during harmonic oscillations, the different types of waves cannot be measured independently, only the superposed velocities or accelerations. So, in order to study the measurements, a way to decompose the superposed waves into basic waves, should be found first.

4.2 Decomposition technique

The problem has been solved for a homogenous, elastic and isotropic soil, which is disturbed by a harmonically oscillating plate on the surface (Figure 4-1). It is assumed that there is no material damping.

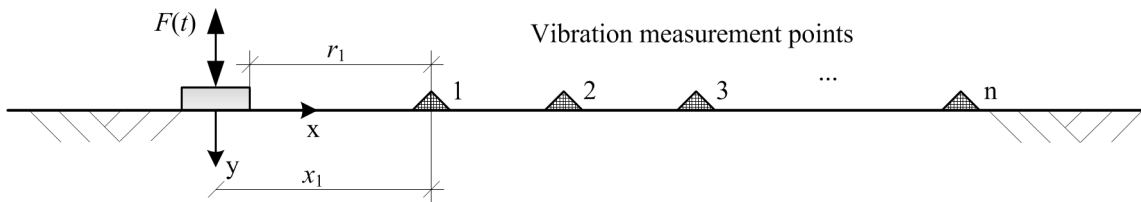


Figure 4-1. Sketch of an oscillating plate and measurement points.

The displacement of each point on the soil surface in direction i can be described as a superposition of the displacements of the three basic waves in that point:

$$u_i(r, t) = u_{p,i}(r, t) + u_{s,i}(r, t) + u_{r,i}(r, t), \quad (4-1)$$

in which:

$$\begin{aligned} u_{j,i}(r, t) &= \text{displacement of the } j\text{-wave in time and space,} & [\text{m}] \\ _i &= \text{index indicating the } x \text{ or } y \text{ direction,} & [-] \\ _j &= \text{index indicating the wave type (P-, S- or R-wave).} & [-] \end{aligned}$$

By taking into account the propagation laws of the general waves, Equation (4-1) can be rewritten for any measurement point as follows:

$$u_x(r, t) = \hat{u}_{p,x} \sin(\omega t - k_p r - \Delta\varphi_p) + \hat{u}_{s,x} \sin(\omega t - k_s r - \Delta\varphi_s) - \hat{u}_{r,x} \cos(\omega t - k_r r - \Delta\varphi_r), \quad (4-2)$$

$$u_y(r, t) = \hat{u}_{p,y} \sin(\omega t - k_p r - \Delta\varphi_p) + \hat{u}_{s,y} \sin(\omega t - k_s r - \Delta\varphi_s) + \hat{u}_{r,y} \sin(\omega t - k_r r - \Delta\varphi_r), \quad (4-3)$$

where:

$\hat{u}_{j,i}$	=	amplitude of the j wave in i direction,	[m]
ω	=	angular frequency,	[m]
k_j	=	wave number,	[m]
i	=	index indicating the x or y direction,	[-]
j	=	index indicating the wave type.	[-]

In order to relate the measured vibrations to different points with different distances, the attenuation laws of the basic waves will be used. The amplitudes of the body waves (P-waves and S-waves) attenuate proportional to x^{-1} and the surface wave (R-wave) attenuates proportional to $x^{-0.5}$, where x is the distance from the axis of symmetry, which is the middle of the plate (Figure 4-1). For high distances or relatively small plates $x \approx r$. Now the vibration in any measurement point $k = 1 \dots m$ can be expressed as a function of amplitudes in any other point, for example the 1st point:

$$u_{x,k}(r,t) = \hat{u}_{p,x,1} \sin(\omega t - k_p r_k - \Delta\varphi_p) \frac{x_1}{x_k} + \hat{u}_{s,x,1} \sin(\omega t - k_s r_k - \Delta\varphi_s) \frac{x_1}{x_k} - \hat{u}_{r,x,1} \cos(\omega t - k_r r_k - \Delta\varphi_r) \sqrt{\frac{x_1}{x_k}} \quad (4-4)$$

$$u_{y,k}(r,t) = \hat{u}_{p,y,1} \sin(\omega t - k_p r_k - \Delta\varphi_p) \frac{x_1}{x_k} + \hat{u}_{s,y,1} \sin(\omega t - k_s r_k - \Delta\varphi_s) \frac{x_1}{x_k} + \hat{u}_{r,y,1} \sin(\omega t - k_r r_k - \Delta\varphi_r) \sqrt{\frac{x_1}{x_k}} \quad (4-5)$$

The idea is that, if one measures at more independent locations (measurement points), then the number of unknowns (the amplitudes of the basic waves) can be found.

The phase shifts $\Delta\varphi_j$ of the basic waves are assumed to be zero (which can be checked), with this, a system of equations can be assembled and solved as follows:

$$[A]\{x\} = \{u\}, \quad (4-6)$$

in which:

$[A]$	=	coefficient matrix,	[-]
$\{x\}$	=	vector of unknowns (the amplitudes),	[m]
$\{u\}$	=	vector of known values (vibration displacements).	[m]

In this case, there are more equations than unknowns (which is made intentionally in order to represent the surface more accurate), the system is over determined and can be solved by using the least squares method. For that both sides of the Equation (4-6) is multiplied by the transpose matrix of coefficients $[A]^T$. In this way, the system becomes a standard square system of linear equations, which are called the normal equations:

$$[A]^T [A] \{x'\} = [A]^T \{u\}, \quad (4-7)$$

where:

$$\{x'\} = \text{the least squares solution.} \quad [\text{m}]$$

The standard square system of linear equations can be solved as follows.

$$\{x'\} = ([A]^T [A])^{-1} [A]^T \{u\}. \quad (4-8)$$

Nevertheless if the phase shifts $\Delta\varphi_j$ of the basic waves are found not to be zero, then the system of equations cannot be solved directly by using the same approach. This is, because the system of equations is not linear anymore. Or in other words, the phase shifts cannot be separated from the coefficient matrix $[A]$ and to be put into vector $\{x\}$. The solution has to be found by using the least squares method in an iterative way. This is an optimisation problem, where the objective function minimises the sum of the squares of differences.

To evaluate the precision of the solution, R^2 value (often referred to as the goodness of fit) is calculated, where 0 means no correlation at all and 1 means the perfect fit.

$$R^2 = 1 - \frac{\sum (u_k - u_k')^2}{\sum (u_k - \bar{u}_k)^2}, \quad (4-9)$$

where:

$$\begin{aligned} R^2 &= \text{correlation factor,} & [-] \\ u_k &= \text{measured displacements,} & [\text{m}] \\ u_k' &= \text{back-calculated displacements,} & [\text{m}] \\ \bar{u}_k &= \text{average of the measured displacements.} & [\text{m}] \end{aligned}$$

In this way, not only the unknown amplitudes of the basic waves are found, but also their phase shifts (which must be zero, according to the current theory). The technique described above, can be used to decompose a measured wave into the three basic waves and to check if the superposition of the basic waves correlates with the measurements. For example – the back-calculated superposed signal can be used as a check, as well as the theoretical ratio of the R-wave's amplitudes on the surface $\hat{u}_{r,x,k} / \hat{u}_{r,y,k}$. A Matlab code for the decomposition technique is provided in 0.

4.3 Numerical simulation

In order to check this technique, for decomposing a superposed wave into its basic waves, a 2-dimensional, axial symmetrical numerical simulation was performed using the Finite Element Method software Plaxis 2D. The same FE model was used, which is described in Chapter 3.2. The material damping was also kept zero (which is assumed in this technique).

Ten calculation points, for recording the displacements, were placed on the soil surface from radius 15 m to 24 m, at 1 m distance from each other. The soil is modelled with 15-node

triangle elements. The oscillating plate has a radius of 0.2 m. In Plaxis 2D there is no rigid plate option and prescribed displacements are not used in order to stay closer to the practical problems, where the force is controlled. Therefore the plate is modelled with plate elements with the bending stiffness $EI = 24 \text{ MNm}^2/\text{m}$ (which is practically rigid for this problem). The interface between the plate and the soil is modelled as rigid. First the plate is loaded with a static load of 20 kPa and later a harmonic load of $\pm 10 \text{ kPa}$ at 10 Hz is introduced. Unit weight of the soil medium $\gamma = 20 \text{ kN/m}^3$.

4.4 Simulation results

The displacements were first used after about 3 cycles, so that the starting up effect of the harmonic load has vanished. The time window for the calculations was also selected such that there are no reflections yet from the absorbing boundaries, since they do not absorb perfectly.

First attempt: Peak displacements

The idea of the first attempt was to use only the displacements which were calculated at a selected time when the displacement reached a peak (see red dots at peak of the dashed line in Figure 4-2). It was assumed that the three basic waves were in phase (phase shifts $\Delta\phi$ are zero) with the original/superposed wave, similar as in the analytical solution of Miller and Pursey (1955). Therefore an assembled system of equations was solved with the least squares method according to Equation (4-8).

From the calculated basic waves, the total/superposed displacement can be back-calculated (when three basic waves are superposed) and compared with the original total wave, see Figure 4-2. The correlation factors between FEM calculation and back-calculated superposed wave are very low. The factor of the vertical component even becomes negative, which means there is no good solution. Also the ratio of the R-wave's amplitudes $\hat{u}_{r,x,k} / \hat{u}_{r,y,k} = 3.73$, which is much greater than the theoretical $\hat{u}_{r,x,k} / \hat{u}_{r,y,k} = 0.682$.

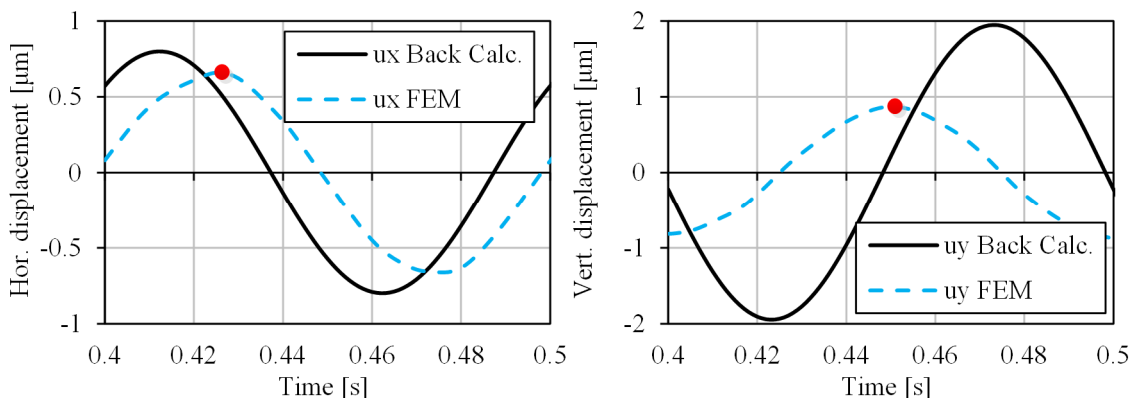


Figure 4-2. First attempt: back-calculated results vs. FEM (Plaxis) for point No. 1.

Only for the selected time (the peak of the dashed line) the solution almost fitted, but clearly not for the rest of the wave.

Second attempt: Phase shifts are not zero & multiple time points

A new attempt was made, but this time with allowing the basic waves to have different phases as the original/superposed wave. This leads to nine unknowns (six amplitudes and three phase shifts). Since the phases of the basic waves are now unknowns, the system of equations is not linear anymore, so the solution had to be found by using the least square method in an iterative way. In this attempt not only the peak values of the time-displacement graph, but all time points of one cycle were used. The period $T = 0.1$ s. The calculations were performed with a time step of $\Delta t = 0.001$ s, which gives 100 time points in a time-displacement graph. Since there are 10 field points with each 2 degrees of freedom (horizontal and vertical); there is a system of 2000 equations. The horizontal and vertical displacements of the basic waves were solved and are shown in Figure 4-3.

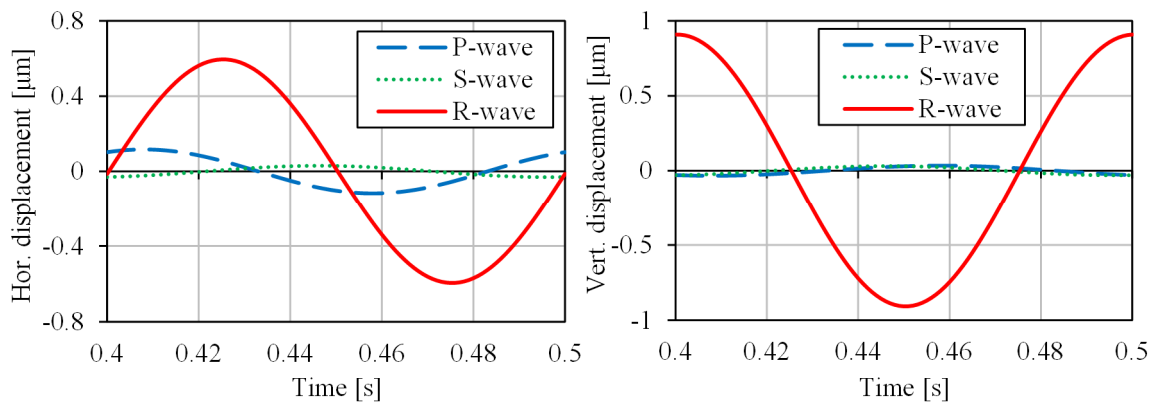


Figure 4-3. Phase shifts: horizontal and vertical displacements of the basic waves for calculation point No. 1.

This time a perfect fit of the wave displacements was found for the back calculated wave with the recorded wave of Plaxis. The correlation factor R^2 is equal to 0.9986 for the combined displacements.

Figure 4-4 shows the displacements on the surface of one cycle of the three basic waves in point 1. Interesting is to note that both the P-wave and the S-wave do not act completely flat (there is a vertical component for the P-wave and a horizontal one for the S-wave).

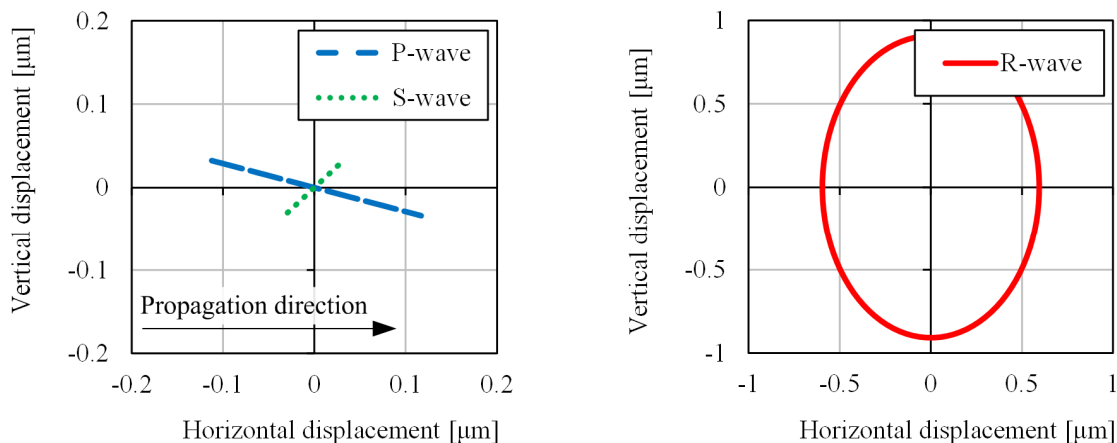


Figure 4-4. Phase shifts: displacements on the surface of one cycle of the three basic waves.

Also interesting is the ratio of the R-wave's amplitudes is found to be $\hat{u}_{r,x,k} / \hat{u}_{r,y,k} = 0.655$, which is in a quite good agreement with the theoretical ratio $\hat{u}_{r,x,k} / \hat{u}_{r,y,k} = 0.682$.

Third attempt: Flat basic body waves

The same attempt was done, but this time with the assumption that the body waves are flat, so the horizontal amplitude of the S-wave and the vertical amplitude of the P-wave are zero. Also the ratio of the theoretical R-wave's amplitudes was used, so ratio $\hat{u}_{r,x,k} / \hat{u}_{r,y,k} = 0.682$. This reduces the amount of unknowns back to six (three amplitudes + three phase shifts).

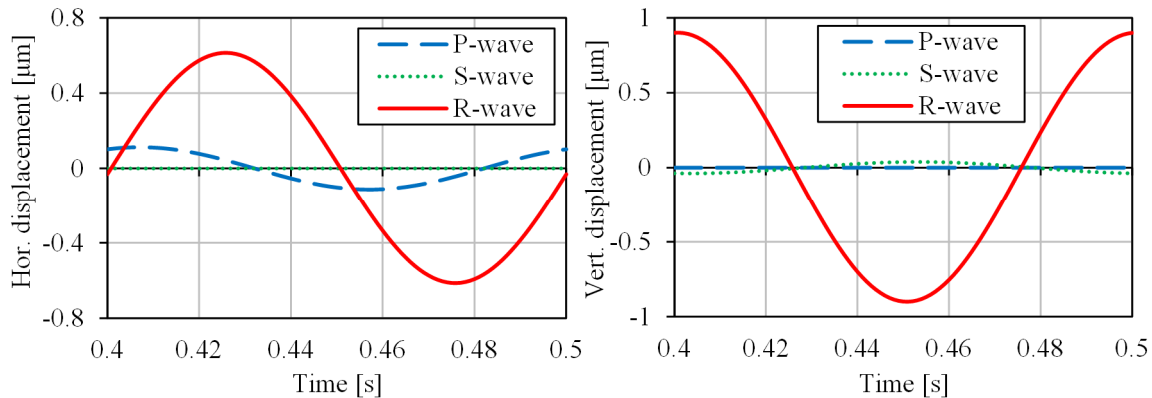


Figure 4-5. Flat waves: horizontal and vertical displacements of the basic waves for calculation point No. 1.

The horizontal and vertical displacements of the basic waves were solved and are shown in Figure 4-5.

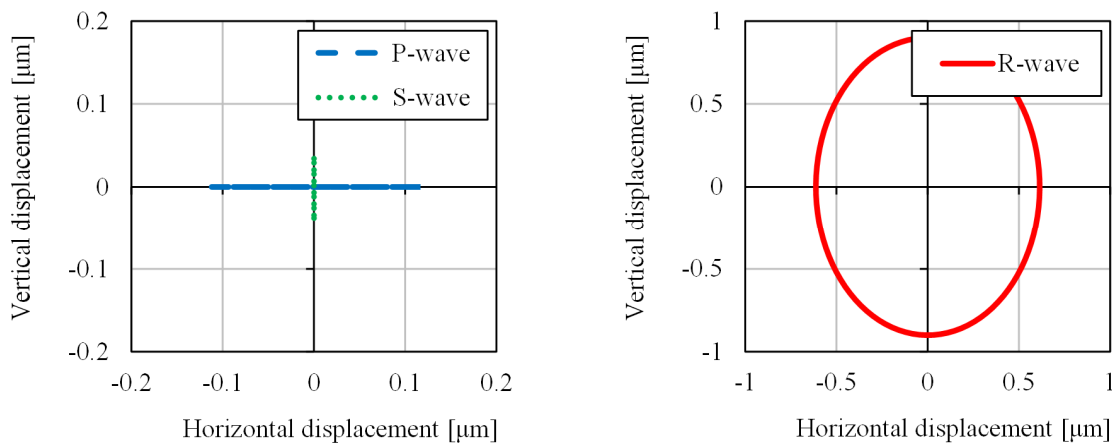


Figure 4-6. Flat waves: displacements on the surface of one cycle of the three basic waves.

Figure 4-6 shows the displacements on the surface of one cycle of the three basic waves in calculation point 1. As prescribed both the P-wave and the S-wave act completely flat (horizontal for the P-wave and vertical for the S-wave) and the ratio of the R-wave's amplitudes is the theoretical one: $\hat{u}_{r,x,k} / \hat{u}_{r,y,k} = 0.682$.

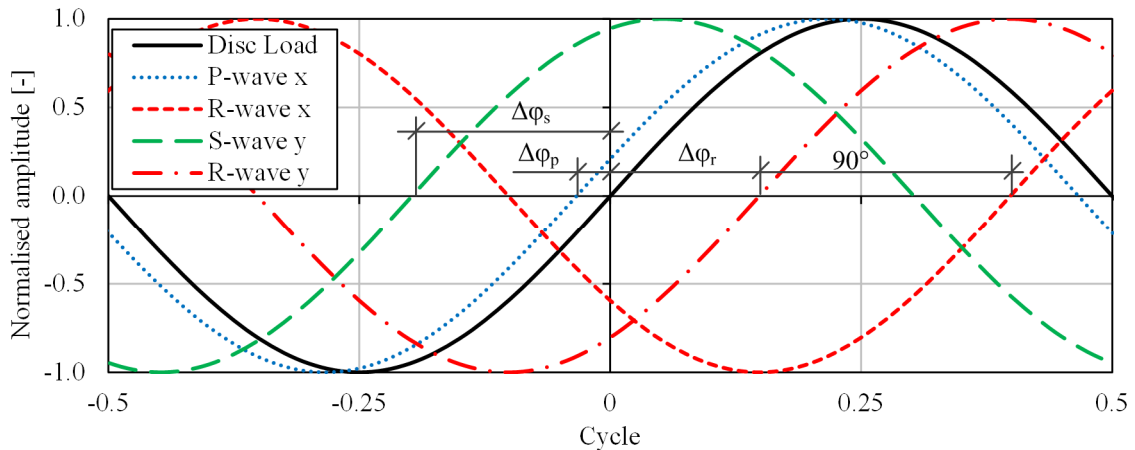


Figure 4-7. Phase shifts of the basic waves (flat waves).

The prescription for the body waves to be flat and for the amplitudes ratio of R-wave to be as the theoretical one, does not change the correlation factor much. The combined mean correlation factor for the horizontal and vertical displacements remains very high $R^2 = 0.9982$. The amplitudes and phase shifts are shown for the 2nd and 3rd attempt in Table 4-1. Mostly the difference between the two attempts is rather small. For the phase shift of the S-wave, the difference was found to be bigger: $\Delta\phi_s = -96.1^\circ$ versus $\Delta\phi_s = -71.1^\circ$.

Table 4-1. Effect of the reduction of unknowns.

Unknown	9 unknowns	6 unknowns	Units
P-wave amplitude (horizontal direction)	0.117	0.113	[μm]
S-wave amplitude (vertical direction)	0.031	0.039	[μm]
R-wave amplitude (horizontal direction)	0.595	0.614	[μm]
P-wave amplitude (vertical direction)	-0.034	-	[μm]
S-wave amplitude (horizontal direction)	0.03	-	[μm]
R-wave amplitude (vertical direction)	0.908	from ratio	[μm]
P-wave phase shift	-8.7	-12.1	[deg]
S-wave phase shift	-96.1	-71.1	[deg]
R-wave phase shift	51.9	53.5	[deg]
<u>Ratio of the R-wave amplitudes</u>			
horizontal / vertical:	0.655	0.682	[-]
average correlation factor R^2 :	0.9986	0.9982	[-]

4.5 Energy balance

Since the wave is now decomposed, the energy balance can be checked. In the finite element model there is no material damping, therefore the emitted energy from the oscillating plate on the surface and the energy carried by the basic waves should be in balance (principle of energy conservation).

Total energy

First the energy emitted from the source was calculated. For displacement recordings one point on the plate was selected. One point is sufficient, because the plate is stiff enough, so its own deformations are negligible.

The emitted energy per cycle from the oscillating plate was calculated from the load displacement ellipse, which represents the work per cycle (Figure 4-8).

$$\Delta E \approx \pi F_0 \hat{u} \sin(\Delta\varphi), \quad (4-10)$$

where:

F_0	$=$	amplitude of vertically exciting force, [N]
\hat{u}	$=$	displacement amplitude of the plate vibration, [m]
$\Delta\varphi$	$=$	phase shift between the exciting force and soil response. [rad]

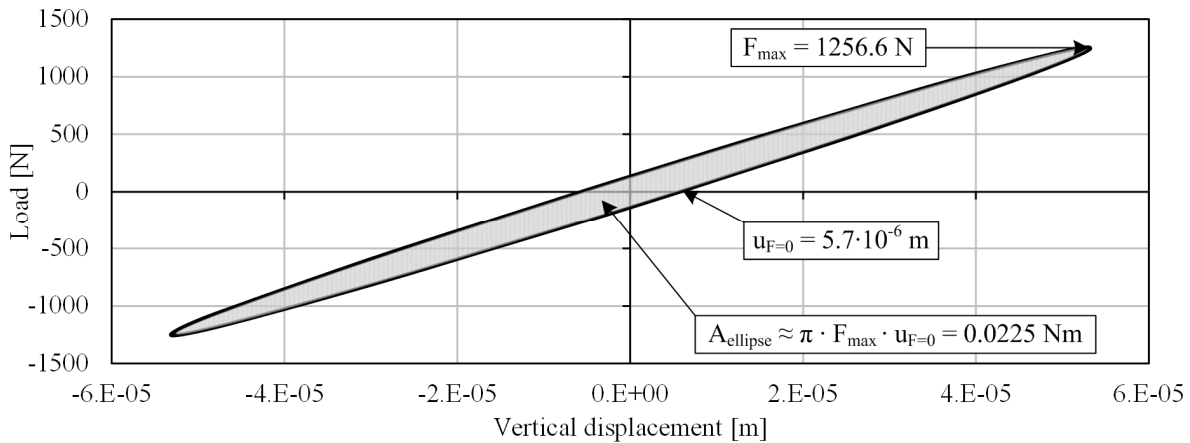


Figure 4-8. Total emitted energy per cycle.

In Equation (4-10) the amplitude of the vertically exciting force is known. The displacement amplitude and the phase shift between the exciting force and soil response can be found using the analytical methods discussed in Chapter 1 and using FEM calculations. Calculations of the vibration amplitudes and phase shifts according as well as the total emitted energy can be seen in Table 4-2.

Table 4-2. Amplitudes, phase shifts and the total emitted energy per cycle.

Method	Displacement amplitude [μm]	Phase shift [rad]	Energy [Nm]
FEM (Plaxis)	53.2	0.1071	0.0225
Reissner (Sung's f_1, f_2)	57.7	0.0996	0.0226
Lysmer	57.4	0.1064	0.0241
Confined Elasticity	57.8	0.0628	0.0143

The total emitted energy in the finite element calculations was found to be 0.0225 Nm per cycle. As it can be seen in Table 4-2, from the analytical solutions, the Lysmer's solution gives the closest match.

Energy in the basic waves

The kinetic and potential energy are in balance per volume in a wave. Therefore, the total energy per volume can be expressed by either of them. The total energy per volume, expressed by the kinetic energy per volume, for a one-dimensional wave, is:

$$E_{tot}^* = 2E_{kin}^* = \frac{1}{2} \rho \omega^2 \hat{u}^2, \quad (4-11)$$

where:

E_{tot}^*	=	total energy per volume,	$[N/m^2]$
E_{kin}^*	=	kinetic energy per volume,	$[N/m^2]$
ρ	=	density of the medium,	$[kg/m^3]$
\hat{u}	=	displacement amplitude.	[m]

The energy in the R-wave was calculated by using the analytical solution of the R-wave's amplitudes in depth. These functions are published in literature of soil mechanics, like Kramer (1996). In order to estimate the total energy in the R-wave per cycle $E_{tot,r}$, the functions of the squared amplitudes (according to Equation (4-11) energy is proportional to the squared of the amplitudes) are integrated over depth for one wave length:

$$E_{tot,r} = \frac{1}{2} \rho \omega^2 (2\pi \lambda_r) \int_{y=0}^{y=\infty} (\hat{u}_{r,x}^2 + \hat{u}_{r,y}^2) dy, \quad (4-12)$$

where:

λ_r	=	length of the R-wave,	[m]
$\hat{u}_{r,i}$	=	amplitude of the R-wave in i direction.	[m]

Unfortunately the analytical amplitude functions of the P- and S-waves, used by Miller and Pursey (1955), exist only for a very large radius, where the amplitudes of the P- and S-waves are equal to zero on the surface. This is clearly not the case here. Therefore first the amplitude functions of the P- and S-waves have to be constructed.

For that, the displacements were recorded in 19 additional points, placed in the soil volume (see Figure 4-9 on the left). By using the amplitudes of the R-wave at the surface and the theoretical amplitude functions in depth, the displacements of the R-wave were calculated for the same 19 points. These displacements in time of the R-wave were subtracted from the recorded total displacements. The residual displacements in x and y directions were projected onto the x' and y' axis (see Figure 4-9 on the right), which are regarded to be the directions of the motion of an individual particle of the P- and S-waves, respectively. In this way, for the P- and S-waves, the amplitudes of the displacements in x' and y' axes were calculated.

Displacement amplitudes of the P- and S-waves according to the solution of Miller and Pursey for the far-field can be seen in Figure 4-10. S-wave amplitudes change their sign, which means that points in different zones of the sign move to the different directions (they are shifted by 180°).

Displacement amplitudes of the P- and S-waves from the decomposed waves, obtained from the Plaxis calculations, are presented in Figure 4-11. Here it should be noted, that the phase shifts of the body waves in the soil body were different from the ones calculated on the surface. Because of that, the amplitudes in the soil body could not be found using only a one dimensional wave equation.

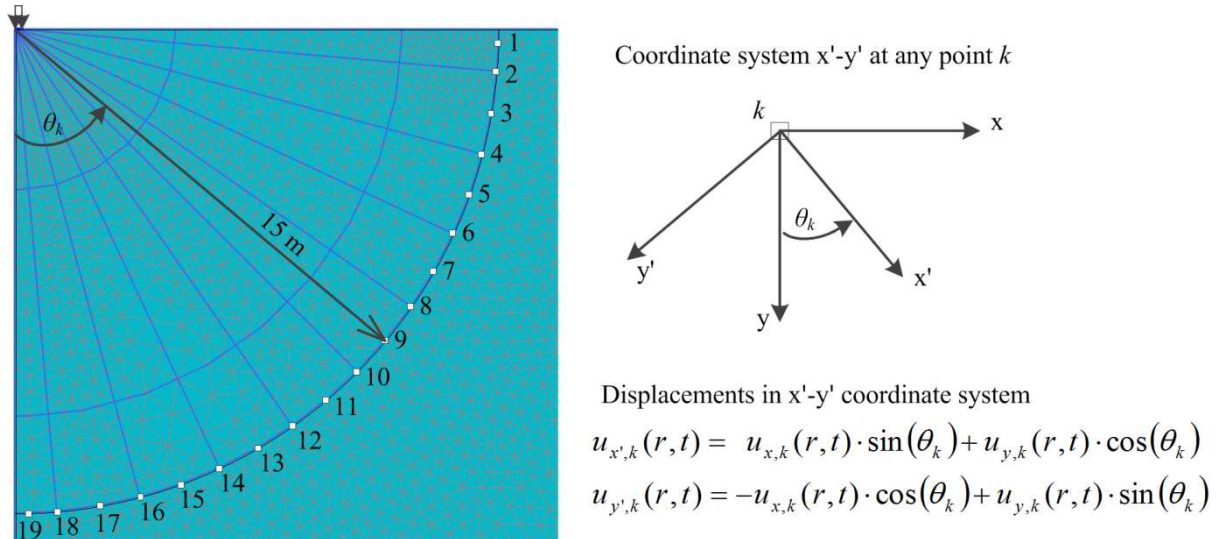


Figure 4-9. Additional points for the amplitudes of S- and P-waves.

The amplitudes were calculated just by taking an average of the maximum and minimum displacements of a body wave with not taking a phase shift into account. Although it has hardly any influence on the energy balance, it is evident that the wave behaviour is much more complicated in depth. Reasons for this could be: the plate diameter makes a curved wave-front (not a half-sphere), but probably more important is that the function of the R-wave amplitudes may not be applicable for the near-field, where some additional calculation points were placed, while the R-wave needs time, or distance, to develop in depth.

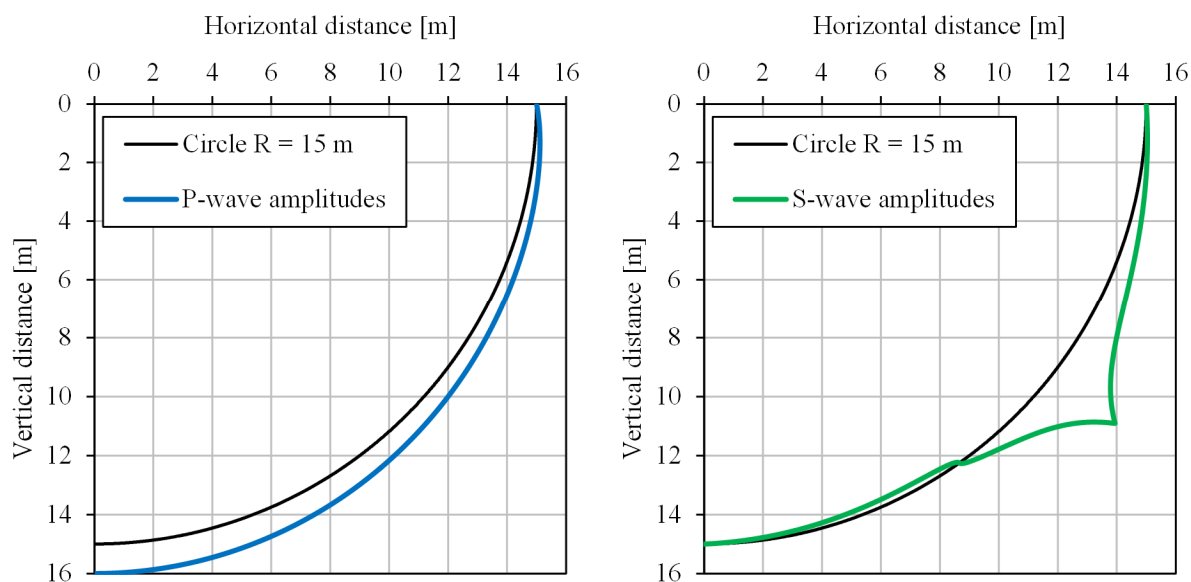


Figure 4-10. Amplitudes of the P- and S-waves (Miller & Pursey, 1955).

The reasons for differences between Figure 4-10 and Figure 4-11, which show the functions of amplitudes for P- and S-waves, are explained in Chapter 4.6.

The total energy in the P- (or S-wave) per cycle $E_{tot,p(s)}$ can be calculated by integrating the squared functions of the amplitudes (energy is proportional to the squared of the amplitudes) over a surface of a half ball for one wave length:

$$E_{tot,p(s)} = \frac{1}{2} \rho \omega^2 (2\pi r \lambda_{p(s)}) \int_{\Theta=0}^{\Theta=\pi/2} (\hat{u}_{p(s)}^2 \cdot \sin \theta \cdot r) d\theta, \quad (4-13)$$

where:

$$\lambda_{p(s)} = \text{length of the P-wave (S-wave). [m]}$$

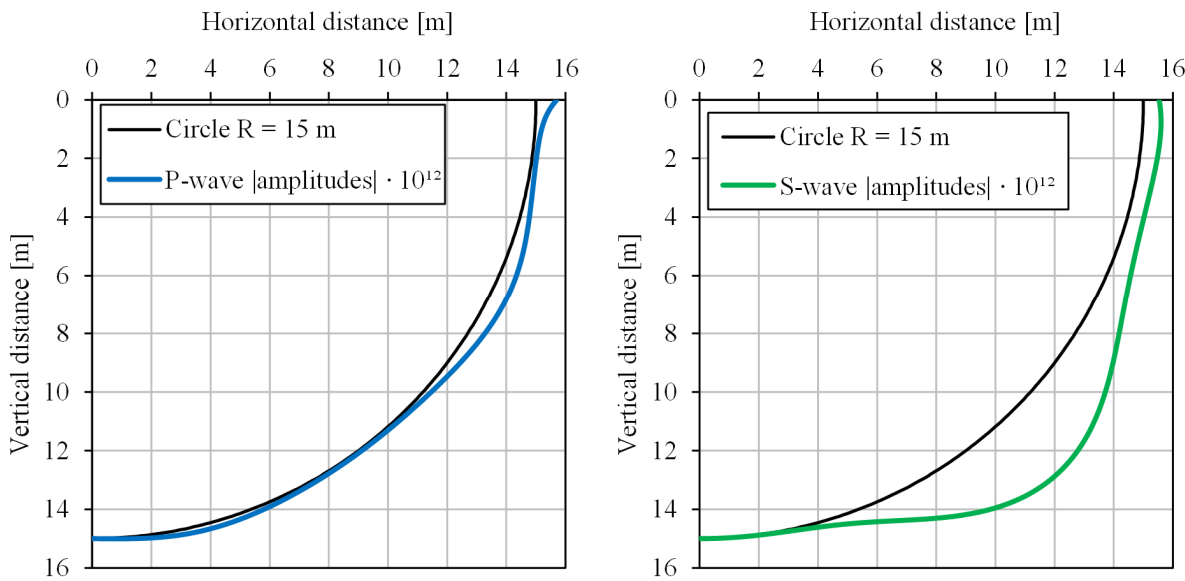


Figure 4-11. Amplitudes of the P- and S-waves obtained from the Plaxis calculations.

The total amount of energy carried by the basic waves was summed and found to be 0.0224 Nm per cycle, which is the same as the total emitted energy of 0.0224 Nm per cycle.

This fact that the emitted energy is the same as the integrated in waves at a distance of 15 m away from the source, shows that the numerical damping of FE model is negligible.

Distribution of Energy in Waves

With this the distribution of the total energy in the basic waves can be checked. This distribution was solved analytically by Miller and Pursey (1955), for soil with Poisson's ratio $\nu = 0.25$, but this has never been checked numerically. The percentages of the total energy distribution in the basic waves can be found in Table 4-3.

As can be seen from this table, the distribution of the energy based on the analytical solution of Miller and Pursey fits reasonably well to the numerical solution, despite the fact that Miller and Pursey were not aware of the phase shifts of the basic waves.

Table 4-3. Distribution of the total energy in the basic waves.

Solution	P-wave [%]	S-wave [%]	R-wave [%]
Analytical	6.9	25.8	67.4
FEM	10.8	28.5	60.7

The small differences can maybe be explained by the different initial conditions between the solutions. First, in the analytical solution no phase shifts were considered. Second, a very small and flexible plate with infinite small radius was used; while in the numerical simulation a rigid plate was used. Third, numerical methods always have residual errors.

4.6 Near-field problem

After the superposed wave is decomposed into basic waves, it is possible to use their propagation and attenuation laws to calculate displacements at any point and any time. By superposing the displacements of the decomposed waves one gets a back-calculated vibration signal. This signal can be compared with the original wave. This has been done for the same FE model calculations. The amplitudes of the back-calculated signal were compared with the FEM output. The comparison can be found in Figure 4-12.

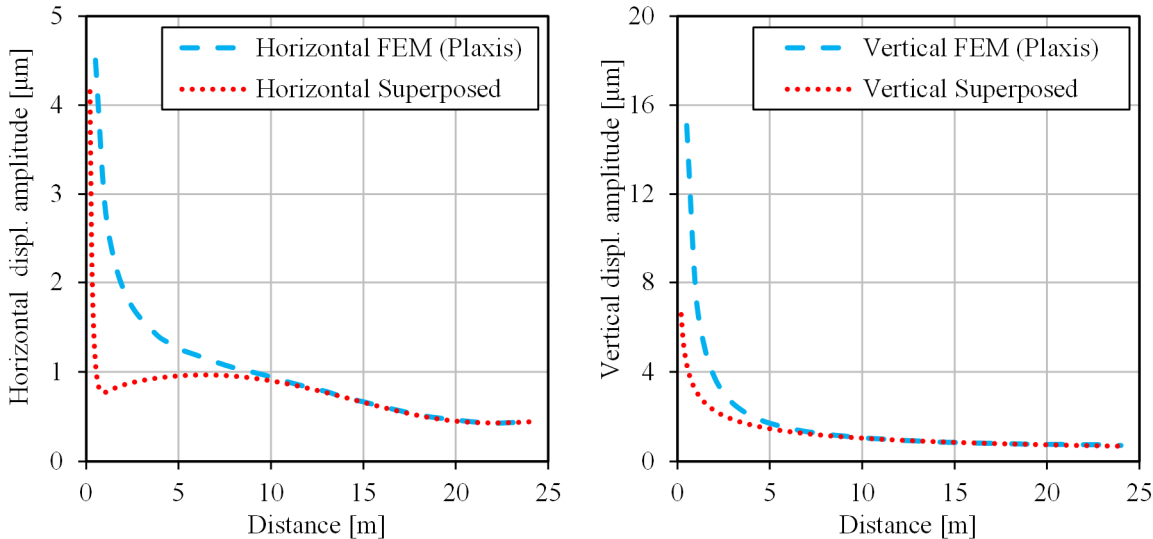


Figure 4-12. Back calculated and superposed amplitudes of the decomposed waves.

The figure shows, that close to the source the back-calculated signal amplitudes differ from the Plaxis calculations. This close distance can be named the near-field. It looks as if in the near-field the total signal has a different attenuation law. One reason for this can be that the basic waves (or at least one of them) have also another attenuation law than is prescribed (r^{-1} for the body waves and $r^{-0.5}$ for the surface wave).

Having the superposed signal amplitudes back-calculated close to the plate, it is possible also to look into the back-calculated signals of the basic waves separately, just on the edge of the plate. This is shown in Figure 4-13. The bold black line represents the vertical movement of the plate. Other sine curves represent different basic waves. When the vertical movement of the plate is compared to the elasto-static Boussinesq solution for the settlement of a rigid plate (the highest purple line in the figure) it can be seen that the elasto-static solution is very

close to the vertical movement of the plate. This means that the biggest part of the plate displacement is caused by the static movement. So it can be assumed, that all the points, close to the plate, are also influenced by this phenomenon. Of course, the elasto-static solution would be not so close to the dynamic displacement of the plate if higher frequencies would be used. However, this property could be used to simplify the dynamic calculations.

This phenomenon can also be explained by an energy transfer from one wave to another. That could explain the results of the superposed signal in the near-field. The most likely energy transfer is from the P- and S-waves to the R-wave. In the source there is no R-wave and this wave is formed gradually, because it needs to reach some depth to get its full shape. This hypothesis is also supported by other researchers, like Wolf (1994), who uses a scenic explanation: “to understand the essence of Rayleigh waves, a biological analogy is helpful. The Rayleigh wave is “conceived” at the source, “born” at the far-field boundary, and “lives” in the far-field. The near-field is the “pregnancy” region, in which the Rayleigh wave gradually develops”.

This also explains the differences between Figure 4-10 and Figure 4-11. In the far- and near-fields the amplitude functions are different because of the near-field phenomenon.

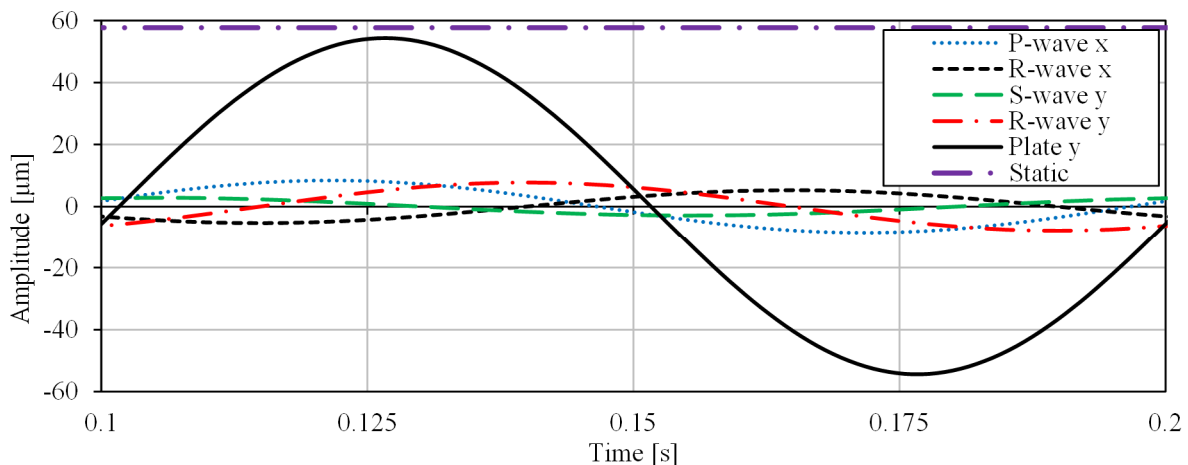


Figure 4-13. Back calculated basic waves on the edge of the rigid plate.

If there is no horizontal displacement, then there is no R-wave just below the oscillating plate, and then the functions of P- and S-wave amplitudes should look like shown in Figure 4-14.

For these distributions the energy balance can be checked. The total energy in the P-wave is:

$$E_{tot,p} = \frac{1}{2} \rho \omega^2 (2\pi r_{pl} \lambda_p) \int_{\Theta=0}^{\Theta=\pi/2} \left(\left(\hat{u} - \frac{2\hat{u}}{\pi} \theta \right)^2 \cdot \sin \theta \cdot r_{pl} \right) d\theta. \quad (4-14)$$

The total energy in the S-wave is:

$$E_{tot,s} = \frac{1}{2} \rho \omega^2 (2\pi r_{pl} \lambda_s) \int_{\Theta=0}^{\Theta=\pi/2} \left(\left(\frac{2\hat{u}}{\pi} \theta \right)^2 \cdot \sin \theta \cdot r_{pl} \right) d\theta. \quad (4-15)$$

Using the vertical displacement amplitude \hat{u} as it was calculated by using FEM, it is found that $E_{tot,p} = 0.0094 \text{ Nm}$ and $E_{tot,s} = 0.0132 \text{ Nm}$. In total this gives $E_{tot} = 0.0226 \text{ Nm}$.

The total calculated energy at the source where only the P- and S-wave exist, $E_{tot} = 0.0226 \text{ Nm}$. This is almost equal to the total emitted energy per cycle 0.0225 Nm (see Chapter 4.5). The difference is negligible and comes from the assumption, that the movement of the plate causes the same effect as the movement of the surface of the half-sphere with the same radius as the plate.

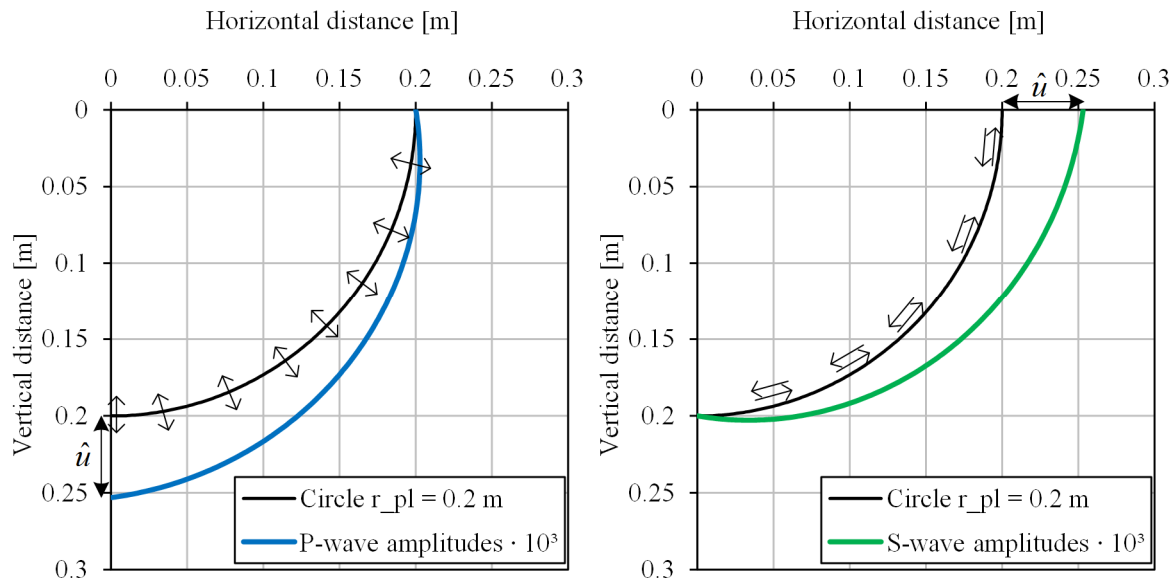


Figure 4-14. P- and S-wave amplitudes under the plate.

The calculations above shows, that the S-wave holds 58.5 % and the P-wave holds 41.5 % of the total energy just below the plate, where the R-wave does not exist yet. Chapter 4.5 shows, that in the far-field P-, S-, and R-waves carries 10.8 %, 28.5 % and 60.7 % of the total energy respectively.

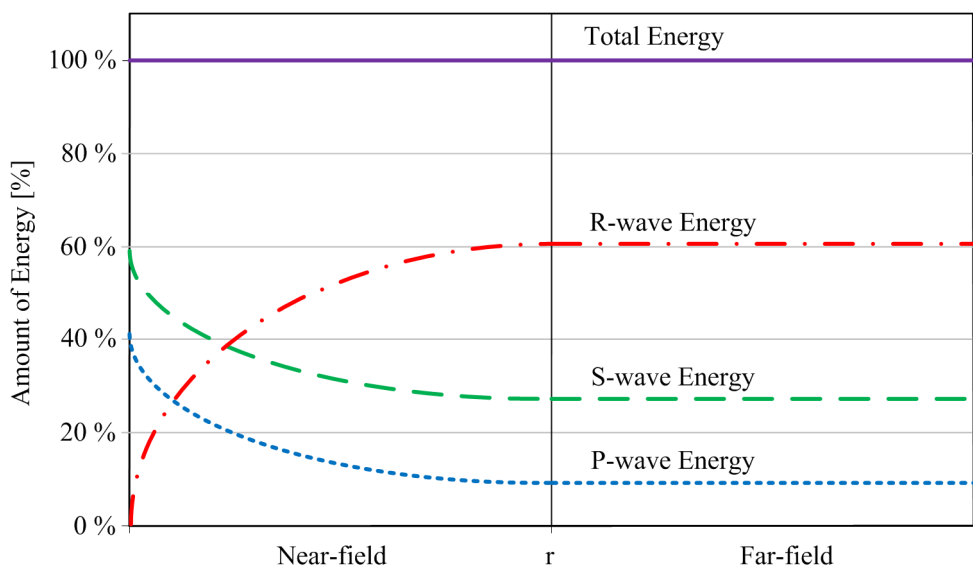


Figure 4-15. Energy transmission between the basic waves.

A possible way to illustrate the energy transmission is by using a gradual law, see Figure 4-15. The idea is that the lack of confinement at the surface for the compressional and shear waves creates additional movements at the surface which results in Rayleigh waves.

Because of this energy transmission, the laws for the amplitude functions will change as well. Graphically they might look like shown in Figure 4-16.

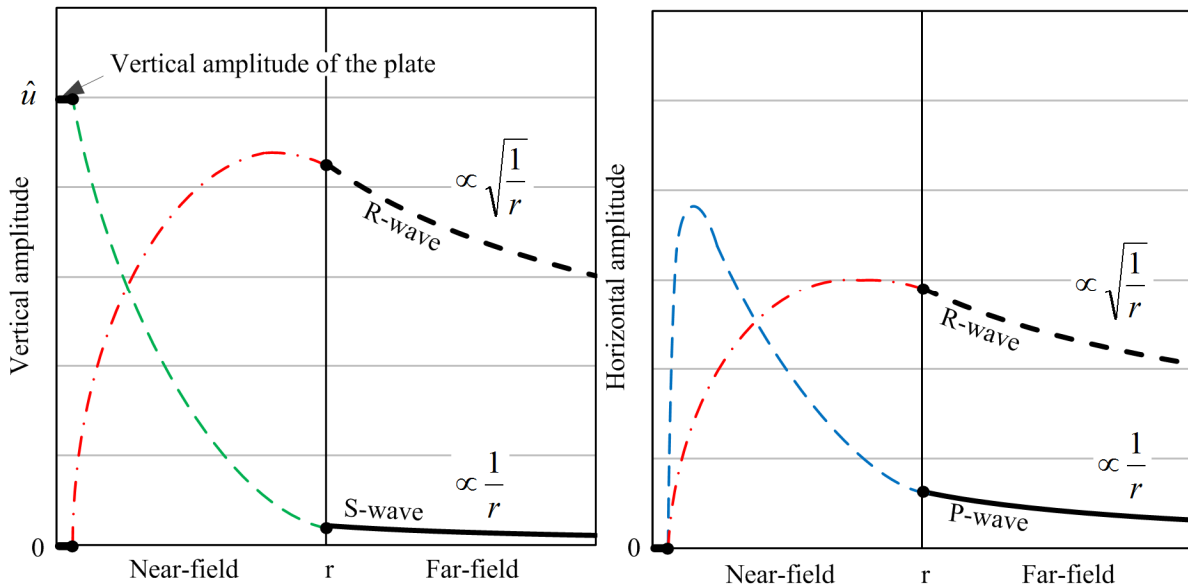


Figure 4-16. Amplitude functions in the Near- and Far-field.

4.7 Conclusions

The finite element model example in this chapter discusses a harmonically oscillating plate on a homogeneous half-space. A method has been developed to decompose a recorded superposed soil wave into its basic waves when multiple geophones are used. From the recorded data a system of non-linear equations can be assembled with six unknown parameters (three amplitudes and three phase shifts). These six parameters can be solved by using an iterative way of the least square method. This leads to a decomposition into the three basic waves, with each its own amplitude and phase shift. The superposition of only these basic waves describes very accurately the recorded superposed soil wave, proving the existence of only these three basic waves. The findings prove also that all three basic waves have phase shifts (in the far-field) and these phase shifts are all different from each other. Both facts were not known before.

The energy balance shows that the amount of emitted energy by the load on the plate is the same as of the sum of energies of the basic waves. This is another type of evidence that only three basic waves exist. The distribution of the energy over the three basic waves based on the analytical solution of Miller and Pursey (1955) fits reasonably well to the numerical solution shown in this chapter, despite the fact that Miller and Pursey were not aware of the phase shifts of the basic waves. The major part of the energy (more than 60 %) from a vertically oscillating plate on the surface goes into the R-wave.

Near the vibrating plate, the displacement amplitudes do not follow the same attenuation law such as further away from the source. This proves the existence of the near-field phenomenon. It must be concluded that the R-wave energy starts at zero just at the source and grows in the near-field zone due to an energy transmission (body waves are transferring energy to the R-wave). After some distance (in the far-field), the R-wave becomes fully developed. This phenomenon is not understood completely yet, but it does explain existence of the phase shifts of the basic waves.

5 SHAKER TEST

5.1 Introduction

Real field tests of a shaker on the ground surface of real soil have been performed in order to compare real vibrations with analytical and FEM calculations. First of all, the shaker design will be explained. Secondly the test site will be introduced, and finally the test results will be presented and discussed and conclusions will be drawn.

5.2 Shaker design

In order to produce harmonic vibrations on the ground surface, a particular shaker should be made. The requirements for it are as follows:

- It should produce sine (or close to sine) vibrations on the surface;
- It should be frequency controlled;
- It should be powerful enough, to create sufficient ground vibrations in the range of limitations of the geophones;
- It should be transportable.

To fulfil the last two requirements together is rather difficult. The more powerful the shaker, the more difficult it is to transport.

It was decided to use two counter rotating electric vibrators (with rotating eccentric masses) to produce a vertically oscillating force. This type of vibrator is frequently used in geotechnical engineering (sheet pile driving, soil densification). The vibrators are connected to a plate of 400 mm in diameter and 20 mm in thickness. Additional square plates are used to vary the total mass of the system. Everything is tightened together with bolts (Figure 5-1).

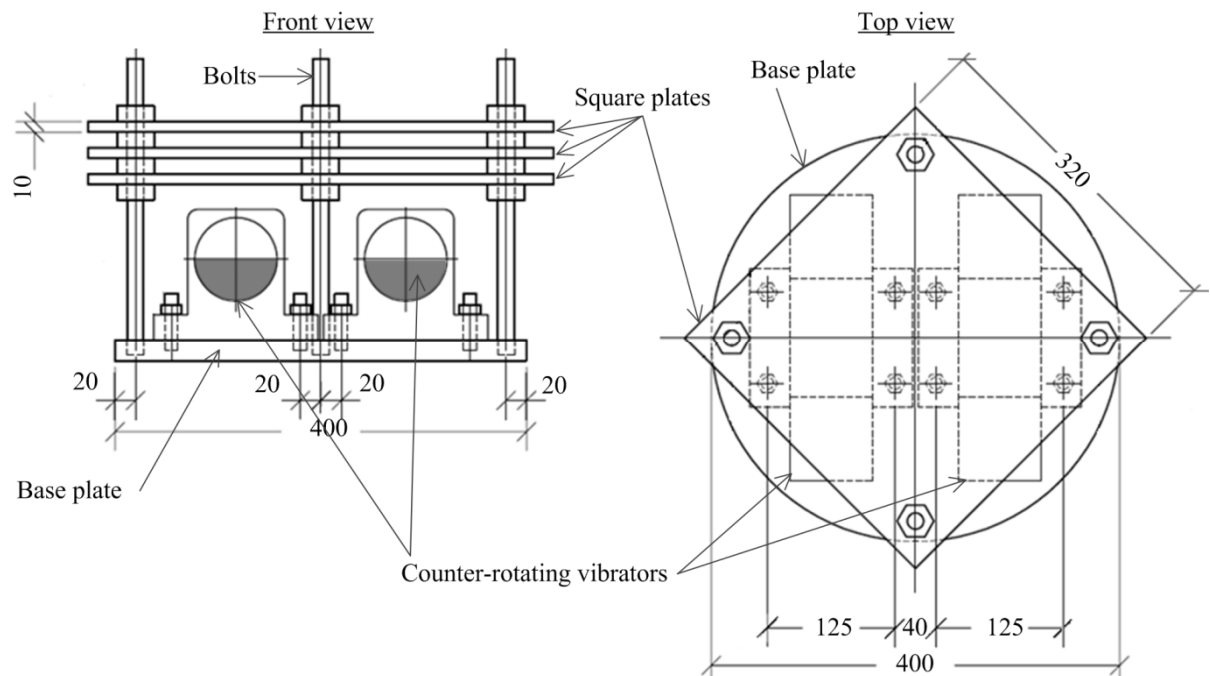


Figure 5-1. Shaker drawings.

Electric 4-poles vibrators (model A10-9.0-4 from Eviro, more information can be found in Appendix B.) were selected for the shaker. Such a vibrator with a grid frequency of 50 Hz rotates 1500 times per minute (25 Hz). By having a maximum eccentric moment of 8.32 kg·cm, the shaker can reach a maximum vertical oscillating force of 2.06 kN. In this shaker test, the total mass of the shaker was 287.4 kg, which corresponds to 2.82 kN.

A frequency inverter (Hitachi L200) was also foreseen, in order to vary the frequency from 0 to 25 Hz. For data acquisition NI USB-6218 acquisition box from National Instruments was used. It has 32 analog inputs. On top of the shaker an accelerometer was placed, in order to measure the exact frequency of shaker. All the components for the vibration tests, including the shaker, accelerometer, frequency inverter, geophones, data acquisition box, power generator and laptop can be seen in a sketch (Figure 5-2).

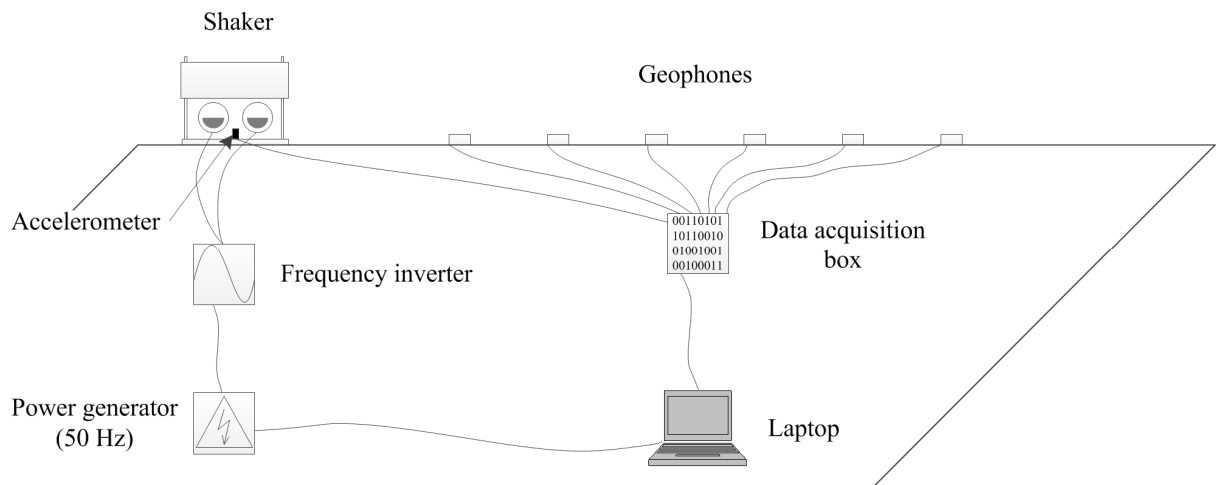


Figure 5-2. Vibration test setup scheme.

After preliminary tests, it was noticed, that the shaker was not powerful enough to produce sufficient ground vibrations. A bigger oscillating force had to be used. In order to produce a sine vibration and avoid a loose contact with the ground, the deadweight must be always bigger than the oscillating force. Therefore it was necessary to add more deadweight on the shaker. For that, the shaker was slightly updated by drilling centre holes in the square plates, and by adding a centre rod. This rod was used to centre extra steel plates (extra deadweight). The extra steel plates were tightened between the square plates (Figure 5-3).

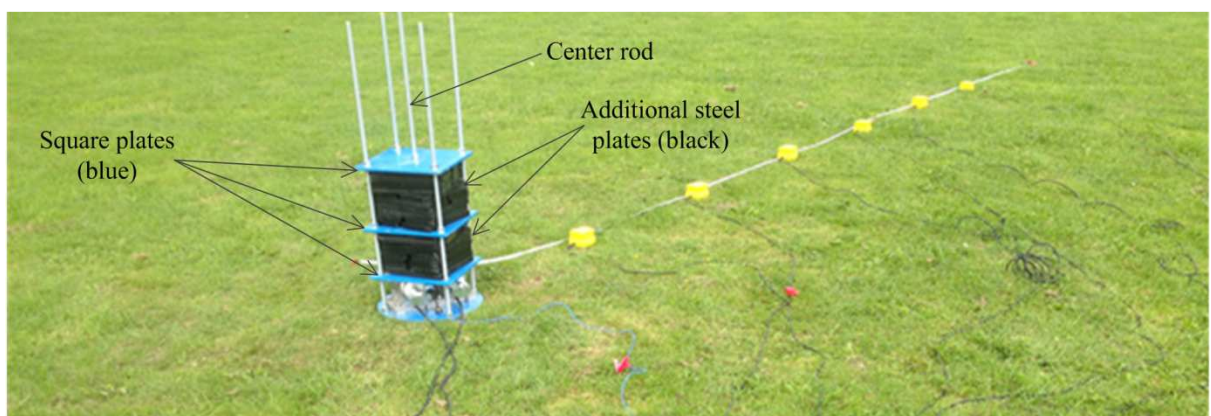


Figure 5-3. Updated shaker.

Analysing the output data of the first tests, it was noticed, that more than 3 meters away from the vibrating plate, the measurements show a considerable noise. Also there was no dominant frequency anymore. The vibrations were not harmonic, and the amplitudes for the geophones could not be determined anymore. This is shown in Figure 5-4.

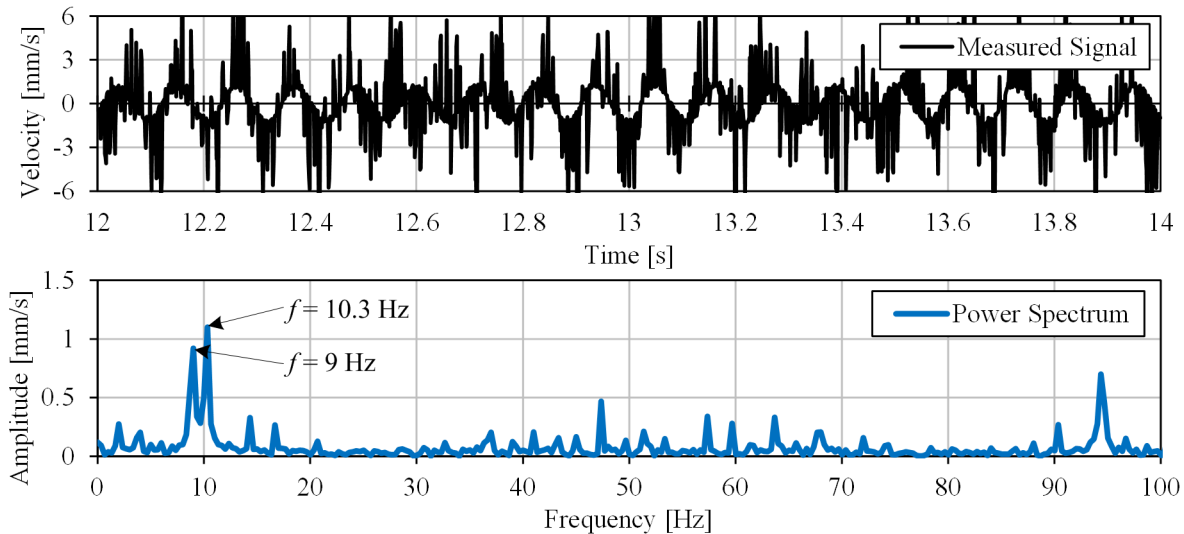


Figure 5-4. Geophone 3 m away from the source.

Several reasons were considered. The most likely ones were 1) the noise from the generator (which vibrates while its engine is working) or 2) problems in the electricity circuit. The first one was checked with a longer cord and rejected. The latter appeared to be true. The problem was in the wiring of the data acquisition box. All the channels were prepared to read signals from the geophones and minuses in the channels were linked to the ground and between themselves (Figure 5-5).

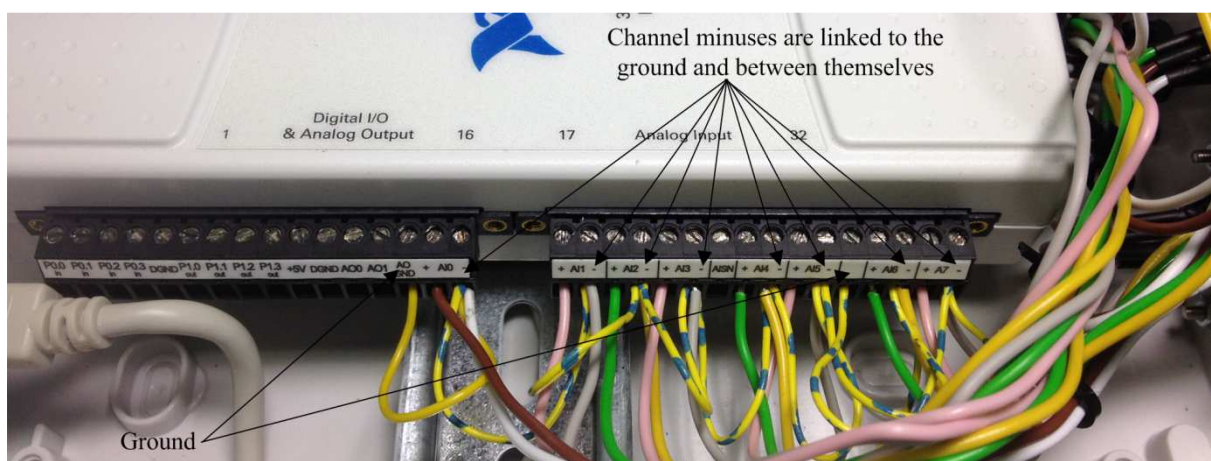


Figure 5-5. Data acquisition box channels linked to the ground and between themselves.

The problem appeared when one of the channels was used for the accelerometer, because the accelerometer is using an additional external power source (where the geophones do not). This external alternating power source was leaking throughout the links in the acquisition box to all the geophones. Two problem solutions were considered – 1) to unlink the channel which was used for the accelerometer or 2) to use a geophone on top of the shaker instead of

the accelerometer. The latter solution was chosen, because on site it was easier and faster to do. Also the geophone on top of the shaker did not go out of its range.

5.3 Information about the site

A potential site for tests should have two major requirements: it should be rather homogeneous and rather soft. Therefore a peaty site in the Netherlands was chosen. The chosen test site is located about 10 km North-East from Amsterdam (area A in Figure 5-6).

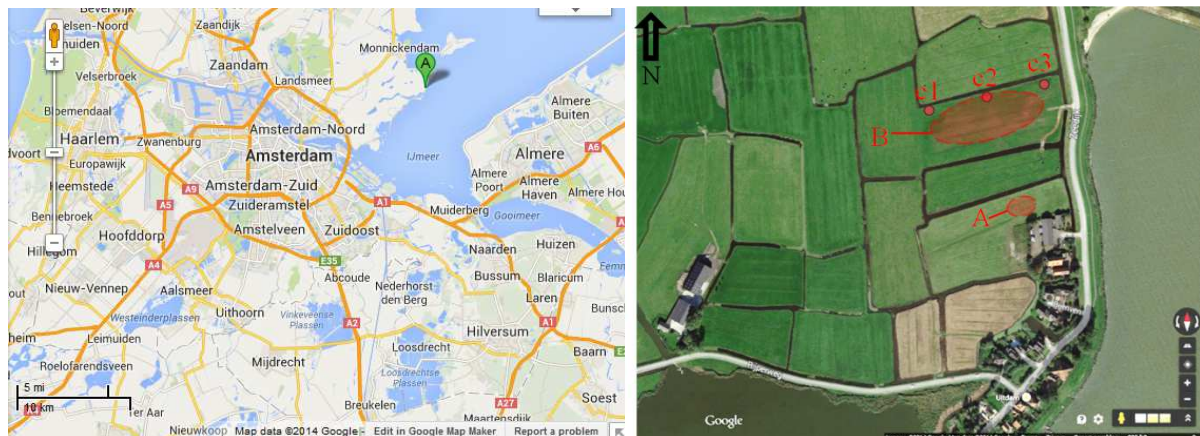


Figure 5-6. Location of the test site (GoogleMap data, 2014).

Near the test area, other research has been made before, related to the strength of peat (Zwanenburg, 2013). The area used for the peat strength research is marked by letter “B” in Figure 5-6. In there, geological investigations have been carried out in May 2012.

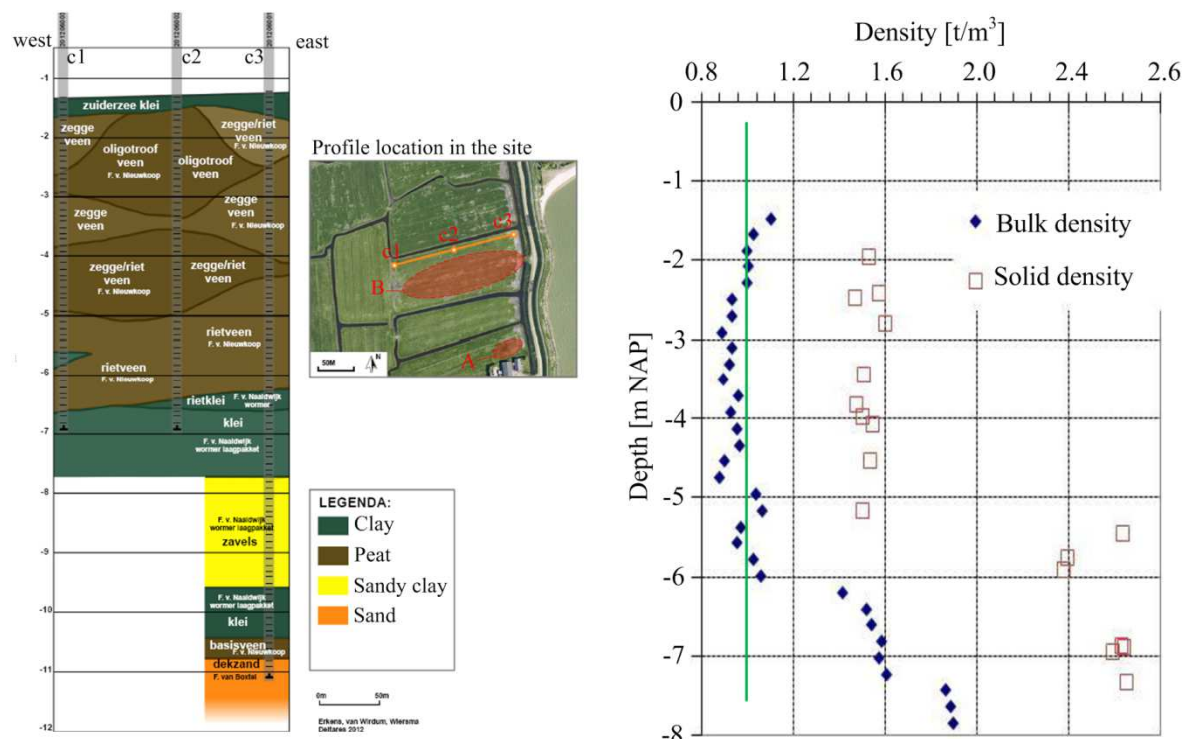


Figure 5-7. Data from previous geological investigations (Zwanenburg, 2013).

Three boreholes have been drilled and they are marked by “c1”, “c2” and “c3”. The stratigraphy and soil density can be found in Figure 5-7. The reference level for the depth of the soil is NAP, which is approximately main sea level. The ground level is approximately NAP -1.4 m. The top layer is a thin clayey layer with a thickness varying between 0.2 m and 0.5 m. Below this layer there is a peat layer of 4.5 m thick. It was reported that the bulk density of the peat layer $\rho = 0.98 \text{ t/m}^3$. The ground water table was about 40 cm below the ground surface.

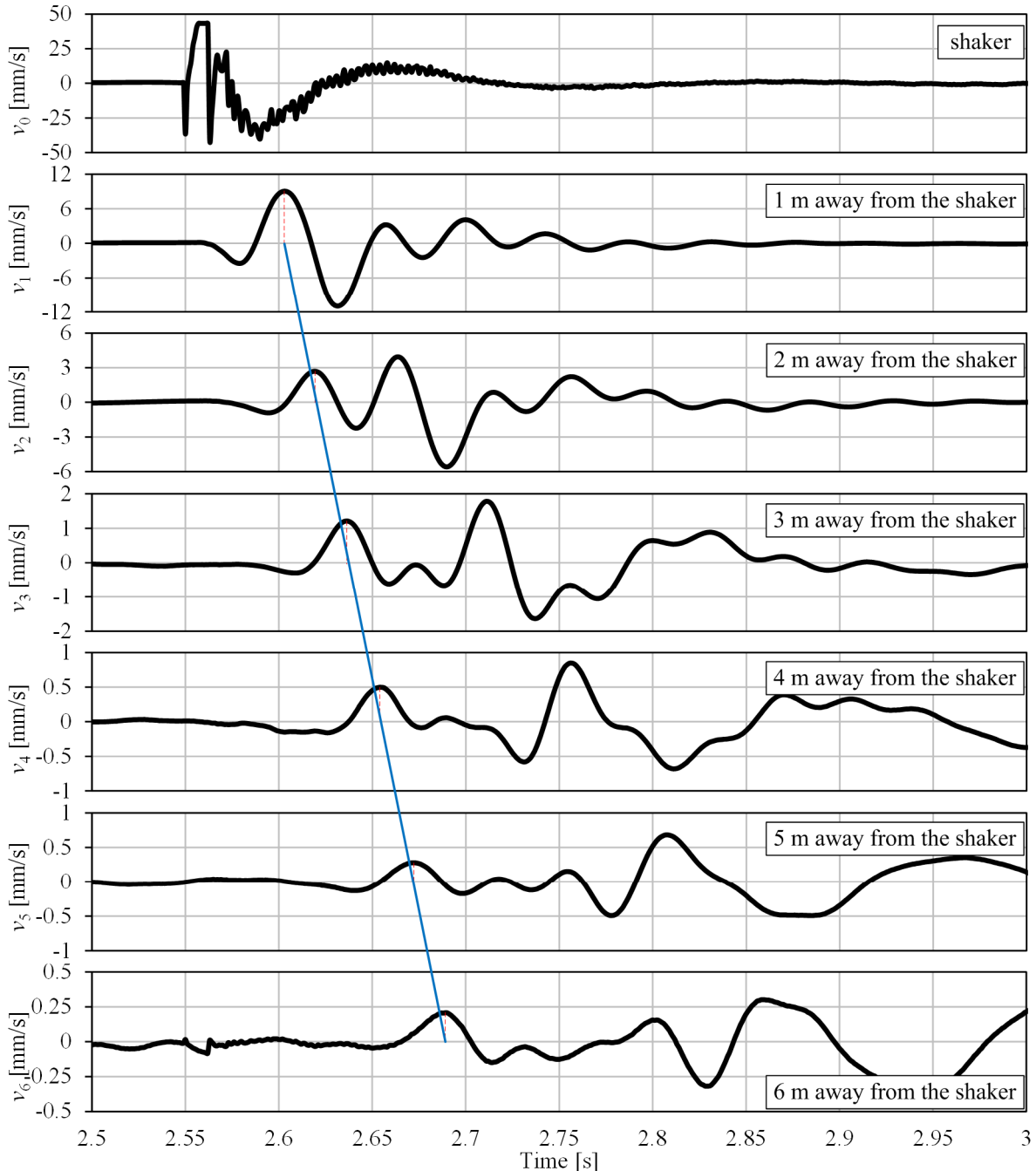


Figure 5-8. P-wave velocity measurements (velocities in radial direction).

In order to determine small strain stiffness parameters of the soil, pressure (P) and shear (S) wave velocity measurements were carried out. This was done by hitting the shaker with a

hammer and measuring the arrival times at the geophones. The geophone on top of the shaker records the input wave. Average of four such tests was used for the velocities determination.

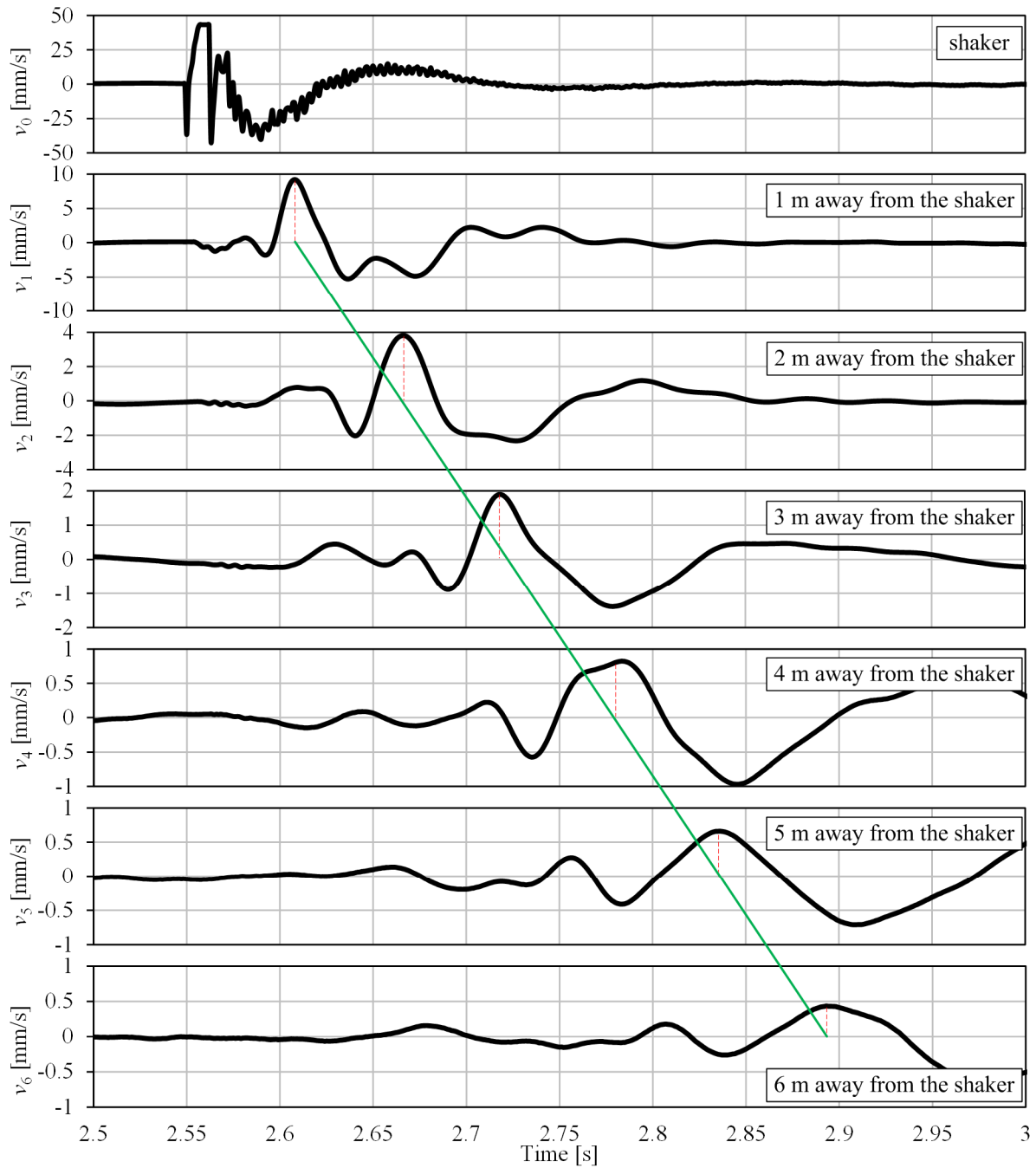


Figure 5-9. S-wave velocity measurements (velocities in vertical direction).

The P-wave velocity was measured from the arrival time differences between of the first radial vibration peaks and the S-wave velocity similarly but of the biggest vertical vibration peaks.

From arrival times at the geophones, placed at known distances (with 1 meter in between), P- and S-wave velocities were determined respectively: $v_p = 66.9$ m/s and $v_s = 17.4$ m/s. Here it should be noted that it is impossible to distinguish S- and R-wave in Figure 5-9. There are

two possibilities here: a) $v_s = 17.4$ m/s and $v_r = 16.5$ m/s or b) $v_s = 18.3$ m/s and $v_r = 17.4$ m/s. In both cases, the difference between the arrival times of these two waves in distance of 6 m would be approximately 0.02 s. Having this time difference in mind, it can be seen from Figure 5-9 that S- and R-wave are overlapping. Also an approximation made by drawing a straight line throughout the peaks of arrival times should be mentioned. Because of these reasons it is very hard to say to which of the two waves the measurement should be assigned. Here a recommendation of Das & Ramana (2011) was followed, which says that for all practical purposes measurements could be treated as S-wave velocity.

The water table in the test site was very high (this is normal, because it is a polder), so the soil was saturated. For the saturated soil the Poisson's ratio is expected to be close to $\nu = 0.5$.

The Poisson's ratio can be calculated by:

$$\nu = 0.5 \frac{\left(v_p/v_s\right)^2 - 2}{\left(v_p/v_s\right)^2 - 1} = \frac{\left(66.9/17.4\right)^2 - 2}{\left(66.9/17.4\right)^2 - 1} = 0.464. \quad (5-1)$$

The R-wave velocity can be calculated from the Poisson's ratio and S-wave velocity: $v_r = 16.5$ m/s. Figure 5-7 shows that the natural density of the soil is $\rho \approx 1000$ kg/m³. With this the small strain stiffness shear modulus of the soil on site can be determined:

$$G_0 = \rho v_s^2 = 1000 \cdot 10^{-3} \cdot 17.4^2 = 303 \text{ kN/m}^2. \quad (5-2)$$

And the Young's modulus:

$$E = 2G_0(1 + \nu) = 2 \cdot 303(1 + 0.464) = 886 \text{ kN/m}^2. \quad (5-3)$$

These properties are determined under the assumption that the soil can be treated as an elastic homogeneous isotropic half-space. This assumption is wrong a priori, because it is known that there is a thin clay cover on the surface and another clay layer at the depth of -6.5 m NAP. Nevertheless it will be used in order to check how good the solutions, discussed earlier, can predict vibrations on this site.

5.4 Vibration measurements

The test setup was the same as described in Chapter 5.2 and shown in Figure 5-2, except for a small change: the geophone on top of the shaker was used instead of the accelerometer. The other geophones were placed with 1 meter distances between their centres. The first geophone on the soil surface was placed with 1 meter distance from the edge of the plate.

The measured signals were transformed into the frequency domain by using the Fast Fourier Transform (FFT). In the frequency domain, the signals were filtered, by removing all the components of higher frequencies than 50 Hz. Afterwards the filtered signals were inverted back to the time domain. The measured signal, power spectrum and the inverted filtered signal of the shaker vibrations can be seen in Figure 5-10. The same data for the 1st and the last (6th) geophone can be seen in Figure 5-11 and Figure 5-12 respectively. In Appendix A vibration signals for all seven geophones can be found.

The shaker was oscillating harmonically with a frequency of 24 Hz. The measured and filtered signal shows that the amplitude of velocity vibrations is $\hat{v} = 44 \text{ mm/s}$. From this, the displacement amplitude can be calculated as follows:

$$\hat{u} = \frac{\hat{v}}{\omega} = 0.292 \text{ mm} = 292 \mu\text{m}. \quad (5-4)$$

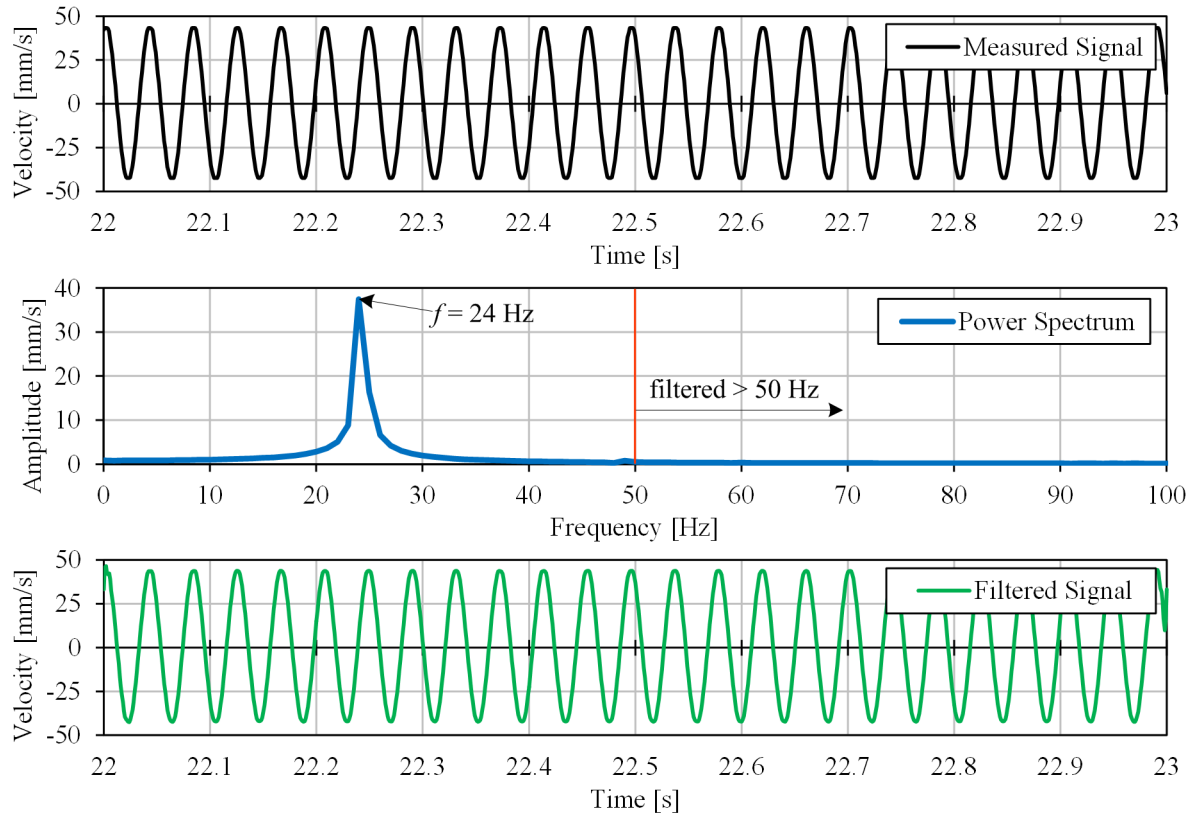


Figure 5-10. Shaker vibrations.

The measured signal of the vibrations velocity from the 1st geophone (placed 1 meter away from the edge of the plate) can be seen in Figure 5-11. The vibrations are also harmonic, and the frequency is the same as it was produced by the shaker - 24 Hz. The signal shows that the amplitude of the vibrations velocity 1 m away is about $\hat{v} = 9.3 \text{ mm/s}$. From this the displacement amplitude can be calculated: $\hat{u} = \hat{v} / \omega = 62 \mu\text{m}$.

In the same manner, Figure 5-12 shows that the measured signal of the vibrations velocity from the 6th geophone (placed 6 meter away) has the amplitude of the vibrations velocity of $\hat{v} = 0.30 \text{ mm/s}$, this gives the displacement amplitude $\hat{u} = \hat{v} / \omega = 2.0 \mu\text{m}$.

The fact, that in the 6th geophone the vibrations were still harmonic and the dominant frequency remained the same shows, that the goal to produce and to measure harmonic oscillations on site was achieved. Now the measurements can be compared with analytical and FEM calculations.

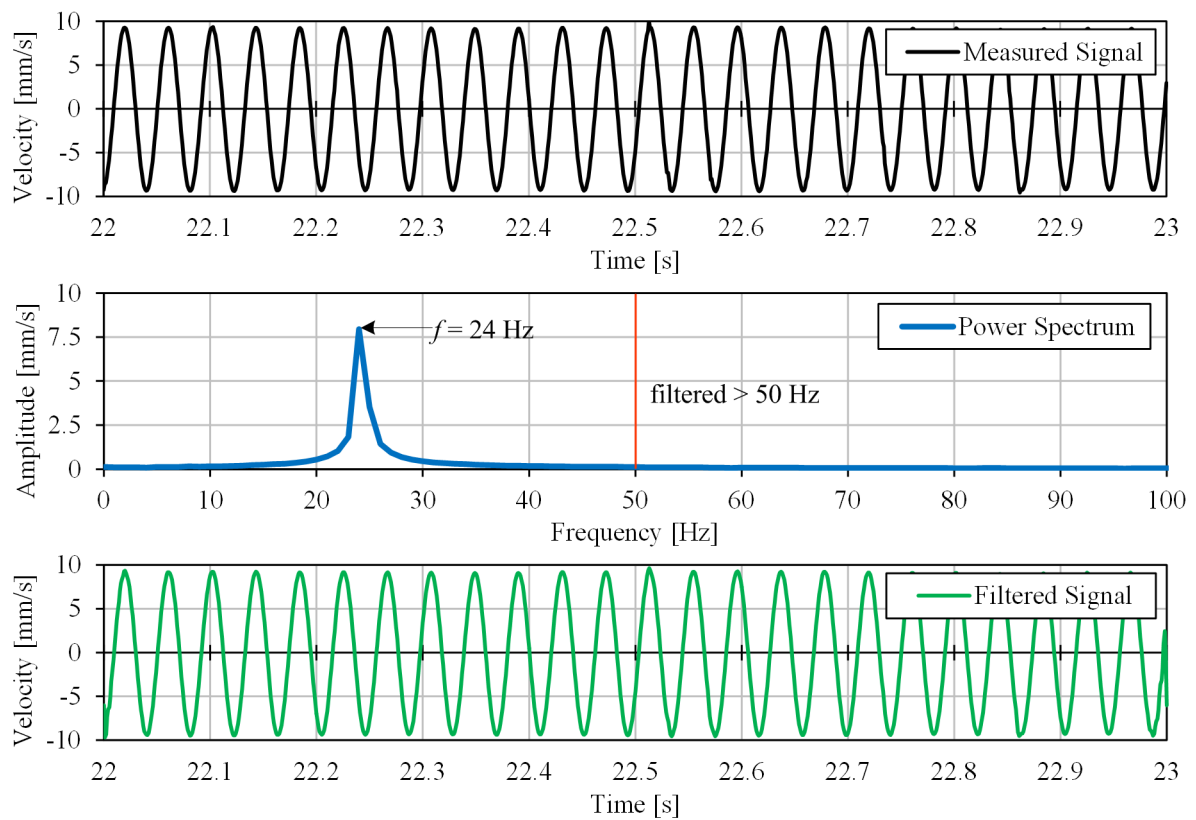


Figure 5-11. Vertical vibrations at geophone 1 m away from the shaker.

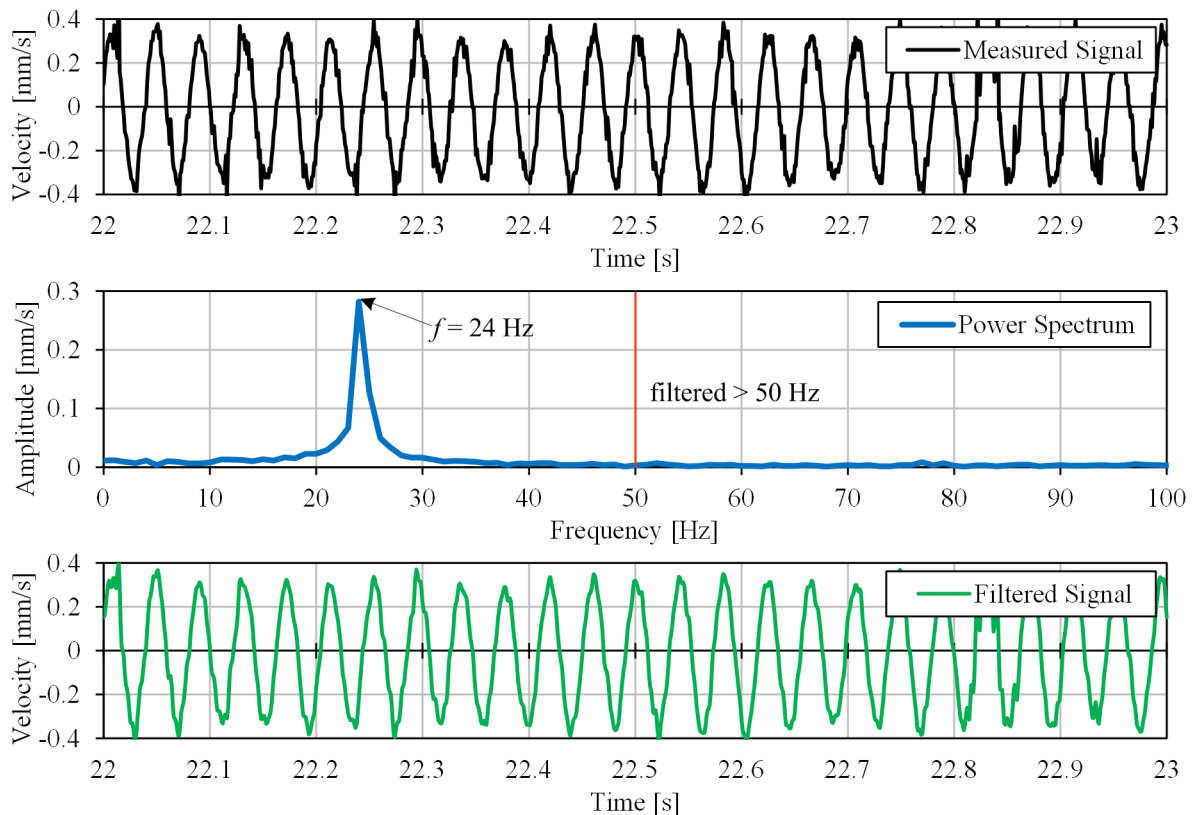


Figure 5-12. Vertical vibrations at geophone 6 m away from the shaker.

5.5 Measurements vs. Analytical and FEM calculations

The measured displacement amplitudes of the shaker and on the ground surface are compared to the analytical and FEM calculations. The homogeneous half-space assumption with the determined elastic material values from P- and S-wave velocity measurements is used for the analytical methods.

For the FEM the same model as described in Chapter 3.2 is used. Elasticity properties defined from the P- and S-wave velocity measurements are used for the calculations. The shaker is defined as a plate element with the axial stiffness $EA = 21$ GN/m, bending stiffness $EI = 17.5$ MN/m and weight $w = 21.94$ kN/m/m. The selected weight corresponds to the total vibrating mass m_{tot} . Because it is a real soil and real measurements, the material damping must be evaluated. A material damping ratio for peat $\xi = 1\%$ is selected. It is weaker than showed in Figure 2-3, where damping ratio for fine grained soils $\xi = 3\%$ was presented, and corresponds to the damping ratios for peat suggested by Coelho (2010) and Moreno & Rodriguez (2004).

The relationship between the Rayleigh damping coefficients α and β (which are used in Plaxis to determine a material damping) and the damping ratio is:

$$\alpha + \beta\omega^2 = 2\omega\xi. \quad (5-5)$$

Solving Equation (5-5) for two target frequencies and two target damping ratios yields:

$$\begin{aligned} \alpha &= 2\omega_1\omega_2 \frac{\omega_1\xi_2 - \omega_2\xi_1}{\omega_1^2 - \omega_2^2}, \\ \beta &= 2 \frac{\omega_1\xi_1 - \omega_2\xi_2}{\omega_1^2 - \omega_2^2}. \end{aligned} \quad (5-6)$$

Nevertheless in this simulation (as well as in the experiment on site) there is only one frequency $\omega = \omega_1 = \omega_2$ and one damping ratio $\xi = \xi_1 = \xi_2$, therefore Equations (5-6) can be simplified and the Rayleigh damping coefficients can be defined by:

$$\begin{aligned} \alpha &= \xi\omega, \\ \beta &= \frac{\xi}{\omega}. \end{aligned} \quad (5-7)$$

In this case, the vibration frequency $f = 24$ Hz, so the angular frequency $\omega = 150.8$ rad/s, which gives $\alpha = 1.508$ and $\beta = 6.63 \cdot 10^{-5}$.

The dimensionless mass ratio, according to Equation (2-37), is $b = m_{vib} / (\rho \cdot r_{pl}^3)$. For this shaker test $b = 287.4 / (1 \cdot 10^3 \cdot 0.2^3) = 35.9$. The modified dimensionless mass ratio, according to Equation (2-44), $B = (1 - v) / 4 \cdot b = (1 - 0.464) / 4 \cdot 35.9 = 4.81$.

Plate vibration amplitude

The analytical methods for the calculation of oscillating plate vibration amplitudes were already discussed in Chapter 2.10. Here, by using those methods, Predicted and Measured

amplitude ratios (P/M) are calculated in order to evaluate how good the predictions are made using the described methods.

For the Reissner's solution, approximate compliance functions for Poisson's ratio $\nu = 0.5$, for a rigid circular foundation and for large values of the frequency ($a_0 > 1.5$, which is also the case in this experiment), according to Kruijzer (2006) were used:

$$f_1 \approx \frac{3}{4a_0^2}, \quad (5-8)$$

$$f_2 \approx \frac{1.93}{a_0^3}. \quad (5-9)$$

Table 5-1 shows that Confined Elasticity method highly over-predicted the amplitude of vibration (this property of the method was already noticed in Chapter 3.2). However by using the other methods, the amplitude of the shaker vibration has been predicted with at least 94 % accuracy. It is also worth to mention that all methods over-predicted the vibration amplitude.

Table 5-1. Comparison between the predicted and the measured shaker vibration amplitudes.

Method	Amplitude [μm]	P/M ratio [-]
Measured	292	1
Reissner (Kruijzer's f_1, f_2)	292	1
Lysmer	309	1.06
Confined Elasticity	510	1.75
FEM	302	1.03

Surface vibration amplitudes using only Barkan's solution

Barkan's near- and far-field solutions for the surface vibration amplitudes were already discussed in Chapter 2.11. Nevertheless the solutions are derived for an elastic half-space, without material damping. In this case the material damping must be taken into account. The solutions are multiplied to the exponential law, which represents the material damping (Bornitz, 1931), described by Equation (2-19), as follows:

$$\hat{u} = \hat{u}_B \cdot e^{-k_m(r-r_0)}, \quad (5-10)$$

where:

$$\begin{aligned} \hat{u}_B &= \text{Barkan's solution for the displacement amplitude,} & [\text{m}] \\ k_m &= \text{empirical absorption coefficient,} & [\text{1/m}] \\ r - r_0 &= \text{distance between two vibrating points.} & [\text{m}] \end{aligned}$$

According to the Equation (5-10), a ratio between two amplitudes at distances r_1 and r_2 can be expressed as $\hat{u}_2 / \hat{u}_1 = \exp[-k_m(r_2 - r_1)]$, or $\hat{u}_1 / \hat{u}_2 = \exp[k_m(r_2 - r_1)]$. Now the absorption coefficient k_m can be expressed as follows:

$$k_m = \frac{1}{r_2 - r_1} \ln \frac{\hat{u}_1}{\hat{u}_2} = \frac{1}{r_2 - r_1} \delta, \quad (5-11)$$

where δ is a logarithmic damping decrement. For small damping ratios, the logarithmic damping decrement can be approximately related to the damping ratio with the following relationship:

$$\delta = 2\pi\xi. \quad (5-12)$$

It is already assumed, that the material damping ratio for peat $\xi = 1\%$. Furthermore by assuming, that most of the vibrations on the soil surface are caused by R-waves (this was shown in Chapter 4.5), the absorption coefficient k_m can be expressed from Equations (5-11) and (5-12), (taking the distance between two vibration peaks at distances r_2 and r_1 equal to the length of the R-wave λ_r) as follows:

$$k_m = \xi \frac{\lambda_r}{2\pi} = \omega\xi / v_r. \quad (5-13)$$

For the vibration frequency $f = 24$ Hz the empirical absorption coefficient $k_m = 0.09 \text{ m}^{-1}$. The P/M ratios between the predicted and the measured surface vibration amplitudes for the far-field can be seen in Table 5-2. The measured and predicted vibration amplitudes on the surface are shown in Figure 5-13.

Table 5-2. Comparison between the predicted and the measured surface vibration amplitudes.

Distance from the shaker centre axis [m]	Predicted / Measured Ratio	
	Barkan-Bornitz far-field ($\xi = 1\%$)	FEM ($\xi = 1\%$)
1.2	4.2	0.6
2.2	6.6	0.9
3.2	8.7	1
4.2	31.4	4.5
5.2	36.5	5.5
6.2	48.9	7.2

The near-field of Barkan-Bornitz method ends before the first measurement point (Figure 5-13), therefore only P/M values for the far-field are calculated. The analytical approach strongly over-predicts the vertical vibrations, whereas the FEM calculations are much better, but still under-predicts for the first 3 meters, and over-predicts further away the vibration amplitudes. For both methods the tendency is the same – P/M is for a growing distance from the shaker.

Figure 5-13 shows weaker damping than expected just next to the shaker and higher damping than expected further away from the shaker. This can be explained as there is less vibration caused by the Rayleigh waves closer to the shaker and more vibrations caused by the Rayleigh waves further away from the shaker. This implies a different damping per basic waves.

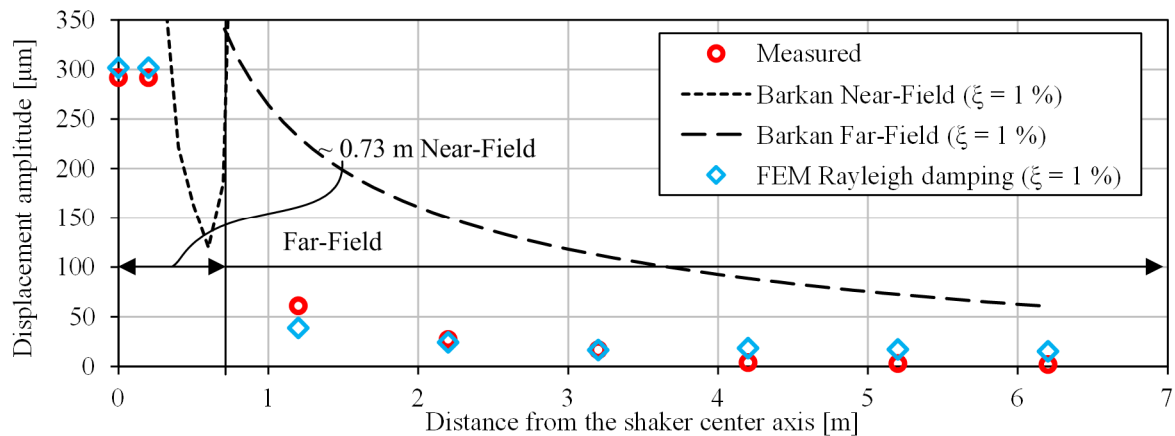


Figure 5-13. Comparison of different solutions for the surface vibration amplitude.

5.6 Conclusions

The shaker vibration amplitudes can be predicted rather accurately with two of the three (except Confined elasticity) analytical approaches: Reissner's or Lysmer's approach and with numerical (FEM) calculations. The accuracy depends on the method used for the prediction, and ranges from 94 % to 100 % (having in mind the Predicted/Measured ratios of 1.00 to 1.06). This means that the amplitude of the shaker can be predicted accurately enough for geotechnical purposes.

The soil surface vibration amplitudes can be predicted with Barkan-Bornitz's analytical approach and with numerical (FEM) calculations. The Barkan-Bornitz approach over-predicted the amplitudes between 4.2 and 48.9 times. The FEM under-predicted the amplitudes for the first three meters and over-predicted up to 7.2 times for the last three meters. This means that the amplitudes of the surface cannot be predicted accurately. The tendency of increasing P/M ratios suggest that material damping ratio of the peat at the test site is higher than 1 %.

The weaker damping than expected just next to the shaker and higher damping than expected further away from the shaker can be explained by thinking, that there is less vibration caused by the Rayleigh waves closer to the shaker and more vibrations caused by the Rayleigh waves further away from the shaker. This implies a different material damping per basic waves.

This confirms the conclusion made by Hölscher and Waarts (2003), that the reliability of man-made vibration prediction methods is disappointingly low.

6 DEVELOPED VIBRATION PREDICTION METHOD

6.1 Introduction

The previous chapter showed that in order to make a good prediction of the soil surface vibration, it is necessary to perform calculations with FEM. The disadvantages of the FEM are that it requires a special software package and long time for modelling and calculations. Therefore it would be very useful to derive a simple model for engineering purposes, which could be used to predict geotechnical vibrations close to the source without a need of a special software and long calculations.

Such a method is suggested in this chapter. The method is derived by having results from the shaker test. The predictions of the developed method are compared with the measurements and calculations of FEM.

6.2 Derivation of the method

By analysing Figure 5-13, it can be seen that the near-field zone in the shaker experiment is rather short, only 0.73 m. This is very close to the length of R-waves, which can be calculated as follows: $\lambda_r = v_r / f = 16.5 / 24 = 0.688$ m.

Also from Figure 5-13 it can be seen, that the attenuation rate of the measured amplitudes is much higher just in the first meter. From this, it can be concluded that in the near-field zone amplitudes attenuate much stronger, and in the far-field zone the attenuation is not so strong anymore.

At this point, the findings from Chapter 4.6 can also be recalled, where in Figure 4-13 was shown, that a big part of the dynamic displacement of the rigid plate could be explained by the elasto-static Boussinesq solution for a rigid plate.

In the experiment on site, the amplitude of the vertically oscillating force can be calculated if the eccentric moment M_e and the frequency f are known: $F_0 = M_e \cdot (2\pi \cdot f)^2 = 0.0832 \cdot (2\pi \cdot 24)^2 = 1.89$ kN. If it would be a static load on a rigid plate, according to the elasto-static solution of Boussinesq, the vertical displacement could be calculated as follows:

$$u_{v,plate} = \frac{1}{2} (1 - \nu^2) \frac{F_0}{r_{pl} \cdot E}. \quad (6-1)$$

Having Poisson's ratio $\nu = 0.464$, the vertical force $F_0 = 1.89$ kN, the radius of the plate $r_{pl} = 0.2$ m and the modulus of elasticity $E = 886$ kPa, the vertical static displacement of the rigid plate would be $u_{v,plate} = 4185$ μm . This is 14.3 times higher, than the dynamic vibration amplitude of the plate, measured during the shaker test (292 μm).

The factor 14.3 here comes from the soil-foundation interaction, which is similar to the behaviour of a mass-spring-dashpot system. The spring plays a static role and the wave propagation determines a dashpot (analogy of conductivity).

At this point it is assumed that the attenuation of the vertical dynamic displacement amplitudes near the oscillating plate (in the near-field) has the same attenuation as a half-space surface deformed by a vertically loaded rigid plate under static conditions.

For the static case, soil surface displacements near the rigid plate can be calculated using a solution from the theory of elasticity:

$$u_v(r) = u_{v,plate} \frac{2}{\pi} \arcsin \left(\frac{r_{pl}}{r} \right). \quad (6-2)$$

For the dynamic case, the dynamic vertical amplitude of an oscillating rigid plate should be used instead of the vertical static displacement. The dynamic amplitude of the plate can be calculated by Lysmer's method, as discussed in Chapter 2.10. By using this vertical displacement amplitudes in the near-field are found as follows:

$$\hat{u}_{v,nf}(r) = \hat{u}_{v,plate} \frac{2}{\pi} \arcsin \left(\frac{r_{pl}}{r} \right). \quad (6-3)$$

In the far-field, mostly the R-wave dominates. Therefore the attenuation law of the amplitudes is known to be proportional to $r^{-0.5}$. Taking the material damping, according to the law, suggested by Bornitz (1931), into account, the far-field amplitudes will be:

$$\hat{u}_{v,ff}(r) = \hat{u}_{v,nf}(r_{ff}) \cdot \sqrt{\frac{r_{ff}}{r}} e^{-k_m(r-r_{ff})}, \quad (6-4)$$

where

$$\begin{aligned} r_{ff} &= \text{start of the far-field} (\approx \lambda_r), & [\text{m}] \\ \hat{u}_{v,nf}(r_{ff}) &= \text{vertical amplitude from the near-field estimation.} & [\text{m}] \end{aligned}$$

If Lysmer's solution is used for the dynamic plate displacement amplitude, Boussinesq's elasto-static solution is used for the amplitudes in the near-field and the R-wave attenuation law together with the material damping law, suggested by Bornitz (1931), is used for the far-field, the vertical vibration amplitudes can be calculated as follows:

$$\hat{u}_v(r) = \begin{cases} \frac{F_0 / k}{\sqrt{(1 - B_z a_0^2)^2 + (0.85 a_0^2)}} & , \quad \text{for } r \leq r_{pl} \text{ (Plate)}, \\ \hat{u}_v(r_{pl}) \frac{2}{\pi} \arcsin \left(\frac{r_{pl}}{r} \right) & , \quad \text{for } r_{pl} < r \leq r_{ff} \text{ (Near - Field)}, \\ \hat{u}_v(r_{ff}) \sqrt{\frac{r_{ff}}{r}} e^{-k_m(r-r_{ff})} & , \quad \text{for } r > r_{ff} \text{ (Far - Field)}. \end{cases} \quad (6-5)$$

6.3 Post-diction of the shaker test vibrations

This approach was used for the post-diction of the measured amplitudes on site. The same value of the absorption coefficient $k_m = 0.09 \text{ m}^{-1}$ for the far-field was used as in Chapter 5.5. This corresponds to the material damping ratio for peat $\xi = 1 \%$, see Equation (5-13). The comparison between the post-diction and the measured vertical vibration amplitudes can be seen in Figure 6-1.

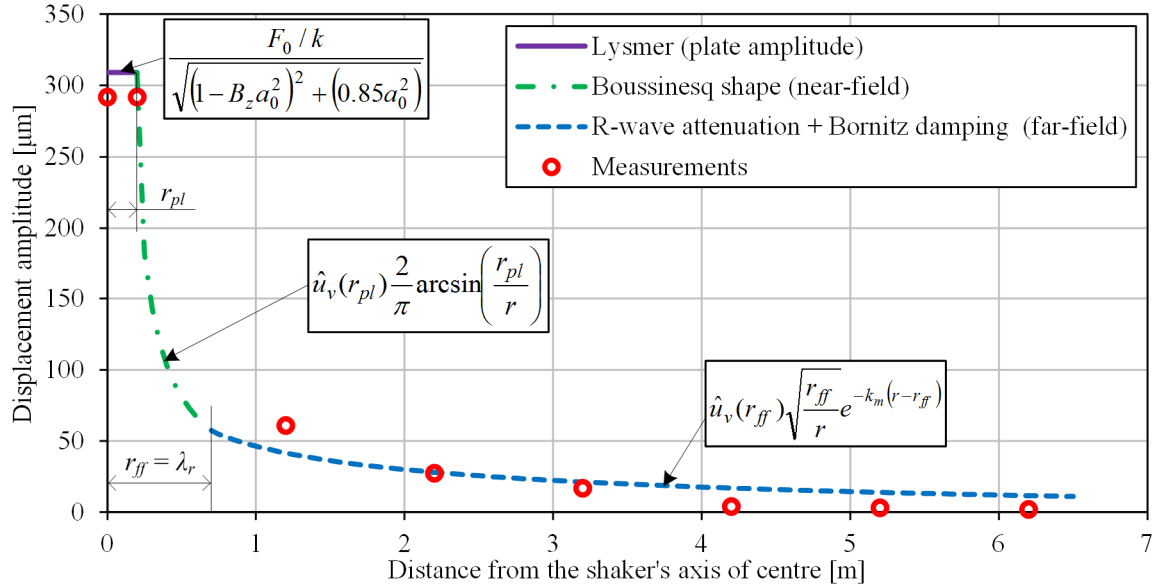


Figure 6-1. Comparison between post-dicted and the measured vibration amplitudes.

Predicted and measured (P/M) ratios are compared with the Barkan-Bornitz far-field solution and FEM calculations in below. It can be seen that with this simple method the amplitudes of vibration for the shaker test can be calculated as good as with the FE-analysis.

Table 6-1. Comparison between the predicted and the measured surface vibration amplitudes.

Distance from the shaker centre axis [m]	Predicted / Measured Ratio		
	Barkan-Bornitz far-field ($\xi = 1 \%$)	FEM ($\xi = 1 \%$)	Developed Method ($\xi = 1 \%$)
1.2	4.2	0.6	0.7
2.2	6.6	0.9	1.0
3.2	8.7	1	1.3
4.2	31.4	4.5	4.2
5.2	36.5	5.5	4.5
6.2	48.9	7.2	5.5

6.4 Comparison with FEM calculations

Because this method gives very close results to the measurements, it is decided to investigate it further by comparing the vibration amplitudes calculated by using FEM and with this developed method, for different frequencies f and different modified mass ratios B .

The amplitudes of the rigid plate, calculated by using FEM, were already compared to the analytical solutions in Chapter 3.2. The results of the surface vibration from the same FE models will be used here to validate the improved prediction method. It should be noted that in the FE models, differently than in the post-diction, there was no material damping used, therefore in the improved prediction method the Bornitz exponential part will not be used.

Another difference is the size of the near-field. In the post-diction the distance r_{ff} , where the near-field ends and the far-field begins, was assumed to be equal to the length of R-waves: $r_{ff} = \lambda_r$. However analysing the FE modelling results it was noticed that results have better match by using half the distance $r_{ff} = 0.5 \cdot \lambda_r$.

The calculations were performed with four different modified mass ratios $B = 0.5, 1.0, 2.0$ and 5.0 and ten different frequencies. This gives 40 plots of displacement amplitudes at different distances. The vibrations were calculated on nine different surface points (from 1 m to 9 m away from the centre of the plate).

Full matrix of the numerical calculations can be seen in Table 6-2.

Table 6-2. Matrix of the numerical calculations with corresponding figure numbers of Appendix A, where the plots can be found.

$B \backslash a_0$	0.179	0.269	0.359	0.449	0.538	0.628	0.718	0.897	1.077	1.346
0.5	D-1	D-2	D-3	D-4	D-5	D-6	D-7	D-8	D-9	D-10
1	D-11	D-12	D-13	D-14	D-15	D-16	D-17	D-18	D-19	D-20
2	D-21	D-22	D-23	D-24	D-25	D-26	D-27	D-28	D-29	D-30
5	D-31	D-32	D-33	D-34	D-35	D-36	D-37	D-38	D-39	D-40

P/M ratio can be expressed as error in percentages as follows:

$$\Delta_{Error} = |P/M - 1| \cdot 100\%. \quad (6-6)$$

Average and maximum errors were calculated for all forty FEM calculations (as an average for 9 surface points) and presented in Table 6-3 and Table 6-4 respectively.

Table 6-3. Matrix of the average errors in percentages.

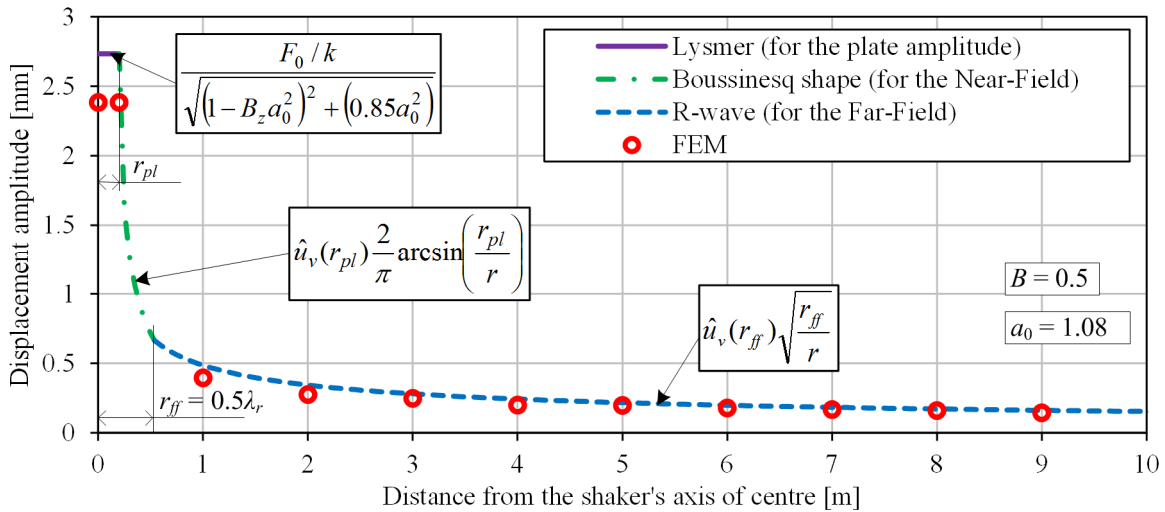
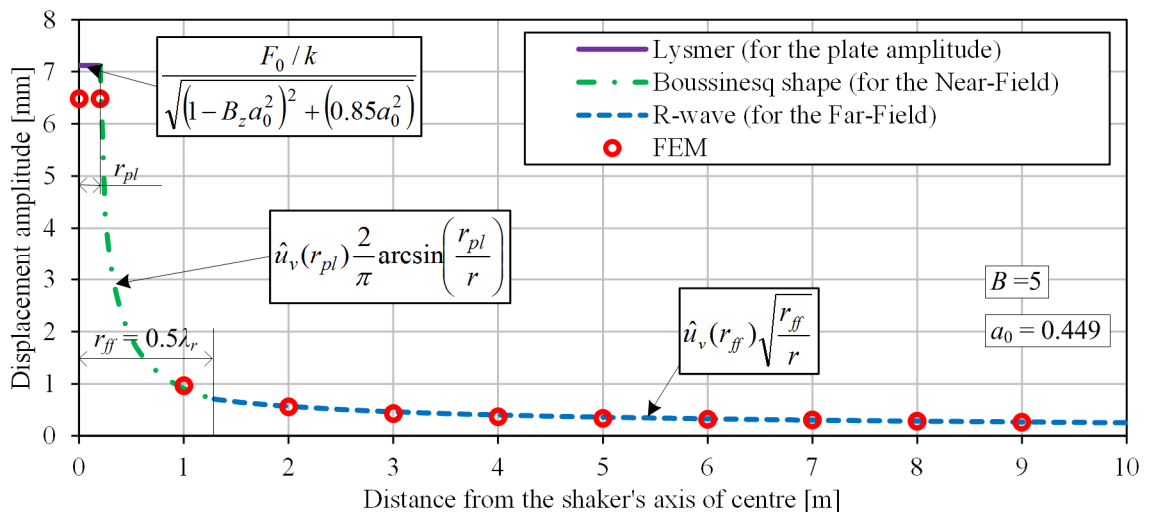
$B \backslash a_0$	0.179	0.269	0.359	0.449	0.538	0.628	0.718	0.897	1.077	1.346
0.5	4.9	5	4.3	5.6	4.7	5.5	5.9	8.3	14.3	8
1	4.7	5.8	5	6.7	5.2	6.1	6.2	7.5	9.5	4.7
2	4.8	5.5	6.2	8.3	6.1	5.3	3.7	5.6	6.6	6
5	5	6.7	10.9	4.9	13.7	9.8	9.2	5.3	4.7	5.5

The biggest average error for 9 calculation points on the surface is 24.1 %, where dimensionless frequency $a_0 = 1.077$ and modified mass ratio $B = 0.5$.

In Figure 6-2 and Figure 6-3, plots for mass ratios $B = 0.5, B = 5$ and dimensionless frequency ratios $a_0 = 1.08, a_0 = 0.449$ can be seen. All 40 plots can be found in Appendix A.

Table 6-4. Matrix of the maximum errors in percentages.

$B \backslash a_0$	0.179	0.269	0.359	0.449	0.538	0.628	0.718	0.897	1.077	1.346
0.5	10.6	10	9.7	12.8	9.6	11	13	19.9	24.1	22.3
1	10	10.5	10.9	13.6	10.8	14.4	14.6	18.7	20.3	11.9
2	11.5	9.6	13.9	15.3	11.9	10.8	7.7	12.6	24.1	12.7
5	10.7	13.3	19.1	9.8	22	19.1	15.9	13.2	14.4	14.4

Figure 6-2. Comparison between vibration amplitudes calculated by using FEM and by improved prediction method for $B = 0.5$ $a_0 = 1.08$.Figure 6-3. Comparison between vibration amplitudes calculated by FEM and by improved prediction method for $B = 5$ $a_0 = 0.449$.

6.5 Conclusions

For engineering purposes, an improved analytical method is developed to estimate the vibration amplitudes next to a harmonically oscillating rigid circular plate on an elastic half-space.

This solution consists of three parts: 1) the analytical Lysmer method for the plate displacement amplitude 2) the shape of the vertical surface displacements of the elasto-static Boussinesq solution in the near-field and 3) the R-wave attenuation law $r^{-0.5}$ with the exponential material damping law ($\exp[-k_m(r-r_{ff})]$) in the far-field. It can be assumed, that the near-field ends at a distance, which is equal to about a half to one length of the R-wave.

It was found, that this approach gives good predictions, when it is compared to the field measurements and FEM calculations.

However, the problem of the weaker damping than expected just next to the shaker and higher damping than expected further away from the shaker did not disappear, because this method cannot reflect a different material damping per basic waves.

7 FRICTIONAL DAMPING MODEL

7.1 Introduction

The measurements from the shaker tests indicated different damping just next to the plate and further away from the plate. The hypothesis was made, that this can be due to different damping per basic waves. In order to reflect this phenomenon, the frictional damping method, first suggested by Van Baars (2011), was decided to use. For that, the suggested 1D method had to be extended to 3D and incorporated into FEM calculation scheme.

7.2 1D state

The original frictional damping model was briefly described in Chapter 2.3. However more detailed explanations will be presented hereafter.

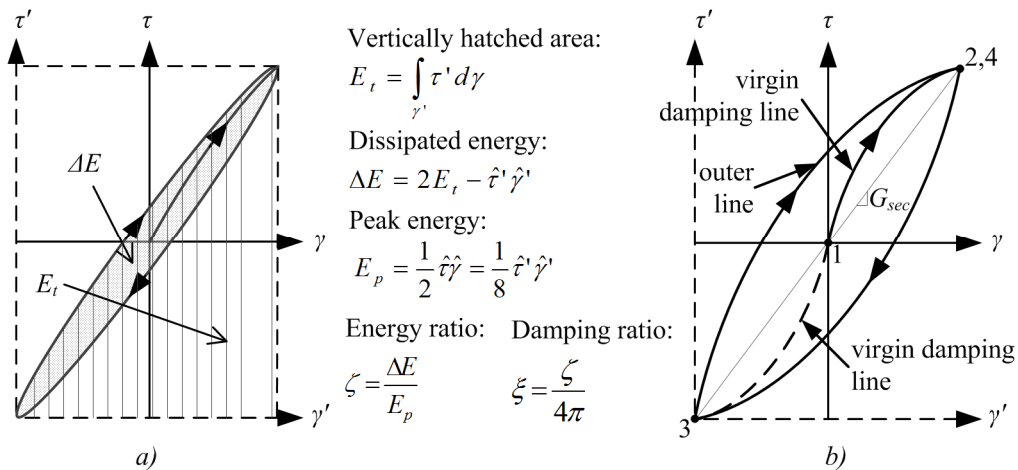


Figure 7-1. 1D frictional damping law.

The frictional damping law, in a $\tau' - \gamma'$ coordinate system, is defined as follows:

$$\tau' = G_{mod}(\gamma')^X, \quad (7-1)$$

where τ' is the shear stress, since the start, or the last change of direction, G_{mod} is the modified shear modulus, γ' is the shear strain amplitude since the start, or the last change of direction and X is the dimensionless damping parameter. The latter is related to the damping ratio ζ or to the energy ratio ζ , which can be measured directly by using various types of laboratory tests (cyclic simple shear test, cyclic torsional simple shear test, cyclic triaxial test or resonant column test):

$$X = \frac{8 - \zeta}{8 + \zeta} = \frac{2 - \pi\xi}{2 + \pi\xi}. \quad (7-2)$$

For the damping ratio $\zeta = 0$, the dimensionless damping parameter $X = 1$, so the shear stress can be calculated as $\tau' = G_{mod}\gamma'$. And in this case $G_{mod} = G_{sec}$. However if $\zeta > 0$, then the

modified shear modulus G_{mod} depends on the shear strain amplitude (see b) in Figure 7-1), so $G_{mod} \neq G_{sec}$. As it is showed in Chapter 2.3, the modified shear modulus G_{mod} can be related to G_{sec} as follows:

$$\frac{G_{mod}}{G_{sec}} = \frac{2\hat{\gamma}}{(2\hat{\gamma})^x}. \quad (7-3)$$

The relationship between G_{mod} and G_{sec} for different damping ratios and different shear strain ranges can be seen in Figure 7-2.

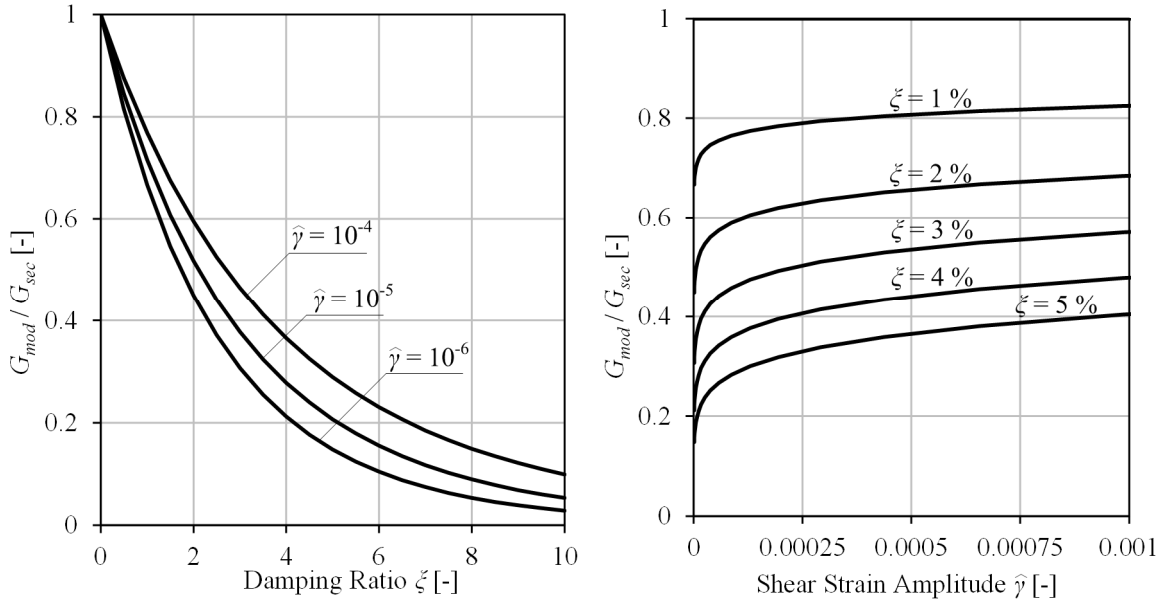


Figure 7-2. The relationship between the modified and maximum shear moduli.

In order to form a constitutive model, the stresses and strains have to be defined in the $\tau - \gamma$ coordinate system, rather than in the $\tau' - \gamma'$. From Figure 7-1, it can be seen, that for multiple constant cycles, $\hat{\gamma}' = 2\hat{\gamma}$ and $\hat{\tau}' = 2\hat{\tau}$. Therefore, the virgin damping line in the $\tau - \gamma$ coordinate system, can be expressed as follows:

$$\tau_{vir} = \frac{G_{mod} (2\hat{\gamma})^x}{2}, \quad (7-4)$$

where:

τ_{vir}	=	virgin shear stress of the soil,	$[\text{N}/\text{m}^2]$
G_{mod}	=	modified shear modulus of the soil,	$[\text{N}/\text{m}^2]$
γ	=	shear strain of the soil,	$[-]$
X	=	dimensionless damping parameter.	$[-]$

Here it should be noted, that for the virgin line $\hat{\gamma} = \gamma$.

In order to calculate the outer line (see b) in Figure 7-1) in the $\tau - \gamma$ coordinate system, the

direction of the shear-strain path must be known as well as the peaks of the last direction change. Then the shear stresses of the outer line are calculated as follows:

$$\tau_{out,up} = \tau_{min} + G_{mod} |\gamma - \gamma_{min}|^x, \quad (7-5)$$

$$\tau_{out,down} = \tau_{max} - G_{mod} |\gamma - \gamma_{max}|^x, \quad (7-6)$$

where:

$\tau_{out,up}$	=	shear stresses of the rising outer line,	$[\text{N/m}^2]$
$\tau_{out,down}$	=	shear stresses of the descending outer line,	$[\text{N/m}^2]$
τ_{min}, τ_{max}	=	stored minimum and maximum shear stresses,	$[\text{N/m}^2]$
$\gamma_{min}, \gamma_{max}$	=	stored minimum and maximum shear strains.	[-]

The outer lines draw an ellipse shaped figure in $\tau - \gamma$ coordinates, which represents the dissipated energy per volume, per cycle. By using this law, the dissipated shear strain energy ratio ζ and the damping ratio ξ are independent from the shear strain amplitude.

7.3 3D state

Before being able to extend this 1D frictional damping model to a 3D model, it should be rewritten. In 1D there is only a pure shear stress and strain. In general, shear strains change only the shape, but not the volume.

The linear stress-strain relationship, or Hook's law, for 3D however, is expressed by the modulus of elasticity E and the Poisson's ratio ν , as follows:

$$\begin{Bmatrix} \sigma_{xx} \\ \sigma_{yy} \\ \sigma_{zz} \\ \sigma_{xy} \\ \sigma_{yz} \\ \sigma_{zx} \end{Bmatrix} = \frac{E}{(1+\nu)(1-2\nu)} \begin{bmatrix} 1-\nu & \nu & \nu & 0 & 0 & 0 \\ \nu & 1-\nu & \nu & 0 & 0 & 0 \\ \nu & \nu & 1-\nu & 0 & 0 & 0 \\ 0 & 0 & 0 & \frac{(1-2\nu)}{2} & 0 & 0 \\ 0 & 0 & 0 & 0 & \frac{(1-2\nu)}{2} & 0 \\ 0 & 0 & 0 & 0 & 0 & \frac{(1-2\nu)}{2} \end{bmatrix} \begin{Bmatrix} \varepsilon_{xx} \\ \varepsilon_{yy} \\ \varepsilon_{zz} \\ \gamma_{xy} \\ \gamma_{yz} \\ \gamma_{zx} \end{Bmatrix}. \quad (7-7)$$

Where σ_{ii} and ε_{ii} are normal stresses and strains respectively, σ_{ij} and γ_{ij} are shear stresses and strains respectively, in which $i,j = x,y$ or z and $i \neq j$. The sign convention for stresses and strains, according to Plaxis Material Models Manual (Plaxis bv, 2015), is presented in Figure 7-3.

This can be written in a matrix form:

$$\{\sigma\} = [D]\{\varepsilon\}, \quad (7-8)$$

where:

$$\{\sigma\} = \text{stress vector,} \quad [\text{N/m}^2]$$

$$[D] = \text{elasticity matrix, } \quad [N/m^2]$$

$$\{\varepsilon\} = \text{strain vector. } \quad [-]$$

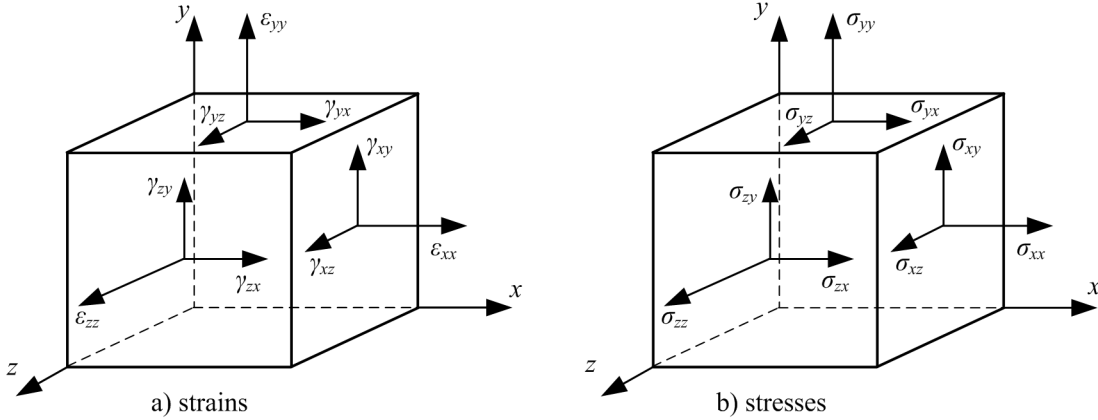


Figure 7-3. The sign convention for the three dimensional stresses and strains.

In a 3D case, there are three pure shear strains and three corresponding pure shear stresses. However they are not the only ones, responsible for the change of the shape. This can be illustrated by decomposing Hook's law into two parts: the deviatoric part, controlled by the shear modulus G , and the volumetric part, controlled by the bulk modulus K :

$$\begin{bmatrix} \sigma_{xx} \\ \sigma_{yy} \\ \sigma_{zz} \\ \sigma_{xy} \\ \sigma_{yz} \\ \sigma_{zx} \end{bmatrix} = G \begin{bmatrix} \frac{4}{3} & -\frac{2}{3} & -\frac{2}{3} & 0 & 0 & 0 \\ -\frac{2}{3} & \frac{4}{3} & -\frac{2}{3} & 0 & 0 & 0 \\ -\frac{2}{3} & -\frac{2}{3} & \frac{4}{3} & 0 & 0 & 0 \\ 0 & 0 & 0 & 1 & 0 & 0 \\ 0 & 0 & 0 & 0 & 1 & 0 \\ 0 & 0 & 0 & 0 & 0 & 1 \end{bmatrix} \begin{bmatrix} \varepsilon_{xx} \\ \varepsilon_{yy} \\ \varepsilon_{zz} \\ \gamma_{xy} \\ \gamma_{yz} \\ \gamma_{zx} \end{bmatrix} + K \begin{bmatrix} 1 & 1 & 1 & 0 & 0 & 0 \\ 1 & 1 & 1 & 0 & 0 & 0 \\ 1 & 1 & 1 & 0 & 0 & 0 \\ 0 & 0 & 0 & 0 & 0 & 0 \\ 0 & 0 & 0 & 0 & 0 & 0 \\ 0 & 0 & 0 & 0 & 0 & 0 \end{bmatrix} \begin{bmatrix} \varepsilon_{xx} \\ \varepsilon_{yy} \\ \varepsilon_{zz} \\ \gamma_{xy} \\ \gamma_{yz} \\ \gamma_{zx} \end{bmatrix}. \quad (7-9)$$

This can be written in a matrix form:

$$\{\sigma\} = [D_G]\{\varepsilon\} + [D_K]\{\varepsilon\}, \quad (7-10)$$

where:

$$[D_G] = \text{elasticity matrix of the shape change, } \quad [N/m^2]$$

$$[D_K] = \text{elasticity matrix of the volume change. } \quad [N/m^2]$$

From the equations above it can be seen, that for the change of the volume, which is controlled by K , the three normal stresses or strains are responsible. However, for the change of the shape, which is controlled by G , all six strains or stresses are responsible.

The deviatoric strains, which are responsible for the change of the shape, may be expressed as follows:

$$\begin{aligned} e_{ii} &= \varepsilon_{ii} - \frac{1}{3} \varepsilon_{vol}, \\ e_{ij} &= \gamma_{ij}, \end{aligned} \quad (7-11)$$

in which $\varepsilon_{vol} = \varepsilon_{xx} + \varepsilon_{yy} + \varepsilon_{zz}$ is the volumetric strain, $i, j = x, y$ or z and $i \neq j$.

The corresponding deviatoric stresses may be calculated by:

$$\begin{aligned} \tau_{ii} &= \sigma_{ii} - \sigma_0, \\ \tau_{ij} &= \sigma_{ij}, \end{aligned} \quad (7-12)$$

where $\sigma_0 = \frac{1}{3}(\sigma_{xx} + \sigma_{yy} + \sigma_{zz})$ is the isotropic stress, $i, j = x, y$ or z and $i \neq j$.

The frictional damping law for a 3D case can be applied by using Equation (7-1) in $\tau' - e'$ coordinates:

$$\begin{aligned} \tau'_{ii} &= G_{mod} (e'_{ii})^x, \\ \tau'_{ij} &= G_{mod} (e'_{ij})^x, \end{aligned} \quad (7-13)$$

where

$$\begin{aligned} \tau'_{ii} &= \text{normal deviatoric stress in } \tau' - e' \text{ coordinates,} & [\text{N/m}^2] \\ \tau'_{ij} &= \text{tangential deviatoric stress in } \tau' - e' \text{ coordinates.} & [\text{N/m}^2] \\ e'_{ii} &= \text{normal deviatoric strain in } \tau' - e' \text{ coordinates,} & [-] \\ e'_{ij} &= \text{tangential deviatoric strain in } \tau' - e' \text{ coordinates.} & [-] \end{aligned}$$

With this, the Cartesian stresses can be calculated:

$$\begin{aligned} \sigma_{ii} &= 2\tau_{ii} + K\varepsilon_{vol}, \\ \sigma_{ij} &= \tau_{ij}. \end{aligned} \quad (7-14)$$

7.4 Damped energy in a 3D state

The damped energy in a three dimensional case cannot be so easily demonstrated graphically as it was done for the one dimensional case in Figure 7-1.

The full potential strain energy per volume can be mathematically expressed as follows:

$$E_p = 0.5(\sigma_{xx}\varepsilon_{xx} + \sigma_{yy}\varepsilon_{yy} + \sigma_{zz}\varepsilon_{zz} + \sigma_{xy}\gamma_{xy} + \sigma_{yz}\gamma_{yz} + \sigma_{zx}\gamma_{zx}). \quad (7-15)$$

The full potential strain energy per volume is the sum of the potential strain energy which changed the volume E_{pV} (related to K) and the potential strain energy which changed the shape E_{pS} (related to G).

Therefore Equation (7-15) may be rewritten:

$$E_p = E_{pV} + E_{pS} . \quad (7-16)$$

The potential strain energy per volume, responsible for the change of the volume, is expressed as:

$$E_{pV} = 0.5 \varepsilon_{vol} \sigma_0 . \quad (7-17)$$

The potential strain energy per volume, responsible for the change of the shape:

$$E_{pS} = 0.5 (\tau_{xx} e_{xx} + \tau_{yy} e_{yy} + \tau_{zz} e_{zz} + \tau_{xy} e_{xy} + \tau_{yz} e_{yz} + \tau_{zx} e_{zx}) . \quad (7-18)$$

The potential strain energy, responsible for the change of the volume, may be called the volumetric potential strain energy. In the same way, the potential strain energy, responsible for the change of the shape, may be called the deviatoric potential strain energy.

Due to the frictional damping, a part of the deviatoric potential strain energy is dissipated. The ratio of the dissipated deviatoric strain energy to the deviatoric potential strain energy can be called the dissipated deviatoric strain energy ratio $\zeta = \Delta E_S / E_{pS}$. With this the frictional damping ratio ξ can be expressed as:

$$\xi = \frac{1}{4\pi} \zeta = \frac{1}{4\pi} \frac{\Delta E_S}{E_{pS}} . \quad (7-19)$$

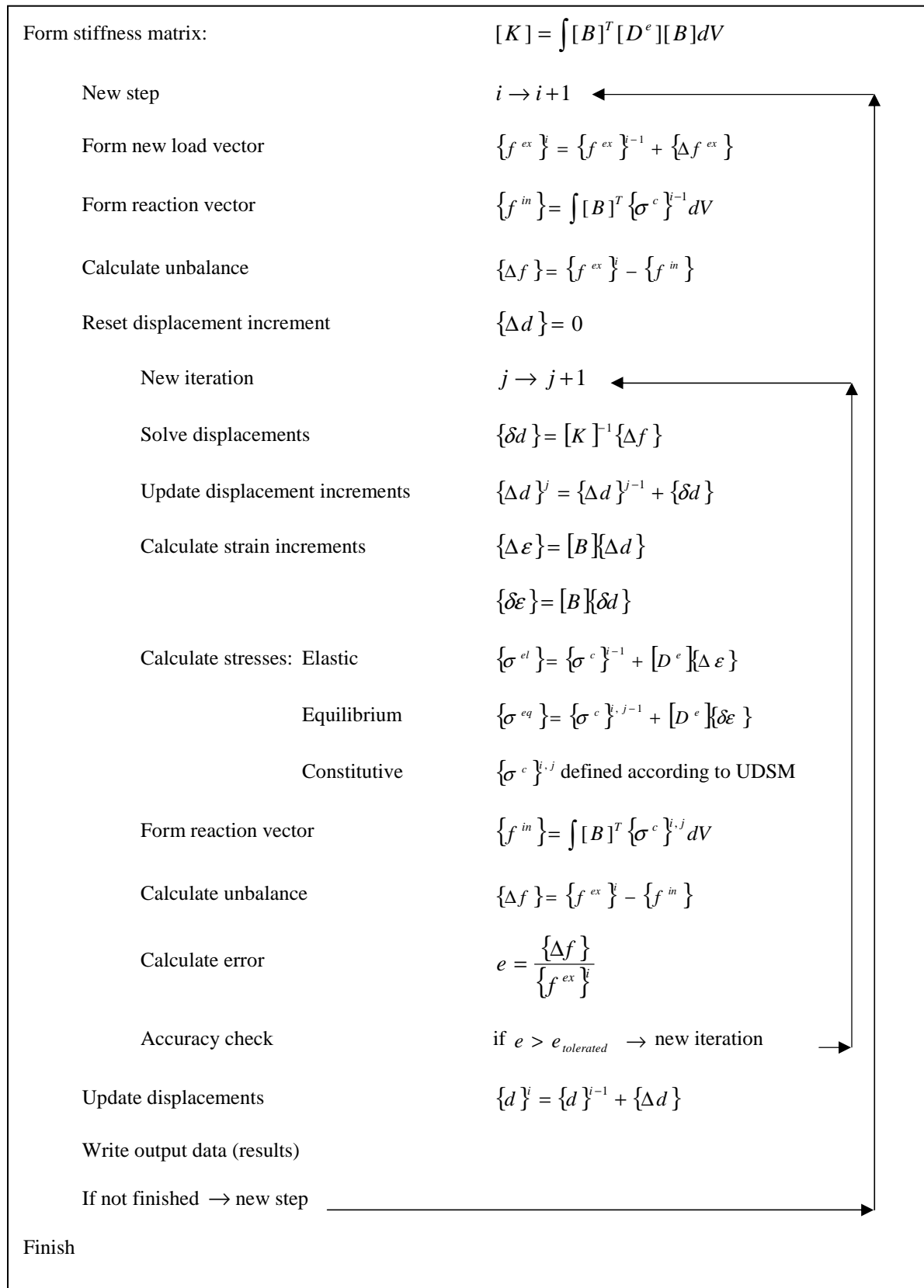
Here it should be noted, that in the frictional damping model, the frictional damping ratio is not related to the full potential strain energy but only to its deviatoric part.

7.5 User defined soil material model

This frictional damping law is implemented into the FEM software of Plaxis 2D, as a user defined soil model (UDSM).

During the first iteration of a loading step, Plaxis provides strains which are calculated assuming linear elasticity. Then, using these provided strains, the stresses are determined according to the user provided constitutive model. The external forces are known and the internal are calculated from the constitutive stresses. As a next step, the unbalance between these internal and external forces is checked. If the error is bigger than tolerated, a new (Newton-Raphson) iteration process is started. The (Newton-Raphson) iteration processes is repeated for a loading step, until the tolerance of the unbalance error is reached (usually 0.01). This calculation process is schematically showed in Table 7-1.

Table 7-1. FEM calculation process in Plaxis (Plaxis bv, 2015).



The UDSM consists of the following steps:

- 1) calculation of the deviatoric strains according (Table 7-2);
- 2) checking the stress-strain path direction (Table 7-3);
- 3) checking the stress-strain amplitudes (Table 7-4);
- 4) calculation of the deviatoric stresses (Table 7-5);
- 5) calculation of the Cartesian stresses (Table 7-6).

Step 4 separates two parts of deformation: the bulk part and the deviatoric part. Because of this, the model becomes independent from axes of coordinates.

In the first step, the deviatoric strains are calculated from the linear step. In this step also the volumetric deformation is defined.

Table 7-2. Step 1: deviatoric strains.

$\{\varepsilon\}^i = \{\varepsilon\}^{i-1} + \{\Delta\varepsilon\}$	//Cartesian strains for the i^{th} step
$\varepsilon_{vol} = \varepsilon_1^i + \varepsilon_2^i + \varepsilon_3^i$	//Volumetric strain
for $k = 1$ to 3 do	
$e_k^i = \varepsilon_k^i - \frac{1}{3}\varepsilon_{vol}$	//Deviatoric strains for normal part
$e_{k+3}^i = \varepsilon_{k+3}^i$	//Deviatoric strains for the shear part

In the second step, the stress-strain paths directions are indicated. It is checked whether a stress-strain path goes up or down.

Table 7-3. Step 2: stress-strain path direction.

for $k = 1$ to 6 do	
if $e_k^i > e_k^{i-1}$	//The stress-strain goes up
then $dir_k^i \rightarrow 1$	
else if $e_k^i < e_k^{i-1}$	//The stress-strain goes down
then $dir_k^i \rightarrow -1$	
else $dir_k^i \rightarrow 0$	//The stress-strain point does not move

When the stress-strain path direction is indicated, it has to be checked whether the direction has changed from the previous step or not.

If the direction has changed, the starting points for the calculation of the deviatoric stresses (amplitudes of the stress and strain) have to be changed to the previous stress-strain points. This is performed in the 3rd step. Once the starting points are defined, the deviatoric stresses can be calculated in the 4th step by using the frictional damping law. The stress-strain paths can follow either a virgin loading line, or a load history line.

Table 7-4. Step 3: the amplitudes of the stresses and strains.

```

for k = 1 to 6
  if  $dir_k^i = 0$  then
     $dir_k^i = dir_k^{i-1}$                                 //Removing the stopovers
  else if  $dir_k^i < dir_k^{i-1}$  then
     $\tau_k^{max,i} = \tau_k^{i-1}$                       //Maximum deviatoric stress was the previous
     $\tau_k^{min,i} = -\tau_k^{max,i}$                   //Minimum deviatoric stress
     $e_k^{max,i} = e_k^{i-1}$                         //Maximum deviatoric strain was the previous
     $e_k^{min,i} = -e_k^{max,i}$                       //Minimum deviatoric strain

  else if  $dir_k^i > dir_k^{max,i-1}$  then
     $\tau_k^{min,i} = \tau_k^{i-1}$                       //Minimum deviatoric stress was the previous
     $\tau_k^{max,i} = -\tau_k^{min,i}$                   //Maximum deviatoric stress
     $e_k^{min,i} = e_k^{i-1}$                         //Minimum deviatoric strain was the previous
     $e_k^{max,i} = -e_k^{min,i}$                       //Maximum deviatoric stress

```

Table 7-5. Step 4: calculation of the deviatoric stresses.

```

for k = 1 to 6 do
  if  $dir_k^i = 1$  and  $e_k^i > e_k^{max,i}$  then          //Going up on the virgin loading line
    if  $e_k^i \geq 0$  then                                //Going up in the positive side
       $\tau_k^i = \frac{G_{mod} (2e_k^i)^X}{2}$ 
    else                                                 //Going up in the negative side
       $\tau_k^i = \frac{-G_{mod} (-2e_k^i)^X}{2}$ 
  else if  $dir_k^i = -1$  and  $e_k^i < e_k^{min,i}$  then      //Going down on the virgin line
    if  $e_k^i \geq 0$  then                                //Going down in the positive side
       $\tau_k^i = \frac{G_{mod} (2e_k^i)^X}{2}$ 
    else                                                 //Going down in the negative side
       $\tau_k^i = \frac{-G_{mod} (-2e_k^i)^X}{2}$ 
  elseif  $dir_k^i = 1$  then                                //Going up on the history line
     $\tau_k^i = \tau_k^{min,i} + G_{mod} |e_k^i - e_k^{min,i}|^X$ 
  elseif  $dir_k^i = -1$  then                                //Going down on the history line
     $\tau_k^i = \tau_k^{max,i} + G_{mod} |e_k^i - e_k^{max,i}|^X$ 
  else                                                 //Standing
     $\tau_k^i = \tau_k^{hist,i}$ 

```

Finally, the deviator stresses are known and the Cartesian stresses can be easily defined and provided to the Plaxis outer iteration loop.

Table 7-6. Step 5: calculation of the Cartesian stresses.

```
for k = 1 to 3
     $\sigma_k^i = 2\tau_k^i + K\varepsilon_{vol}$  //Normal stresses
     $\sigma_{k+3}^i = \tau_{k+3}^i$  //Tangential stresses
```

In this way, the UDSM calculates and provides stresses and strains according to the frictional damping law. Therefore, the displacements, compared to the linear elastic stress state, change. The change will be caused only by the reduction of the deviatoric strains, while the volumetric strains will be kept equal to the linear elastic stress state. A code in Pascal for the frictional damping UDSM can be found Appendix A. This code can be compiled into a dll file, which later can be used as a user defined model in Plaxis.

7.6 Verification tests

In order to verify if the UDSM behaves according to the analytical frictional damping law, two verification tests are performed:

- 1) a cyclic simple shear test, and
- 2) a cyclic triaxial test.

The cyclic simple shear test is modelled in plain strain conditions, and the cyclic triaxial test – in axisymmetric conditions. The following soil properties for the verification tests are chosen: the modified shear modulus $G_{mod} = 100 \text{ kN/m}^2$ and the bulk modulus $K = 166.67 \text{ kN/m}^2$. Two different damping ratios are used: $\xi = 5 \%$ and 10% . Such high damping ratios are selected in order to have wider loops in the plots. The verification tests are performed with the quasi-static loading.

Cyclic simple shear test

The simple shear test scheme, for a quarter of a cycle, is presented in Figure 7-4.

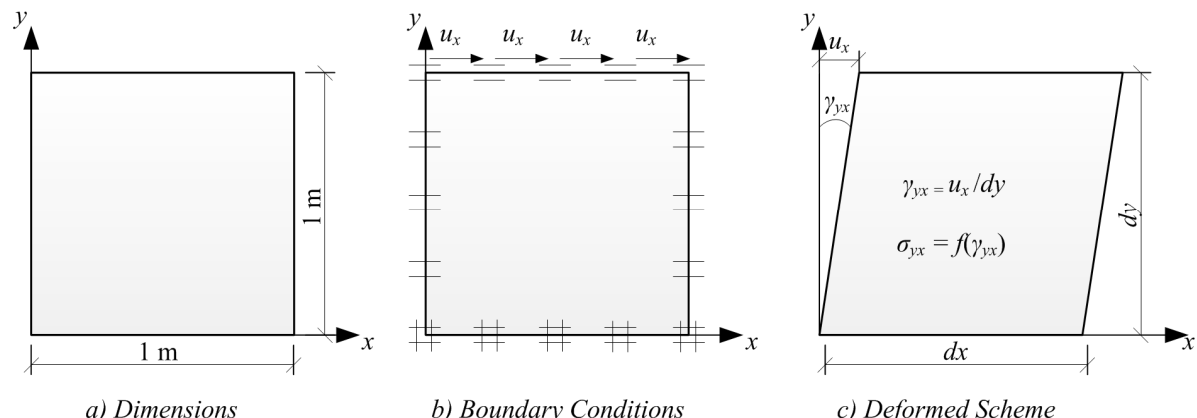


Figure 7-4. Scheme of the simple shear test in the FE model.

The horizontal displacements on top of the sample are controlled, which in this particular case causes only pure shear deformations and no volumetric change. One cycle with the horizontal displacement u_x of 1 m was initiated by equal steps Δu_x of 0.10 m. The shear strain amplitude was 1 (or 100 %). The results of the FEM calculations are the same as the analytical solution. The comparison can be seen in Figure 7-5 a).

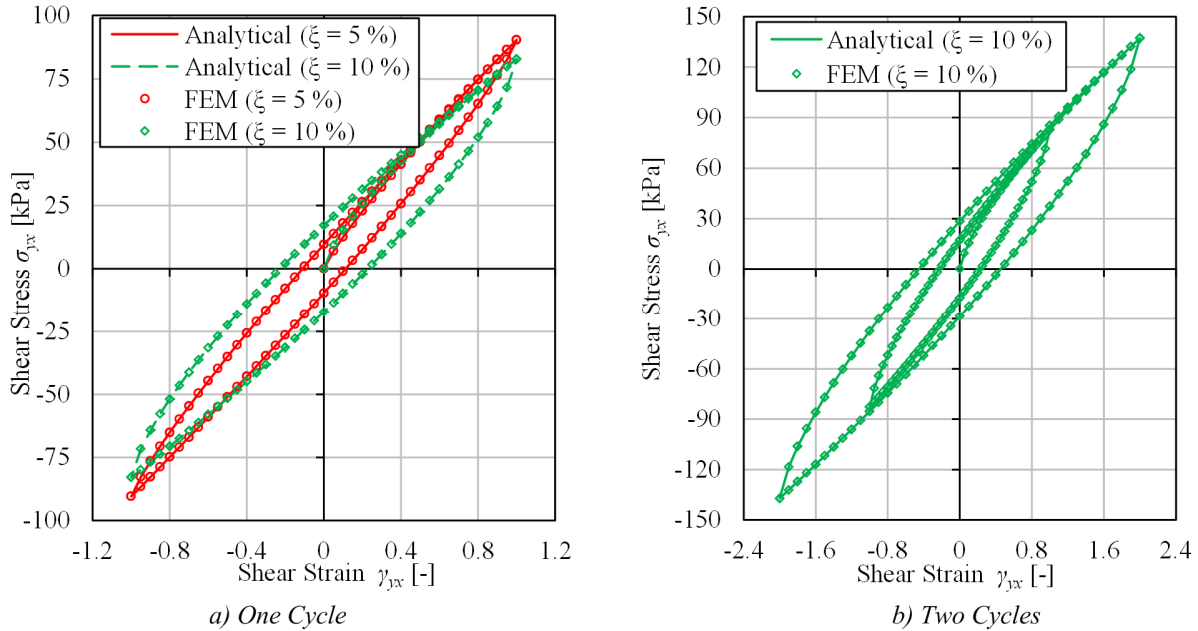


Figure 7-5. Cyclic shear test: analytical solution vs. UDSM results.

The same approach is used to simulate the calculation with double amplitude of a horizontal displacement u_x (2 m) in the second cycle. The shear strain amplitude, in the second cycle, is 2 (or 200 %). In order to have a better view, the results are shown only for the damping ratio ξ of 10 % in Figure 7-5 b).

It can be seen, that in the second cycle, the stress-strain curve first of all follows the virgin line until it reaches the peak and later it follows a new stress history line. Both cycles represent the same damping ratio $\xi = 10 \%$, but have different shear stress and shear strain amplitudes.

Cyclic triaxial test

The triaxial test of a soil sample of 10 m in length and 5 m in diameter is modelled in FEM software as an axisymmetric problem. In the cyclic triaxial test a deformed state is created such, that there is a distortional deformation is caused by normal stresses only whereas the shear stresses are zero. This is reached by using prescribed displacements on top and on the right edge of the sample.

Because it is an axisymmetric problem, the horizontal displacements in the middle are zero. Also the vertical displacements at the bottom boundary are zero. These make the horizontal displacements on top of the sample and the vertical displacements along the side of the sample to be linear functions. On the contrary, the vertical displacements on top of the sample and the horizontal displacements along the side of the sample are constant. The prescribed displacements schematically are illustrated in Figure 7-6 b). The subsequent

deformed scheme, together with a script of calculations for stresses and strains, is presented in Figure 7-6 c).

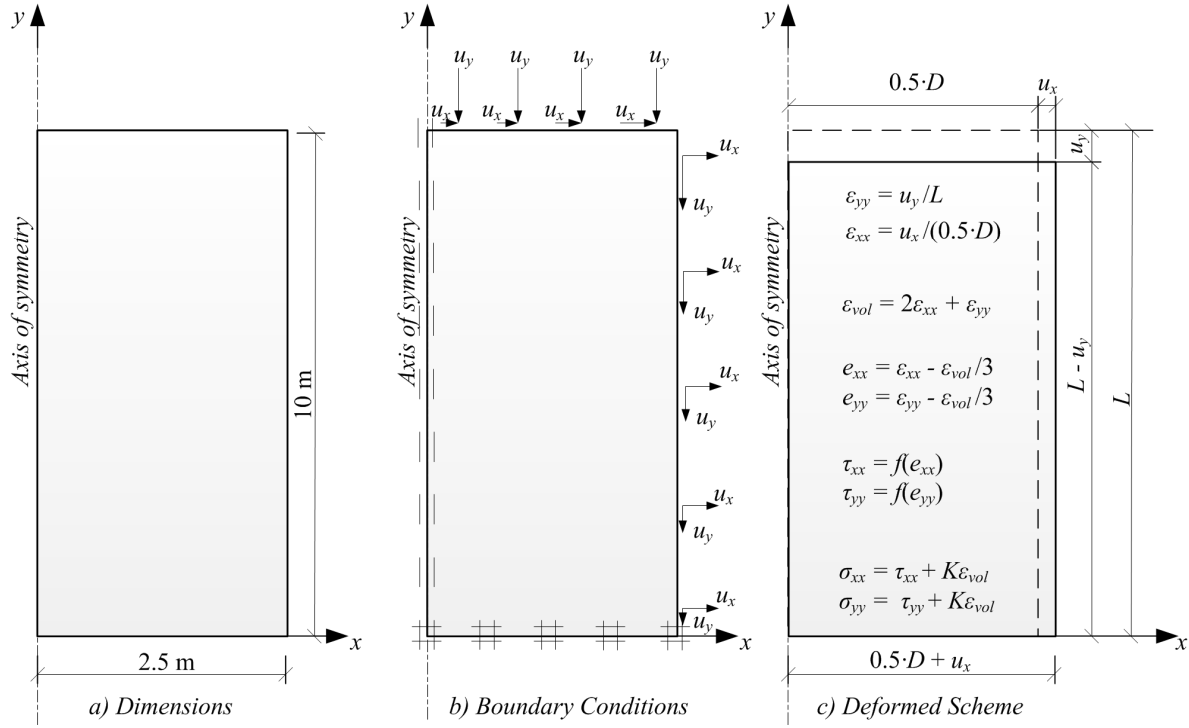


Figure 7-6. Scheme of the triaxial test in the FE model.

Figure 7-7 shows the stress-strain history for the horizontal (left side of the figure) and vertical (right side of the figure) directions, which are also the principal directions in this case, for a damping ratio ξ of 5 %. The calculations are performed for two cycles, where in the second cycle the strain amplitude was doubled.

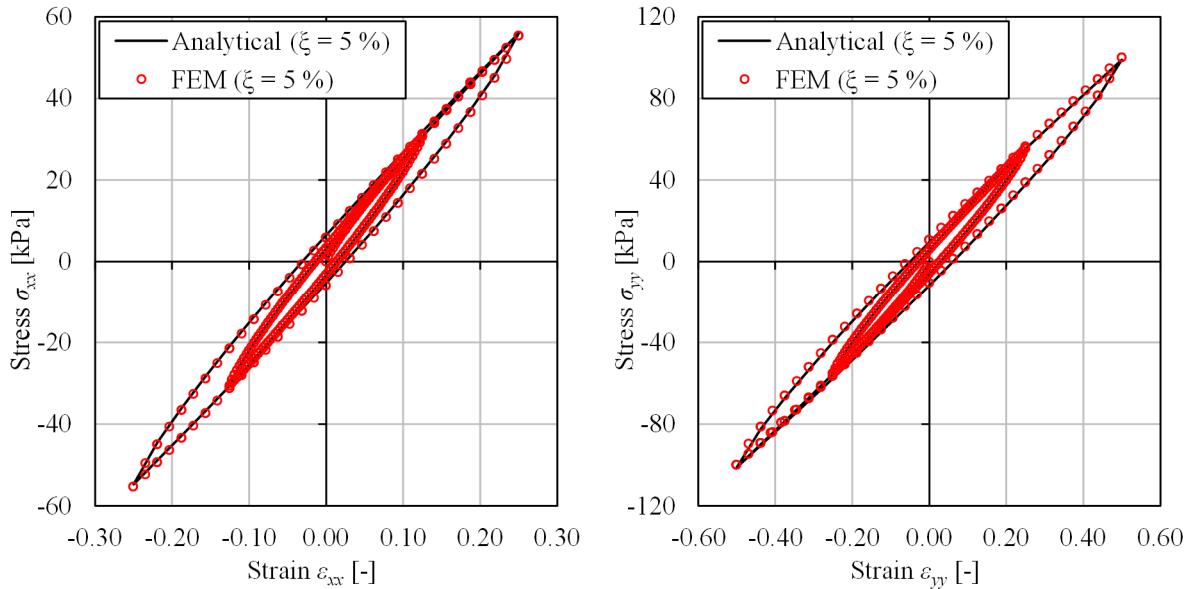


Figure 7-7. Cyclic triaxial test: two cycles, $\xi = 5 \%$; analytical solution vs. UDSM results.

Accordingly, for two cycles and for a damping ratio ξ of 10 %, are presented in Figure 7-8. It can be seen, that the match between the analytical and FEM user defined soil material model calculations is good.

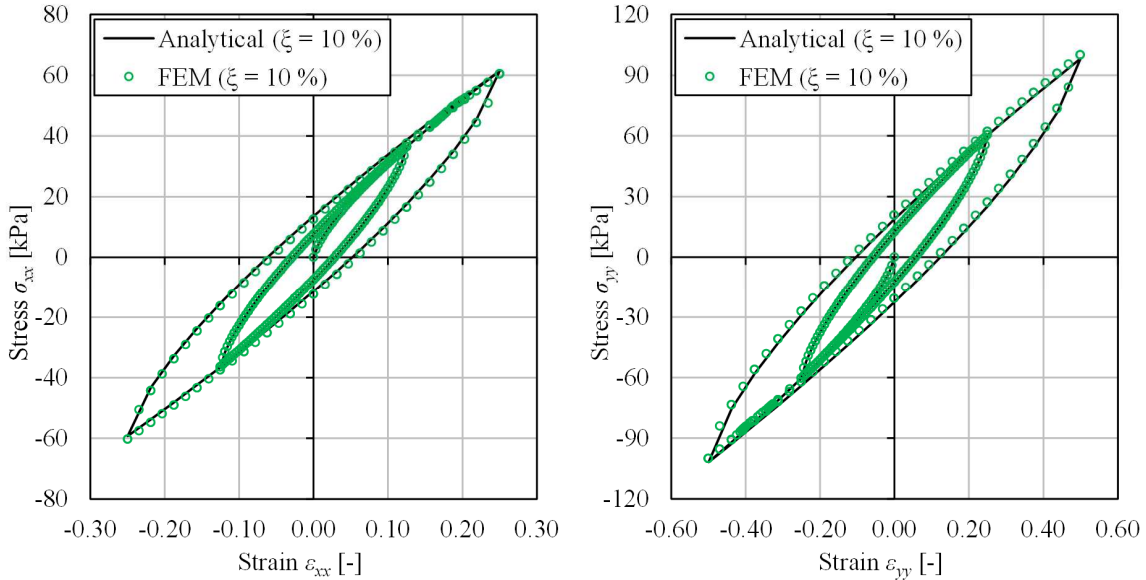


Figure 7-8. Cyclic triaxial test: two cycles, $\xi = 10\%$; analytical solution vs. UDSM results.

The damping ratio can be checked directly, by measuring the area of the ellipses, which represent the dissipated shear energy per cycle ΔE_s and by checking the maximum potential shear strain energy per volume E_{ps} . Having these two quantities, the damping ratio can be calculated by using Equation (7-19). This is done for the material with the damping ratio ξ of 10 %, for the smaller loading cycle.

In order to measure the total dissipated energy per cycle ΔE_s , the ellipses should be used in the deviatoric coordinates $\tau - e$. This is can be seen in Figure 7-9.

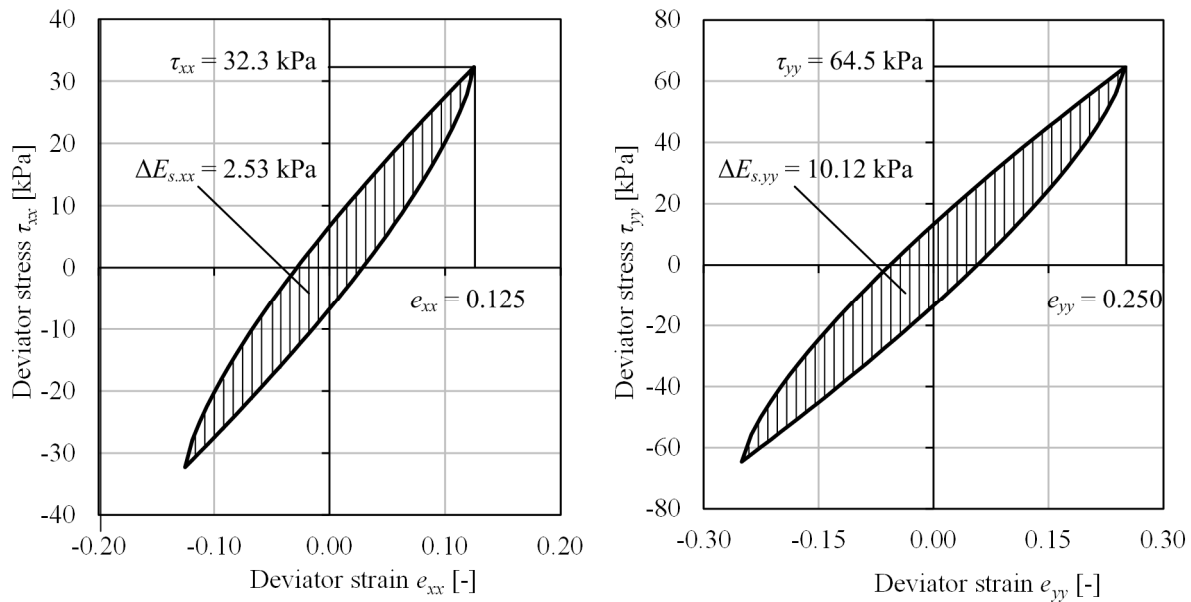


Figure 7-9. Dissipation of the shear strain energy: one cycle, $\xi = 10\%$.

In a triaxial test, stresses and strains in x and z directions are equal, so the dissipated energy in x direction and z directions is also equal: $\Delta E_{S,xx} = \Delta E_{S,zz}$. The dissipated shear strain energy per cycle $\Delta E_S = \Sigma(\Delta E_{S,xx} + \Delta E_{S,yy} + \Delta E_{S,zz} + \Delta E_{S,xy} + \Delta E_{S,yz} + \Delta E_{S,zx})$. Using the areas of the ellipses in Figure 7-9 it can be calculated, that $\Delta E_S = (2.53 + 10.12 + 2.53 + 0 + 0 + 0) = 15.2 \text{ kPa}$.

In the same manner, the potential deviatoric strain energy per volume can be calculated according to Equation (7-18): $E_{pS} = 0.5(\tau_{xx}e_{xx} + \tau_{xx}e_{xx} + \tau_{zz}e_{zz} + \tau_{xy}\gamma_{xy} + \tau_{yz}\gamma_{yz} + \tau_{zx}\gamma_{xz})$, which is in this case $E_{pS} = 0.5(32.3 \cdot 0.125 + 64.5 \cdot 0.250 + 32.3 \cdot 0.125 + 0 + 0 + 0) = 12.1 \text{ kPa}$.

Finally, the damping ratio is checked according to Equation (7-19): $\xi = \Delta E_S / (4\pi E_{pS})$, which gives the damping ratio of 0.10 or 10 %. This matches the input damping ratio and also confirms that the UDSM works well.

7.7 Validation tests

Just like any other constitutive model, the frictional damping model has to be validated. The validation is used to check how good a constitutive model can represent the reality (real tests). The real tests, shaker tests, were already described in Chapter 1. Here the frictional damping model will be used to simulate the shaker tests.

Soil and FE-model properties

The dynamic soil properties, for the shaker test, were defined in Chapter 5.3 from the P- and S-wave velocities and the earlier geological investigations. The measured small strain shear modulus $G_0 = 303 \text{ kN/m}^2$ is assigned to be equal to the shear secant modulus $G_{sec} = G_0$. Other defined parameters are as follows: Poisson's ratio $\nu = 0.464$, Young's modulus $E = 886 \text{ kN/m}^2$ and the natural density of the soil is $\rho \approx 1000 \text{ kg/m}^3$.

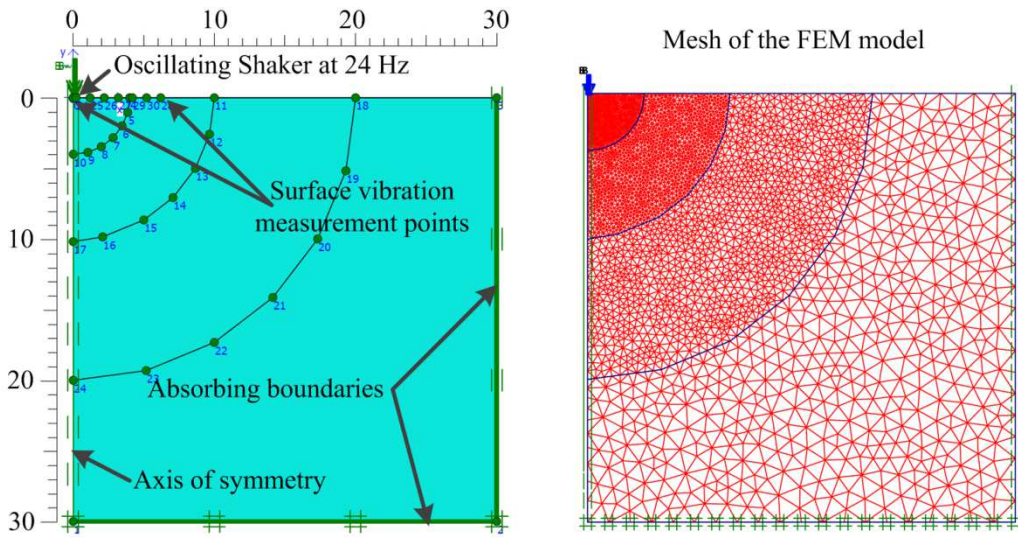


Figure 7-10. FEM geometry and mesh.

From modelling with elastic parameters it was measured, that average shear strain amplitude (in the domain of interest) is in the range of 10^{-4} . The frictional damping ratio $\xi = 1 \%$ will be used (however this is different from the Rayleigh damping ratio $\xi = 1 \%$, because here only the deviatoric part is damped). This results in the following three parameters for the frictional

damping model: 1) the dimensionless damping coefficient, according to Equation (7-2), $X = 0.969$, 2) the modified shear modulus, according to Equation (7-3), $G_{mod} = 232.8 \text{ kN/m}^2$ and 3) the bulk modulus, obtained from the compressional and shear wave velocities, $K = 4102 \text{ kN/m}^2$. An axisymmetric mesh with length and depth of 30 m is used as it is shown in Figure 7-10. 15-node elements used to model the soil.

Vibration amplitudes vs. distance

In Chapter 5.5 the vibration amplitudes of the shaker tests were already measured and presented in Figure 5-13. The tests results were presented together with the FE model, where a Rayleigh damping ratio ζ of 1 % was used. This figure is updated with the results obtained by using the frictional damping model, see now Figure 7-11 which shows that both damping methods: the Rayleigh damping and the frictional damping model, demonstrate close results. However they still do not agree well with the measurements.

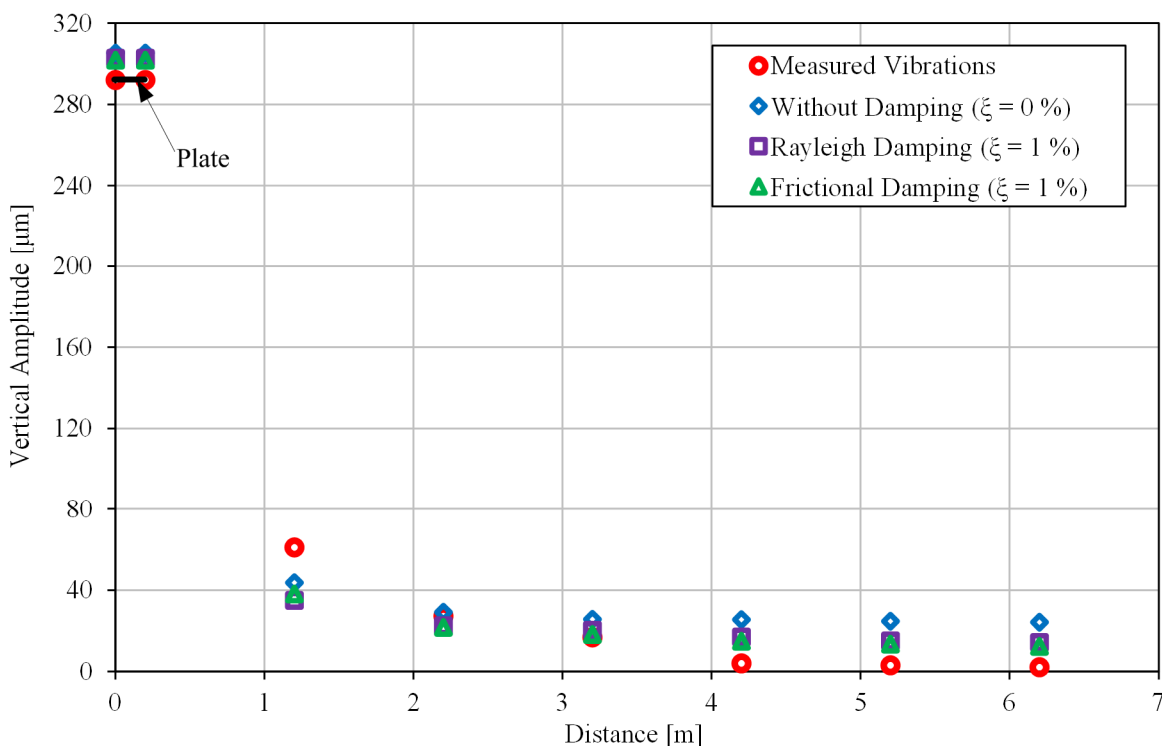


Figure 7-11. Measured vertical vibration amplitudes vs. calculated by FEM.

The calculated vertical vibration amplitudes have quite good match with the measured ones. However, the difference between the frictional damping method and the commonly used Rayleigh damping method is very small. This means that, the frictional damping model works as good as the Rayleigh damping method for the harmonic oscillations. But it also means that to use a more conventional method of damping, Rayleigh damping, is enough for harmonic oscillations. This conclusion is not a surprise, because the damping ratio in the Rayleigh damping method can, for harmonic oscillations, be selected precisely for the applied frequency, because in harmonic oscillations there is only one frequency.

Checking the horizontal vibration amplitudes, see Figure 7-12, it can be seen, that in the first three meters the measured horizontal amplitudes are much bigger than the calculated. The differences, between the measured and calculated horizontal vibration amplitudes, might be

caused by the reflected waves from a deeper soil layer. This additional energy reflecting from the deeper layer is causing higher horizontal vibrations (also slightly changing the vertical vibrations in the first meter, see Figure 7-11, but the vertical vibrations are, in general, higher so the influence of the reflection is smaller). Also here the assumption should be recalled, which had been made in Chapter 5.3, that the site is homogeneous even though it was known a priori, from the earlier geological investigations, that it is not fully homogeneous. Other aspects than layering were also discussed in Chapter 2, like anisotropy, saturation, air-content, etc. From these, the degree of saturation could have caused a second P-wave to appear. The second P-wave could not be captured by FEM, because it is a product of multiphase behaviour.

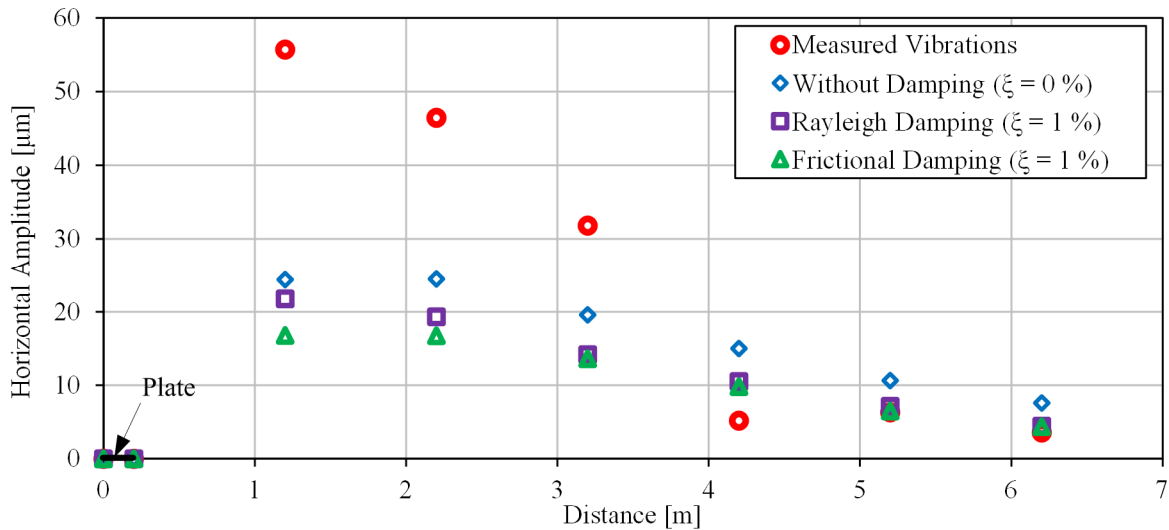


Figure 7-12. Measured horizontal vibration amplitudes vs. calculated by FEM.

The values of the vibration amplitudes of FEM calculations and measurements can be better seen in the following tables.

Table 7-7. Vertical vibration amplitudes: FEM vs. measurements.

Distance [m]	Vertical vibration amplitudes [μm]				Measured
	No damping	Rayleigh damping $\xi = 1 \%$	Frictional damping $\xi = 1 \%$		
0	305.3	302.7	301.9		292
0.2	305.3	302.7	301.9		292
1.2	43.71	35.04	38.07		61.01
2.2	29.13	22.55	21.81		27.32
3.2	25.73	20.32	18.21		16.84
4.2	25.50	16.98	15.01		4.05
5.2	24.72	15.11	13.61		3.12
6.2	24.29	14.30	12.50		2.12

As it can be seen from Figure 7-13, the calculations with damping tend to follow the linear elastic solution (without damping) and similarly underestimate the vibrations closer to the source, and overestimate further away from the source (with respect to the measurements).

From the validation results, it can be concluded that the frictional damping model can predict the geotechnical vibrations caused by harmonic oscillations with at least the accuracy of

Rayleigh damping. And as it was stated earlier, it is because for the harmonic oscillations (only one frequency) – correct Rayleigh damping coefficients can be selected.

Table 7-8. Horizontal vibration amplitudes: FEM vs. measurements.

Distance [m]	Horizontal vibration amplitudes [μm]			Measured
	No damping	Rayleigh damping $\xi = 1\%$	Frictional damping $\xi = 1\%$	
0	0	0	0	0
0.2	0	0	0	0
1.2	24.39	21.74	16.80	55.70
2.2	24.48	19.33	16.75	46.42
3.2	19.56	14.16	13.6	31.83
4.2	14.99	10.50	9.81	5.17
5.2	10.65	7.13	6.51	6.30
6.2	7.57	4.42	4.37	3.58

However, for an impact pulse, the differences between the two damping methods should be more visible. The advantage of the frictional damping may be apparent, because the frictional damping damps all the frequencies equally.

Vertical vs. Horizontal velocity amplitudes

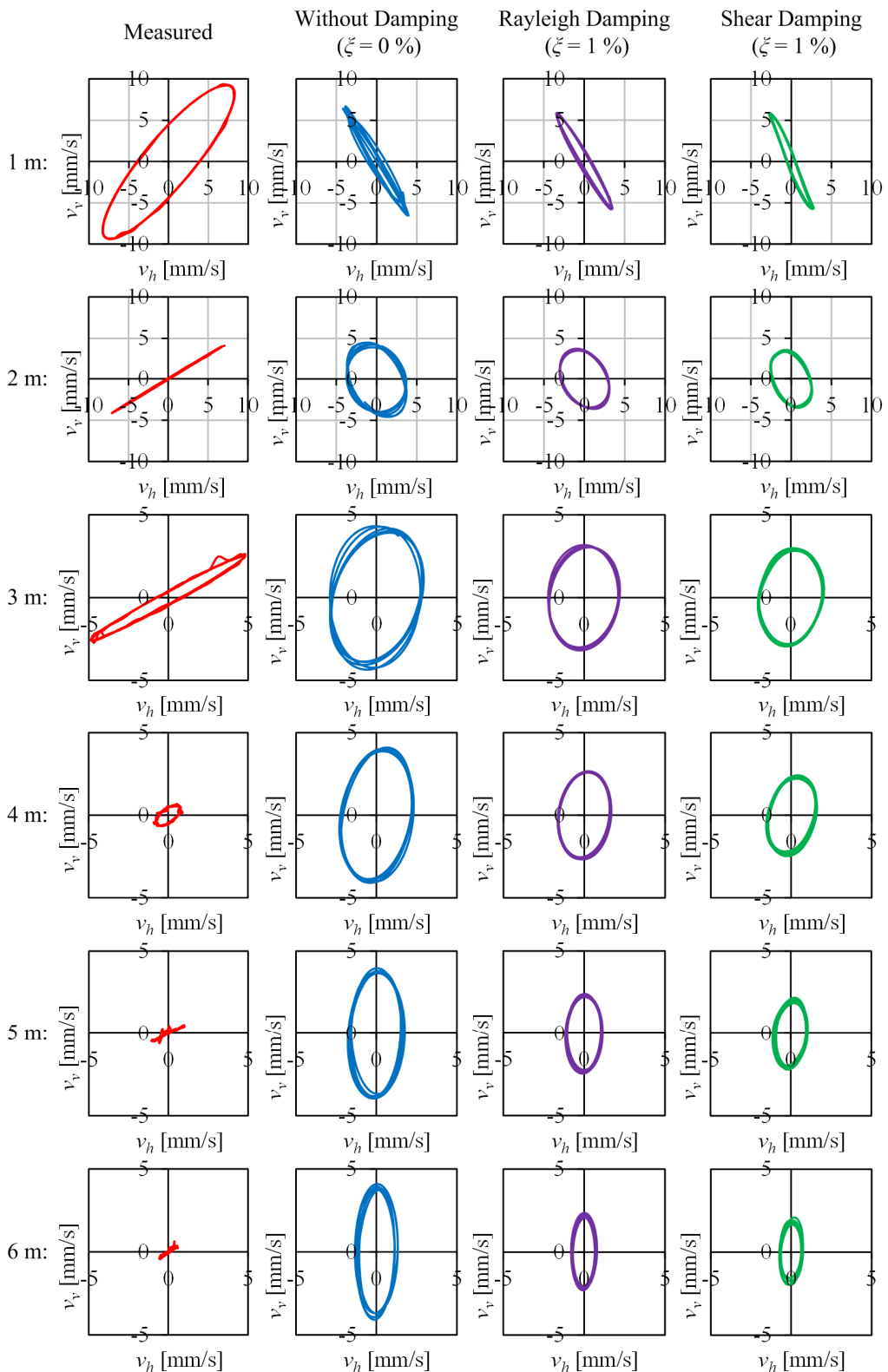


Figure 7-13. Velocity trajectories.

7.8 Pulse load – Rayleigh damping versus frictional damping

In order to check the differences between Rayleigh damping and the frictional damping methods for pulse loading, a numerical simulation of a pulse signal was performed.

Soil and FE model properties

The Rayleigh damping (available in Plaxis), is unfortunately frequency dependent and also damps deformations of all wave types, instead of only the deviatoric part. Because of this, this, Rayleigh damping will be compared to the frictional damping model, which does not have these problems. For this a pulse load on a circular area on the soil surface is modelled numerically. The pulse load of 2 kN is modelled as a maximum vertical stress of 63.66 kN/m² over the area on the soil surface with a diameter of 0.1 m. The vertical stress is introduced in a time period from 0 to 0.005 s, with its peak at 0.0025 s (Figure 7-14).

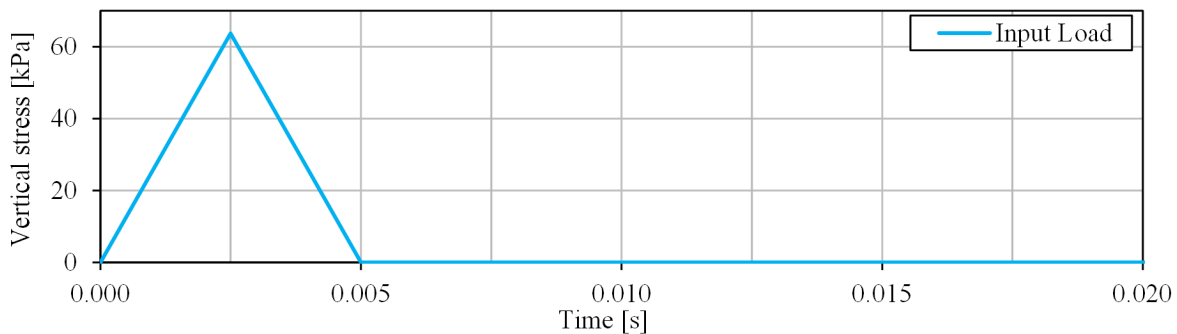


Figure 7-14. Input pulse load.

An axisymmetric mesh with a length and depth of 50 m is used. The geometry and mesh is presented Figure 7-15.

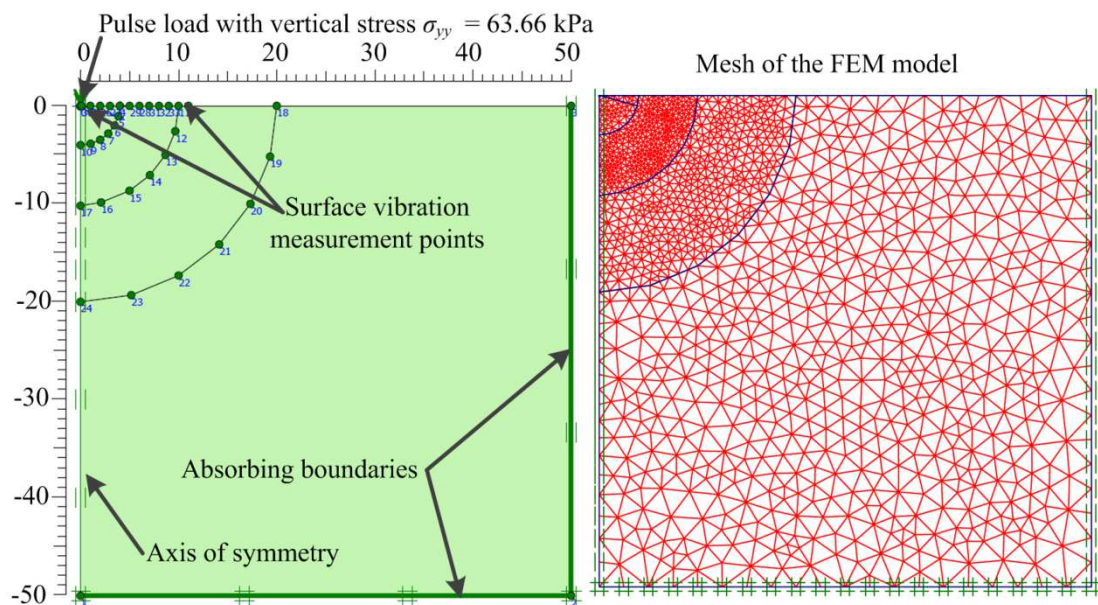


Figure 7-15. Geometry and mesh of a pulse load FE model.

The dynamic problem is calculated first without damping, second with Rayleigh damping and third with frictional damping. A damping ratio will be used of $\xi = 3\%$. The compressional wave velocity of the soil medium $v_p = 200$ m/s, the shear wave velocity $v_s = 60$ m/s and the density $\rho = 1.5$ t/m³. From this follows the small strain stiffness shear modulus $G_0 = \rho \cdot v_s^2 = 5400$ kN/m² and the Poisson's ratio ν of 0.451. Here the secant shear modulus G_{sec} is set to be equal to the small strain stiffness shear modulus G_0 .

In this case, for the Rayleigh damping, the target damping ratios are equal $\xi_1 = \xi_2 = 3\%$. Unfortunately, there is no other way than selecting two different target frequencies. From the undamped calculations it was measured, that most of the pulse energy travels in the frequency range between $f_1 = 5$ Hz and $f_{II} = 25$ Hz, then the angular frequencies: $\omega_1 = 2\pi f_1 = 31.42$ rad/s and $\omega_2 = 2\pi f_{II} = 157.08$ rad/s. So the damping coefficients according to Equation (5-6) are respectively $\alpha_R = 1.571$ and $\beta_R = 3.183 \cdot 10^{-4}$.

For the frictional damping model, the average shear strain amplitude is in the range of 10^{-5} . The frictional damping ratio $\xi = 3\%$, results in the following three parameters for the frictional damping model: 1) the dimensionless damping coefficient, according to Equation (7-2) $X = 0.910$, 2) the modified shear modulus, according to Equation (7-3), $G_{mod} = 2039$ kN/m² and 3) the bulk modulus, obtained from the compressional and shear wave velocities, $K = 52\,800$ kN/m².

Results

Figure 7-16 shows the peak displacements versus distance from the centre. The left side of the figure shows the horizontal peak displacements and the right side shows the vertical peak displacements.

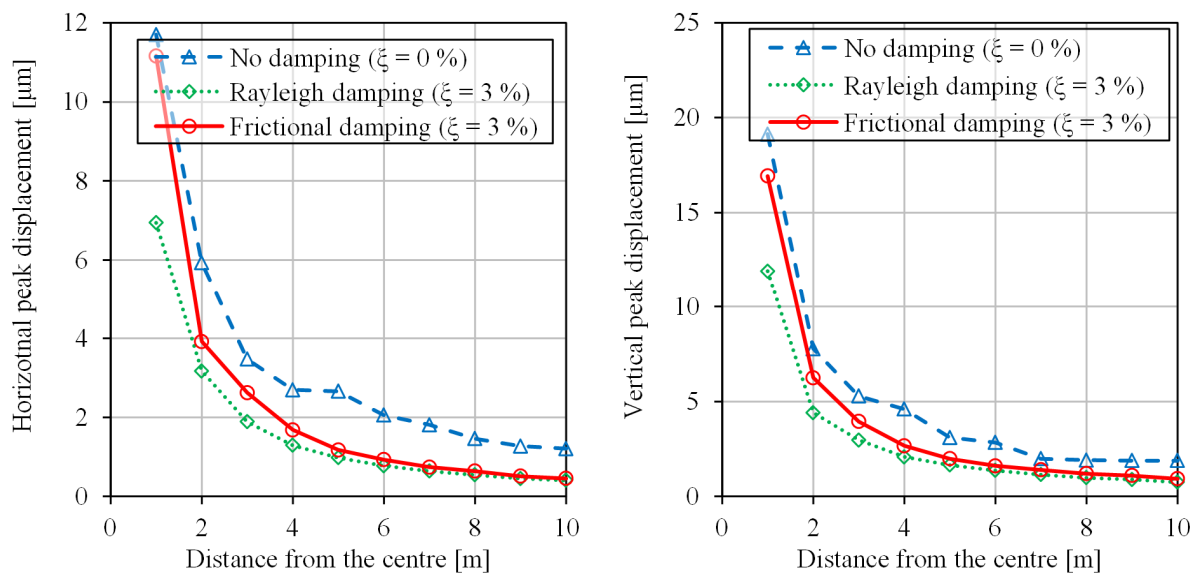


Figure 7-16. Peak displacement at different distances.

From Figure 7-16 follows that by applying frictional damping, the peak displacements (horizontal and vertical) are higher than by applying Rayleigh damping, especially closer to the source. This can be explained by the fact, that near the source, there are only compressional and shear waves and the Rayleigh wave is not yet developed. The

compressional waves change mostly the volume and hardly the shape. On the contrary, the shear waves change only the shape. The frictional damping damps only the changes of the shape, so only the shear waves and a small part of the compressional waves. In contrary the Rayleigh damping damps all waves equally, so also the displacements of the compressional waves.

Further away from the source, the Rayleigh wave is emerging and starts to dominate. It causes more changes of the shape rather than the volume; therefore the differences between the peak displacements, obtained by the two different damping models, are getting smaller.

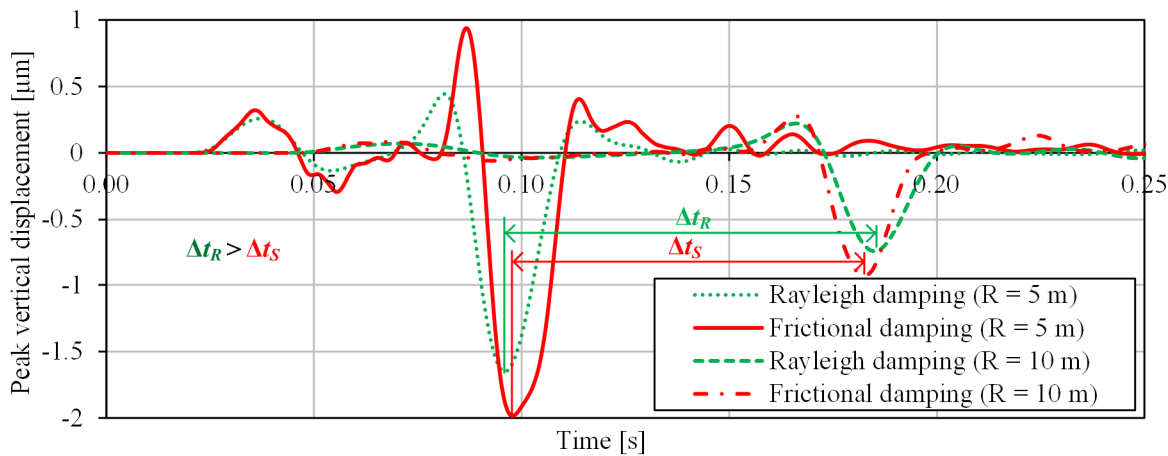


Figure 7-17. Vertical vibration records at 5 m and 10 m distances.

In Figure 7-17, the vertical vibration records can be seen for two different distances from the centre of the source: at 5 m and at 10 m. The red colour lines show the results obtained with the frictional damping model, and the green lines – with Rayleigh damping.

The arrival times of the peak displacements are very close, but not exactly the same. Comparing the time differences Δt between the red and the green peaks, it can be seen, that the signal travels faster with the frictional damping model. This is because the modified shear modulus G_{mod} is selected for average shear strain amplitudes of 10^{-5} , whereas the shear strain amplitudes become smaller for larger distances. The shear strain amplitudes decrease because of both the radiation damping and the material damping. This result in a stiffer behaviour of the deviatoric term, therefore the pulse travels faster.

7.9 Conclusions

A 3D frictional damping model has been developed and incorporated into the FEM software Plaxis as a user defined soil model. The verification cyclic simple shear and cyclic triaxial tests showed good agreement with analytical solutions. This confirms that the 3D frictional damping law was correctly incorporated into the FEM code as UDSM.

The validation tests proved, that the frictional damping model can predict the geotechnical vibrations caused by harmonic oscillations with at least the accuracy of Rayleigh damping. Even though the measured vibration amplitudes were not exactly the same as the numerically predicted, the numerical predictions are more accurate than analytical ones by using the

analytical method of Barkan-Bornitz. On the other hand, the results obtained with the frictional damping model and Rayleigh damping are very close. This means that the frictional damping model did not solve the problem of the different amount of damping just next to the plate and further away from the plate.

Despite this, the advantage of the frictional damping model becomes clear in the case of a pulse load, in which a lot of different frequencies are generated. The frictional damping model demonstrates a different physical behaviour of the soil, in comparison to the Rayleigh damping, because it is able to damp only deviatoric strains and its damping remains constant for all frequencies. Closer to the source, the peak displacements are bigger, due to the fact that only the deviatoric part of the strains is damped. This means all basic waves (compressional, shear, Rayleigh) are damped differently. Further away from the source, the peak displacements are almost the same, regardless which model is used. However, the arrival times obtained by the frictional damping model are shorter in comparison to the Rayleigh damping. This is due to increasing stiffness in the far-field.

In the frictional damping model, the energy dissipation is a result of the non-linearity of the soil. Because of this non-linear behaviour, the stiffness matrix is a function of the strains and solved by an iterative Newton-Raphson procedure. During calculations, the stiffness matrix is updated during each incremental load step. This process costs much calculation time. In the Rayleigh damping model however, the same stiffness matrix is used during the calculation, therefore it is considerably faster.

The shaker test showed that for problems with harmonic oscillations, with only one frequency, Rayleigh damping can be used, instead of the frictional damping, and almost the same results can be obtained. And at the same time a considerable amount of calculation time can be saved.

Also, the frictional damping model is very sensitive to the damping ratio. This follows from the fact that a power law is used. The FEM code has difficulties to converge for very high damping ratios ($\zeta > 5\%$). But on the other hand, this model is intended for man-made vibrations, where the damping is constant and small ($\zeta < 3\%$).

8 CONCLUSIONS AND RECOMMENDATIONS

8.1 Conclusions

There are a few analytical methods to calculate the vibration amplitudes and phase shifts of an oscillating plate on an elastic, homogeneous and isotropic half-space. The comparison of the analytical solutions with the FEM showed that for the vertical vibration amplitude of an oscillating rigid plate, Lysmer's analytical solution demonstrates similar results as the FEM calculations. The confined elasticity solution as well as the Reissner's solution (with Sung's displacement functions) could be used for very low dimensionless frequencies only.

For the amplitudes of the soil surface there is only one analytical method, Barkan's method, to calculate the amplitudes and phase shifts. The comparison of Barkan's solution, which is unfortunately for weightless plates only, and FEM showed similar results only for the near-field zone, whereas the far-field zone gave similar results for the FEM calculations only for low dimensionless frequencies ($a_0 < 0.3$). However, the far-field solution could be still used for higher dimensionless frequencies if it is adjusted by removing a jump between the near- and far-fields.

The disagreements between some analytical solutions and FEM results, encouraged to investigate the problem of an oscillating circular rigid plate more carefully, by inspecting the wave-field itself. For a better understanding it was needed to decompose the wave signal into three basic waves (P-wave, S-wave and R-wave).

A wave decomposition method has been developed which can decompose a recorded superposed soil wave into its basic waves when multiple geophones are used. From the recorded data a system of non-linear equations can be assembled with six unknown parameters (three amplitudes and three phase shifts). These six parameters can be solved by using an iterative way of the least square method. This leads to a decomposition into the three basic waves, with each its own amplitude and phase shift. The superposition of only these basic waves describes very accurately the recorded superposed soil wave, proving the existence of only these three basic waves. The findings prove also that all three basic waves have phase shifts (in the far-field) and these phase shifts are all different from each other.

The energy balance shows that the amount of emitted energy by the load on the plate is the same as of the sum of energies of the basic waves. This is another type of evidence that only three basic waves exist. Near the vibrating plate, the displacement amplitudes do not follow the same attenuation law such as further away from the source. This proves the existence of the near-field phenomenon. The R-wave energy starts at zero just at the source and grows in the near-field zone due to an energy transmission (body waves are transferring energy to the R-wave). After some distance (in the far-field), the R-wave becomes fully developed. This phenomenon is not understood completely yet, but it does explain the phase shifts of the basic waves.

A real field test of a shaker on the surface of a real soil has been performed in order to compare the vibrations with analytical and FEM calculations. In this case, one of the soil mechanical aspects is introduced – the material damping. The shaker test showed, that the vibration amplitudes of the plate can be predicted with Reissner's or Lysmer's approach or with numerical (FEM) calculations. The accuracy depends on the method used for the prediction, and ranges from 94 % to 100 % (which corresponds to Predicted/Measured ratio

of 1.06 and 1.00 respectively). This means that the amplitude of the shaker can be predicted accurately enough for geotechnical purposes.

The soil surface vibration amplitudes can be predicted with Barkan-Bornitz's analytical approach and with numerical (FEM) calculations. The Barkan-Bornitz approach over-predicted the amplitudes between 4.2 and 48.9 times. The FEM under-predicted the amplitudes for the first three meters and over-predicted up to 7.2 times for the last three meters. This means that the amplitudes of the surface cannot be predicted with higher than 25 % accuracy.

The measurements from the shaker test indicated different amount of damping just next to the plate and further away from the plate. This is theoretically possible in case of different damping per basic waves. There is a method reflecting this phenomenon, which is the frictional damping method, first suggested by Van Baars (2011). In order to be able to use this 1D method, it had to be extended to 3D and incorporated into the FEM calculation scheme.

This 3D frictional damping model has been developed and incorporated into the FEM software Plaxis as a user defined soil model. As verification, cyclic simple shear and cyclic triaxial tests have been modelled. The results show good agreement with analytical solutions, confirming that the 3D frictional damping law was correctly incorporated into the FEM code. As a validation test, the shaker test was used. Even though the numerically calculated amplitudes are not exactly the same as the measured on site, they are still more accurate than the analytically ones, calculated by Barkan-Bornitz's approach. On the other hand, the results obtained with the frictional damping model and Rayleigh damping are very close. This means that the frictional damping model did not solve the problem of the different amount of damping just next to the plate and further away from the plate.

Despite this, the advantage of the frictional damping model becomes clear in the case of a pulse load, in which a lot of different frequencies are generated. The frictional damping model demonstrates a different physical behaviour of the soil, in comparison to the Rayleigh damping, because it is able to damp only deviatoric strains and its damping remains constant for all frequencies. Closer to the source, the peak displacements are bigger, due to the fact that only the deviatoric part of the strains is damped. This means all basic waves (compressional, shear, Rayleigh) are damped differently. Further away from the source, the peak displacements are almost the same, regardless which model is used. However, the arrival times obtained by the frictional damping model are shorter in comparison to the Rayleigh damping. This is due to increasing stiffness in the far-field.

In the frictional damping model, the energy dissipation is a result of the non-linearity of the soil. Because of this non-linear behaviour, the stiffness matrix is a function of the strains and solved by an iterative Newton-Raphson procedure. During calculations, the stiffness matrix is updated during each incremental load step. This process costs much calculation time. In the Rayleigh damping model however, the same stiffness matrix is used during the calculation, therefore it is considerably faster.

The shaker test showed that for problems with harmonic oscillations, with only one frequency, Rayleigh damping can be used, instead of the frictional damping, and almost the same results can be obtained. And at the same time a considerable amount of calculation time can be saved.

Also, the frictional damping model is very sensitive to the damping ratio. This follows from the fact that a power law is used. The FEM code has difficulties to converge for very high damping ratios ($\xi > 5\%$). But on the other hand, this model is intended for man-made vibrations, where the damping is constant and small ($\xi < 3\%$).

8.2 Recommendations

For calculations of the vertical vibration amplitude of an oscillating rigid circular plate, Lysmer's analytical solution may be used. However for a plate with different stiffness or non-circular shape, the more general, Reissner's solution together with corresponding and unknown displacement functions f_1 and f_2 should be used.

In order to predict the surface displacements of an oscillating rigid circular plate, an improved solution for the vibration predictions can be used. This solution consists of three parts: 1) the analytical Lysmer method for the plate displacement amplitude 2) the shape of the vertical surface displacements of the elasto-static Boussinesq solution in the near-field and 3) the R-wave attenuation law $r^{-0.5}$ with the exponential material damping law ($\exp[-k_m(r - r_{ff})]$) in the far-field. It is recommended to end the near-field at a distance, equal to about a half to one length of the R-wave. This approach gives good predictions, if compared to the measurements or FEM calculations.

For future research on vibrating plates, it is recommended to use a bigger shaker than described in the thesis. The tests on sites, which are stiffer than the peaty test site, showed that the vibration amplitudes are damped very rapidly and cannot be measured after the first two meters anymore because the ambient noise becomes higher than the vibrations. However using a bigger shaker means also bigger transportation problems, as well as the possibility of plastic deformations under the plate. Also a denser grid of measurement points, especially in the first meter away from the shaker, should be used.

The frictional damping model is recommended to be used for impulse load problems, but first it should be validated with an impulse load test. The model is designed for small strain problems where the damping is small and constant. Very close to the load source, close to a pile or just under a dropped mass, a soil body might be deformed with much higher shear strains. Therefore, close to the source, where the damping is high and not constant, the soil should be modelled by using another model, for example the Hardening Soil model for small strains.

BIBLIOGRAPHY

Ali, H., Castellanos, J., Hart, D. & Nukunya, B., 2003. *Real-time Measurement of the Impact of Pile Driving Vibrations on Adjacent Property During Construction*. Washington, Transportation Research Board (TRB) Annual Meeting.

Amick, H. & Gendreau, M., 2000. *Construction Vibrations and Their Impact on Vibration-Sensitive Facilities. Presented at , Florida, February 22..* Florida, ASCE Construction Congress 6 Orlando.

Andersen, L., 2006. *Linear Elastodynamic Analysis. DCE Lecture Notes No.* Aalborg University ed. Aalborg: s.n.

Arnold, R., Bycroft, G. & Warburton, G., 1955. Forced Vibration of a body on an Infinite Elastic Stratum. *J. Applied Mechanics, Trans. ASME*, Volume September, pp. 391-400.

Athanasopoulos, G. & Pelekis, P., 2000. Ground vibrations from sheetpile driving in urban environment: measurements, analysis and effects on buildings and occupants. *Soil Dynamics and Earthquake Engineering*, 19(5), pp. 371-387.

Auersch, L., 1995. *Some effects of the layering of the soil on wave propagation and foundation vibrations.* Greece, s.n., pp. 283-290.

Auersch, L. & Said, S., 2010. Attenuation of ground vibrations due to different technical sources. *Journal of Earthquake Engineering and Engineering Vibration*, 9(3), pp. 337-344.

Baidya, D., 2000. *Natural Frequency of Vibrating Foundation on Layered Soil - an Experimental Investigation.* Australia.

Barends, F. B. J., 1980. Dynamics of elastic plates on a flexible subsoil. *LGM-Mededelingen*, Volume 21, pp. 127-134.

Barkan, D. D., 1962. *Dynamics of bases and foundations.* New York: McGraw-Hill Book Company, Inc.

Biot, M., 1941. General theor of three-dimensional consolidation. *Journal of Applied Physics*, Volume 12, pp. 155-164.

Biot, M., 1955. Theory of elasticity and consolidation for a porous anisotropic solid. *Journal of Applied Physics*, 26(2), pp. 182-185.

Biot, M., 1956a. Theory of deformation of a porous viscoelastic anisotropic solid. *Journal of Applied Physics*, 27(5), p. 459–467.

Biot, M., 1956b. Theory of propagation of elastic waves in a fluid-saturated porous solid. I. Lowfrequency range. *The Journal of the Acoustical Society of America*, 28(2), p. 168–178.

Bodare, A., 1998. *Non destructive test methods of stone and rock.*

Bolton, M. D. & Wilson, J., 1990. *Soil stiffness and damping.* s.l., Proceedings of The International Conference on Structural Dynamics, Eurodyn '90, University of Bochum, pp. 209-216.

Bornitz, G., 1931. *Über die Ausbreitung der von Großkolben Maschinen erzeugten Bodenschwingungen in die Tiefe.* Berlin: Springer-Verlag.

Bycroft, G., 1956. Forced Vibrations of a Rigid Circular Plate on a Semi-Infinite Elastic Space and on an Elastic Stratum. *Philosophical Transactions of the Royal Society*, Vol. 248(Ser. A), pp. 327-368.

Bycroft, G., 1977. Soil-Structure Interaction at High Frequency Factors. *International Journal of Earthquake Engineering and Structural Dynamics*, Volume 5, p. 235-248.

Carcione, J. et al., 2004. Wave propagation in partially saturated porous media: simulation of a second slow wave. *Wave motion*, Volume 39, pp. 227-240.

Chowdhury, I. & Dasgupta, S. P., 2009. *Dynamics of Structure and Foundation – A Unified Approach. I Fundamentals.* Leiden: CRC Press/Balkema.

Coelho, B., 2010. *Dynamics of railway transition zones in soft soils: Doctoral thesis.* Delft: Delft University of Technology.

Das, B. & Ramana, G., 2011. *Principles of Soil Dynamics. International SI Edition.* Stamford: Cengage Learning.

Hall, J. R. J., 1967. *Coupled Rocking and Sliding Oscillations of Rigid Circular Footings.* Albuquerque, NM, USA, Proc. Int. Symp. On Wave Propagation and Dyn. Properties of Earth Materials.

Helbig, K., 1993. Simultaneous observation of seismic waves of different polarization indicates subsurface anisotropy and might help to unravel its cause.. *Journal Applied Geophysics*, Volume 30, pp. 1-24.

Hölscher, P., 1995. *Dynamical response of saturated and dry soils: Doctoral thesis.* Delft: Delft University of Technology.

Hölscher, P. & Waarts, P. H., 2003. *Reliability of vibration prediction and reducing measures.* Delft: Delft Cluster.

Hsieh, T., 1962. Foundation Vibrations. *Proc. of Inst. of Civil Engineers*, Volume 22, p. 211-226.

Jones, S. & Hunt, H. E. M., 2012a. Predicting surface vibration from underground railways through inhomogeneous soil. *Journal of Sound and Vibration*, 331(9), pp. 2055-2069.

Jones, S. & Hunt, H. E. M., 2012b. The effect of inclined soil layers on surface vibration from underground railways using the thin-layer method. *Journal of Engineering Mechanics*, 137(12), pp. 887-900.

Kramer, S., 1996. *Geotechnical Earthquake Engineering*. New Jersey: Prentice Hall.

Kruijzer, G., 2006. *The vertical motion of foundations and pontoons. (Reprinted)*. Delft: VSSD.

Lamb, H., 1904. On propagation of tremors over the Surface of an elastic solid. *Phil. Trans. of Royal Soc.*, Volume 203, p. 1-42.

Love, A., 1927. *The Mathematical Theory of Elasticity*,. 4th ed. Cambridge: University Press.

Lysmer, J., 1965. *Vertical motion of rigid footings. Report to WES Contract Report*, Michigan: Department of Civil Engineering, University of Michigan.

Masoumi, H., Degrande, G. & Holeyman, A., 2008. *Pile response and free field vibrations due to low strain dynamic loading*. Portugal, Proceedings of the 8th International Conference on the Application of Stress-Wave Theory to Piles, pp. 307-314.

Masoumi, H., François, S. & Degrande, G., 2008b. *Vibration prediction for vibratory and impact pile driving using a non-linear dynamic soil-structure interaction analysis*. Portugal, Proceedings of the 8th International Conference on the Application of Stress-Wave Theory to Piles, pp. 299-306.

Miller, G. & Pursey, H., 1955. On the Partition of Energy between Elastic Waves in a Semi-Infinite Solid. *Proceedings of the Royal Society of London Series A, Mathematical and Physical Sciences*, 233(1192), pp. 55-69.

Moreno, C. A. & Rodriguez, E. E., 2004. *Dynamic behaviour of Bogota's subsoil peat and it's effect in seismic wave propagation*. Vancouver, B.C., Canada, 13th World Conference on Earthquake Engineering.

Nakagawa, K. & Soga, K., 1995. *Observation of propagating elastic waves in granular soils by the pulse transmission method*. Greece, Proceedings of the 7th International Conference on Soil Dynamics and Earthquake Engineering, pp. 299-307.

Okur, D. & Ansar, A., 2007. Stiffness degradation of natural fine grained soils during cyclic loading. *Soil Dynamics and Earthquake Engineering*, 27(9), pp. 843-854.

Plaxis bv, 2015. *Plaxis 2015*. Delft: Plaxis bv.

Quinlan, P., 1953. The Elastic Theory of Soil Dynamics. *Special Technical Publication No. 156, ASTM, Symposium on Dynamic Testing of Soils*, pp. 3-34.

Rao, P., 1993. *Effect of pile geometry and soil saturation in the behavior of no displacement piles installed by vibration: Master Thesis*. Houston: University of Houston.

Rayleigh, L., 1885. On waves propagated along the plane surface of an elastic solid, *Proceedings of the London Mathematical Society*. Volume 17, pp. 4-11.

Reissner, E., 1936. Staionare axilasymmetrische durch eine schuterende Masse erregte Schwingungen eines homogenen elastischen Halbraumes. *Ingenieur Archiv*, 22(December), pp. 381-396.

Reissner, E., 1996. *Selected Works in Applied Mechanics and Mathematics*. Sudbury, Massachusetts: Jones and Bartlett Publishers.

Reissner, E. & Sagoci, H., 1944. Forced torsional oscillations of an elastic halfspace. *J. of Appl. Physics*, Volume 15, pp. 652-662.

Smeulders, D., 1992. *On wave propagation in saturated and partially saturated porous media: Doctoral thesis*. Eindhoven: Eindhoven University of Technology.

Sung, T., 1953. Vibrations in semi infinite solids due to Periodic surface loading. *Special Technical Publication No. 156, ASTM, Symposium on soil dynamics*, July.p. 35–64.

Van Baars, S., 2009. *Soil Dynamics. Lecture Notes*. Delft: Delft University of Technology.

Van Baars, S., 2011. *Modelling of frictional soil damping in finite element analysis*. Cavtat-Dubrovnik, International Symposium on Computational Geomechanics.

Van Baars, S. & Hölscher, P., 2010. *AFR PhD Application Form*. Luxembourg: s.n.

Van Wijk, K. & Levshin, A. L., 2004. Surface wave dispersion from small vertical scatterers. *Geophysical Research Letters*, 31(L20602), pp. 1-4.

Verruijt, A., 2006. *Soil Dynamics*. Delft: Delft University of Technology.

Viking, K., 2002. *Vibro-driveability – a field study of vibratory driven sheet piles in non-cohesive soils: Doctoral thesis*. Stockholm: Royal Institute of Technology.

Wang, H., 1994. *Experimental study and finite element analysis of driveability and static behaviour of various piles installed by vibratory driving: Doctoral thesis*. Houston: University of Houston.

Westergaard, H. M., 1938. A problem of elasticity suggested by a problem in soil mechanics: soft material reinforced by numerous strong horizontal sheets. *Contributions to the Mechanics of Solids*, Volume Stephen Timoshenko 60th Anniversary.

Wiss, J., 1981. Construction vibrations. State of the Art. *American Society of Civil Engineering, Journal of Geotechnical Engineering*, 107(GT2), pp. 167-181.

Wolf, J. P., 1994. *Foundation vibration analysis using simple physical models*. Upper Saddle River: PTR Prentice Hall.

Woods, R., 1968. *Screening of Surface Waves in Soils*. Michigan: The University of Michigan.

Zwanenburg, C., 2013. De bepaling van sterke-eigenschappen van veen. *Geotechniek*, Volume Juli, pp. 26-32.

APPENDIX A. MATLAB code for decomposition of waves

The wave decomposition technique consists of three files: wave_decomp.m, amplitudes.m and constraint.m. The scripts of the files are presented in the following Boxes.

Box A-1. Main calculation file wave_decomp.m.

```
%%%%%%%%%%%%%% wave_decomp.m %%%%%%%%
%
%% PART I - DECOMPOSITION
%
clear all; close all; clc;
%
set(0,'DefaultFigureWindowStyle','docked')
%
global w t kc ks kr r ra ux uy dd      % Introducing global variables
%
nu = 0.25;                                % Poisson's ratio
alfa = sqrt((1-2*nu)/(2-2*nu));           % Ratio between cs and cc
ro = 20000/9.81;                           % density kg/m3
%
% Calculation of the Rayleigh wave speed to Shear wave speed ratio (cr/cs)
%
e33 = 0.000001;
f33 = 1;
b33 = (1-nu)/8;
%
if nu > 0.1;
while f33>e33;
    a33=b33;
    b33=(1-nu)/(8*(1+a33)*(nu+a33));
    f33=abs(b33-a33);
    e33=e33+e33;
end
%
else
    while f33>e33;
        a33=b33;
        b33=sqrt((1-nu)/(8*(1+a33)*(1+nu/a33)));
        f33=abs(b33-a33);
        e33=e33+e33;
    end
end
%
beta = 1./sqrt(1+a33);                    % Ratio between cr and cs
%
cc = 173.2;                                % Compressional (P) wave velocity
cs = cc*alfa;                             % Shear (S) wave velocity
cr = cs*beta;                            % Rayleigh (R) wave velocity
%
f = 10;                                     % Frequency
w = 2*pi*f;                                % Angular frequency
%
% Ratio of the R-wave amplitudes on the surface Arx/Ary
%
dd = 2*sqrt(1-beta^2)/beta^2 - 2/(sqrt(1-alfa^2*beta^2)*beta^2) ...
    + 1/(sqrt(1-alfa^2*beta^2));
%
kc = w/cc;                                  % Compressional (P) wave number
ks = w/cs;                                % Shear (S) wave number
kr = w/cr;                                % Rayleigh (R) wave number
%
```

Continuation of Box A-1.

```
lc = cc/f;                                % Compression wave length
ls = cs/f;                                % Shear wave length
lr = cr/f;                                % Rayleigh wave length
%
ra = 15:1:24;    % Distance from the centre axis to the measurement points
rpl = 0.2;        % Radius of the plate
r = ra-rpl;      % Distance from the edge of the plate to the measurement p.
%
% Reading Plaxis output data from excel file plaxis_output1.xlsx
%
for i=1:10
    t(:,i) = xlsread('plaxis_output1.xlsx', i, 'K402:K502');    % time values
    uxr(:,i) = xlsread('plaxis_output1.xlsx', i, 'L402:L502'); % horiz. displ.
    uyr(:,i) = xlsread('plaxis_output1.xlsx', i, 'P402:P502'); % vert. displ.
end
%
ux=uxr*10^6;      % Converting to micro-meters
uy=-uyr*10^6;      % Converting to micro-meters and changing the sign of y
%
% Decomposing waves by using an optimisation technique
%
options = optimset('Display','iter','Algorithm','active-set');
%
x0 = [0 0 0 0 0 0]; % initial guess for the unknowns
%
[x,fval] = fmincon(@amplitudes,x0,[],[],[],[],[],[],[],@constraint,options);
%
% Back-Calculation of the superposed wave
%
Upx=x(1);          % Horizontal amplitude of the P-wave
Urx=x(2);          % Horizontal amplitude of the R-wave
Usy=x(3);          % Vertical amplitude of the S-wave
Ury=x(2)/(-dd);    % Vertical amplitude of the R-wave
%
FyC=x(4);          % Phase shift of the P-wave
FyS=x(5);          % Phase shift of the S-wave
FyR=x(6);          % Phase shift of the R-wave
%
% Total back-calculated signals
%
for i=1:10
    uxb(:,i) = Upx*sin(w*t(:,i)-kc*r(i)-FyC)*(ra(1)/ra(i))^1 - ...
                Urx*cos(w*t(:,i)-kr*r(i)-FyR)*(ra(1)/ra(i))^(1/2);
    uyb(:,i) = Usy*sin(w*t(:,i)-ks*r(i)-FyS)*(ra(1)/ra(i))^1 + ...
                Ury*sin(w*t(:,i)-kr*r(i)-FyR)*(ra(1)/ra(i))^(1/2);
end
%
% Back-calculated P-wave
%
for i=1:10
    uxbp(:,i) = Upx*sin(w*t(:,i)-kc*r(i)-FyC)*(ra(1)/ra(i))^1;
end
%
% Back-calculated S-wave
%
for i=1:10
    uybs(:,i) = Usy*sin(w*t(:,i)-ks*r(i)-FyS)*(ra(1)/ra(i))^1;
end
%
% Back-calculated R-wave
%
for i=1:10
    uxbr(:,i) = - Urx*cos(w*t(:,i)-kr*r(i)-FyR)*(ra(1)/ra(i))^(1/2);
    uybr(:,i) = Ury*sin(w*t(:,i)-kr*r(i)-FyR)*(ra(1)/ra(i))^(1/2);
end
```

Continuation of Box A-1.

```

%
% Figures of the total back-calculated signal vs. the Plaxis output
%
figure
plot(t(:,1),uyb(:,1),t(:,1),uy(:,1))      % uy for the 1st measurement point
figure
plot(t(:,1),uxb(:,1),t(:,1),ux(:,1))      % ux for the 1st measurement point
figure
plot(t(:,10),uyb(:,10),t(:,10),uy(:,10)) % uy for the 10th measurement p.
figure
plot(t(:,10),uxb(:,10),t(:,10),ux(:,10)) % ux for the 10th measurement p.
%
% Calculation of the Correlation coefficients at all the measurement points
%
for i=1:10
    uxp = ux(:,i);    % Plaxis ux
    uyp = uy(:,i);    % Plaxis uy
    uxbb = uxb(:,i);  % Plaxis ux
    uybb = uyb(:,i);  % Plaxis uy
%
    R2x = 1 - sum((uxp - uxbb).^2) / sum((uxp-mean(uxp)).^2);
    R2y = 1 - sum((uyp - uybb).^2) / sum((uyp-mean(uyp)).^2);
%
    Rx(i) = R2x;      % Correlation at ith measurement point in x direction
    Ry(i) = R2y;      % Correlation at ith measurement point in y direction
end
%
% Figure of the Correlation factors at different distances
%
figure
plot(ra, Rx, ra, Ry)
xlabel('Distance, [m]');
ylabel('Correlation factor, [-]');
legend('R^2x', 'R^2y');
ylim([0 1]);
%
% Mean Correlation for all the directions and all points
%
meanRx = mean(Rx);      % Mean Correlation factors for horizontal direction
meanRy = mean(Ry);      % Mean Correlation factors for vertical direction
meanR = mean([Rx Ry]);  % Mean Correlation factors for h. and v. directions
%
%% PART II - FUNCTIONS OF AMPLITUDES OF THE WAVES ON ADDITIONAL POINTS
%
Upx=x(1)*10^-6;          % Horizontal amplitude of the P-wave in meters
UrRx=x(2)*10^-6;          % Horizontal amplitude of the R-wave in meters
Usy=x(3)*10^-6;          % Vertical amplitude of the S-wave in meters
UrRy=x(2)/(-dd)*10^-6;    % Vertical amplitude of the R-wave in meters
%
FyC=x(4);                % Phase shift of the P-wave
FyS=x(5);                % Phase shift of the S-wave
FyR=x(6);                % Phase shift of the R-wave
%
r0 = 15;                  % Radius of a sphere on which the additional
                           % points were placed
%
q = sqrt(kr^2-w^2/cc^2);  % Coefficient of the R-wave amplitude function
s = sqrt(kr^2-w^2/cs^2);  % Coefficient of the R-wave amplitude function
%
% R-wave relative amplitude function in depth
%
depth_hor = @(v) (kr*(-exp(-q*v)+2*q*s/(s^2+kr^2)*exp(-s*v))) / ...
                           (kr*(-exp(-q*0)+2*q*s/(s^2+kr^2)*exp(-s*0)));
depth_ver = @(v) (q*(-exp(-q*v)+2*kr^2/(s^2+kr^2)*exp(-s*v))) / ...
                           (q*(-exp(-q*0)+2*kr^2/(s^2+kr^2)*exp(-s*0)));

```

Continuation of Box A-1.

```

%
width = @(h) sqrt(r0./h);
%
% Reading the coordinates of the measurement points on a circle
%
h = xlsread('plaxis_output2.xlsx', 21, 'F2:F21'); % Horizontal distance
v = xlsread('plaxis_output2.xlsx', 21, 'G2:G21'); % Vertical distance
%
teta=atan(h./v); % Angle with vertical line of the point
rad=sqrt(h.^2+v.^2); % Radial distance of the point
%
Arx = depth_hor(v).*Urx; % R-wave amplitudes x in depth
Ary = depth_ver(v).*Ury; % R-wave amplitudes y in depth
%
% Time vector which corresponds with time in plaxis_output2.xlsx
%
tt = xlsread('plaxis_output2.xlsx', 1, 'A2:A102');
%
for j=1:20
    % R-wave displacements in x axis of "j" point
    urxt = - Arx(j)*cos(w*tt-kr*h(j)-FyR)*(ra(1)/h(j))^(1/2);
    %
    % R-wave displacements in y axis of "j" point
    uryt = Ary(j)*sin(w*tt-kr*h(j)-FyR)*(ra(1)/h(j))^(1/2);
    %
    %
    % Plaxis output for "j" point in x axis
    utotx = xlsread('u_total_15.xlsx', j, 'B2:B102');
    %
    % Plaxis output for "j" point in y axis
    utoty = -xlsread('u_total_15.xlsx', j, 'C2:C102');
    %
    uresx = utotx-urxt; % Residual displ. in x axis (Plaxis ux - R ux)
    uresy = utoty-uryt; % Residual displ. in y axis (Plaxis uy - R uy)
    %
    % Projecting residual displacements into the directions of P- and
    % S-waves
    %
    for i=1:length(tt),
        u_compr(i,j)= uresx(i) * sin(teta(j)) + uresy(i)*cos(teta(j));
        u_shear(i,j)= -uresx(i) * cos(teta(j)) + uresy(i)*sin(teta(j));
    end
end
%
% Calculating the amplitudes of the P- and S-waves on the "j" points
%
for j=1:20
    amp_c(j) = (max(u_compr(:,j))-min(u_compr(:,j)))/2;
    amp_s(j) = (max(u_shear(:,j))-min(u_shear(:,j)))/2;
end
%
% Checking the back-calculated P- and S-waves on a "j" point
%
j=7; % Selecting a desirable points "j"

u_back_c=amp_c(j)*sin(w*tt-kc*rad(j)-FyC); % Back-calculated P-wave
u_back_s=amp_s(j)*sin(w*tt-ks*rad(j)-FyS); % Back-calculated S-wave
%
figure
plot(tt,u_shear(:,j),tt,u_back_s);
figure
plot(tt,u_compr(:,j),tt,u_back_c);
%
%% PART III - CALCULATION OF THE ENERGY IN WAVES
%

```

Continuation of Box A-1.

```

pc_Ar=polyfit(teta,amp_c',6);    % 6th order polynomial fit for the P-wave
pc_At=polyfit(teta,amp_s',6);    % 6th order polynomial fit for the S-wave
%
% Functions of the P, S and R-wave on the radius r0
%
funC = @(x) ((pc_Ar(1).*x.^6 + pc_Ar(2).*x.^5 + pc_Ar(3).*x.^4 + ...
    pc_Ar(4).*x.^3 + pc_Ar(5).*x.^2 + pc_Ar(6).*x + ...
    pc_Ar(7))).^2.*sin(x)*r0;
funS = @(x) ((pc_At(1).*x.^6 + pc_At(2).*x.^5 + pc_At(3).*x.^4 + ...
    pc_At(4).*x.^3 + pc_At(5).*x.^2 + pc_At(6).*x + ...
    pc_At(7))).^2.*sin(x)*r0;
funR = @(y) ((kr*(-exp(-q*y)+2*q*s/(s^2+kr^2)*exp(-s*y))) / ...
    (kr*(-exp(-q*0)+2*q*s/(s^2+kr^2)*exp(-s*0))).*Urx).^2 + ...
    ((q*(-exp(-q*y)+2*kr^2/(s^2+kr^2)*exp(-s*y))) / ...
    (q*(-exp(-q*0)+2*kr^2/(s^2+kr^2)*exp(-s*0))).*Ury).^2;
%
tta=0:0.01:pi/2;    % Step of the angle
%
C=funC(tta);        % P-wave amplitudes
S=funS(tta);        % S-wave amplitudes
EC=C.^2;            % P-wave amplitudes^2
ES=S.^2;            % S-wave amplitudes^2
%
[yc,xc] = sph2cart(tta, 0, 15);
[ys,xs] = sph2cart(tta, 0, 15);
%
[cy1,cx1] = sph2cart(tta, 0, 10^12*C+15);
[sy2,sx2] = sph2cart(tta, 0, 10^12*S+15);
%
[ecy1,ecx1] = sph2cart(tta, 0, 10^24*EC+15);
[esy2,esx2] = sph2cart(tta, 0, 10^24*ES+15);
%
plot(xc,-yc,cx1,-cy1);
xlabel('Horizontal distance, [m]');
ylabel('Vertical distance, [m]');
legend('15 m', 'P-wave |amplitudes| * 10^1^2');
%
figure
plot(xs,-ys,sx2,-sy2);
xlabel('Horizontal distance, [m]');
ylabel('Vertical distance, [m]');
legend('15 m', 'S-wave |amplitudes| * 10^1^2');
%
figure
plot(xc,-yc,ecx1,-ecy1);
xlabel('Horizontal distance, [m]');
ylabel('Vertical distance, [m]');
legend('15 m', 'P-wave |amplitudes|^2 * 10^2^4');
%
figure
plot(xs,-ys,esx2,-esy2);
xlabel('Horizontal distance, [m]');
ylabel('Vertical distance, [m]');
legend('15 m', 'S-wave |amplitudes|^2 * 10^2^4');
%
% Energy in the basic waves
%
Ec = 0.5*ro*w^2*quad(funcC,0,(pi/2))*(2*pi*r0*lc);    % P-wave energy
Es = 0.5*ro*w^2*quad(funS,0,(pi/2))*(2*pi*r0*ls);    % S-wave energy
Er = 0.5*ro*w^2*quad(funR,0,3*lr)*(2*pi*r0*lr);      % R-wave energy
%
E = Er + Es + Ec; % Total energy
%%%%% End of wave_decomp.m %%%%%%

```

Box A-2. Optimisation function amplitudes.m.

```

function f=amplitudes(x)
%
global w t kc ks kr r ra ux uy dd
%
for i=1:length(t)
%
    for j=1:10
        ux_c(i,j) = x(1)*sin(w*t(i)-kc*r(j)-x(4))*(ra(1)/ra(j))^1 - ...
                     x(2)*cos(w*t(i)-kr*r(j)-x(6))*(ra(1)/ra(j))^(1/2);
    end
%
    for j=1:10
        uy_c(i,j) = x(3)*sin(w*t(i)-ks*r(j)-x(5))*(ra(1)/ra(j))^1 + ...
                     x(2)/(-dd)*sin(w*t(i)-kr*r(j)-x(6))*(ra(1)/ra(j))^(1/2);
    end
end
%
f=(sum(sum((ux-ux_c).^2)) + sum(sum((uy-uy_c).^2)));

```

Box A-3. Optimisation constrains function constraint.m.

```

function [c, ceq] = constraint(x)
%
ceq = [];
c = [];

```

APPENDIX B. Technical data of vibrators and geophones

Two electric 4-poles vibrators (model A10-9.0-4 from Eviro) were used for the shaker. An exploded view is presented in the figure below.

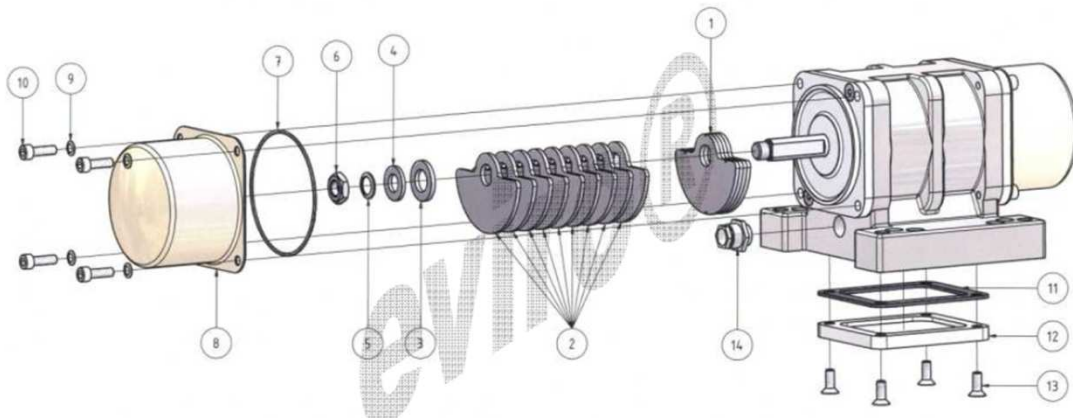


Figure B-1. Exploded view of A10-90-4 vibrator (eviro.com).

The properties of the vibrator can be found in the following table.

Table B-1. Technical data sheet for A10-9.0-4 vibrator from Eviro.

Technical feature	Marking	Dimensions	Value
Max. eccentric moment	M_e	[kgcm]	8,32
Max. centrifugal force	F	[kN]	1,03
Rated voltage	U_N	[V]	400
Power consumption	P	[kW]	0,18
Rated current	I_N	[A]	0,34
Power factor	$\cos\varphi$	[\cdot]	0,78
Ratio starting / Rated current	I_A/I_N	[\cdot]	2,3
Rated mains frequency	f_N	[Hz]	50
Max. speed (at rated mains frequency)	n_N	[rpm]	1500
Number of poles	-	[\cdot]	4
Total mass	M	[kg]	8,1
Motor length	X	[mm]	281

Seven 3D geophones were used (showed in a) of Figure B-2), which consist of three seismic detectors: one DS11-4.5-VT (vertical) and two DS11-4.5-HT (horizontal) (showed in b) of Figure B-2).

The technical data of the DS11-4.5 can be found in Table B-2. Output vs. Frequency respons chart is presented in Figure B-3.



a)

b)

Figure B-2. a) three dimensional geophone; b) seismic detector GS-11D; (not to scale).

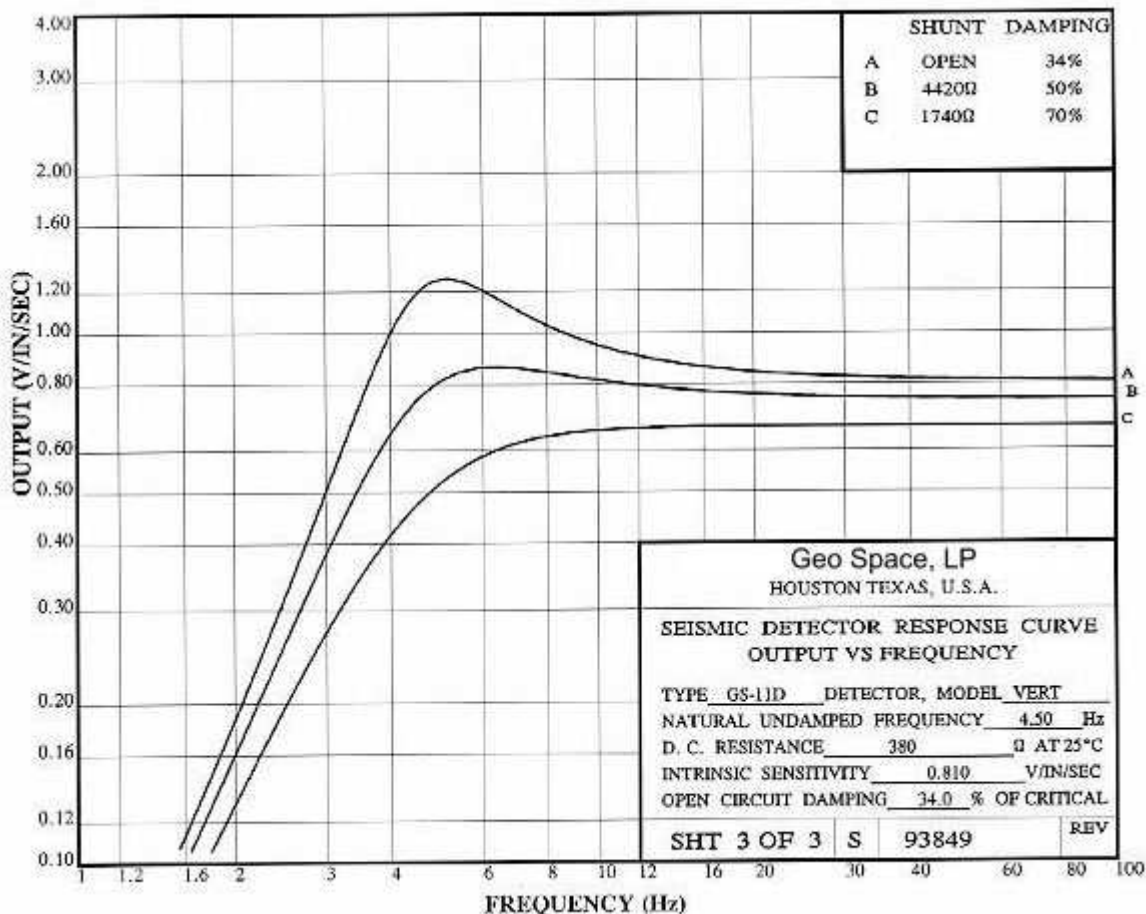


Figure B-3. GS-11D seismic detector response curve. Output vs. frequency chart.

Table B-2. Technical data sheet for A10-9.0-4 vibrator from Eviro.

Technical feature	Dimensions	Value
Natural frequency	[Hz]	4.5 ± 0.75
Coil Resistance @ 25° C (± 5 %)	[Ohm]	380
Intrinsic Voltage Sensitivity with 380 Ohm Coil ± 10 %	[V/cm/s]	0.32
Normalised Transduction Constant	[V/in/s]	0.42 sq. root of Rc
Open Circuit Damping	[-]	0.34 ± 20 %
Damping Constant with 380 Ohm Coil	[-]	762
Optional Coil Resistances ± 5 %	[Ohm]	4000
Moving Mass ± 5 %	[g]	23.6
Typical Case to Coil Motion P-P	[cm]	0.18
Height	[cm]	3.35
Diameter	[cm]	3.18
Weight	[g]	111

APPENDIX C. Vibration measurements on peat site

Hereby the radial and vertical vibrations (from the vibration tests on a peaty site) of every geophone are presented. For the first two geophones (1 meter and 2 meters away from the shaker respectively) also the measurements of the transversal vibrations are showed.

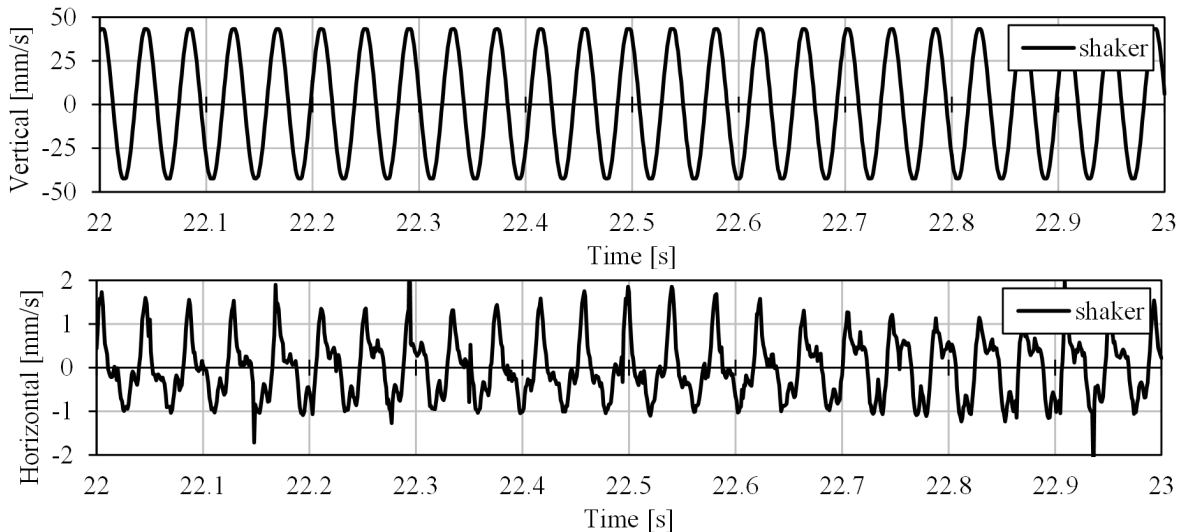


Figure C-1. Shaker Vibrations.

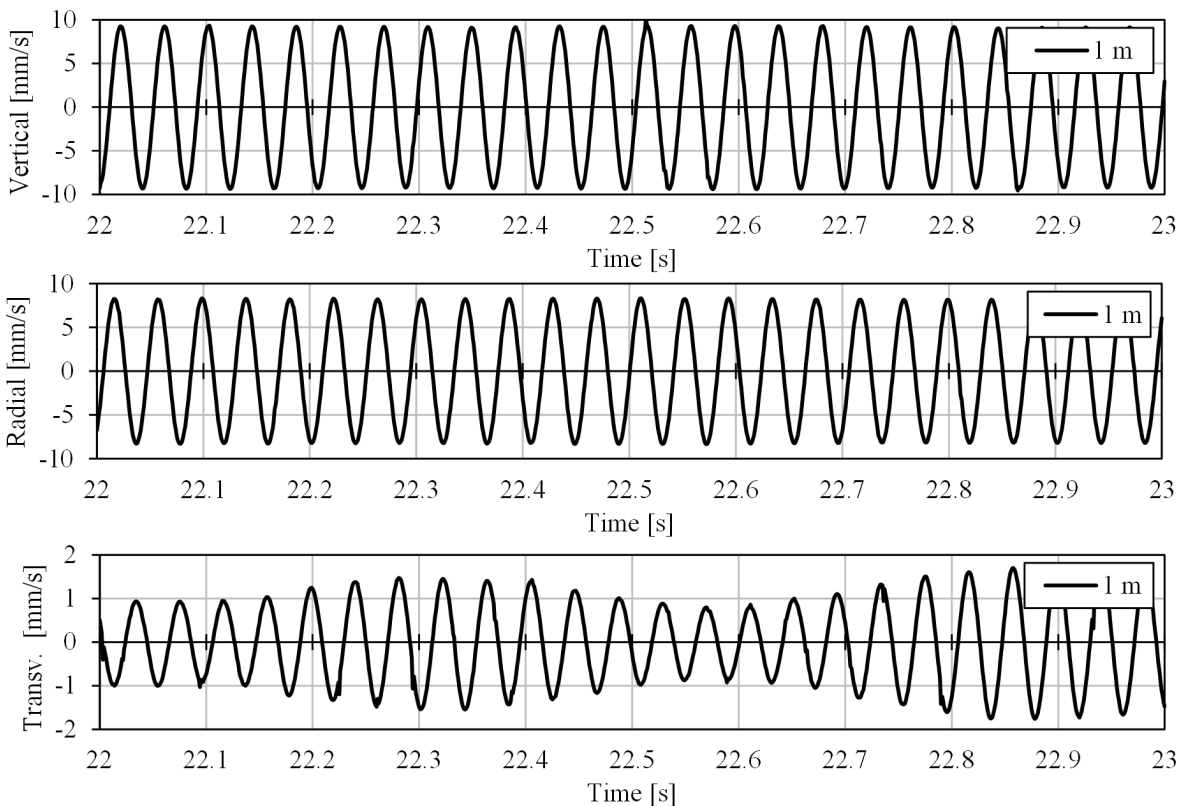


Figure C-2. Surface vibrations 1 m away from the shaker.

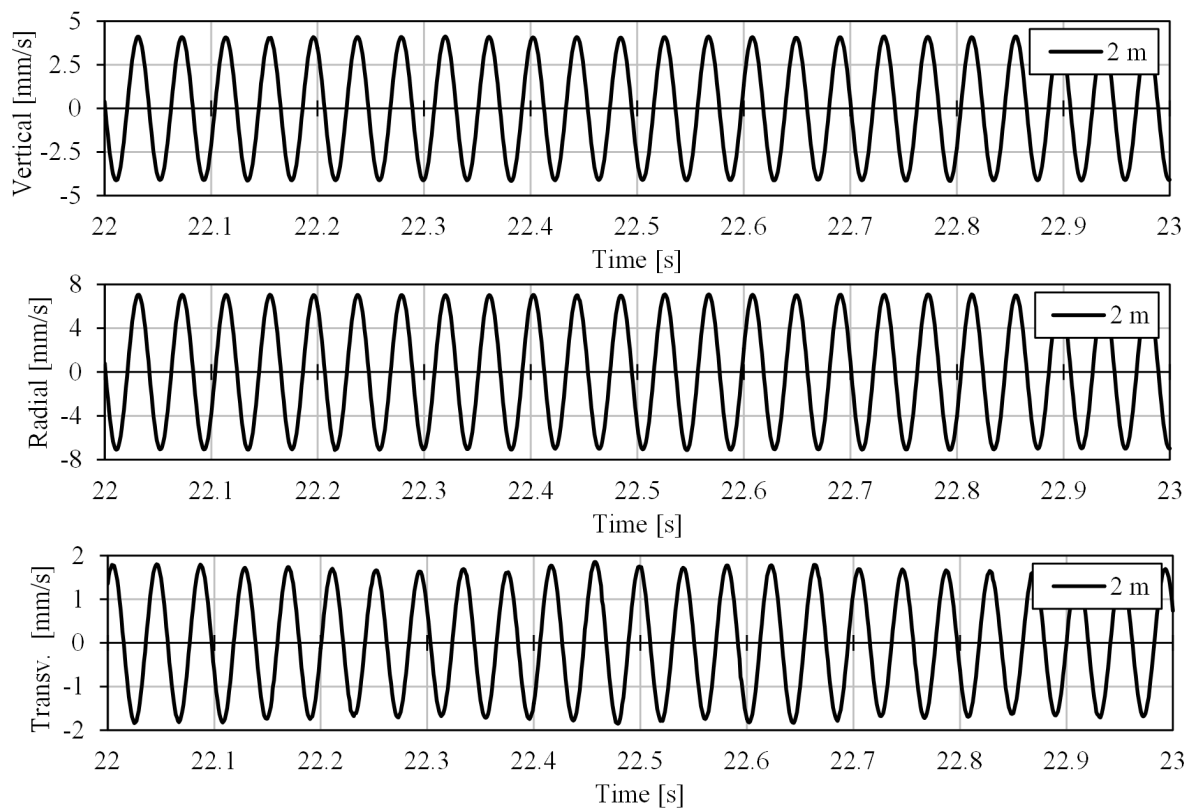


Figure C-3. Surface vibrations 2 m away from the shaker.

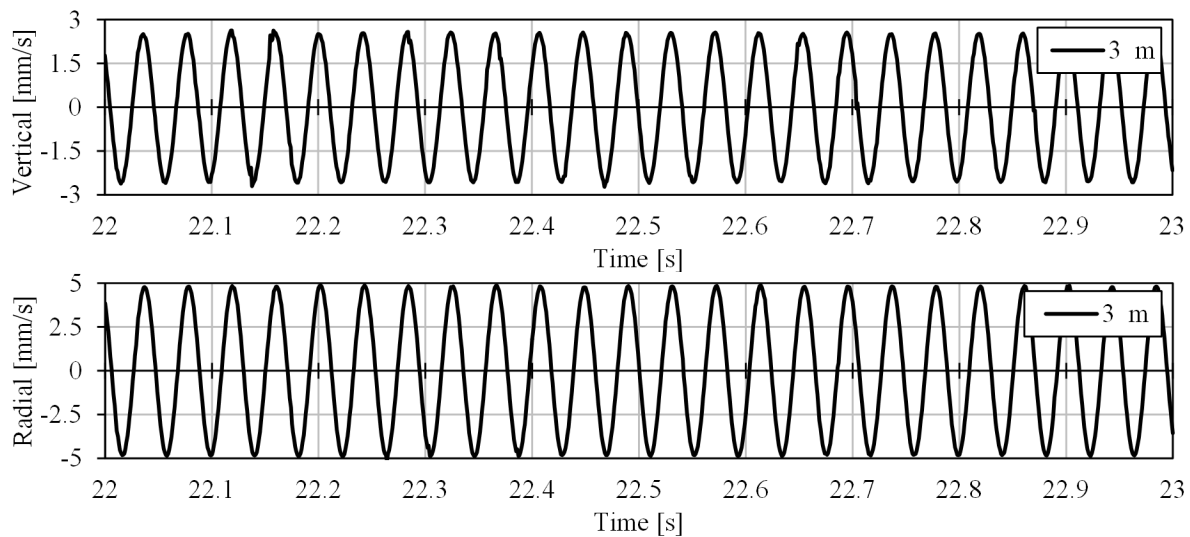


Figure C-4. Surface vibrations 3 m away from the shaker.

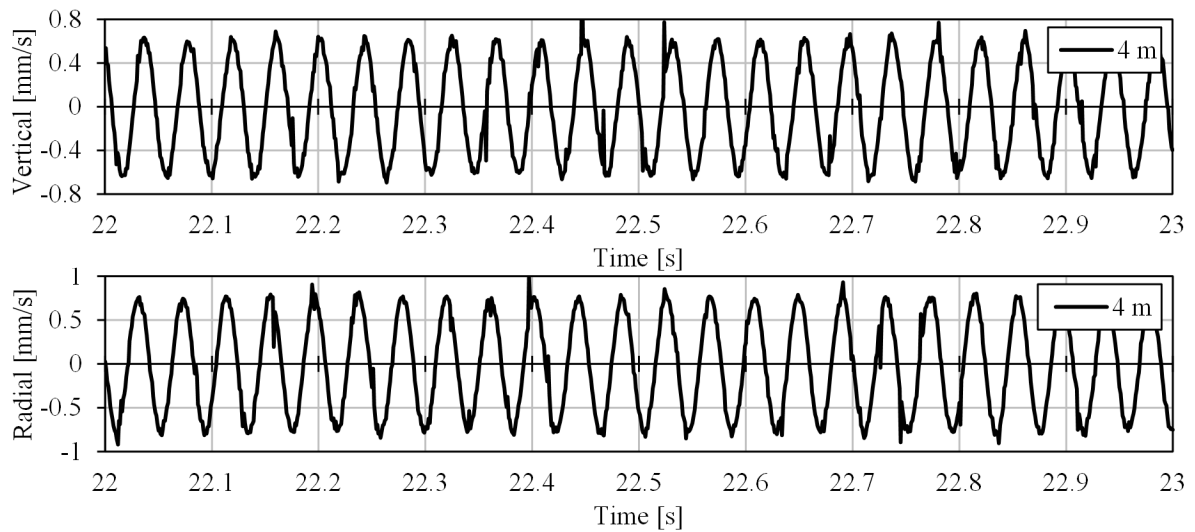


Figure C-5. Surface vibrations 4 m away from the shaker.

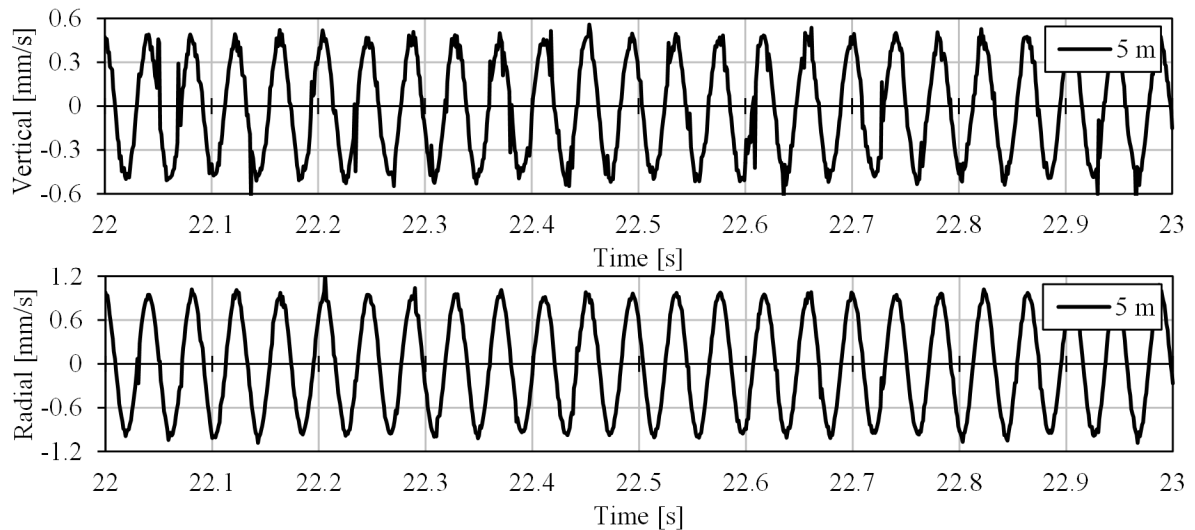


Figure C-6. Surface vibrations 5 m away from the shaker.

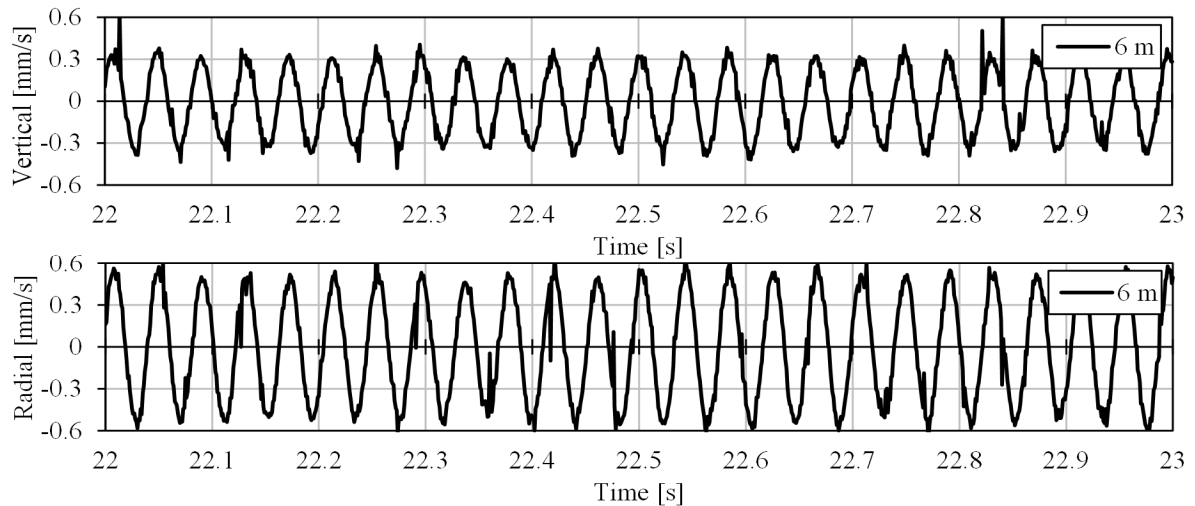


Figure C-7. Surface vibrations 6 m away from the shaker.

APPENDIX D. Developed vibration prediction method comparison with FEM results

Hereby all forty plots (according to the table below) of the comparison between the vertical vibrations obtained by FE modelling and the calculations by the improved prediction method are presented.

Table D-1. Matrix of the numerical calculations with numbers of the corresponding figures.

$B \backslash a_0$	0.179	0.269	0.359	0.449	0.538	0.628	0.718	0.897	1.077	1.346
0.5	D-1	D-2	D-3	D-4	D-5	D-6	D-7	D-8	D-9	D-10
1	D-11	D-12	D-13	D-14	D-15	D-16	D-17	D-18	D-19	D-20
2	D-21	D-22	D-23	D-24	D-25	D-26	D-27	D-28	D-29	D-30
5	D-31	D-32	D-33	D-34	D-35	D-36	D-37	D-38	D-39	D-40

Table D-2. Matrix of the average errors in percentages.

$B \backslash a_0$	0.179	0.269	0.359	0.449	0.538	0.628	0.718	0.897	1.077	1.346
0.5	4.9	5	4.3	5.6	4.7	5.5	5.9	8.3	14.3	8
1	4.7	5.8	5	6.7	5.2	6.1	6.2	7.5	9.5	4.7
2	4.8	5.5	6.2	8.3	6.1	5.3	3.7	5.6	6.6	6
5	5	6.7	10.9	4.9	13.7	9.8	9.2	5.3	4.7	5.5

Table D-3. Matrix of the maximum errors in percentages.

$B \backslash a_0$	0.179	0.269	0.359	0.449	0.538	0.628	0.718	0.897	1.077	1.346
0.5	10.6	10	9.7	12.8	9.6	11	13	19.9	24.1	22.3
1	10	10.5	10.9	13.6	10.8	14.4	14.6	18.7	20.3	11.9
2	11.5	9.6	13.9	15.3	11.9	10.8	7.7	12.6	24.1	12.7
5	10.7	13.3	19.1	9.8	22	19.1	15.9	13.2	14.4	14.4

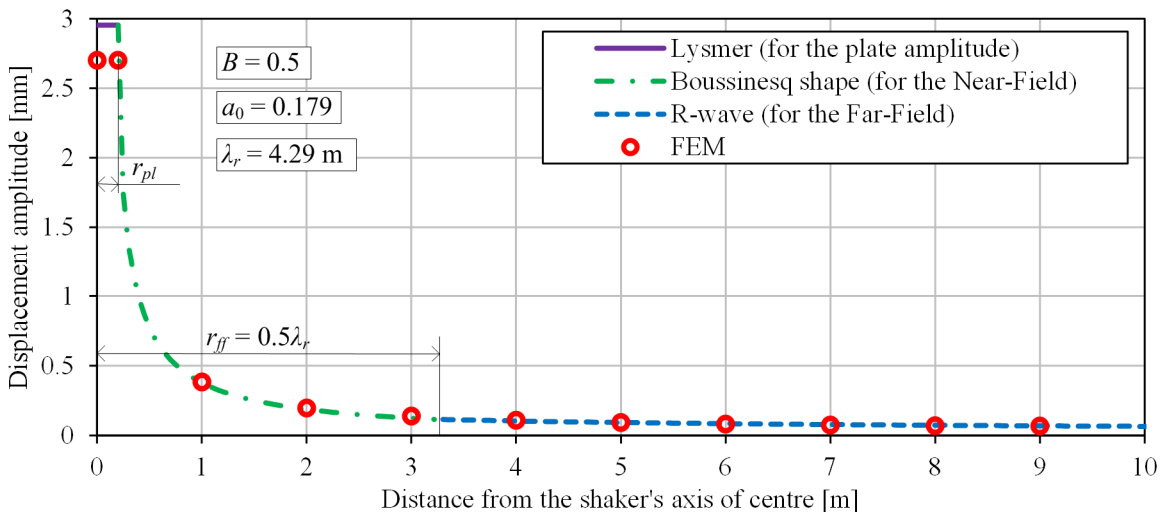


Figure D-1. Vertical vibration amplitudes of the surface ($B = 0.5$, $a_0 = 0.179$).

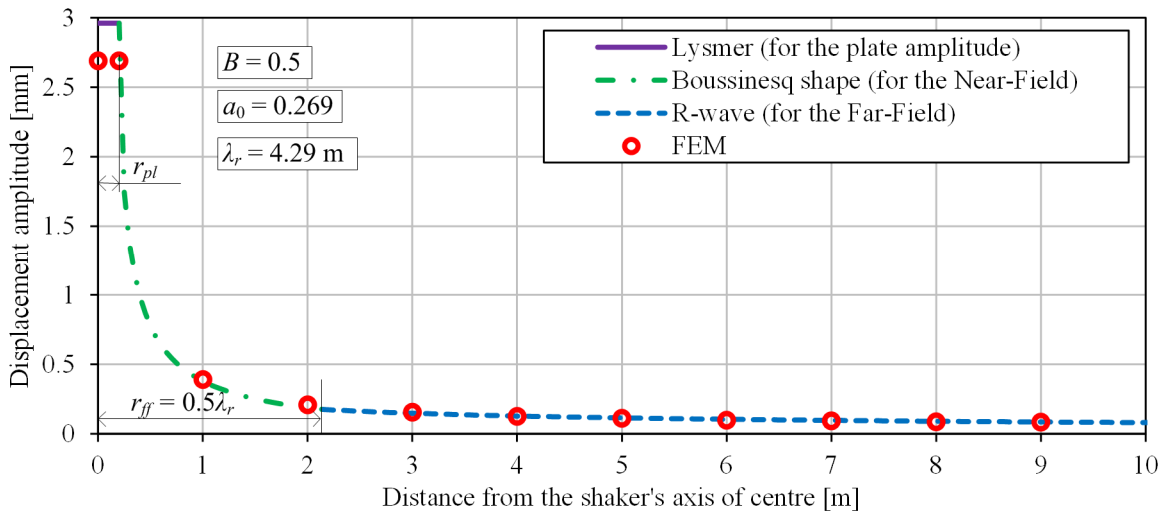


Figure D-2. Vertical vibration amplitudes of the surface ($B = 0.5$, $a_0 = 0.269$).

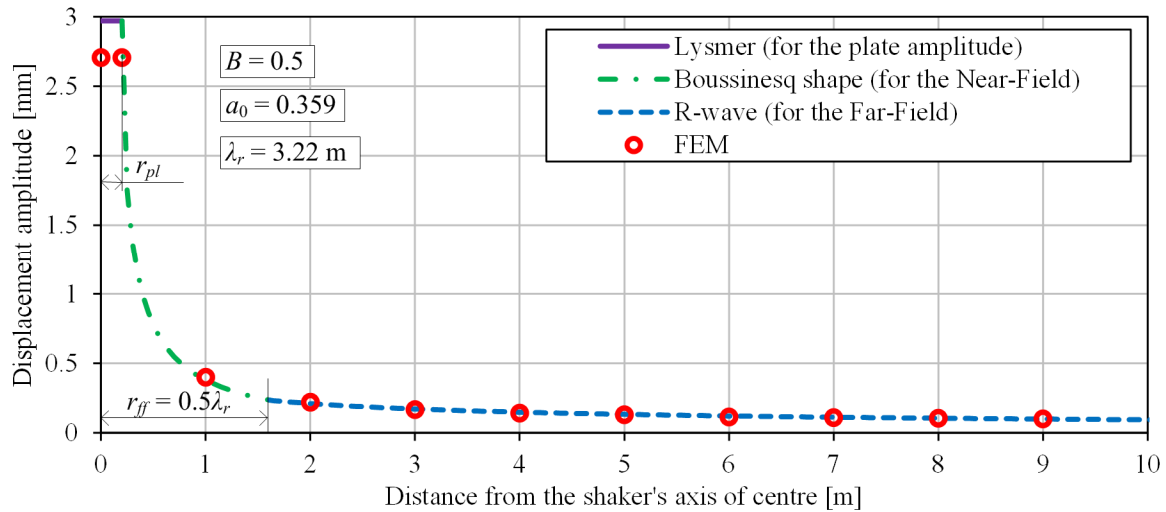


Figure D-3. Vertical vibration amplitudes of the surface ($B = 0.5$, $a_0 = 0.359$).

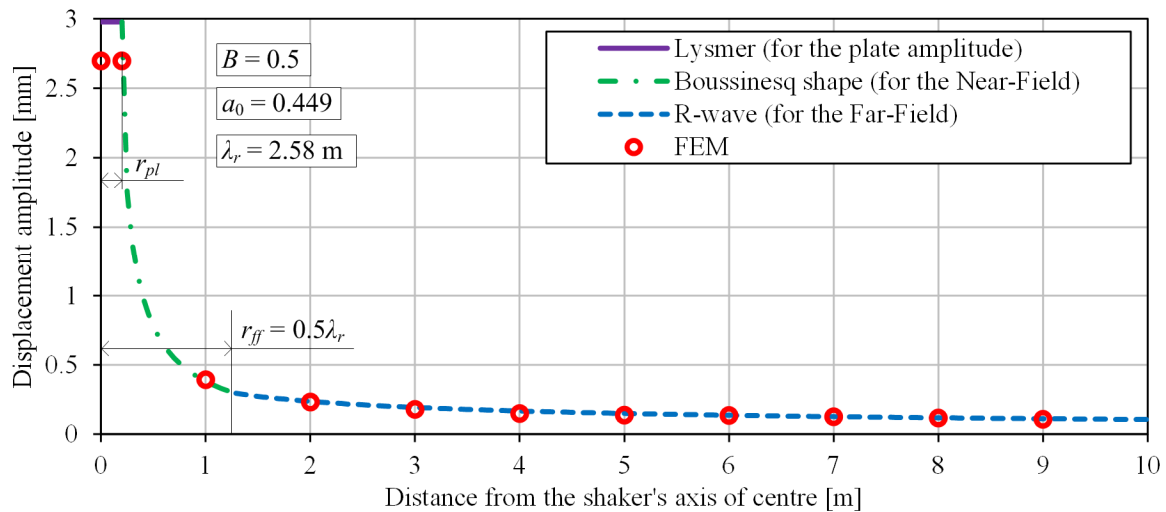


Figure D-4. Vertical vibration amplitudes of the surface ($B = 0.5$, $a_0 = 0.449$).

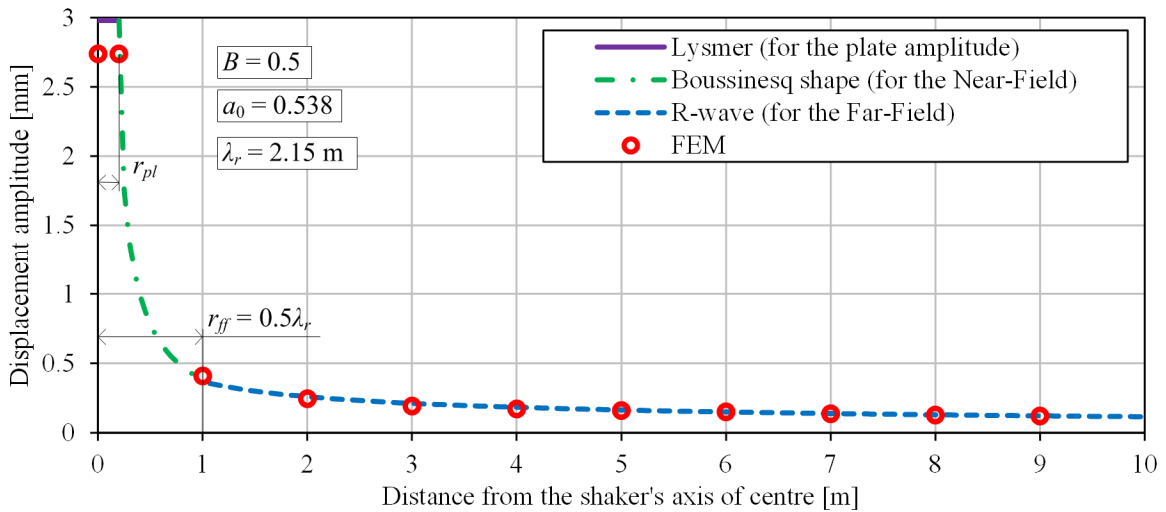


Figure D-5. Vertical vibration amplitudes of the surface ($B = 0.5$, $a_0 = 0.538$).

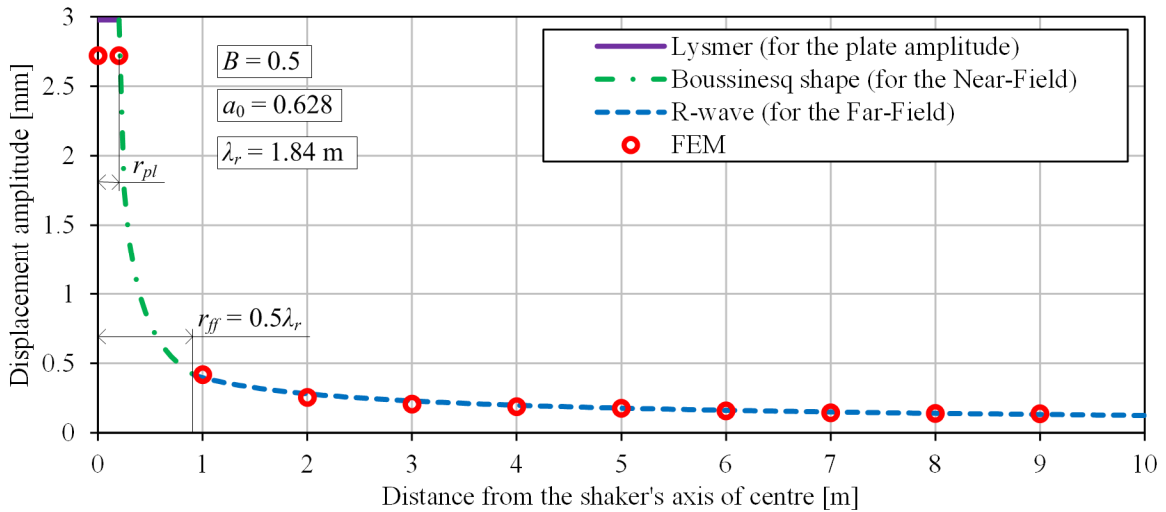


Figure D-6. Vertical vibration amplitudes of the surface ($B = 0.5$, $a_0 = 0.628$).

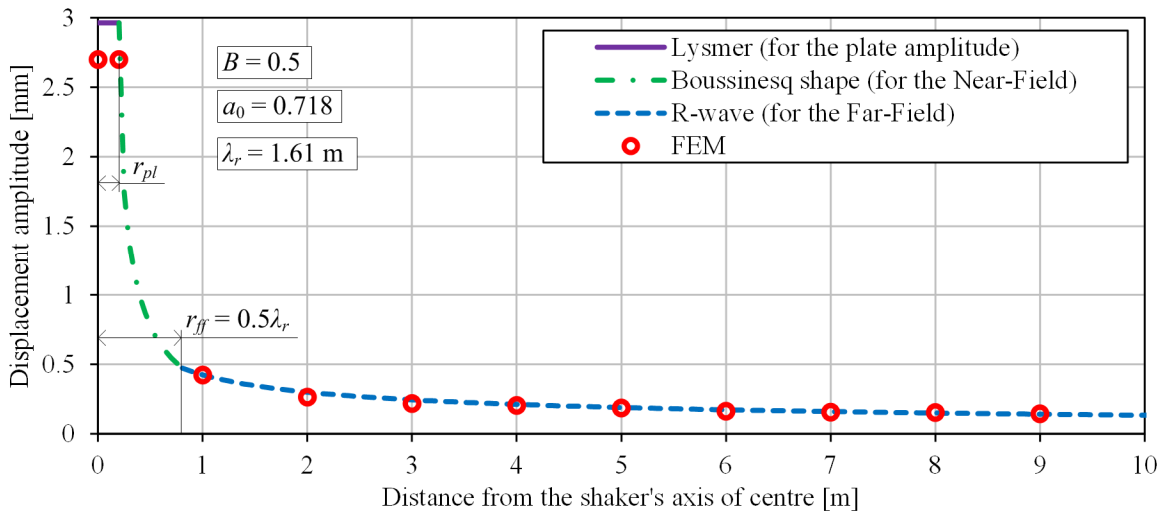


Figure D-7. Vertical vibration amplitudes of the surface ($B = 0.5$, $a_0 = 0.718$).

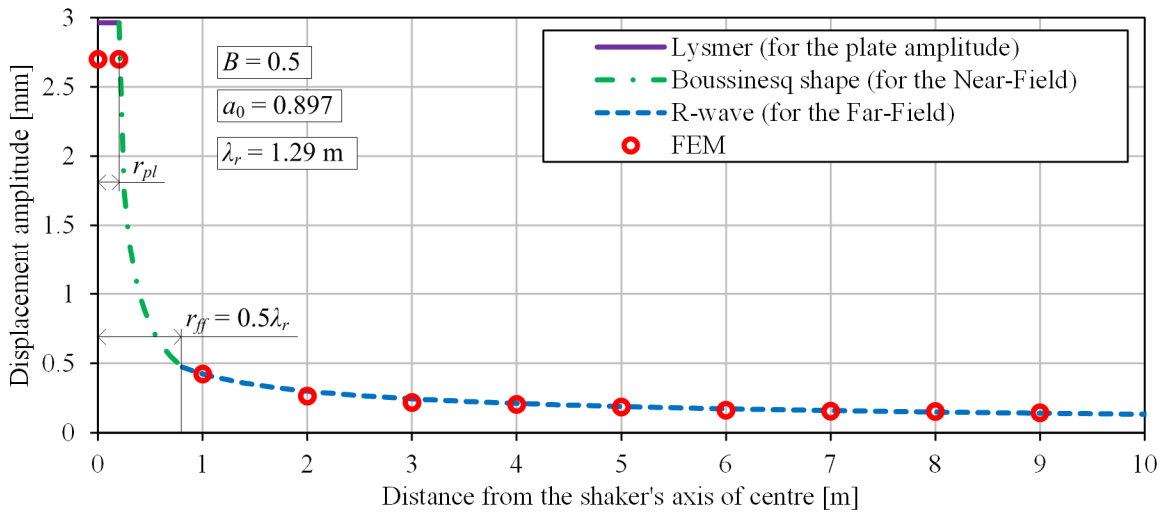


Figure D-8. Vertical vibration amplitudes of the surface ($B = 0.5$, $a_0 = 0.897$).

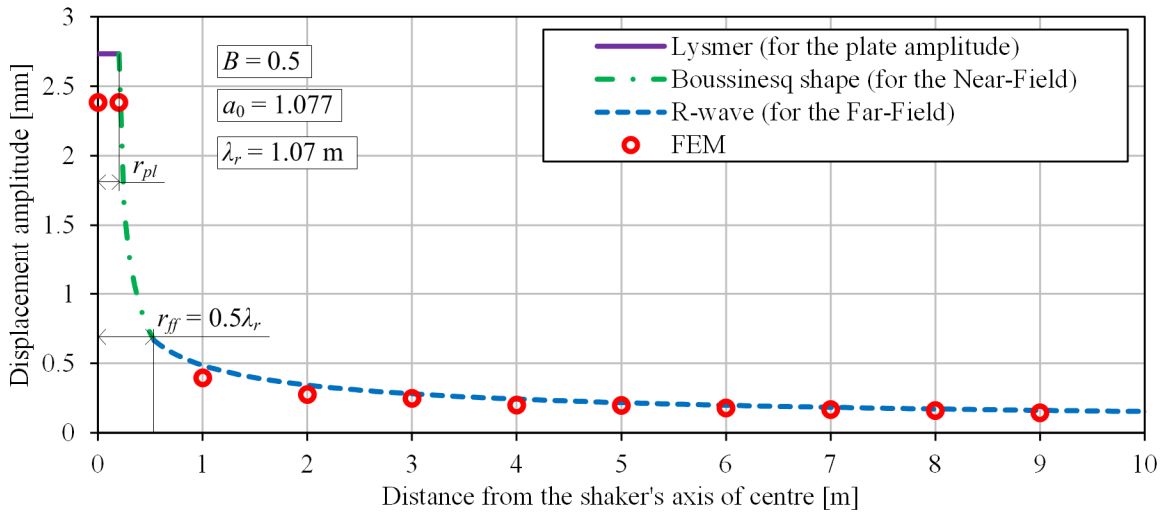


Figure D-9. Vertical vibration amplitudes of the surface ($B = 0.5$, $a_0 = 1.077$).

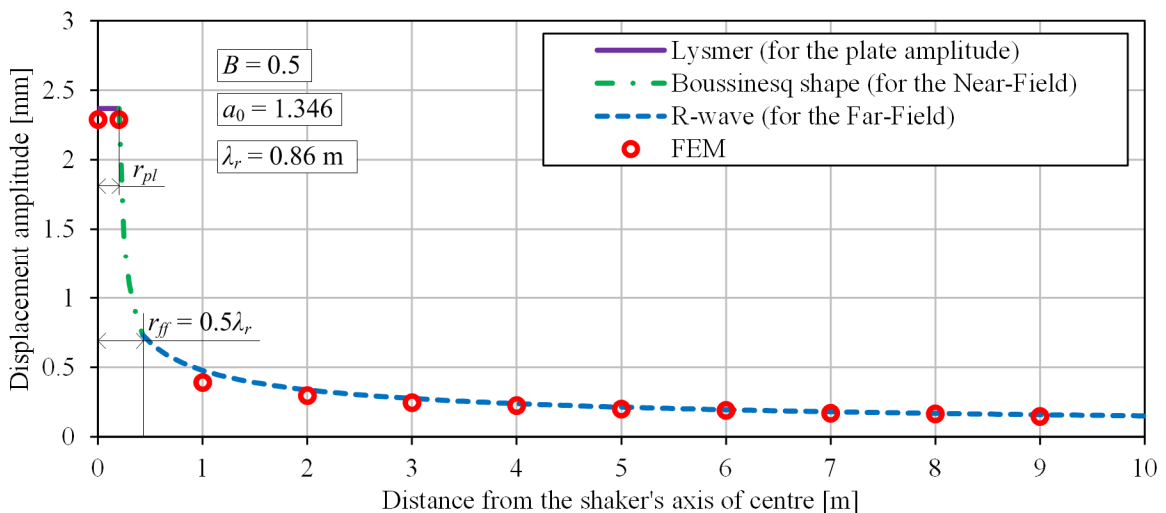


Figure D-10. Vertical vibration amplitudes of the surface ($B = 0.5$, $a_0 = 1.346$).

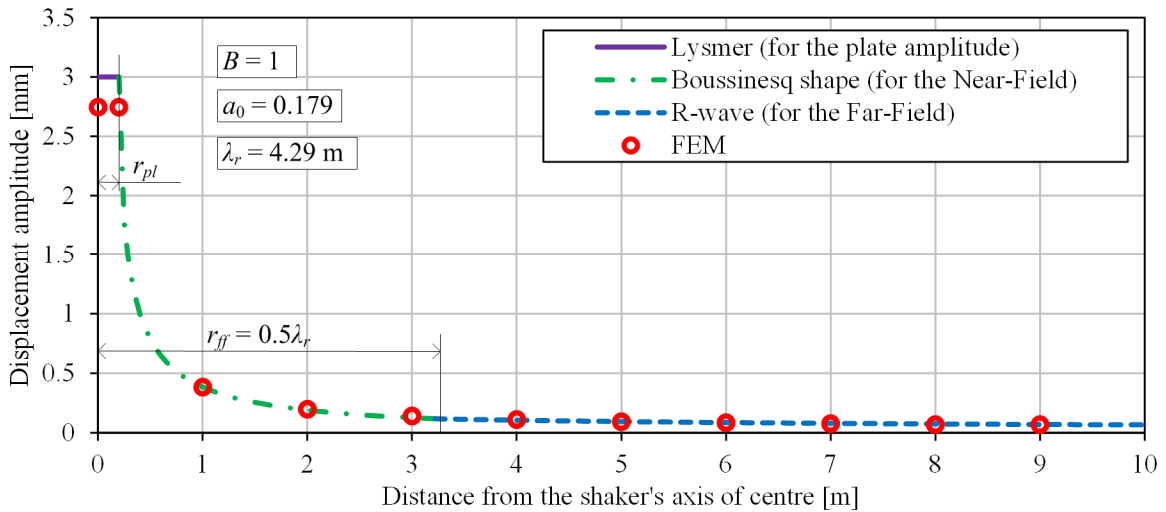


Figure D-11. Vertical vibration amplitudes of the surface ($B = 1$, $a_0 = 0.179$).

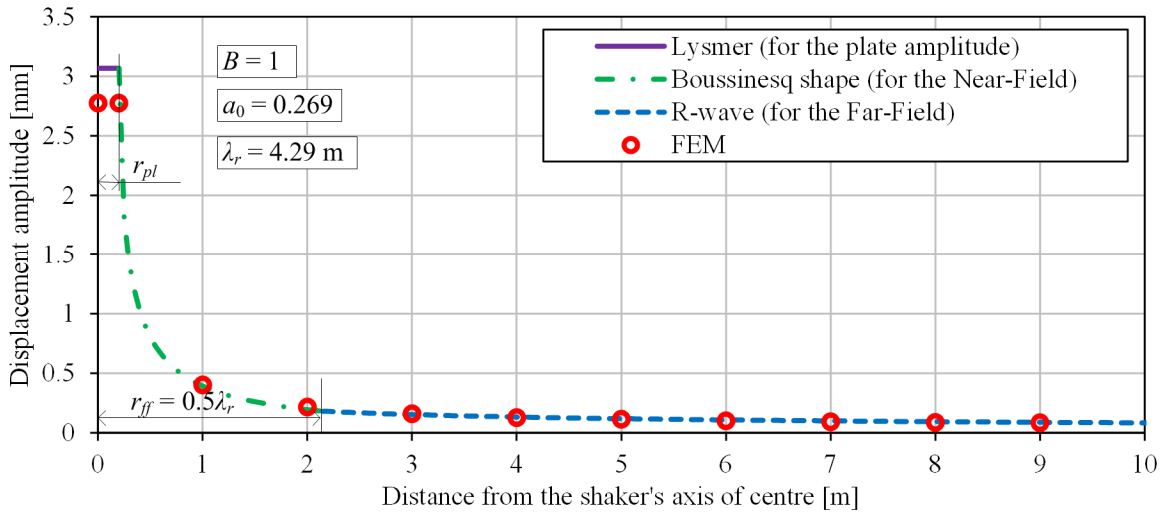


Figure D-12. Vertical vibration amplitudes of the surface ($B = 1$, $a_0 = 0.269$).

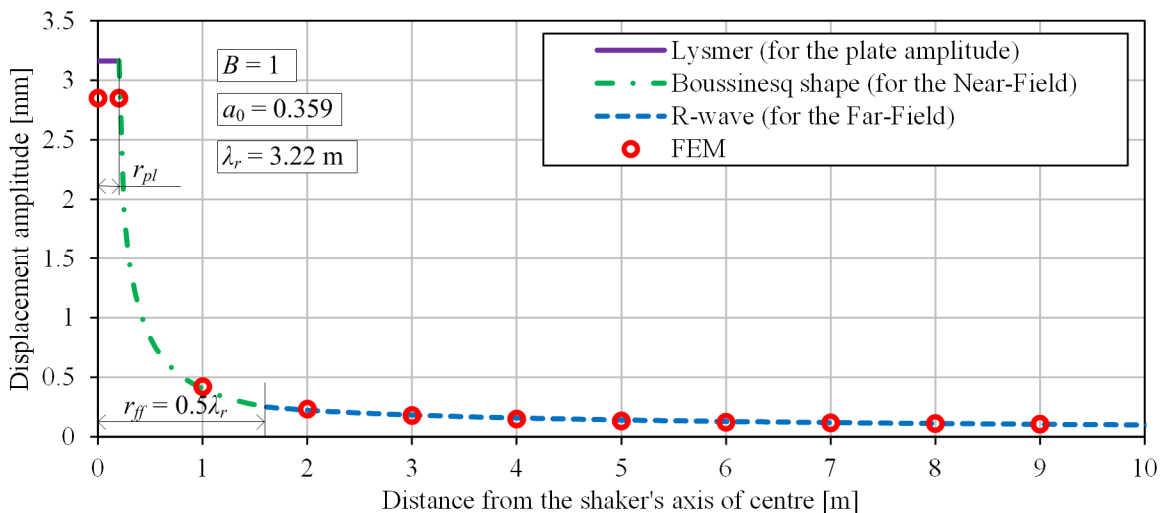


Figure D-13. Vertical vibration amplitudes of the surface ($B = 1$, $a_0 = 0.359$).

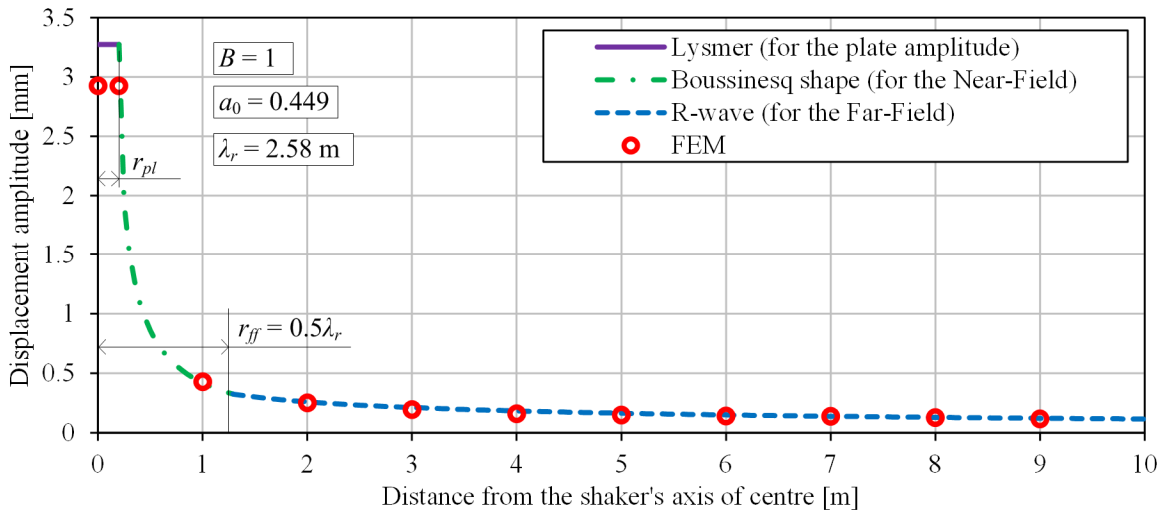


Figure D-14. Vertical vibration amplitudes of the surface ($B = 1$, $a_0 = 0.449$).

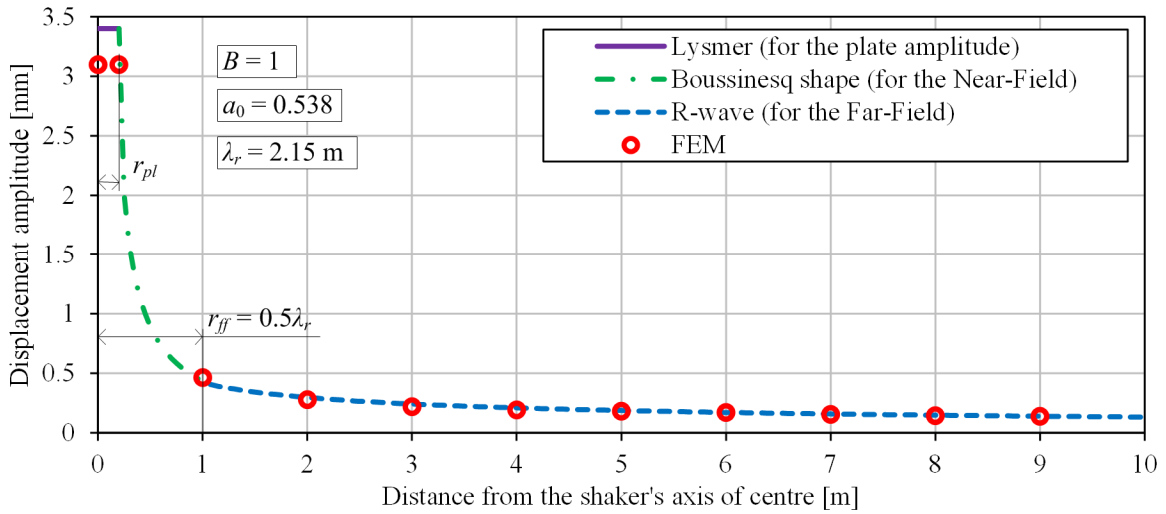


Figure D-15. Vertical vibration amplitudes of the surface ($B = 1$, $a_0 = 0.538$).

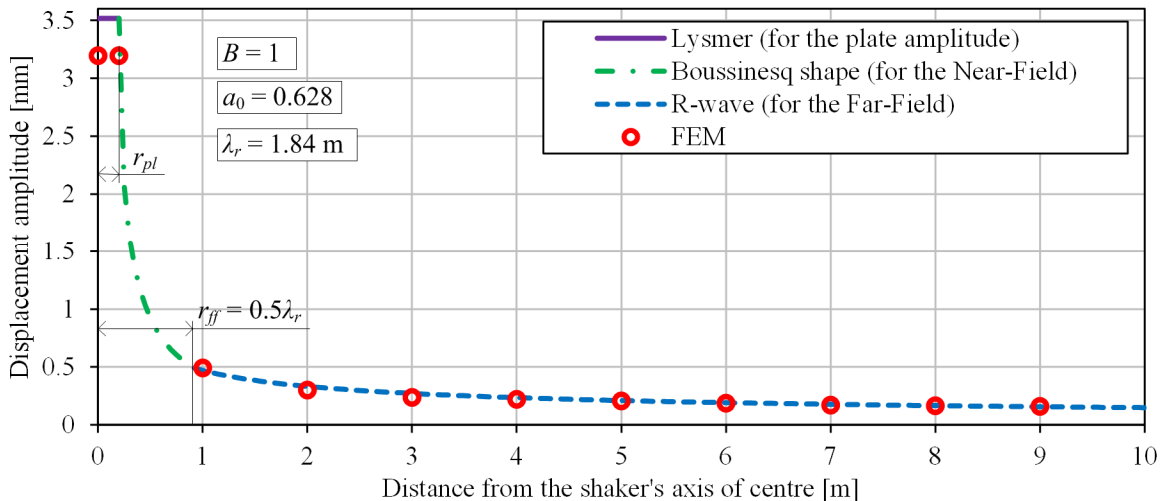


Figure D-16. Vertical vibration amplitudes of the surface ($B = 1$, $a_0 = 0.628$).

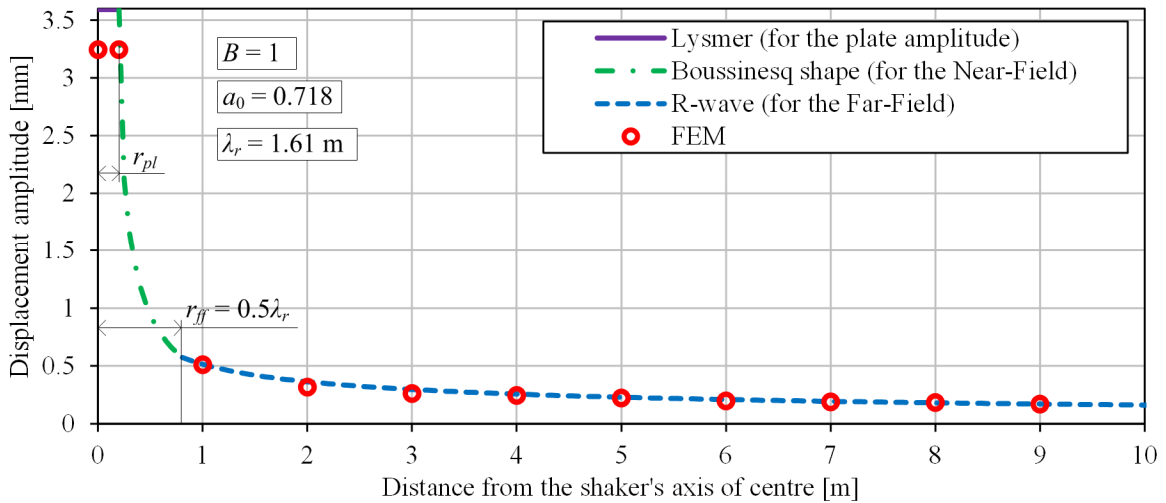


Figure D-17. Vertical vibration amplitudes of the surface ($B = 1$, $a_0 = 0.718$).

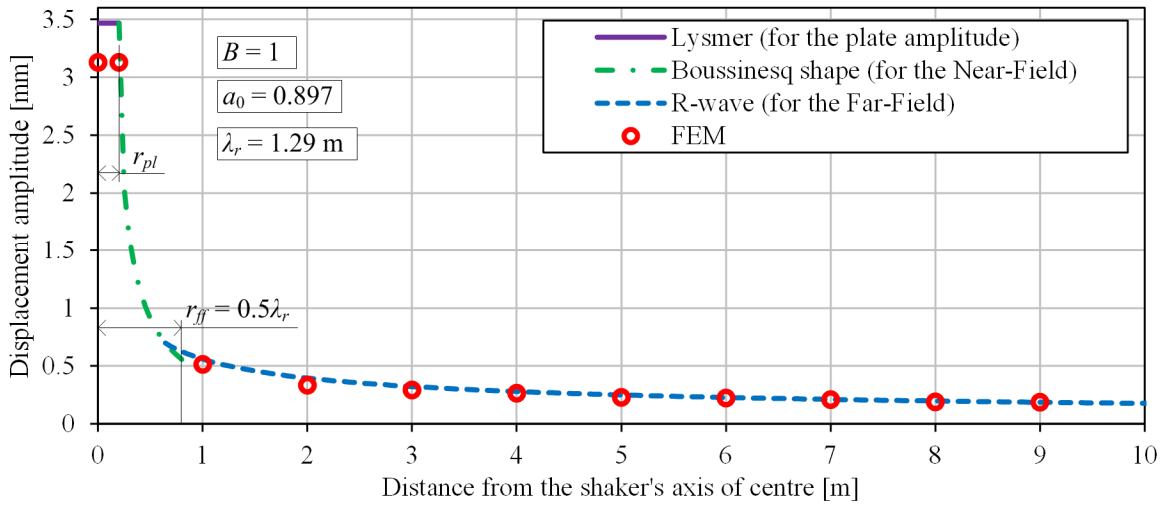


Figure D-18. Vertical vibration amplitudes of the surface ($B = 1$, $a_0 = 0.897$).

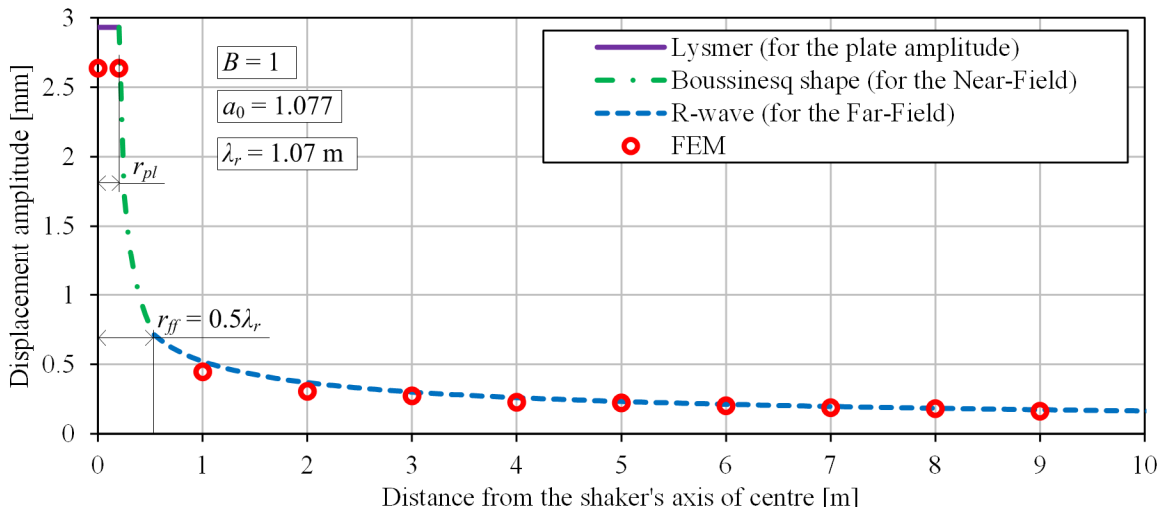


Figure D-19. Vertical vibration amplitudes of the surface ($B = 1$, $a_0 = 1.077$).

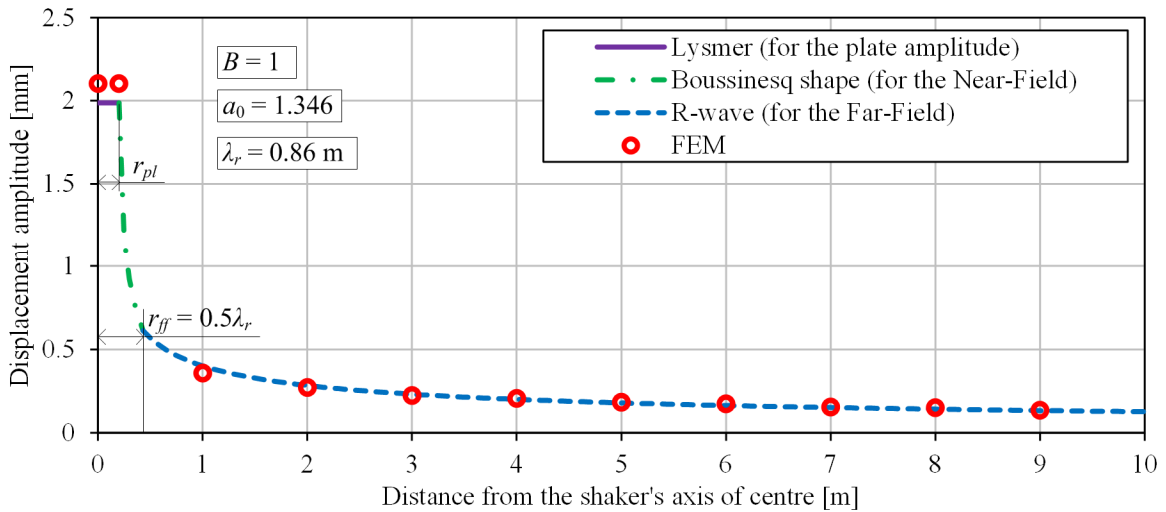


Figure D-20. Vertical vibration amplitudes of the surface ($B = 1, a_0 = 1.346$).

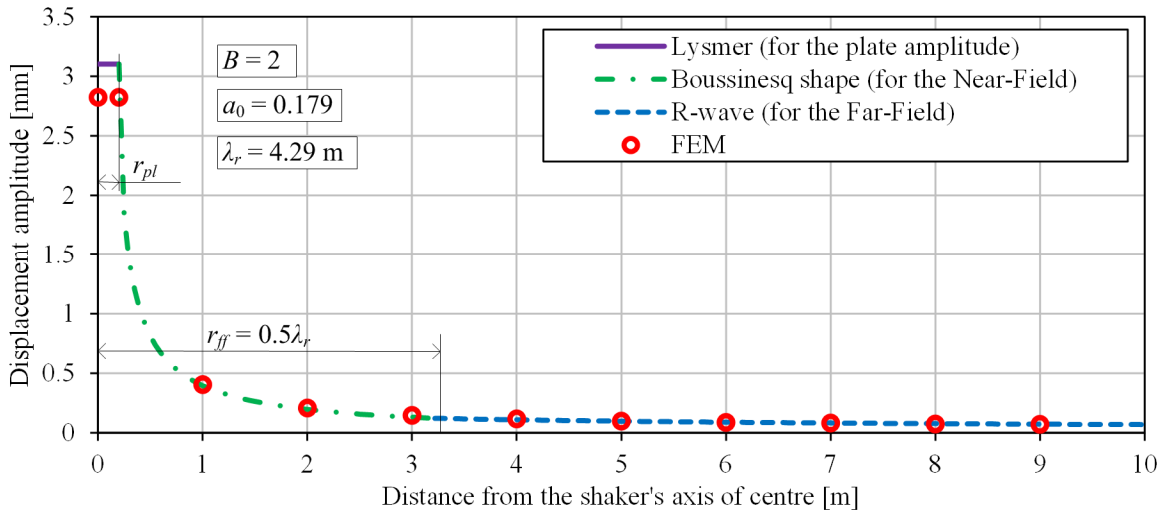


Figure D-21. Vertical vibration amplitudes of the surface ($B = 2, a_0 = 0.179$).

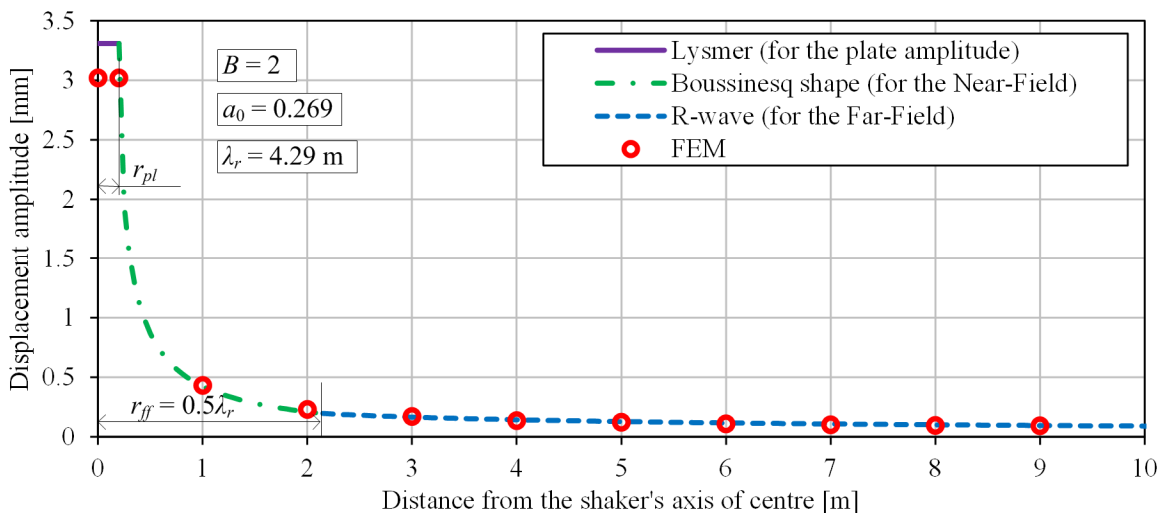


Figure D-22. Vertical vibration amplitudes of the surface ($B = 2, a_0 = 0.269$).

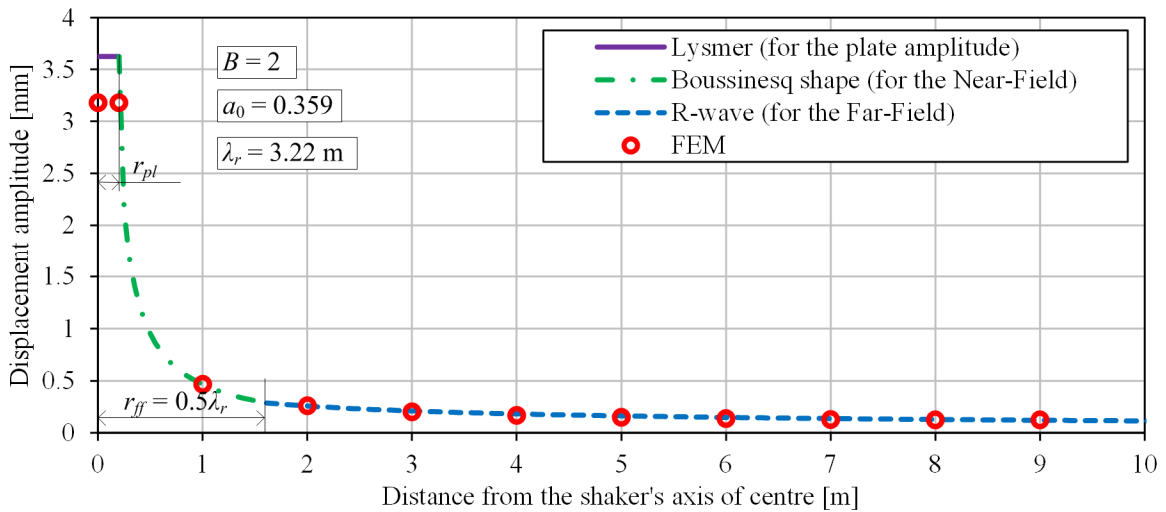


Figure D-23. Vertical vibration amplitudes of the surface ($B = 2$, $a_0 = 0.359$).

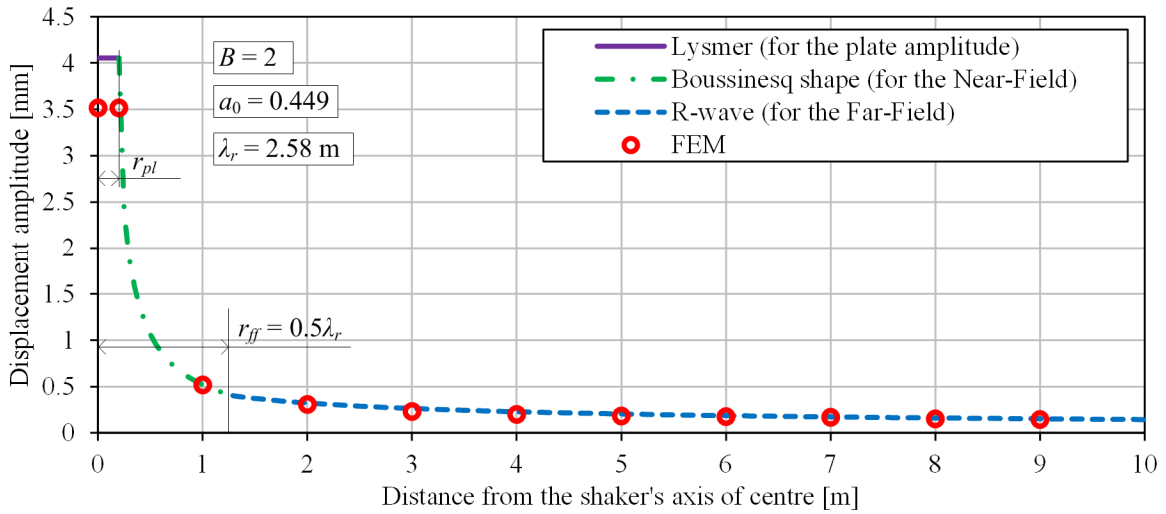


Figure D-24. Vertical vibration amplitudes of the surface ($B = 2$, $a_0 = 0.449$).

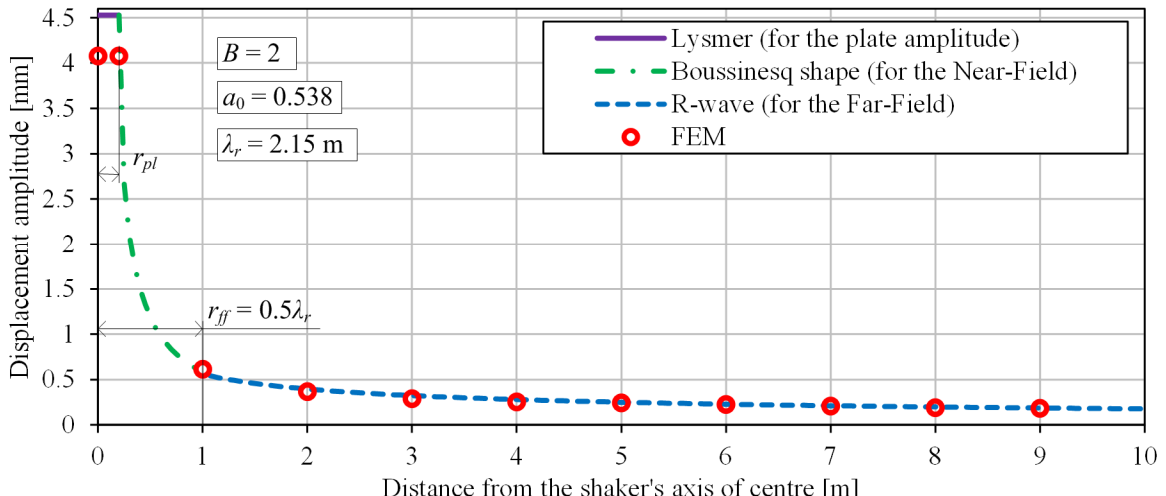


Figure D-25. Vertical vibration amplitudes of the surface ($B = 2$, $a_0 = 0.538$).

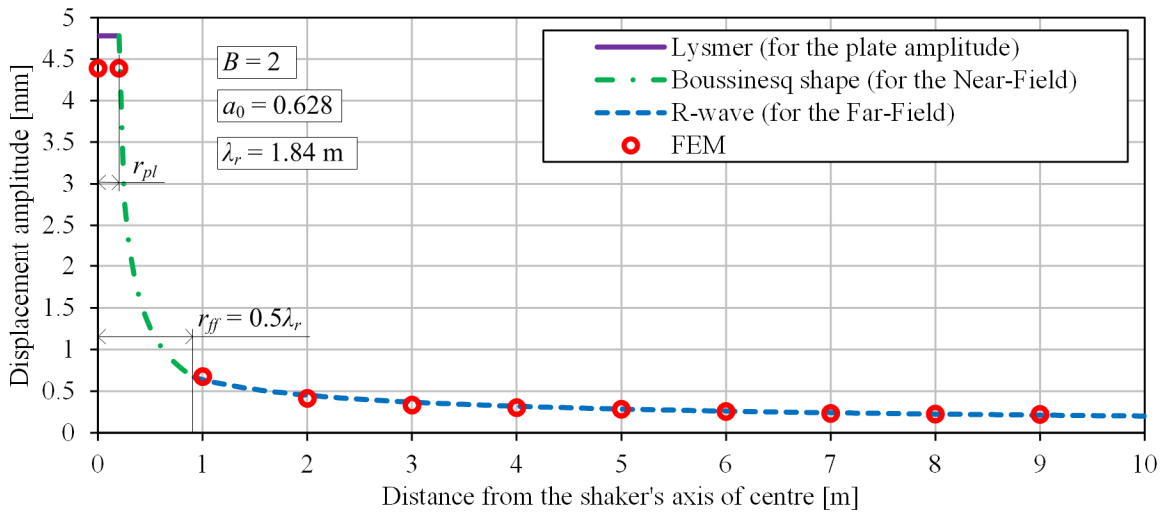


Figure D-26. Vertical vibration amplitudes of the surface ($B = 2, a_0 = 0.628$).

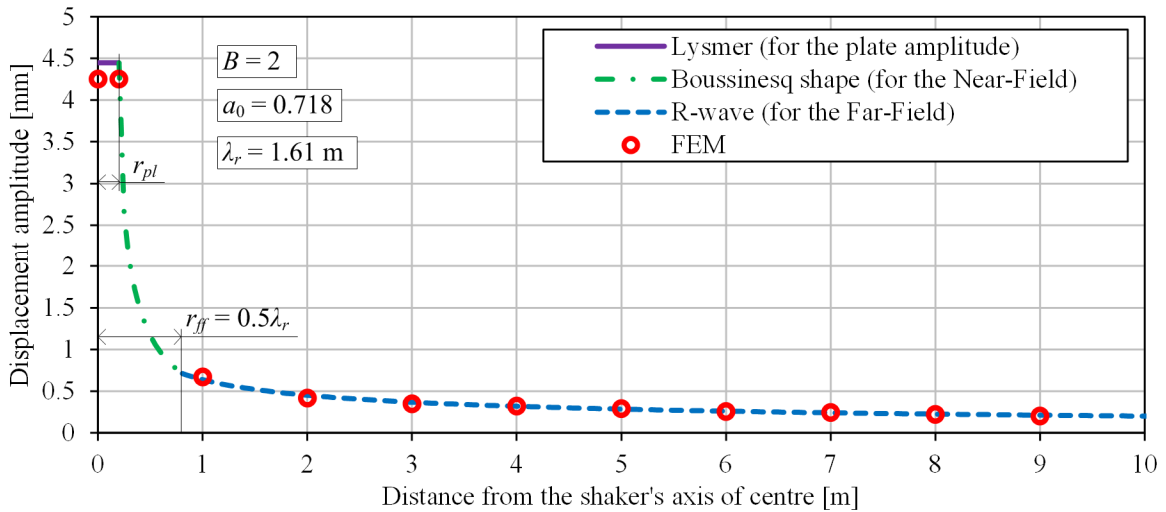


Figure D-27. Vertical vibration amplitudes of the surface ($B = 2, a_0 = 0.718$).

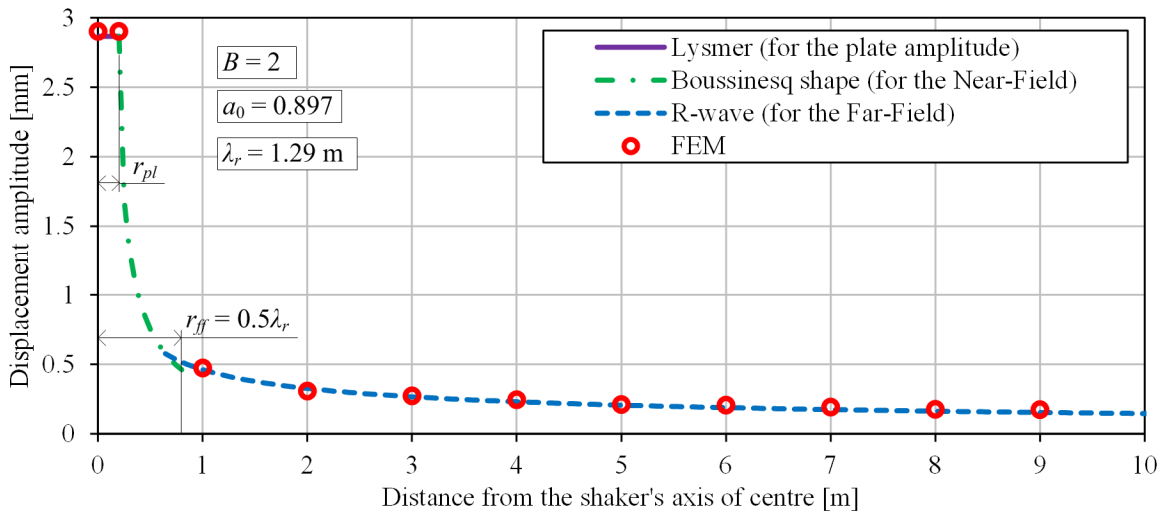


Figure D-28. Vertical vibration amplitudes of the surface ($B = 2, a_0 = 0.897$).

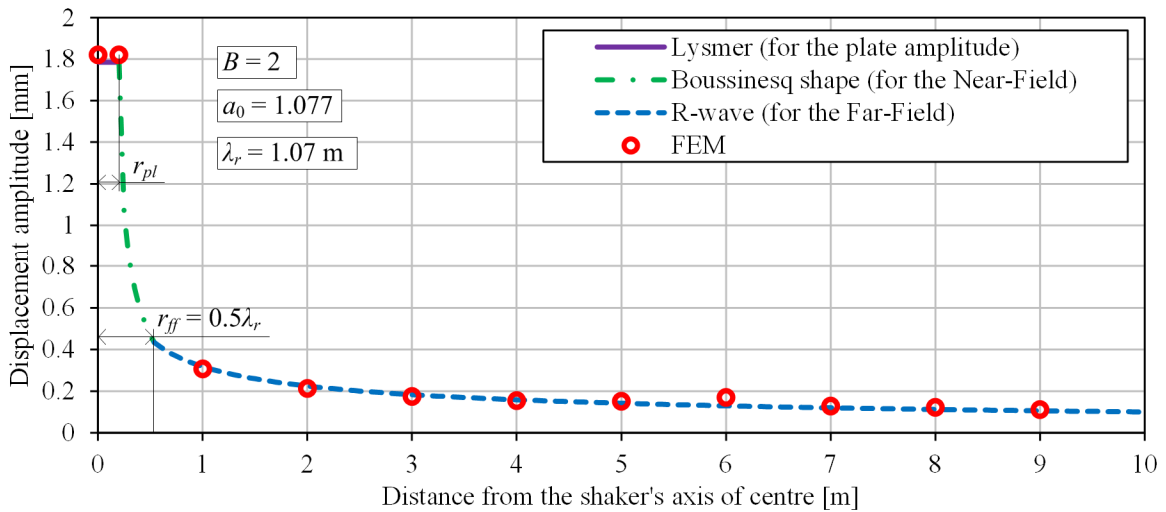


Figure D-29. Vertical vibration amplitudes of the surface ($B = 2$, $a_0 = 1.077$).

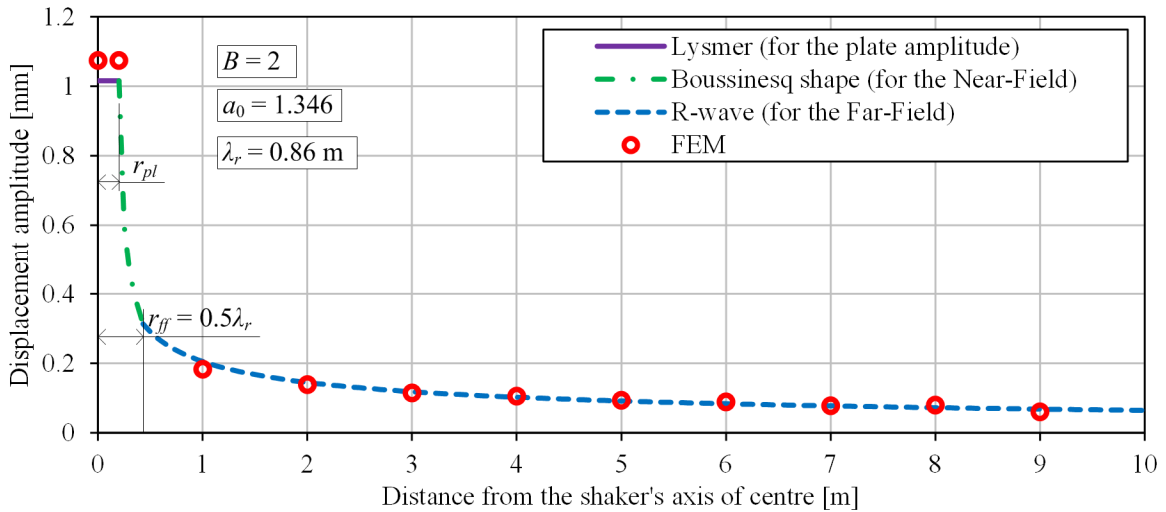


Figure D-30. Vertical vibration amplitudes of the surface ($B = 2$, $a_0 = 1.346$).

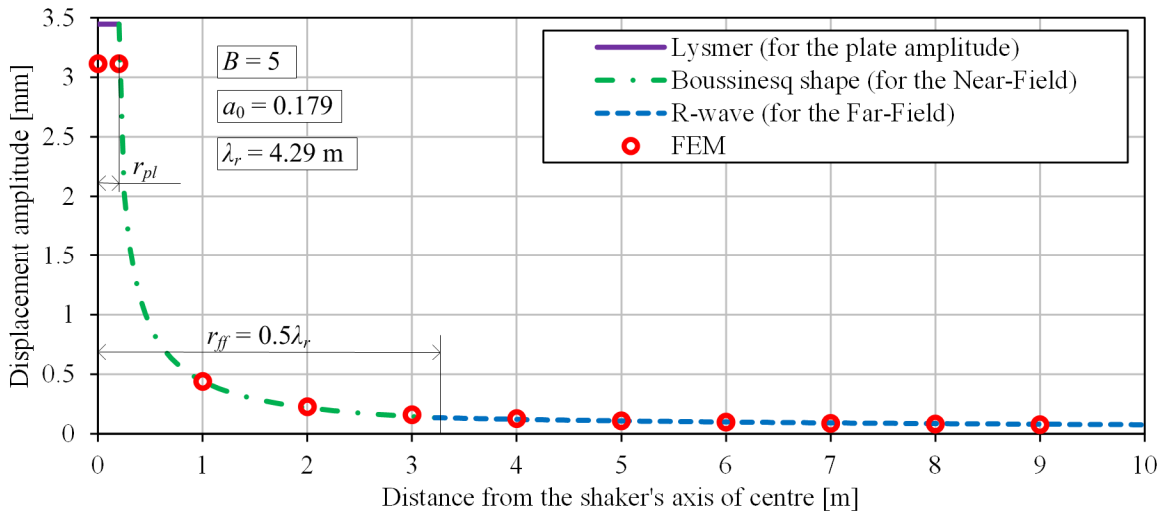


Figure D-31. Vertical vibration amplitudes of the surface ($B = 5$, $a_0 = 0.179$).

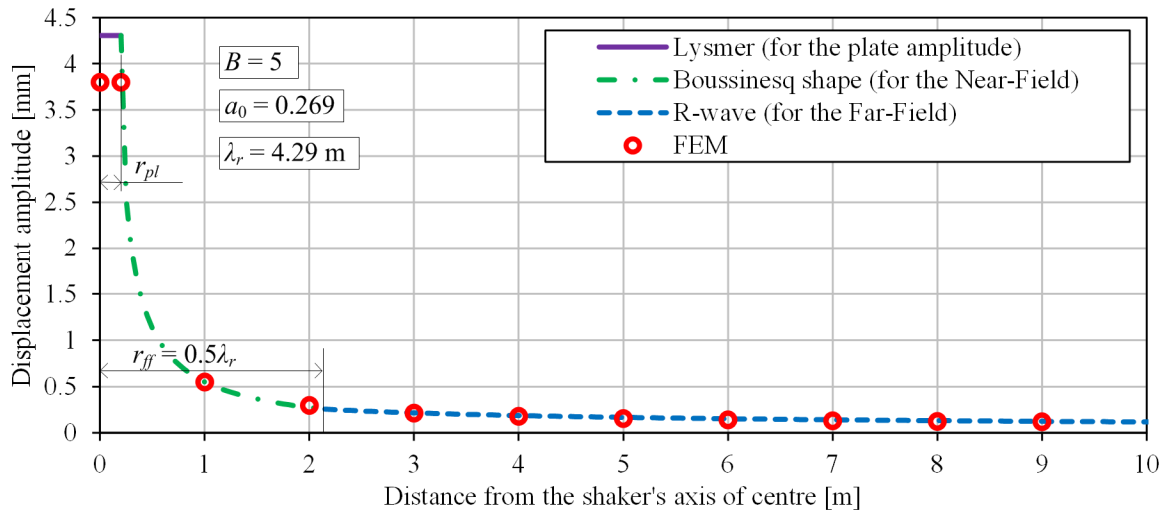


Figure D-32. Vertical vibration amplitudes of the surface ($B = 5$, $a_0 = 0.269$).

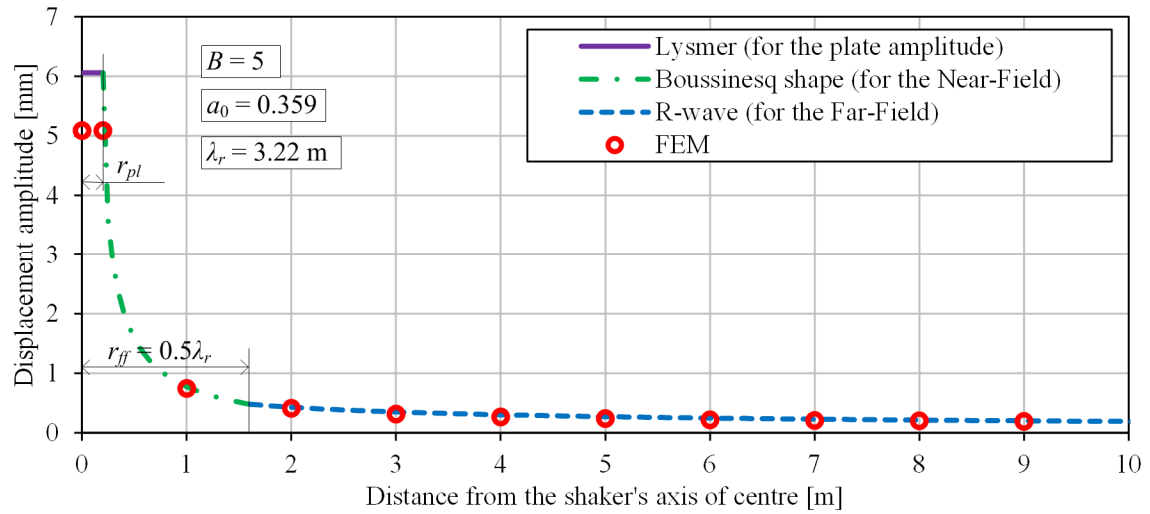


Figure D-33. Vertical vibration amplitudes of the surface ($B = 5$, $a_0 = 0.359$).

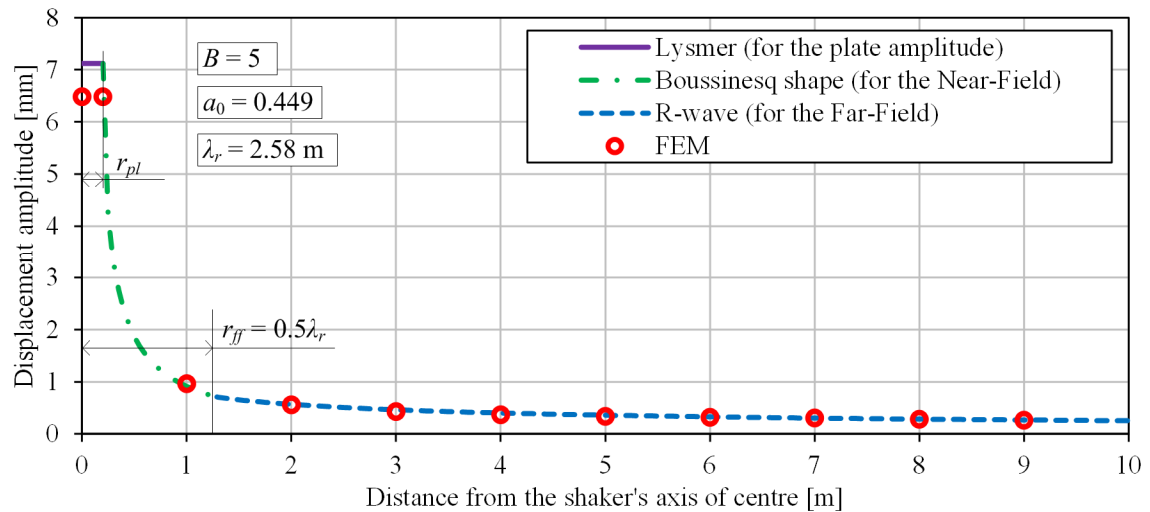


Figure D-34. Vertical vibration amplitudes of the surface ($B = 5$, $a_0 = 0.449$).

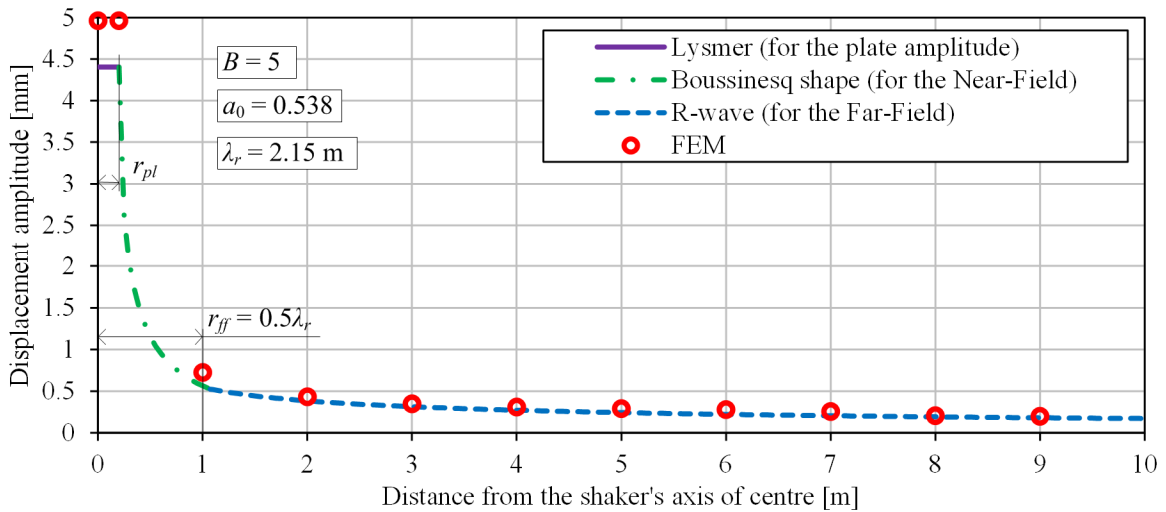


Figure D-35. Vertical vibration amplitudes of the surface ($B = 5$, $a_0 = 0.538$).

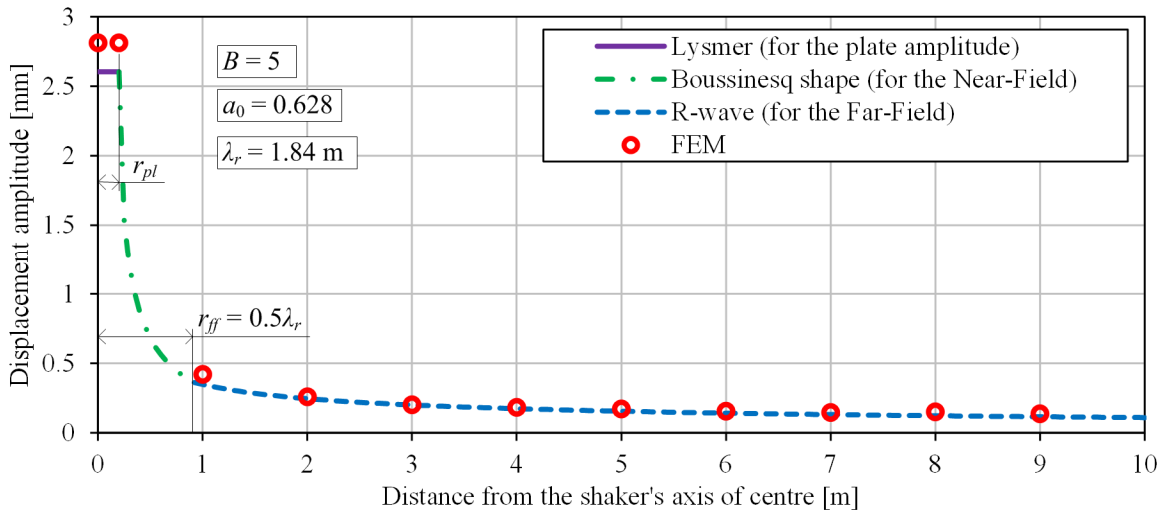


Figure D-36. Vertical vibration amplitudes of the surface ($B = 5$, $a_0 = 0.628$).

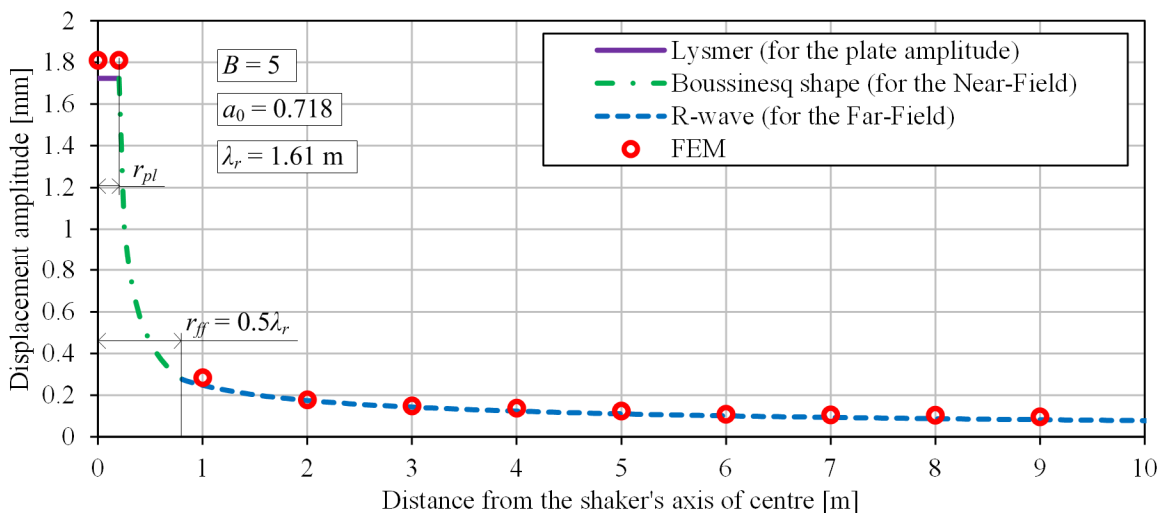


Figure D-37. Vertical vibration amplitudes of the surface ($B = 5$, $a_0 = 0.718$).

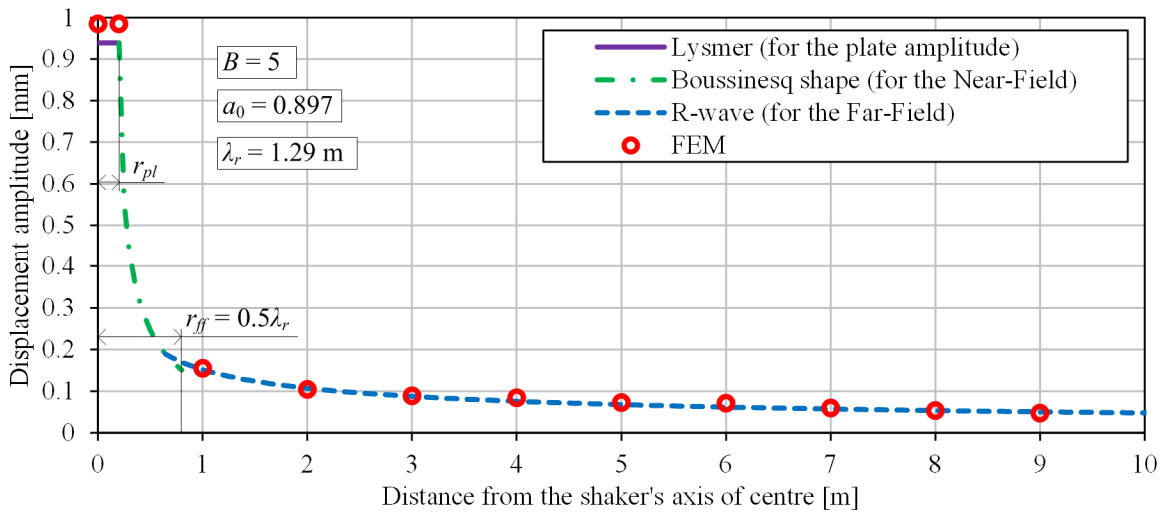


Figure D-38. Vertical vibration amplitudes of the surface ($B = 5$, $a_0 = 0.897$).

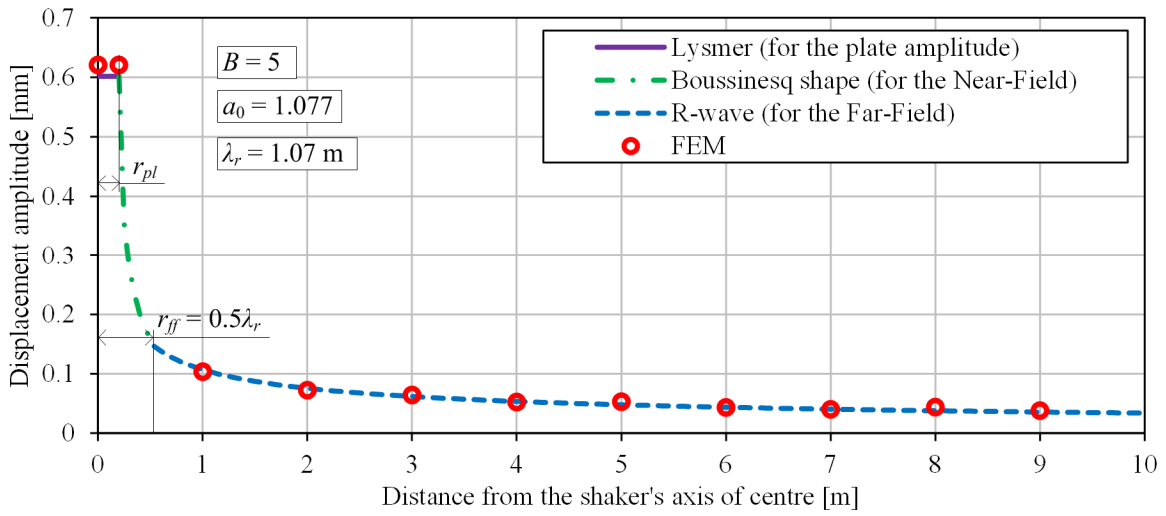


Figure D-39. Vertical vibration amplitudes of the surface ($B = 5$, $a_0 = 1.077$).

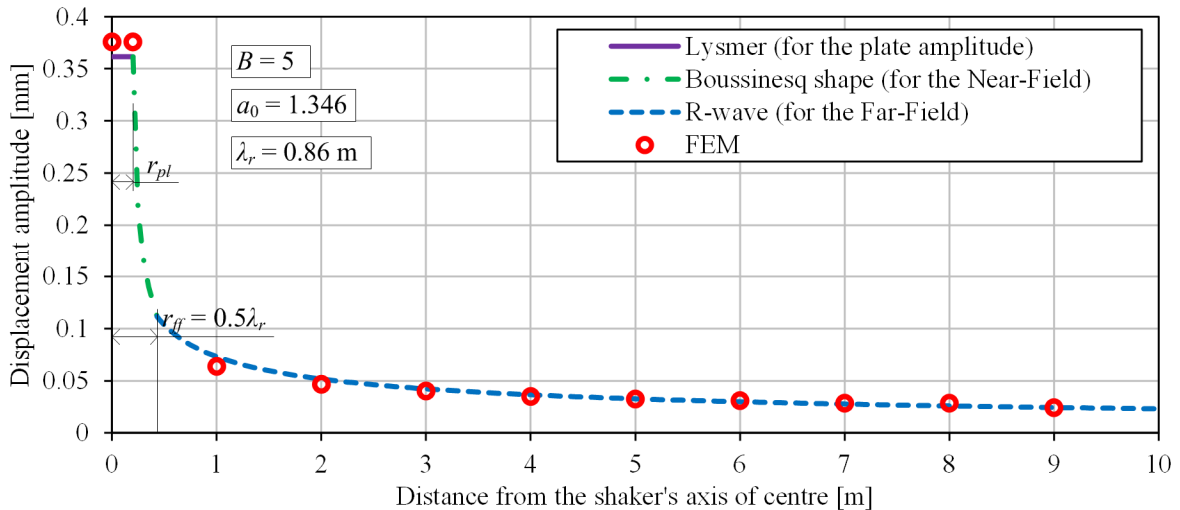


Figure D-40. Vertical vibration amplitudes of the surface ($B = 5$, $a_0 = 1.346$).

APPENDIX E. Pascal code for UDSM of Frictional damping model

Hereby a Pascal code is provided, which can be used in order to generate a DLL file. The file is made to be used as a User Defined Soil Model in Plaxis software. Free Pascal Lazarus (v. 1.2.6) was used for programming the DLL file and Plaxis 2D v9.02 was used for soil vibration calculations.

Box E-1. Pascal Code for UDSM of Shear damping.

```

library FricDamp;

// Two Soil models:
// 
// 1. Linear Elastic Soil Model
// 2. Shear Damping Soil Model
// 

{$mode Delphi}{$H+}
{$calling stdcall}

uses
  //ShareMem,
  SysUtils,
  Classes,
  Math;

const  NumbVar = 48;
       incr = 1e-10;
type   vector = array[1..6] of double;    // Sigma
        epsvector = array[1..12] of double; //dEps
        mediumvector = array[1..20] of double; //Sig0
        matrix = array[1..6,1..6] of double; //D
        longvector = array[1..50] of double; //Props
        statevector = array[1..NumbVar] of double; //StatVar { from 1 to
NumbVar }
var    Xd,G,v,E,Fac,Term1,Term2,Term3,K,dz:double; // Parameters(Props,iMod);
       EpsVol:double;                                // CalcGamma
       Gamma:vector;                                // CalcGamma;
       Eps,GammaHist,GammaMax,GammaMin,TauHist,TauMax,TauMin,DirHist:vector;
//CallHistory(StVar0,dEps)
       Dir:vector;                                // CalcDir
       Tau:vector;                                // CalcTau

{$R *.res}

procedure GetModelCount(var C:longint);stdcall;export;
begin
  C := 2;
end;

procedure GetModelName(var iModel:longint;
                      var Name:shortstring);stdcall;export;
begin
  case iModel of
    1 : Name := 'Linear Elastic';
    2 : Name := 'Shear Damping';
  else
    Name := '';
  end ;
end;

```

Continuation of Box E-1.

```

procedure GetParamCount(var iModel:longint;
                      var C:longint);stdcall;export;
begin
  case iModel of
    1 : C := 2;
    2 : C := 4;
  else
    C := 0;
  end ;
end;

procedure GetParamName(var iModel,iParam:longint;
                      var Name:shortstring);stdcall;export;
begin
  case iModel of
    1 : case iParam of
      1 : Name := 'E';
      2 : Name := '@n';
    else
      Name := '';
    end;
    2 : case iParam of
      1 : Name := '@x';
      2 : Name := 'G_mod#';
      3 : Name := 'K';
      4 : Name := '@z';
    end;
  else
    Name := '';
  end;
end;

procedure GetParamUnit(var iModel,iParam:longint;
                      var Units:shortstring);stdcall;export;
begin
  case iModel of
    1: case iParam of
      1 : Units := '[F/L^2#]';
      2 : Units := '[-]';
    else
      Units := '';
    end;
    2: case iParam of
      1 : Units := '[%]';
      2 : Units := '[F/L^2#]';
      3 : Units := '[F/L^2#]';
      4 : Units := '[-]';
    else
      Units := '';
    end;
  else
    Units := '';
  end;
end;

procedure GetStateVarCount(var iModel:longint;
                           var C:longint);stdcall;export;
begin
  case iModel of
    1 : C := 1;
    2 : C := 48;
  else
    C := 0;
  end;
end;

```

Continuation of Box E-1.

```

procedure GetStateVarName(var iModel,iParam:longint;
                           var Name:shortstring);stdcall;export;
begin
  case iModel of
    1: case iParam of
        1 : Name := 'p''';
        else
          Name := '';
        end;
    2: case iParam of
        // Current Strains
        1 : Name := '@e_xx#';
        2 : Name := '@e_yy#';
        3 : Name := '@e_zz#';
        4 : Name := '@e_xy#';
        5 : Name := '@e_yz#';
        6 : Name := '@e_xz#';
        // History of the deviatoric strains
        7 : Name := '@g_hist.xx#';
        8 : Name := '@g_hist.yy#';
        9 : Name := '@g_hist.zz#';
        10: Name := '@g_hist.xy#';
        11: Name := '@g_hist.yz#';
        12: Name := '@g_hist.xz#';
        // History of the max deviatoric strains
        13: Name := '@g_max.xx#';
        14: Name := '@g_max.yy#';
        15: Name := '@g_max.zz#';
        16: Name := '@g_max.xy#';
        17: Name := '@g_max.yz#';
        18: Name := '@g_max.xz#';
        // History of the min deviatoric strains
        19: Name := '@g_min.xx#';
        20: Name := '@g_min.yy#';
        21: Name := '@g_min.zz#';
        22: Name := '@g_min.xy#';
        23: Name := '@g_min.yz#';
        24: Name := '@g_min.xz#';
        // History of the deviatoric stresses
        25: Name := '@t_hist.xx#';
        26: Name := '@t_hist.yy#';
        27: Name := '@t_hist.zz#';
        28: Name := '@t_hist.xy#';
        29: Name := '@t_hist.yz#';
        30: Name := '@t_hist.xz#';
        // History of the max deviatoric stresses
        31: Name := '@t_max.xx#';
        32: Name := '@t_max.yy#';
        33: Name := '@t_max.zz#';
        34: Name := '@t_max.xy#';
        35: Name := '@t_max.yz#';
        36: Name := '@t_max.xz#';
        // History of the min deviatoric stresses
        37: Name := '@t_min.xx#';
        38: Name := '@t_min.yy#';
        39: Name := '@t_min.zz#';
        40: Name := '@t_min.xy#';
        41: Name := '@t_min.yz#';
        42: Name := '@t_min.xz#';
        // History of the deviatoric strains' directions
        43: Name := 'dir_xx#';
        44: Name := 'dir_yy#';
        45: Name := 'dir_zz#';
        46: Name := 'dir_xy#';
        47: Name := 'dir_yz#';

```

Continuation of Box E-1.

```
48: Name := 'dir_xz#';
else
  Name := '';
end;
else
  Name := '';
end;
end;

procedure GetStateVarUnit(var iModel,iParam:longint;
                           var Units:shortstring);stdcall;export;
begin
  case iModel of
  1: case iParam of
    1 : Units := 'F/L^2#';
    else
      Units := '';
    end;
  2: case iParam of
    // Current Strains
    1 : Units := '[-]';
    2 : Units := '[-]';
    3 : Units := '[-]';
    4 : Units := '[-]';
    5 : Units := '[-]';
    6 : Units := '[-]';
    // History of the deviatoric strains
    7 : Units := '[-]';
    8 : Units := '[-]';
    9 : Units := '[-]';
    10: Units := '[-]';
    11: Units := '[-]';
    12: Units := '[-]';
    // History of the max deviatoric strains
    13: Units := '[-]';
    14: Units := '[-]';
    15: Units := '[-]';
    16: Units := '[-]';
    17: Units := '[-]';
    18: Units := '[-]';
    // History of the min deviatoric strains
    19: Units := '[-]';
    20: Units := '[-]';
    21: Units := '[-]';
    22: Units := '[-]';
    23: Units := '[-]';
    24: Units := '[-]';
    // History of the deviatoric stresses
    25: Units := '[F/L^2#]';
    26: Units := '[F/L^2#]';
    27: Units := '[F/L^2#]';
    28: Units := '[F/L^2#]';
    29: Units := '[F/L^2#]';
    30: Units := '[F/L^2#]';
    // History of the max deviatoric stresses
    31: Units := '[F/L^2#]';
    32: Units := '[F/L^2#]';
    33: Units := '[F/L^2#]';
    34: Units := '[F/L^2#]';
    35: Units := '[F/L^2#]';
    36: Units := '[F/L^2#]';
    // History of the min deviatoric stresses
    37: Units := '[F/L^2#]';
    38: Units := '[F/L^2#]';
    39: Units := '[F/L^2#];
```

Continuation of Box E-1.

```

40: Units := '[F/L^2#]';
41: Units := '[F/L^2#]';
42: Units := '[F/L^2#]';
// History of the deviatoric strains' directions
43: Units := '[-]';
44: Units := '[-]';
45: Units := '[-]';
46: Units := '[-]';
47: Units := '[-]';
48: Units := '[-]';
else
  Units := '';
end;
else
  Units := '';
end;
end;

procedure Parameters(var Props:longvector;
                      var iMod:longint);
var DP:double;
begin
  case iMod of
    1:begin
      if Props[1] < 0 then Props[1] := -Props[1]; // E
      E := max(Props[1],incr);
      if Props[2] < 0 then Props[2] := -Props[2]; // v
      v := min(Props[2],0.495);
      G := 0.5*E/(1.0+v);
      Fac := 2*G/(1.0-2*v);
      Term1 := Fac*(1-v);
      Term2 := Fac*v;
    end;
    2:begin
      if Props[1] < 0 then Props[1] := -Props[1]; // D [%]
      DP := max(Props[1],0);
      Xd := (8-4*pi*(DP/100)) / (8+4*pi*(DP/100)); // Xd [-]
      if Props[2] < 0 then Props[2] := -Props[2]; // Gmod
      G := max(Props[2],incr);
      if Props[3] < 0 then Props[3] := -Props[3]; // K
      K := max(Props[3],incr);
      if Props[4] <= 0 then Props[4] := 1; // dz
      dz := max(Props[4],1);
      v := (3*K - 2*G) / (2*(3*K+G));
      E := 2*G*(1+v);
      Fac := 2*G/(1.0-2*v);
      Term1 := Fac*(1-v);
      Term2 := Fac*v;
    end;
  end;
end;

procedure makeD(var D:matrix);
begin
  D[1,1] := Term1;
  D[1,2] := Term2;
  D[1,3] := Term2;
  D[2,1] := Term2;
  D[2,2] := Term1;
  D[2,3] := Term2;
  D[3,1] := Term2;
  D[3,2] := Term2;
  D[3,3] := Term1;
  D[4,4] := G;
  D[5,5] := G;

```

Continuation of Box E-1.

```

D[6,6] := G;
end;

procedure makeDStiffer(var D:matrix);
begin
  D[1,1] := Term1*dz;
  D[1,2] := Term2*dz;
  D[1,3] := Term2*dz;
  D[2,1] := Term2*dz;
  D[2,2] := Term1*dz;
  D[2,3] := Term2*dz;
  D[3,1] := Term2*dz;
  D[3,2] := Term2*dz;
  D[3,3] := Term1*dz;
  D[4,4] := G*dz;
  D[5,5] := G*dz;
  D[6,6] := G*dz;
end;

procedure CallHistory(var StVar0:statevector;
                      var dEps:epsvector);
var i:longint;
begin
  for i := 1 to 6 do
  begin
    Eps[i] := StVar0[i] + dEps[i]; // 1..6
    GammaHist[i] := StVar0[i+6]; // 7..12
    GammaMax[i] := StVar0[i+12]; // 13..18
    GammaMin[i] := StVar0[i+18]; // 19..24
    TauHist[i] := StVar0[i+24]; // 25..30
    TauMax[i] := StVar0[i+30]; // 31..36
    TauMin[i] := StVar0[i+36]; // 37..42
    DirHist[i] := StVar0[i+42]; // 43..48
  end;
end;

procedure CalcGamma();
begin
  EpsVol := Eps[1]+Eps[2]+Eps[3];
  Gamma[1] := Eps[1] - EpsVol/3;
  Gamma[2] := Eps[2] - EpsVol/3;
  Gamma[3] := Eps[3] - EpsVol/3;
  Gamma[4] := Eps[4];
  Gamma[5] := Eps[5];
  Gamma[6] := Eps[6];
end;

procedure CalcDir();
var i:longint;
begin
  for i := 1 to 6 do
  begin
    if Gamma[i] > GammaHist[i] then // Going UP
      Dir[i] := 1
    else
      begin
        if Gamma[i] < GammaHist[i] then // Going DOWN
          Dir[i] := -1
        else
          Dir[i] := 0 // Standing
      end;
  end;
end;

```

Continuation of Box E-1.

```

procedure MinMax();
var i:longint;
    st:longint;
begin
    for i := 1 to 6 do
    begin
        if Dir[i] = 0 then Dir[i] := DirHist[i]; // Remove stopovers
        if Dir[i] = DirHist[i]                      // Keeping the same direction or
            keep standing
        then st := 1
        else if Dir[i] < DirHist[i] // After going Up, Goes Down
        then st := 2
        else if Dir[i] > DirHist[i] // After going Down, Goes Up
        then st := 3
        else st := 4;
        case st of
            1 :
            begin
                TauMax[i] := TauMax[i];
                TauMin[i] := TauMin[i];
                GammaMax[i] := GammaMax[i];
                GammaMin[i] := GammaMin[i];
            end;
            2 :
            begin
                TauMax[i] := TauHist[i];           // Maximum Stress Reset TauHist[i]
                TauMin[i] := -TauMax[i];
                GammaMax[i] := GammaHist[i];       // Maximum Strain Reset
                GammaHist[i];
                GammaMin[i] := -GammaMax[i];       // Minimum Strain Reset acc. to Max
                -GammaHist[i];
            end;
            3 :
            begin
                TauMin[i] := TauHist[i];           // Minimum Stress Reset TauHist[i]
                TauMax[i] := -TauMin[i];
                GammaMin[i] := GammaHist[i];       // Minimum Strain Reset
                GammaHist[i];
                GammaMax[i] := -GammaMin[i];       // Maximum Strain Reset acc. to Min
                -GammaHist[i];
            end;
            4:
            begin
                TauMax[i] := 999;                // Error
                TauMin[i] := 999;                // Error
                GammaMax[i] := 999;              // Error
                GammaMin[i] := 999;              // Error
            end;
        end;
    end;
end;

procedure CalcTau();
var i:longint;
    std:longint;
begin
    for i := 1 to 3 do
    begin
        if (Dir[i] = 1) and (Gamma[i] > GammaMax[i]) then
            std := 1 // Virgin UP
        else
            begin if (Dir[i] = -1) and (Gamma[i] < GammaMin[i]) then
                std := 2 // Virgin DOWN
    end;
end;

```

Continuation of Box E-1.

```

else begin
  if Dir[i] = 1 then
    std := 3 // History UP
  else begin
    if Dir[i] = -1 then
      std := 4 // History DOWN
    else std := 5; // Standing
  end;
end;
end;

case std of
  1 : if Gamma[i] >= 0 then
    Tau[i] := (G*power((2*Gamma[i]),Xd))
  else
    Tau[i] := (-1*G*power((-2*Gamma[i]),Xd));
  2 : if Gamma[i] >= 0 then
    Tau[i] := (G*power((2*Gamma[i]),Xd))
  else
    Tau[i] := (-1*G*power((-2*Gamma[i]),Xd));
  3 : Tau[i] := TauMin[i] + 2*G*power((abs(Gamma[i] - GammaMin[i])),Xd);
  4 : Tau[i] := TauMax[i] - 2*G*power((abs(Gamma[i] - GammaMax[i])),Xd);
  5 : Tau[i] := TauHist[i];
end;
end;

for i := 4 to 6 do
begin
  if (Dir[i] = 1) and (Gamma[i] > GammaMax[i]) then
    std := 1 // Virgin UP
  else
    begin if (Dir[i] = -1) and (Gamma[i] < GammaMin[i]) then
      std := 2 // Virgin DOWN
    else begin
      if Dir[i] = 1 then
        std := 3 // History UP
      else begin
        if Dir[i] = -1 then
          std := 4 // History DOWN
        else std := 5; // Standing
      end;
    end;
  end;
end;

case std of
  1 : if Gamma[i] >= 0 then
    Tau[i] := (G*power((2*Gamma[i]),Xd))/2
  else
    Tau[i] := (-1*G*power((-2*Gamma[i]),Xd))/2;
  2 : if Gamma[i] >= 0 then
    Tau[i] := (G*power((2*Gamma[i]),Xd))/2
  else
    Tau[i] := (-1*G*power((-2*Gamma[i]),Xd))/2;
  3 : Tau[i] := TauMin[i] + G*power((abs(Gamma[i] - GammaMin[i])),Xd);
  4 : Tau[i] := TauMax[i] - G*power((abs(Gamma[i] - GammaMax[i])),Xd);
  5 : Tau[i] := TauHist[i];
end;
end;

end;

procedure CalcDampStress(var Sig:vector);
var i:longint;
begin
  for i := 1 to 3 do

```

Continuation of Box E-1.

```

begin
  Sig[i] := Tau[i] + K*EpsVol;
  Sig[i+3] := Tau[i+3];
end;
end;

procedure SaveHist(var StVar:statevector);
var i:longint;
begin
  for i := 1 to 6 do
  begin
    StVar[i] := Eps[i];           // 1..6
    StVar[i+6] := Gamma[i];      // 7..12
    StVar[i+12] := GammaMax[i]; // 13..18
    StVar[i+18] := GammaMin[i]; // 19..24
    StVar[i+24] := Tau[i];       // 25..30
    StVar[i+30] := TauMax[i];   // 31..36
    StVar[i+36] := TauMin[i];   // 37..42
    StVar[i+42] := Dir[i];      // 43..48
  end;
end;

procedure CalcStress(var Sig:vector;
                     var dEps:epsvector;
                     var Sig0:mediumvector;
                     var D: matrix);
var i,j : longint;
begin
  for i := 1 to 6 do
  begin
    Sig[i]:= Sig0[i];
    for j := 1 to 6 do
    begin
      Sig[i] := Sig[i]+D[i,j]*(dEps[j]);
    end;
  end;
end;

procedure User_Mod(var IDTask,
                   iMod,
                   IsUndr,
                   iStep,
                   iTer,
                   Iel,
                   Int:longint;
                   var X,
                   Y,
                   Z:double;
                   var Time0,
                   dTime:double;
                   var Props:longvector;
                   var Sig0:mediumvector;
                   var Swp0:double;
                   var StVar0:statevector;
                   var dEps:epsvector;
                   var D:matrix;
                   var Bulk_W:double;
                   var Sig:vector;
                   var Swp:double;
                   var StVar:statevector;
                   var ipl,
                   nStat,
                   NonSym,
                   iStrsDep,

```

Continuation of Box E-1.

```

        iTimeDep,
        iTang,
        iPrjDir,
        iPrjLen,
        iAbort:longint);stdcall;export;

var pp: double;
var i,j:longint;
begin
  case IDtask of
  1:begin
      {initialise state variables StVar0}
      case iMod of
      1 : begin
          {Linear Elastic Model}
          pp := (Sig0[1] + Sig0[2] + Sig0[3])/3;
          StVar0[1] := Min(StVar0[1],pp);
          end;
      end; {iMod}
      end; {of IDTask = 1}

  2:begin
      {calc constitutive stresses Sig}
      case iMod of
      1: begin
          Parameters(Props,iMod);
          makeD(D);
          CalcStress(Sig,dEps,Sig0,D);
        end;
      2: begin
          Parameters(Props,iMod);
          CallHistory(StVar0,dEps);
          CalcGamma;
          CalcDir;
          MinMax;
          CalcTau;
          CalcDampStress(Sig);
          SaveHist(StVar);
          end;
      end; {of iMod}
      end; {of IDTask = 2}

  3:begin
      case iMod of
      1:
        begin
        Parameters(Props,iMod);
        makeD(D);
        end;
      2:
        begin
        Parameters(Props,iMod);
        makeDStiffer(D);
        end;
      end;
      end; {of IDTask = 3}

  4:begin
      {state variables nstat}
      nStat := 48;
      end; {of IDTask = 4}

  5:begin
      {matrix attributes}
      case iMod of

```

Continuation of Box E-1.

```

1: begin
  NonSym := 0;
  iStrsDep := 0;
  iTimeDep := 0;
  iTang := 0;
  end;
2: begin
  NonSym := 1;
  iStrsDep := 1;
  iTimeDep := 1;
  iTang := 0;
  end;
end; {of iMod}
end; {of IDTask = 5}

6:begin
  {elastic matrix De}
  case iMod of
  1:
  begin
  Parameters(Props,iMod);
  makeD(D);
  end;
  2:
  begin
  Parameters(Props,iMod);
  makeDStiffer(D);
  end;
  end;
end; {of IDTask = 6}
end;{of case}
end; {of User_Mod}

exports
  User_Mod name 'USER_MOD',
  GetModelCount,
  GetmodelName,
  GetParamCount,
  GetParamName,
  GetParamUnit,
  GetStateVarCount,
  GetStateVarName,
  GetStateVarUnit;
end.

```

CURRICULUM VITAE

Personal details

Full name: Darius Macijauskas
Birthday: January 25th, 1986 in Utena, Lithuania
Marital status: Single
Nationality: Lithuanian

Education

02/2012 – 01/2016 PhD in Geotechnical Engineering at University of Luxembourg
09/2009 – 12/2009 Erasmus internship at Vienna University of Technology, Institute of Geotechnics
09/2008 – 06/2010 MSc in Geotechnical Engineering at Vilnius Gediminas Technical University
09/2004 – 06/2008 BSc in Civil Engineering at Vilnius Gediminas Technical University

Experience

02/2016 – present Project Manager at ArcelorMittal Sheet Piling
02/2012 – 01/2016 Doctoral Candidate at University of Luxembourg, FSTC
11/2010 – 01/2012 Geotechnical Engineer at Visagino Atomine Elektrine, UAB
10/2006 – 10/2010 Engineer at Geostatyba, UAB

Languages

Lithuanian	Native
English	Professional working proficiency
German	Limited working proficiency
French	Elementary proficiency
Russian	Elementary proficiency